LIVE LOAD EFFECTS OF RAILROADS ON RETAINING WALLS AND TEMPORARY SHORING

A Dissertation

by

MEHDI MOHAMMADRAJABI

Submitted to the Office of Graduate and Professional Studies of
Texas A&M University
in partial fulfillment of the requirements for the degree of

DOCTOR OF PHILOSOPHY

Chair of Committee,	Charles Aubeny
Committee Members,	Frederick Chester
	Gary Fry
	Marcelo Sanchez
Head of Department,	Robin Autenrieth

August 2016

Major Subject: Civil Engineering

ABSTRACT

Analysis of the causes of major train derailment and its effect on accident rates shows that the second most common reason for train derailment is changes in track geometry. Excavation near railroads is a significant potential cause of changes in the track geometry. Soldier pile walls and sheet pile walls are widely used as temporary shoring systems to minimize the vertical track settlement associated with nearby excavations. Design methods for these temporary shoring systems are typically based on (1) simple limit equilibrium calculations for dead loads from the soil self-weight and (2) elastic solutions for idealized geometries for predicting the effects of live loads. Both approaches involve significant simplifications, so conservative approaches are usually adopted to offset uncertainties in the analysis methodology.

The work in this dissertation focuses on the effects of live loads on temporary shoring systems. The results of this study indicate that while existing methodology is often conservative, it can be un-conservative under certain soil and site conditions. On the one hand, excessive conservatism can lead to needless costs. On the other hand, situations can arise where simplified methods are un-conservative. All of this points to the need for improved understanding of the mechanics of the response of temporary shoring systems to live loads in specific conditions.

The existing analysis methods, when tempered by engineering judgment, usually lead to safe designs. Thus, the intent of the completed research is not to supplant existing analysis methods with complex numerical models. Rather, the goal is to improve understanding of shored wall system behavior to provide guidelines on (1) when existing

simplified analysis methods are appropriate and (2) when the simplified methods are potentially unsafe and more rigorous analyses should be undertaken. Generally, based on the finite element results it could be concluded that Boussinesq theory predicts more deflection for stiff soil and less deflection for soft soil. It means for stiff soil, the Boussinesq theory is conservative and for soft soil, it underestimates the deflection.

DEDICATION

This dissertation is dedicated to my loving parents, Rahmatollah and Zohreh, for their endless love, support and encouragement. To my wife, Somayeh, for her unyielding love, inspiration and being the best partner in this difficult journey. To my son, Mana, for being a new hope and peace in my life.

ACKNOWLEDGEMENTS

So many people helped me make this research and, consequently, this degree happen. I hardly know where to start with all of my thanks.

My deepest gratitude is to my advisor, Professor Charles Aubeny. I have been amazingly fortunate to have an advisor who gave me the freedom to explore on my own and at the same time the guidance to recover when my steps faltered. Professor Aubeny taught me how to question thoughts and express ideas. His patience and support helped me overcome many crisis situations and finish this dissertation. Besides my advisor, I would like to thank the rest of my committee, Dr. Frederick Chester, Dr. Gary Fry, and Dr. Marcelo Sanchez, for their insightful comments and encouragement as well as their guidance and support throughout this project. My dear friends have also been a great source of support and encouragement, especially Adel Khodakarami, Mohsen Mahdavi and Amir Nikooienejad, who have helped me stay sane through these challenging years. Their support and care helped me overcome setbacks and stay focused on my studies and work.

Most importantly, none of this would have been possible without the love and patience of my family. My immediate family, to whom this dissertation is dedicated, has been a constant source of love, support, and strength all these years. I would like to express my heart-felt gratitude to them all. Finally, this research would not have been possible without the support of the Texas Department of Transposition, Texas Transportation Institute, Union Pacific Railroad, and the Center for Railway Research, and I would like to express my gratitude to them all.

TABLE OF CONTENTS

Page

LIST OF FIGURES

Page

LIST OF TABLES

1 INTRODUCTION

1.1 Overview of Railroads in the United States of America

Railroads have played a prominent role in the social and economic development of the United States of America (US) since their invention and development in the early nineteenth century (Association of American Railroads, 2012).The miles of railroad operated in the U.S. was about 168,851 miles by the end of 2010, according to statistics from American Railroad Associations, making it the world's largest railroad network in terms of total length. Figure 1 shows rail line ownership based on the 2011 National Transportation Atlas Database published by the U.S. DOT's Bureau of Transportation Statistics (Association of American Railroads, 2012).

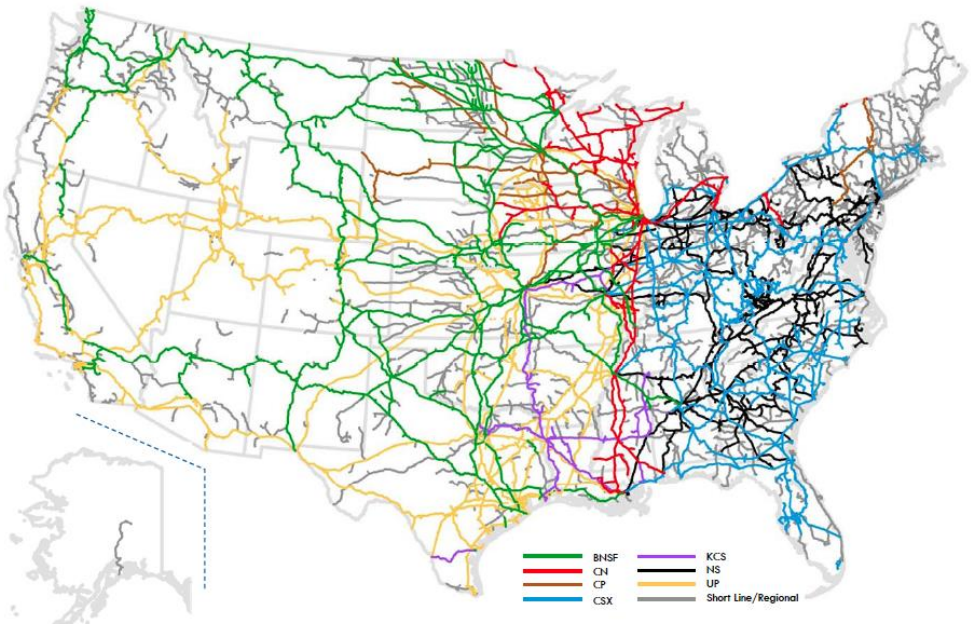

Figure 1. Railroad network in the United States of America in 2011 (Association of American Railroads, 2012)

The total length of the US railway system exceeds the combined length of those of Russia and China, which are ranked as the second and third largest railroad networks in the world. The U.S. freight railroads generated the revenue of about $59.6 billion in the year of 2010, which surpassed the revenue generated by trucks, air, and water as shown in Figure 2 (Association of American Railroads, 2012). All in all, transportation is the key to the way our modern society works and the railroads play preeminent role in this way especially in the US economy.

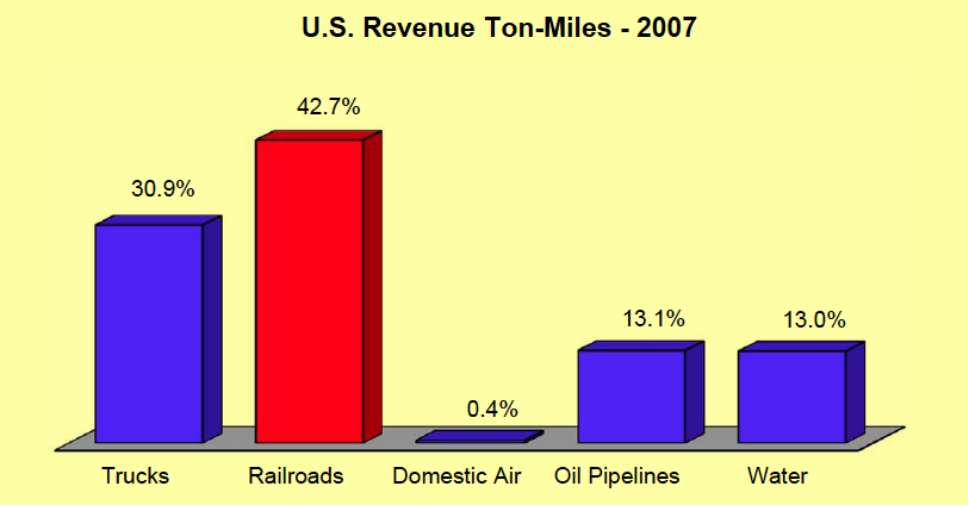

Figure 2. Comparison of the revenue (Association of American Railroads, 2012)

Currently, there are about 565 freight railroads in the US railroad system, employing nearly 170,000 workers. The top 9 major North American freight railroads are listed in Table 1, among which Union Pacific (UPRR) railroad and Burlington Northern

Santa Fe (BNSF) railroad are the largest and second largest railroad networks, respectively in US (Association of American Railroads, 2012).

Table 1. Major North American freight railroads (Association of American Railroads, 2012)

BNSF	Burlington Northern Santa Fe Railway
CN	Canadian National Railway
CP	Canadian Pacific Railway
CSX	CSX Transportation
FXE	Ferrocarril Mexicano
KCS	Kansas City Southern Railway
NS	Norfolk Southern
KCSM	Kansas City Southern de Mexico
UPRR	Union Pacific railroad

The state of Texas continues to have more railroad mileage than any other states and the largest number of railroad employees. Based on the statistic by the Association of American Railroads, the numbers of freight railroads are 47, the freight railroad mileage is about 10,384, and the numbers of freight rail employees are 15,534. Figure 3 presents the rail line ownership in Texas based on the 2011 National Transportation Atlas Database published by the U.S. DOT's Bureau of Transportation Statistics. UPRR and BNSF are

also the two major railroad networks in the state of Texas (Association of American Railroads, 2012).

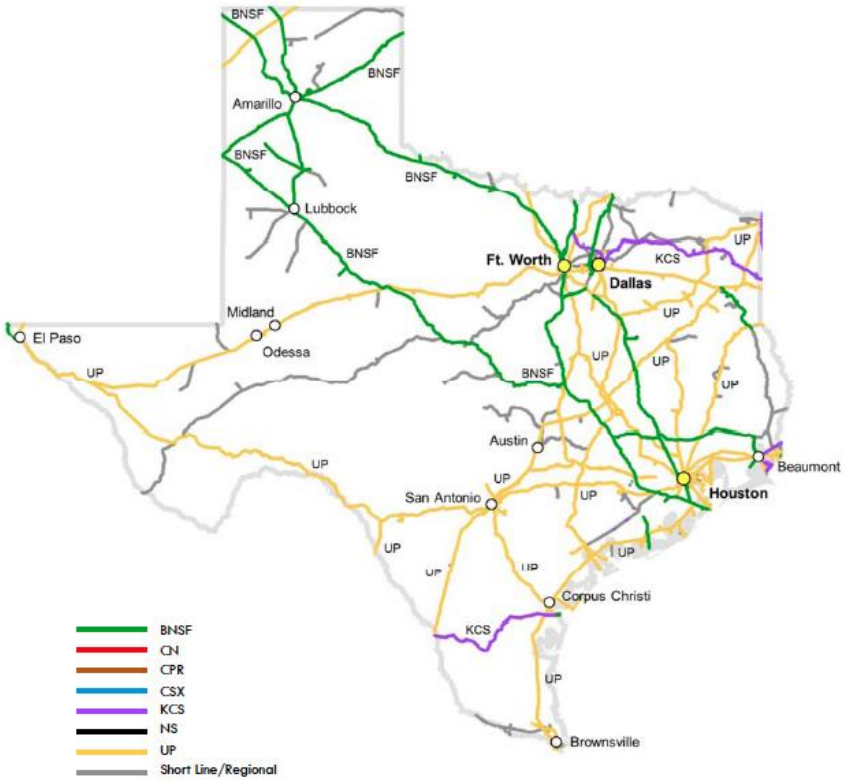

Figure 3. Railroad network in Texas at 2011(Association of American Railroads, 2012)

The new construction of railroads has become negligible in recent years. There has been no significant increase in the total length of the railroad since 2006. The maintenance and upgrade of the existing railroad structures are the primary activities of the railroad. Meanwhile, the US highway system is experiencing major reconstruction and widening. The construction activity of the US highways sometimes is extended into the influence

zone of the railroads. Volume 1, Part 8 of American Railway Engineering and Maintenance-of-Way Association (AREMA, 2010) presents the rules, policies, and safety regulations when highway construction or railroad construction enters the influence zone of the other.

1.2 Retaining Walls

Retaining walls and temporary shoring are extensively used to provide permanent and temporary support for excavation near railroads (Tatsuoka et al. 1996; Smethurst and Powrie 2007). The Manual for Railway Engineering published by American Railway Engineering and Maintenance-of-Way Association (AREMA) in 2010 and the Guidelines for Temporary Shoring (GTS) published jointly by the Burlington North Santa Fe Railway (BNSF) and the Union Pacific (UPRR) in 2004 are the two major guidelines for retaining walls and shoring practice in railroads in the US. The commonly used retaining walls and temporary shoring for railroads are listed in Table 2.

Table 2. Retaining wall and shoring types (GTS 2004; AREMA 2010)

Retaining walls						
Type	Gravity wall	Counterfort wall	Buttress wall	Crib wall	MSE wall	Anchored walls
Applicable conditions	General	General	General	General	General	*
Temporary shoring						
Type	Shoring box	Anchored system with tiebacks	Cantilever sheet pile	Cantilever soldier beam with lagging	Braced excavation	Cofferdam
Applicable conditions	No railroad live load	*	Only in granular soil or stiff clay	General	General	Primarily used with steel sheet pile

*Retaining walls and temporary shoring using tieback anchors are discouraged since the anchors may be in conflict with existing or future utility lines (Burlington North Santa Fe Railway and Union Pacific 2004).

General shoring requirements are showed in Figure 4 (GTS 2004). GTS recommendations indicate that: "no excavation should be permitted closer than 12 ft. 0 in. measured at a right angle from the centerline of track to the trackside of a shoring system; lateral clearances must provide sufficient space for construction of the required ditches parallel to the standard roadbed section, and the shoring system must be designed to support the theoretical embankment shown for zones A and B"

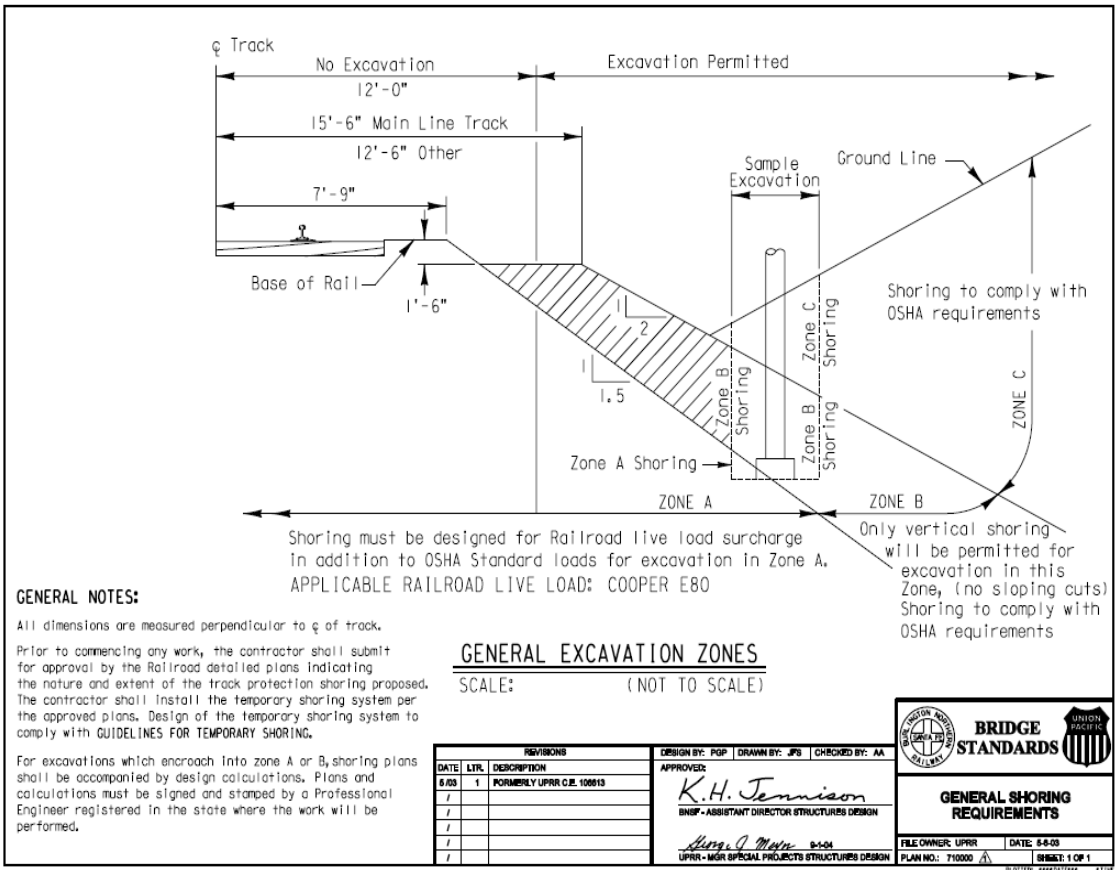

Figure 4. General shoring requirements (GTS, 2004)

1.3 Overview of Temporary Shoring System

Shoring systems are supporting structures providing lateral support for a mass of soil and slopes when an excavation and separation is required. The most common types of temporary shoring systems are sheet pile walls and soldier pile walls whose resistance depends on the passive resisting capacity of the soil below the depth of excavation and the tensile resistance of the anchors if an anchor was used. In these kinds of walls, passive resistance is determined by the depth of embedment to prevent the wall rotation. This depth required is determined by using the difference between the passive and the active

pressure acting on the wall. The theoretical depth of pile penetration below the depth of excavation is obtained by equating horizontal forces and by taking moments about an assumed bottom of piling. Based on the Guidelines for Temporary Shoring (GTS, 2004), the temporary shoring systems can be classified as follows:

1. “A shoring box comprised of a prefabricated shoring system installed as the excavation progresses: This shoring system is not accepted by the railroad.

2. An anchored system with tiebacks: This type of system is discouraged since tiebacks are an obstruction to future utility installations and may also damage existing utilities.

3. An anchored sheet pile wall.

4. An anchored soldier beam with lagging wall: These are generally designed as flexible structures with sufficient lateral movement to mobilize active earth pressures and a portion of the passive pressure.

5. A cantilever sheet pile wall: This structure is designed to provide lateral support for a soil mass and derives stability from passive resistance of the soil in which the sheet pile is embedded. Cantilever sheet pile walls should be used only in granular soils or stiff clays.

6. A cantilever soldier beam with lagging wall.

7. A braced excavation.

8. A cofferdam: This is an enclosed temporary structure used to keep water and soil out of an excavation for a permanent structure such as a bridge pier, abutment,

or similar structure. These guidelines consider cofferdams primarily constructed with steel sheet piles)".

According to the trenching and shoring manual (California Department of Transportation, 2011), shoring systems are generally classified as restrained shoring systems either anchored or braced walls and unrestrained (non-gravity cantilevered) constructed of vertical structural members consisting of partially embedded soldier piles or continuous sheet piles. The economical height of this type of wall is generally limited to a maximum of 18 ft. (California Department of Transportation, 2011).

Two types of unrestrained shoring systems, sheet pile walls and soldier pile walls, exist:

- Sheet pile: Cantilever sheet pile retaining walls may develop large deflections, thus, they are mainly used for temporary excavations not greater than about 18 ft. in depth. . However, the use of struts and/or anchors can increase acceptable/safe wall height in sheet pile walls.
- Soldier pile: The maximum height of soldier pile walls is limited to competence of the foundation material and the moment resisting capacity of the vertical structural members. The economical height of this type of wall is generally limited to a maximum of 18 ft. (California Department of Transportation state of California, 2011).

1.3.1 Soldier Pile Walls

Soldier pile walls are one of the oldest forms of retaining systems used in deep excavations. The main components of such soldier wall excavation support systems are

steel H-piles placed vertically with lagging between the piling to retain the soil. An example of a soldier wall is presented in Figure 5.

Figure 5. The soldier pile wall installed by Union Pacific

The lagging can be made of timber, metal, or even concrete. H-piles can be installed by driving, vibrating, or drilling a hole and wet setting the pile in a grout column at the bottom of the excavation. Soldier piles are placed prior to excavation, and as the excavation advances, lagging is placed between the soldier piles. Construction of soldier pile walls is shown in Figure 6; this process encompasses five main stages as follows:

1. Drilling the holes,
2. Installing the H-piles,
3. Continuing the excavation to the planed level,
4. Installing the lagging, and

5. In case it is needed, stabilizing the wall by anchors or struts.

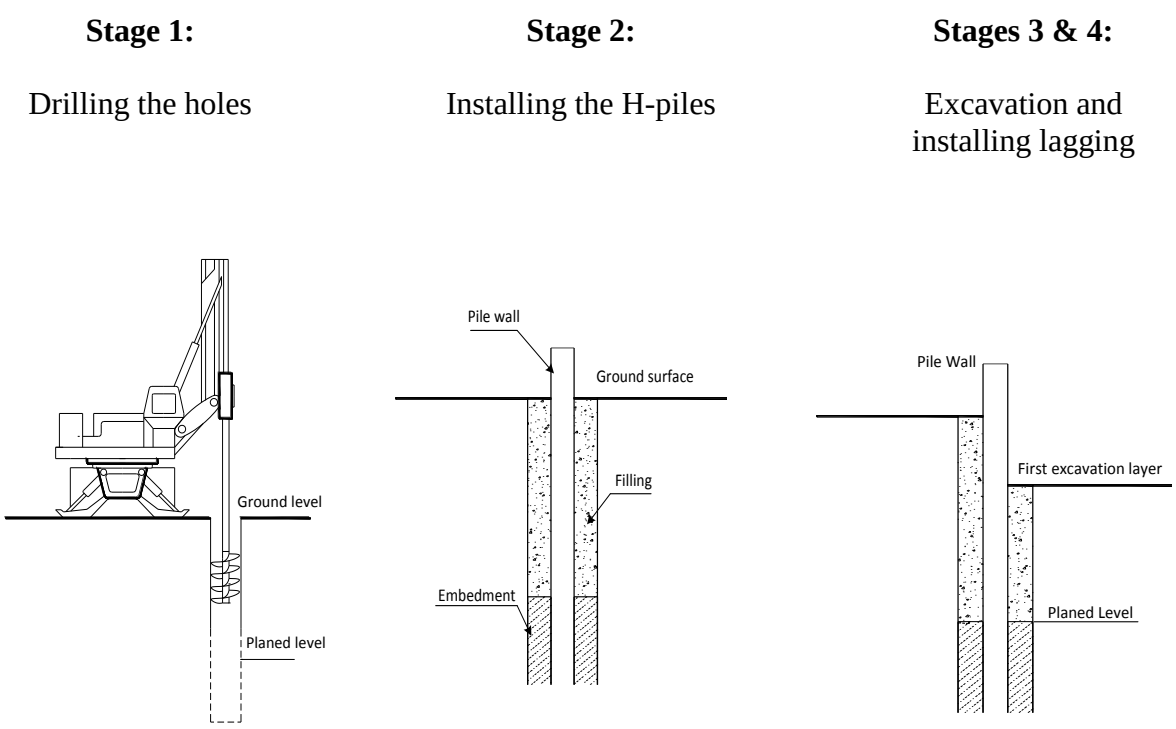

Figure 6. Diagram of the construction of a soldier pile wall

1.3.2 Sheet Pile Walls

In these kind of walls, a series of sheet panels with interlocking connections are used. Sheets can be made of steel, vinyl, plastic, wood, reinforced concrete, and fiberglass. They are installed before the excavation with the impact or the vibrating hammer based on the soil type to form a vertical wall that support the soil. Figure 7 shows a sheet pile wall as a supportive wall.

Figure 7. Sheet pile wall installed by Union Pacific

Construction of sheet pile walls is shown in Figure 8. This process involves four main steps as follows:

1. Driving (or vibrating) the individual sheet piles into the ground to the desired depth.

2. Driving the interlocking sheet pile between the first sheet pile and second "locked."

3. Repeating steps 2 & 3 until the perimeter wall is completed.

4. Using connector elements when more complex shapes are used.

Stage 1. Installing the first pile

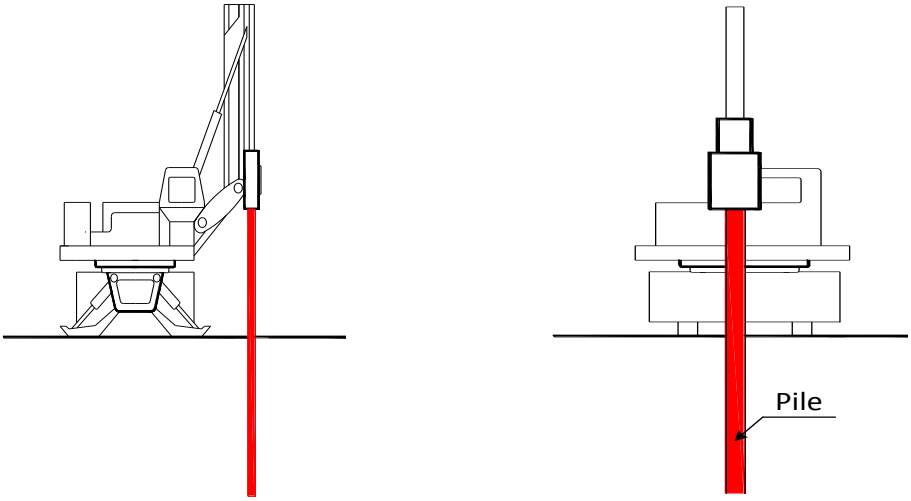

Figure 8. Diagram of the construction of a sheet pile wall

Stage 2. Installing the second pile

Stage 3. Repetition of process

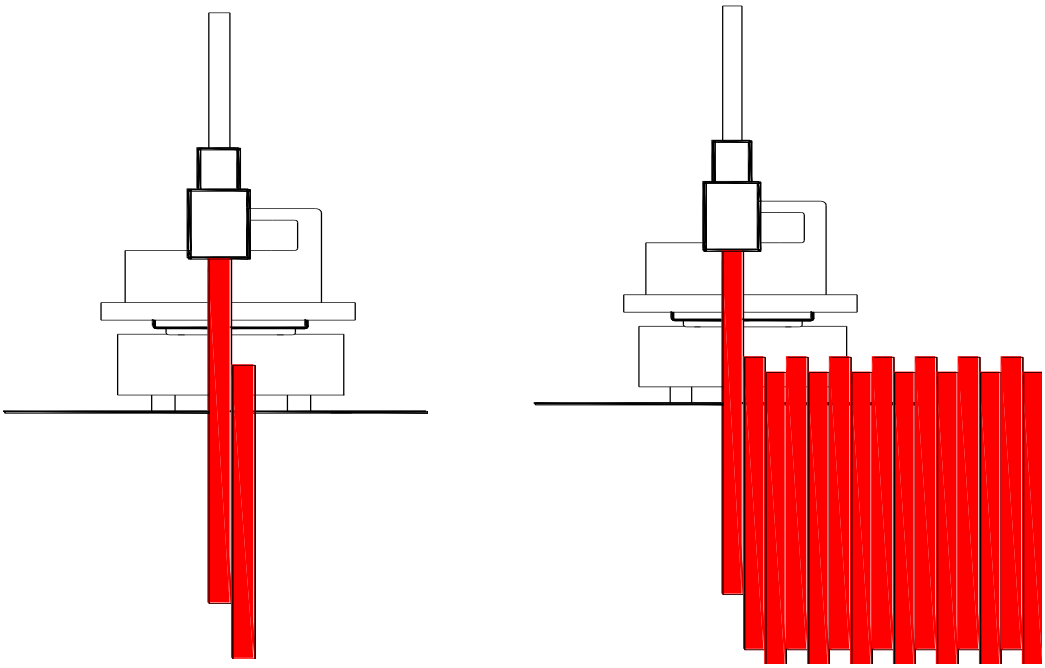

Figure 8. Continued

1.4 Outline and Objective of Research

1.4.1 Problem Statement

Excavation near railroads creates special problems including changes in the track geometry and more settlement beneath the track due to the excavation, both of which can increase the chance of train derailment (Liu et al., 2012). (Figure 9).

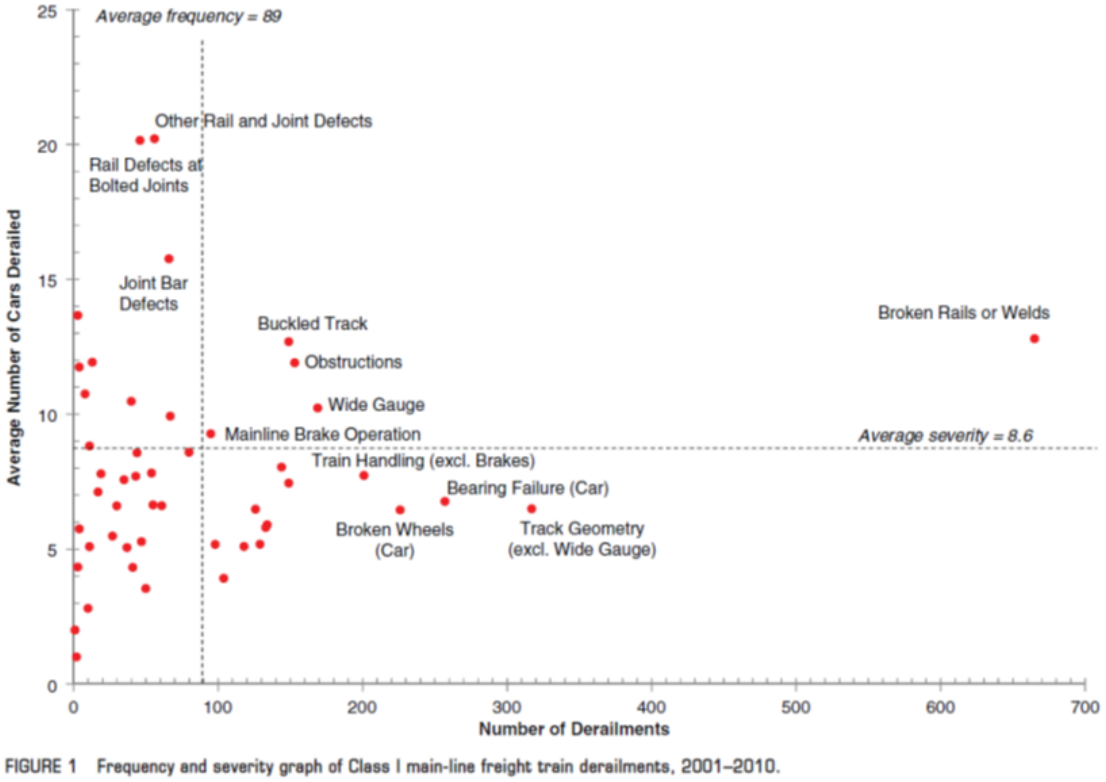

FIGURE 1 Frequency and severity graph of Class I main-line freight train derailments, 2001–2010.

Figure 9. Analysis of the causes of major train derailments and their effect on accident rates (Liu et al., 2012).

In fact, excavation near the railroads results in larger vertical deflection in the subsoil due to the combination of static and dynamic load. The main goal of this research is to obtain an improved understanding of shored wall system behavior in order to provide guidelines as to (1) when existing simplified analysis methods are appropriate and (2) when the simplified methods are potentially unsafe and more rigorous analyses are necessary.

For example, the use of simplified analysis methods may be appropriate for a wall embedded in dense sand or stiff clay. By contrast, if soft clay layers are present, the

simplified analysis may prove insufficient, in which case a more rigorous analysis is warranted.

The judgment as to when more rigorous analysis is needed can only be made based on a thorough understanding of the mechanics of a shored wall system. Factors that significantly affect wall response include the depth of wall embedment, wall height, wall length, wall stiffness, and soil stiffness. For soldier pile and timber lagging systems, additional complexities arise in connection with arching and load transfer to the piles

Vertical track settlement is typically of prime importance to railroad safety. Thus, lateral deflections of wall systems are indirectly related to safety, since lateral movements in the soil mass tend to increase vertical settlement. Strictly speaking, a comprehensive study of live load effects must ultimately address vertical settlement. However, this study is limited in time and budget, so the scope and focus are limited to lateral wall movements. Once an understanding of lateral wall movements has been achieved, the relationship between lateral wall movement and vertical settlement beneath the track needs to be undertaken in future research.

1.4.2 Organization

In order to fulfill the purpose of this work, it is organized as follows. Chapter two consists of a literature review and collection of information available from railroad networks. The literature review covers the major scientific and engineering databases. Chapter three covers the results of site investigations and geotechnical laboratory tests used in this research. Chapter four provides the results on the lateral deflection in the various temporary shoring systems under different conditions. Results of the static lateral

deflection were compared to the results of some conventional methods such as Boussinesq theory. Furthermore, the results of a number of numerical analyses are given, which were completed using ABAQUS, in order to show the effects of different stiffness systems, different depths of excavation, different soils, and different distances between loads and walls. Chapter five introduces the dynamic behavior of the soil due to the cyclic loading. Finally, the summary of research and some recommendations for future studies are presented in chapter six.

2 LITERATURE REVIEW

2.1 Overview of Soil Classification and Backfill Material

In this section, some soil classifications, backfill materials, as material behind the wall, whether undisturbed ground or fill, contributing to the pressure against the wall, and deposits based on soil conditions are defined. Backfill is defined as material behind the wall, whether undisturbed ground or fill, contributing to the pressure against the wall

2.1.1 Soil Classification by California Occupational Safety and Health Standards for Excavations

A system of soil classification that may be used for the proper selection of a shoring system is contained in Appendix A to Construction Safety Order Section 1541.1. Per this document, soil and rock deposits are classified into type A, type B, and type C based on decreasing stability. The definitions of these soils are as follows (California Department of Transportation, 2011):

- ***"Type A soil***

Type A soil is cohesive soil with an unconfined compressive strength of 1.5 tons/ft.^{2} (tsf) or greater. Clay, silty clay, sandy clay, clay loam and, in some cases, silty clay loam and sandy clay loam are cohesive-soils. Cemented soils such as caliche and hardpan are also considered Type A. However, no soil that meets any one of the following conditions is Type A:

1. The soil is fissured;
2. The soil is subject to vibration from heavy traffic, pile driving, or similar effects;

3. The soil has been previously disturbed;
4. The soil is part of a sloped, layered system where the layers dip into the excavation on a slope of four horizontal to one vertical (4H:lV) or greater; or
5. The material is subject to other factors that would require it to be classified as a less stable material.

- ***Type B soil***

Soils that fall into the Type B category are less cohesive than Type A and more cohesive than Type C, as logically follows from the fact that the types are in order of descending stability. In order to be considered Type B, soils meet one of the following conditions:

1- Cohesive soil with an unconfined compressive strength greater than 0.5 tsf but less than 1.5 tsf.
2- Granular, cohesionless soils including angular gravel (similar to crushed rock), silt, silt loam, sandy loam and, in some cases, silty clay loam and sandy clay loam.
3- Previously disturbed soils, except those which would otherwise be classified as Type C soil.
4- Soil meeting the unconfined compressive strength or cementation requirements for Type A but which is fissured or subject to vibration.
5- Dry rock that is not stable.

6- Material that is part of a sloped, layered system where the layers dip into the excavation on a slope less steep than four horizontal to one vertical (4H:1V), but only if the material would otherwise be classified as Type B.

- ***Type C soil***

1- The least cohesive class of soil according to this source is Type C. Classification into this category is based on the following criteria:Cohesive soil with an unconfined compressive strength of 0.5 tsf or less.

2- Granular soils including gravel, sand, and loamy sand.

3- Submerged soil or soil from which water is freely seeping.

4- Submerged rock that is not stable".

2.1.2 Soil Classification by the California Department of Transportation

The California Department of Transportation (Caltrans, 2011) *Soil and Rock Logging, Classification, and Presentation Manual*, published and maintained by California Geotechnical Services, presents the department's practice for identification, classification, description, and presentation of soil and rock for all investigations after August 1, 2007. The group name and symbol of a soil type is determined using one of the following guides.

- If laboratory testing is *not performed*, ASTM D 2488-06, "Standard Practice for Description and Identification of Soils (Visual-Manual Procedure)," is applied.
- In the case that laboratory particle size analysis and plasticity index tests are performed, ASTM D 2487-06, "Standard Practice for Classification of Soils for

Engineering Purposes (Unified Soil Classification System)," is used to classify the soil.

In this Caltrans manual, soils are identified or classified as either coarse grained (gravel and sand) or fine grained (silts and clays). Natural soil consists of one or any combination of gravel, sand, silt, or clay, and may also contain boulders, cobbles, and organic materials. Coarse-grained soils are classified as soils in which more than 50% of the materials are at or above the no. 200 sieve (0.075 mm) size. Gravel (G) and sand (S) are further classified according to the following characteristics: well graded (W) or poorly graded (P), silt content (M), or clay content (C). The properties of granular soils are presented in tables 3 and 4.

Table 3. Properties of granular soils (California Department of Transportation, 2011)

Apparent Density	Relative Density (%)	SPT, N60 (blows/ft.)	Friction Angle, Ø (deg)	Unit Weight (pcf)	
				Moist	Submerged
Very Loose	0-15	N60 < 5	<28	<100	<60
Loose	16-35	5 ≤ N60 < 10	28-30	95-125	55-65
Medium Dense	36-65	10 ≤ N60< 30	31-36	110-130	60-70
Dense	66-85	30 ≤ N60 < 50	37-41	110-140	65-85
Very Dense	86-100	N60 ≥ 50	>41	>130	>75

Table 4. Simplified typical soil values (California Department of Transportation, 2011)

Soil Classification	Ø Friction angle of the soil	Density or Consistency	γ Soil unit weight (pcf)	K_a Coefficient of active earth pressure
Gravel, Gravel-Sand mixture, coarse sand	41	Dense	130	0.21
	34	Medium Dense	120	0.28
	29	Loose	90	0.35
Medium sand	36	Dense	117	0.26
	31	Medium Dense	110	0.32
	27	Loose	90	0.38
Fine sand	31	Dense	117	0.32
	27	Medium Dense	100	0.38
	25	Loose	85	0.41
Fine silty sand, Sandy silt	29	Dense	117	0.35
	27	Medium Dense	100	0.38
	25	Loose	85	0.41
Silt	27	Dense	120	0.38
	25	Medium Dense	110	0.41
	23	Loose	85	0.44

In the absence of field or laboratory test results, cohesive soils can be classified according to shear strength and density, as shown in Table 5.

Table 5. Properties of cohesive soils. (California Department of Transportation, 2011)

Consistency	Unconfined Compressive Strength (psf.)	Moist Unit Weight (pcf)
Very Soft	0-500	<100-110
Soft	500-1,000	100-120
Medium Stiff	1,000-2,000	110-125
Stiff	2,000-4,000	115-130
Very Stiff	4,000-8,000	120-140
Hard	>8,000	>132

Typically, Caltrans uses one or more of the following techniques to determine a soil's identification, classification, description, and strength:

- Standard Penetration Test (SPT) with visual/manual methods
- Cone Penetration Test (CPT)
- Laboratory Testing

Table 6. Field and laboratory test reliability of soil shear strength measurements (California Department of Transportation, 2011)

Test Method	Coarse-grained Soil	Fine-grained Soil
Standard Penetration Test (SPT) (ASTM D 1588)	Good	Poor
Cone Penetration Test (CPT) (ASTM D 3441)	Good	Fair
Pocket Penetrometer	Not applicable	Fair
Vane Shear (ASTM D 2573)	Not applicable	Very good
Triaxial Compression (UU,CU) (ASTM D 2850)	Very good*	Very Good
Unconfined Compression (ASTM D 2166)	Not applicable	Very good
Direct Shear (ASTM D 3080)	Good*	Fair

2.1.3 Backfill Soil Characteristics by Guidelines for Temporary Shoring System (GTS)

Wall design should always be based on the type of backfill soil used. According to GTS (2004), backfill should be investigated and classified with reference to the soil types described in Table 7 (AREMA Table 8-5-1, 2010). In the GTS manual, backfill soils are classified in five categories based on particle size and other characteristics. Backfill types 4 and 5 should be used only with special permission from the engineer.

Table 7. Types of backfill for retaining walls (Table 8-5-1 AREMA, 2010)

Backfill Type	Backfill Description
1	Coarse-grained soil without admixture of fine soil particles, very free-draining (clean sand, gravel, or broken stone).
2	Coarse-grained soil of low permeability due to admixture of particles of silt size.
3	Fine, silty sand; granular materials with conspicuous clay content; or residual soil with stones.
4	Soft or very soft clay, organic silt, or soft silty clay.
5	Medium or stiff clay that may be placed in such a way that a negligible amount of water will enter the spaces between the chunks during floods or heavy rains.

The unit weight, cohesion, and angle of internal friction of the backfill material should be determined directly by means of soil tests or, if the expense of such tests is not justifiable, by means of tables 8 and 9 (AREMA, Table 8-5-2 and 8-20-3), which refer to the soil types defined in Table 7. According to the GTS manual, unless the minimum cohesive strength of the backfill material can be evaluated reliably, cohesion should be neglected and only the internal friction considered (GTS 2004).

Table 8. Properties of backfill materials (Table 8-5-2 AREMA, 2010)

Type of Backfill	Unit Weight (pcf)	Cohesion "c"	Angle of Internal Friction
1	105	0	33°-42°(38°for broken stone)
2	110	0	30°
3	125	0	28
4	100	0	0
5	120	240	0

Table 9. Unit weight of soils and coefficients of earth pressure (Table 8-20-3 AREMA, 2010)

Type of soil	Unit weight of moist soil, pcf		Unit weight of submerged soil, pcf		Coefficient of active earth pressure, K_a				Coefficient of passive earth pressure, K_p		
					For Backfill	For Soil in place	Friction angles		For soil in place	Friction angles	
	Minimum	Maximum	Minimum	Maximum			φ	δ		φ	δ
Clean Sand											
Dense	110	140	65	78		0.2	38	20	9	38	25
Medium	110	130	60	68		0.25	34	17	7	34	23
Loose	90	125	56	63	0.35	0.30	30	15	5	30	20
Silty Sand											
Dense	110	150	70	88		0.25			7		
Medium	95	130	60	68		0.30			5		
Loose	80	125	50	63	0.5	0.35			3		
Silt and Clay											
	$\frac{165(1+w)}{1+2.65w}$		$\frac{103}{1+2.65w}$		1	$1 - \frac{q_u}{P+\gamma\bar{z}}$			$1 + \frac{q_u}{P+\gamma\bar{z}}$		

2.2 Lateral Pressure on Temporary Shoring Systems

2.2.1 Earth Pressure

The physical properties of backfill, the interaction at the soil-pile wall interface, the location of the groundwater table, seepage forces, surcharge loads, and deformation in the soil-pile wall system all affect the intensity of earth pressure on the temporary shoring systems. In addition, the time dependent nature of soil strength could change the magnitude of earth pressure. The lateral deformation of a pile wall was a major feature in developing earth pressure.

Horizontal stresses acting on a retaining wall are commonly classified in terms of three deformation states: active, passive, and at-rest. The at-rest state corresponds to zero lateral stress, which would correspond to a relatively rigid shoring system. Passive earth pressure can develop in regions where the wall pushes into the soil, while active earth pressure develops in systems in which the wall deforms away from the soil mass.

Active and passive earth pressure conditions are limited states that require a sufficient level of deformation to develop. In the case of active pressure, large deformations are not typically required. However, large deformations usually must occur for a passive condition to mobilize, which can be a consideration in design. Typical values of these mobilizing movements relative to the wall height are given in Table 10 (Clough and Duncan 1991).

Table 10. Mobilized wall movements (Clough and Duncan 1991; AASHTO 2010)

Type of Backfill	Value of Δ/H*	
	Active	Passive
Dense Sand	0.001	0.01
Medium Dense Sand	0.002	0.02
Loose Sand	0.004	0.04
Compacted Silt	0.002	0.02
Compacted Lean Clay	0.010	0.05
Compacted Fat Clay	0.010	0.05

*Δ is the movement of the top of the wall required to achieve minimum active or maximum passive pressure, either by tilting or lateral translation; H is the height of wall.

Lateral earth pressure is typically related to vertical effective stress through earth pressure coefficients, with K_o defined as at-rest earth pressure coefficient, K_a as the active earth pressure coefficient, and K_p as the passive earth pressure coefficient.

For at-rest conditions in normally consolidated soils and vertical walls, the K_o can be calculated by Equation 1 (California trenching and shoring manual, 2011):

$$K_o = (1 - \sin\emptyset)(1 - \sin\beta) \quad (1)$$

where:

$\emptyset$ = Effective friction angle of soil; K_0 = Coefficient of at-rest lateral earth pressure; and β = Slope angle of backfill surface behind retaining wall.

For over-consolidated soils, level backfill, and vertical walls, this coefficient may be taken by Equation 2 (California trenching and shoring manual, 2011)

$$K_o = (1 - \sin\emptyset)(OCR)^{\sin\emptyset} \quad (2)$$

where OCR is the over-consolidation ratio.

For active and passive conditions, two well-known classical earth pressure theories exist: the Rankine Theory (1857) and the Coulomb Theory (1776). The Rankine theory is simpler and is based on the plastic equilibrium condition. In Figure 10, a visual representation of the Rankine Theory is presented.

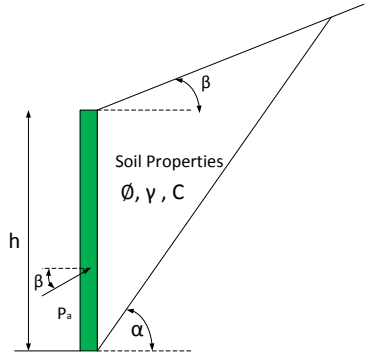

Figure 10. Earth pressure calculated using the Rankine Theory (after California trenching and shoring manual, 2011)

In Equations 3 and 4, values of the coefficient of the active (Eq. 3) and the passive (Eq. 4) earth pressure in the Rankine Theory are presented (California trenching and shoring manual, 2011):

$$K_a = \cos\beta \frac{\cos\beta - \sqrt{\cos^2\beta - \cos^2\emptyset}}{\cos\beta + \sqrt{\cos^2\beta - \cos^2\emptyset}} \quad (3)$$

$$K_p = \cos\beta \frac{\cos\beta + \sqrt{\cos^2\beta - \cos^2\emptyset}}{\cos\beta - \sqrt{\cos^2\beta - \cos^2\emptyset}} \quad (4)$$

The magnitude of active and passive earth pressure can be calculated using Equations 5 (active) and 6 (passive):

$$P_a = \gamma h k_a - 2c\sqrt{k_a} \quad (5)$$

$$P_P = \gamma\, h\, k_p + 2c\sqrt{k_p} \quad (6)$$

where P_a is active earth pressure; P_p is passive earth pressure; gamma is unit weight; h is height; k_a is active earth pressure coefficient; k_p is passive earth pressure; and c is cohesion.

The Rankine theory neglects the friction between the wall and the soil; however, this friction can affect the magnitude of the lateral pressure on the wall. In contrast, the Coulomb theory does consider the effect of wall friction (δ) in the lateral earth pressure. For the active case, when the active wedge slides downward relative to the wall, the wall friction (δ) is defined as positive. In the passive case, when the passive wedge slides upward relative to the wall, wall friction is defined as negative. Figure 11 shows the Coulomb earth pressure.

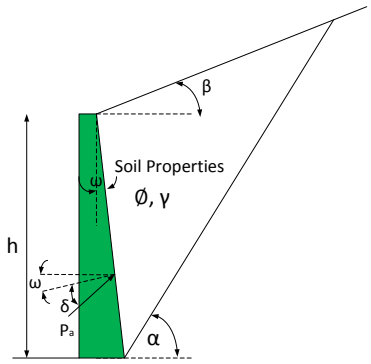

Figure 11. Earth pressure calculated using the Coulomb Theory (after California trenching and shoring manual, 2011)

In the Coulomb case, the active earth pressure (K_a) and passive earth pressure (K_p) can be calculated by Equations 7 and 8, respectively (California trenching and shoring manual, 2011).

$$K_a = \frac{\cos^2(\emptyset-\omega)}{\cos^2\omega*\cos(\delta+\omega)\left[1+\sqrt{\frac{\sin(\delta+\emptyset)\sin(\emptyset-\beta)}{\cos(\delta+\omega)\cos(\omega-\beta)}}\right]^2} \quad (7)$$

$$K_p = \frac{\cos^2(\emptyset+\omega)}{\cos^2\omega*\cos(\delta-\omega)\left[1-\sqrt{\frac{\sin(\delta+\emptyset)\sin(\emptyset+\beta)}{\cos(\delta-\omega)\cos(\beta-\omega)}}\right]^2} \quad (8)$$

2.3 Surcharge Loads

Live loads for railroads are based on the Cooper E80 loading. Cooper E80 was designed to approximate two locomotives with 80 kips per axle pulling an infinite train of 8 kips per foot. Figure 12 presents the Cooper E80 loading. In addition to the Cooper E80 loading, a minimum surcharge of 72 psf. must be applied at the top the shoring system.

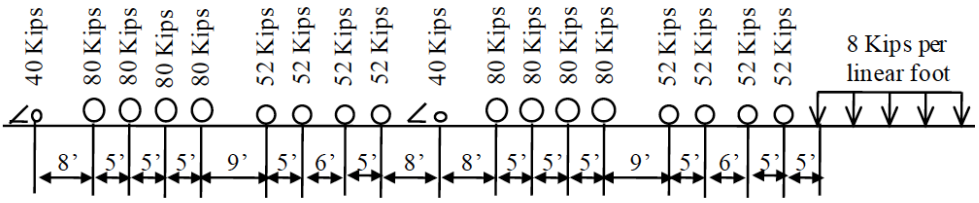

Figure 12. Cooper E80 loading (GTS, 2004)

The design specifications for live load and lateral earth pressure methods for retaining walls and temporary shoring are identified in the AREMA manual (2010) and

the GTS (GTS, 2004), respectively. The different specifications on design live load and lateral earth pressure for retaining walls and temporary shoring are listed in Table 11.

Table 11. Comparison of the design specifications for live load and lateral earth pressure

Structures	Guideline	Live load	Lateral earth pressure method
Retaining walls	AREMA manual (2010)	E – 80 + Proper impact load*	Trial wedge method (i.e., Culmans' method)
Temporary shoring	GTS (Burlington North Santa Fe Railway and Union Pacific 2004)	E – 80	Boussinesq solution

*The impact load varies depending on the class of the railroad, the rails, and other factors.

The application of the Cooper E80 live load and Boussinesq theory in order to find the lateral earth pressure due to the live load in railroads was shown in Figure 13.

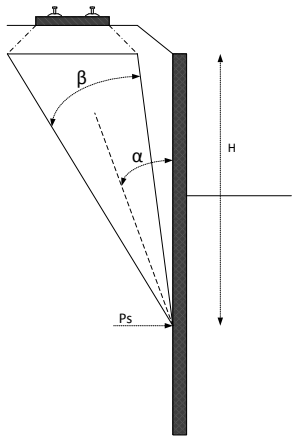

Figure 13. Boussinesq theory – strip loads

The intensity of a strip load due to E80 railroad live load (q) can be calculated using Equation 9 (GTS, 2004):

$$q = \frac{\text{Axle Load}}{(\text{Axle spacing})\ (\text{track}+H_1)} = \frac{80000}{5_{ft}\ (Ld)} \tag{9}$$

for $H_1 = 0$, Ld = Length of Tie or for $H_1 > 0$, Ld = Length of Tie + H1 ft. (Ld)

In order to find the lateral earth pressure using the Boussinesq theory, two different cases can be defined. The first case is when the tracks are parallel to the shoring system and the lateral live load pressure P_s due to E80 loading can be calculated using the Boussinesq Strip Load Equation (Eq. 10) (GTS, 2004)

$$P_S = \frac{2\,q}{\pi}\,[\,\beta - \sin\beta\cos(2\alpha)] \tag{10}$$

In the second case, the track is at a right angle to the shoring system and the live load pressure due to E80 loading can be derived by Equation 11 (GTS, 2004)

$$P_S = K_a\,q \tag{11}$$

where K_a is the active earth pressure coefficient. General loading characteristic by GTS, 2004 showed in Figure 14.

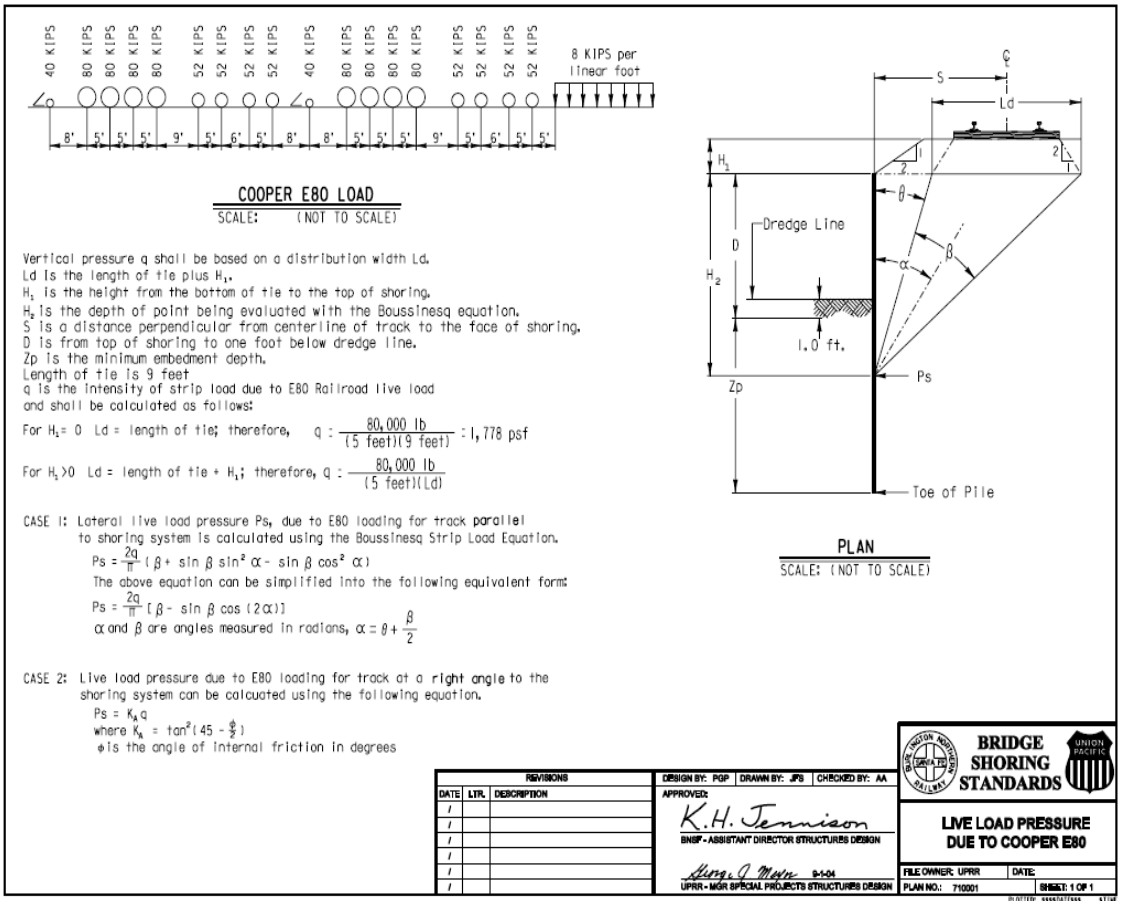

Figure 14. General loading characteristic (GTS, 2004)

In contrast, AREMA (2010) specifies that the trial wedge method (i.e., Culmans' method) should be used to calculate the lateral earth pressure induced by surcharge; however, this method appears to over-estimate the lateral pressure even for walls of significant stiffness (Rowe 1950).

Since the GTS (2004) and AREMA (2010) manuals specify different methods to calculate the lateral earth pressure induced by surcharge as listed in Table 11, a comparison between these two methods (i.e., Boussinesq and trial wedge method) was performed for three different wall heights and the results are presented in Table 12.

Table 12. Comparison between Boussinesq theory and trial wedge theory

Method	Lateral earth force (kip./ft.)			Wall configuration
	H=10´	H=15´	H=20´	
Boussinesq	6.5	10.7	15.5	
Trial wedge	2.8	7.2	12.5	
NOTE:	Q = 80000lbs/(5ft.)(9ft.) = 1778 psf. 12´ is the allowed minimum distance from the shoring. Lateral earth force: the lateral earth force per linear length of wall/shoring			

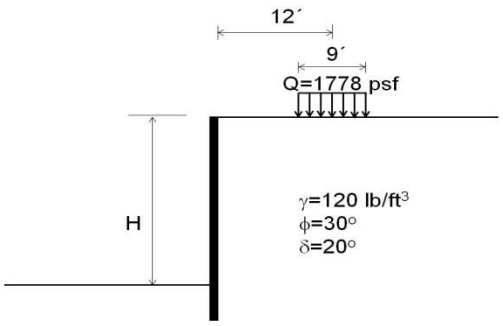

Clearly, the two methods are not consistent with one another. The Boussinesq solution yields a higher lateral force than the trial wedge method.

2.4 Research on Lateral Earth Pressure Induced by Surcharge

The lateral earth pressure induced by surcharge has been studied from multiple perspectives such as configurations of the surcharge loads, i.e., uniformly distributed, line, or concentrated load (e.g., Motta 1994; Greco 2006), and the influences of the soil properties (e.g., Wang 2007). Motta (1994) points out that in many practical problems

surcharge as well as soil weight contribute to lateral pressure on retaining systems. He attempts to derive a solution in which the effect of the distance between the wall and the surcharge is taken into consideration. Because the Boussinesq theory is not reliable due to its neglect of the effect of soil strength, Motta uses the Coulomb approach, which is based on the limit equilibrium method. Furthermore, the different boundary conditions in solving the earth pressure problem can be applied using the Coulomb theory (Motta 1994). The geometry of the problem in the Coulomb method is shown in Figure 15. In this figure, the failure plane inclines at an angle of $\propto$ and the surcharge load q has a distance d to the wall.

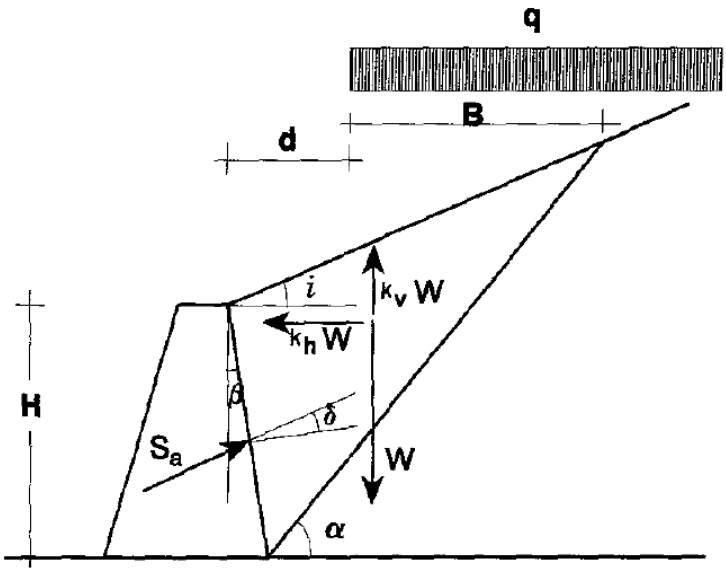

Figure 15. Geometry of the problem (Motta, 1994)

As a result of his research, Motta developed Equation 12 to calculate the lateral earth pressure on the wall (Motta 1994).

$$S_a = \frac{1}{2}\,\gamma\,(1-k_v)H^2K_{a,\gamma} + q(1-k_v)HK_{a,q} \tag{12}$$

$$K_{a,\gamma} = \frac{\tan(\alpha-\phi) + {k_h}/{(1-k_v)}}{(\tan\alpha - \tan i)[\cos\delta\tan(\alpha-\phi)]}$$

$$K_{a,q} = [1-\lambda\,(\tan\alpha - \tan i)]\;K_{a,\gamma}$$

$$\lambda = \frac{d}{H}$$

where k_h and k_v are the horizontal and vertical seismic coefficients. For a specific case, $K_{a,\gamma}$ can be derived by using Figure 16 (Motta, 1994).

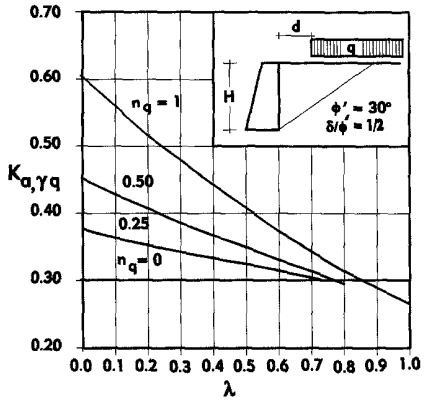

Figure 16. Earth pressure coefficient with λ (Motta, 1994)

Georgiadis et al. (1998) conducted a series of tests to investigate the effect of surcharge strip loads on the sheet pile walls. The bending moments are compared for different methods, and the result of the test to find the validity of these methods. In addition, they compared these results with a finite element model. In their experimental programs, several tests and models with different depths of excavation, loads, and

distances between loads and walls were conducted. As expected, with increasing load weights and decreasing distances between the wall and load, the bending moment increases. The result of four different methods– the elastic solution, the 45^{o} distribution approach, the Coulomb analysis, and the Beton-Kalender approach were compared with the test results for a specific test using 250 mm excavation and 12 kN/mm^{2} (Figure 17).

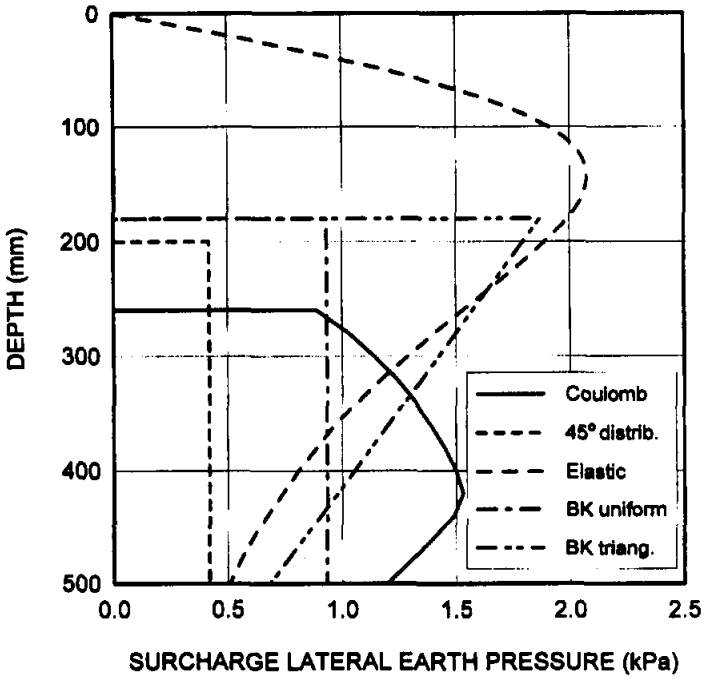

Figure 17. Lateral surcharge pressures calculated using different methods (Georgiadis et al., 1998)

Georgiadis et al. (1998) obtained the best predictions using the Coulomb and 45^{o} distribution approaches. The difference between the results of these tests using the two methods were less than 20%. The elastic solution results were extremely large and

unrealistic. The results of Beton-Kalender approach were also excessively large. These results are presented in Figure 18. Finally, they compared their results with finite element analyses to identify which lateral wall deformations produced the best match to bending moment measurements.

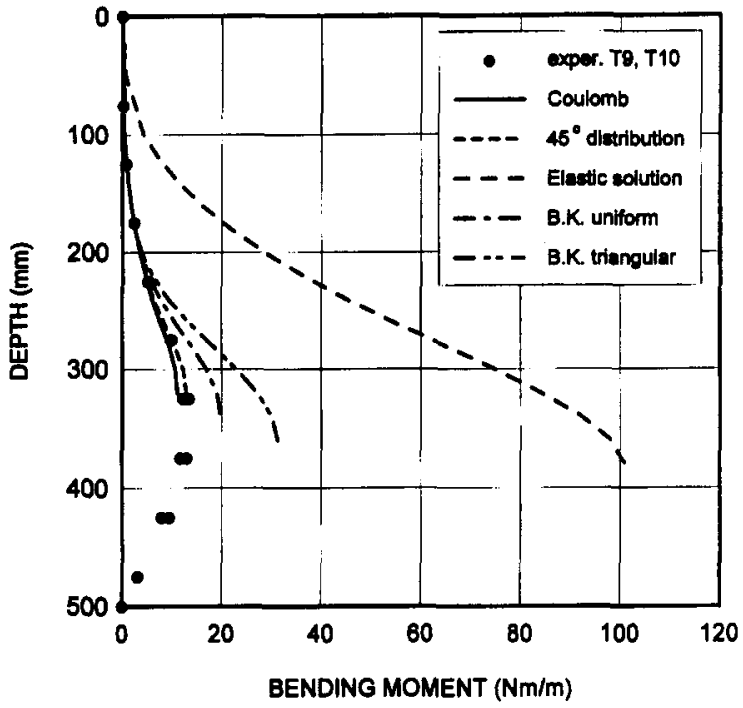

Figure 18. Comparison of measurements and calculations using different methods (Georgiadis et al., 1998)

Baker et al. (2002) evaluate the effect of live load surcharges on retaining walls and abutments in highways. With reference to the AASHTO (1996), the lateral earth pressure due to surcharge loads in highways can be estimated by adding an equivalent height (h_{eq}) of backfill, which was about a 600 mm layer of backfill. In addition to this

standard, the 1994 AASHTO LRFD suggests different h_{eq} for walls of different heights. According to Baker et al. (2002), using a constant h_{eq} for all walls was not reasonable. In fact, Baker et al. (2002) show that the appropriate h_{eq} for highways depends on the height of the wall, the distance between the wall and load, and the direction of load, parallel or perpendicular loading. They considered the effect of truck and tandem loads as a point loads and used the Boussinesq theory to find the distribution of the horizontal pressure behind the walls. Their studies show that the h_{eq} can be determined by matching the lateral bending moment from actual pressure distribution with those from convention uniform soil pressure. Figure 19 shows these horizontal earth pressure distributions.

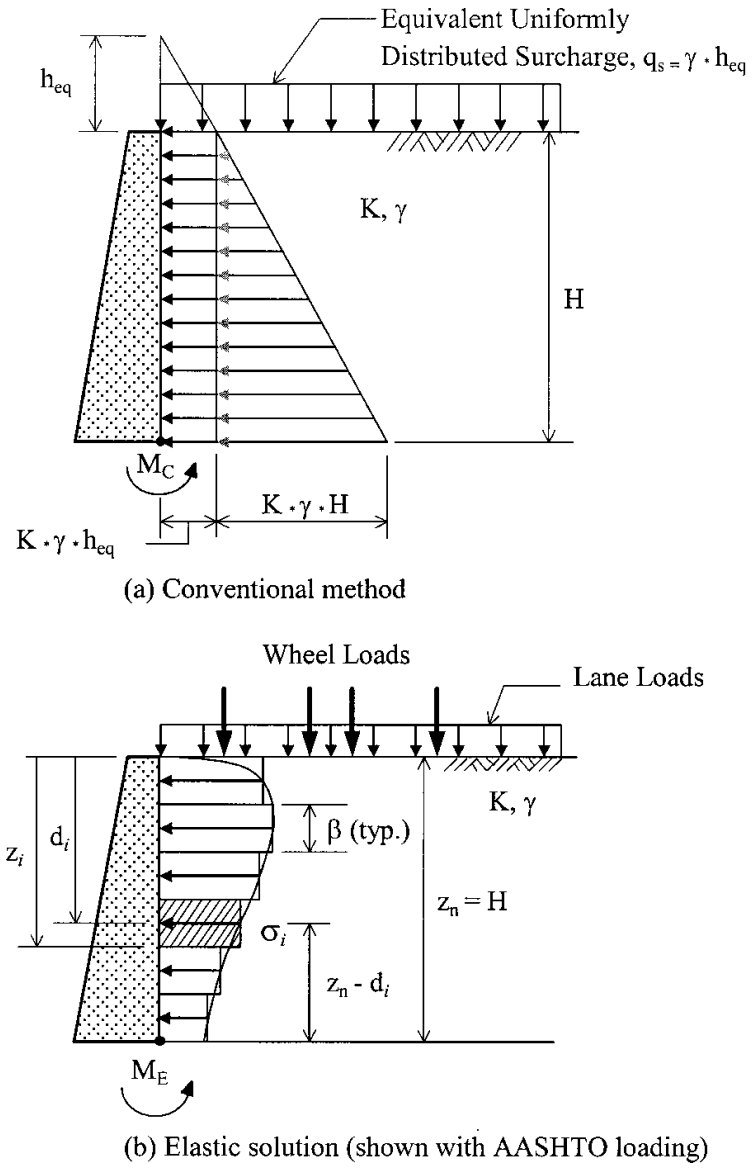

Figure 19. Bending moment by conventional method and elastic solution (Baker et al., 2002)

Baker at al. (2002) also show that h_{eq} can be varied in different cases and some new h_{eq} should be suggested. Figure 20 presents the results for a specific case with s as the distance between the load and the wall with a parallel load and k as the same distance with

a perpendicular load. They calculate that for a parallel loading, the maximum horizontal pressure is when s = 0, and for a perpendicular load, the maximum horizontal pressure is when k = 0.15 m. Based on these results, the following scenarios are calculated: h_{eq} with three different depths (z = 1500 mm, 3000 mm, and 6000 mm) and two different distances between the wall and load (s = 0 mm and 300 mm) for both parallel and perpendicular conditions.

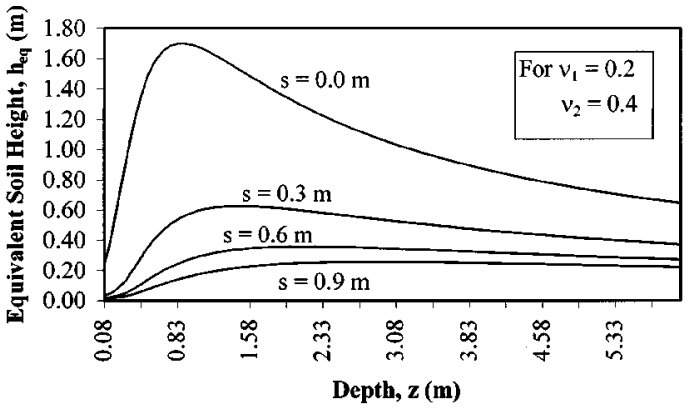

(a) Values of h_{eq} for various distances, s - Truck parallel to wall

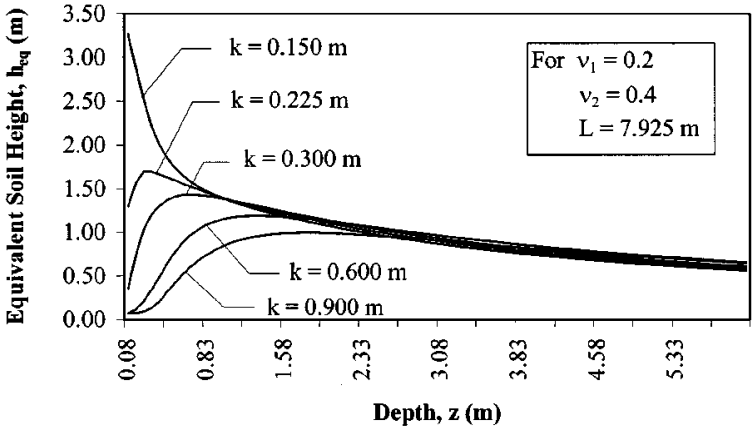

(b) Values of h_{eq} for various distances, k - Tandem perpendicular to wall

Figure 20. Values of equivalent height for various distances (Baker et al., 2002)

Greco (2006) presents an analytical approach to evaluate the active earth pressure based on the soil self-weight and strip surcharge. He uses the Coulomb method as a reference method. Greco (2006) shows the influence of surcharge distance to the wall in his research. The critical distance ($d_{critical}$) between the wall system and the surcharge and the critical inclination of the failure plane due to the surcharge are defined. He shows that the surcharge has an effect on the wall when the distance between the wall and surcharge is less than the critical distance. In addition, the effect of surcharge intensity is evaluated in Greco's research (2006). He concludes that the lateral earth pressure based on the Coulomb method is much reliable than that calculated using the Boussinesq theory.

Wang (2007) assesses the influence of soil properties on lateral earth pressure. In Wang's research, different formulas are developed to evaluate the lateral pressure for different kind of surcharges like point load, line load, and rectangular load. The results of this research lead to the conclusion that the magnitude of lateral pressure derived by integrating the stress behind the wall and the centroid location are profoundly affected by the type and degree of geometrical anisotropy, the distance between the wall and loading, and the direction of the load, either horizontal or vertical. Wang (2007) uses the five elastic engineering constants $E, E', \nu, \nu', and\ G'$ defined to show the effect of soil anisotropy on the lateral forces. The results for seven different soil types are obtained, and the geometry of these examples is shown in Figure 21.

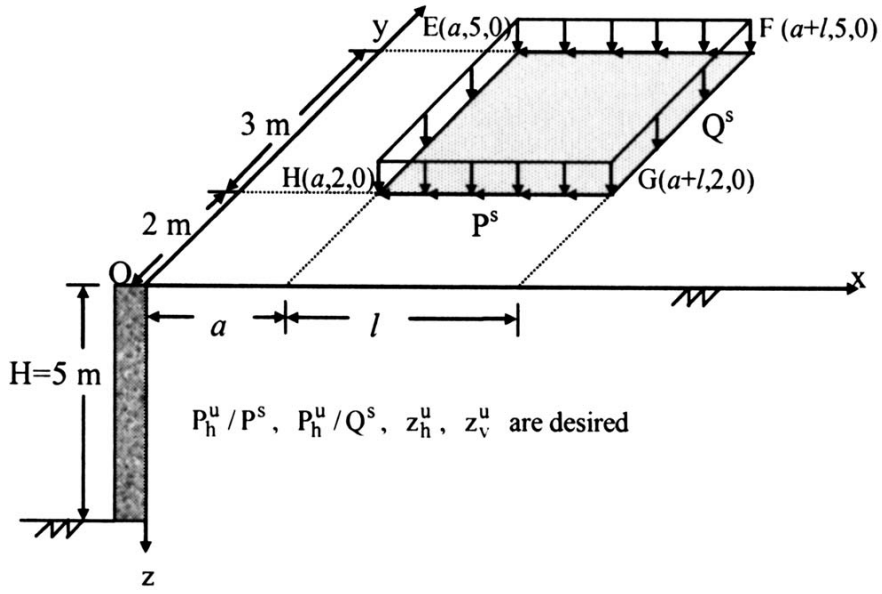

Figure 21. Geometry of Wang's examples (Wang, 2007)

The influence of the degree of anisotropy is stated by the relations $\frac{E}{E'}$, $\frac{\nu}{\nu'}$, and $\frac{G}{G'}$. The relationship between the lateral force and soil anisotropy is shown in Figure 22. Wang's results show that the effect of the soil properties is noticeable (Wang, 2007).

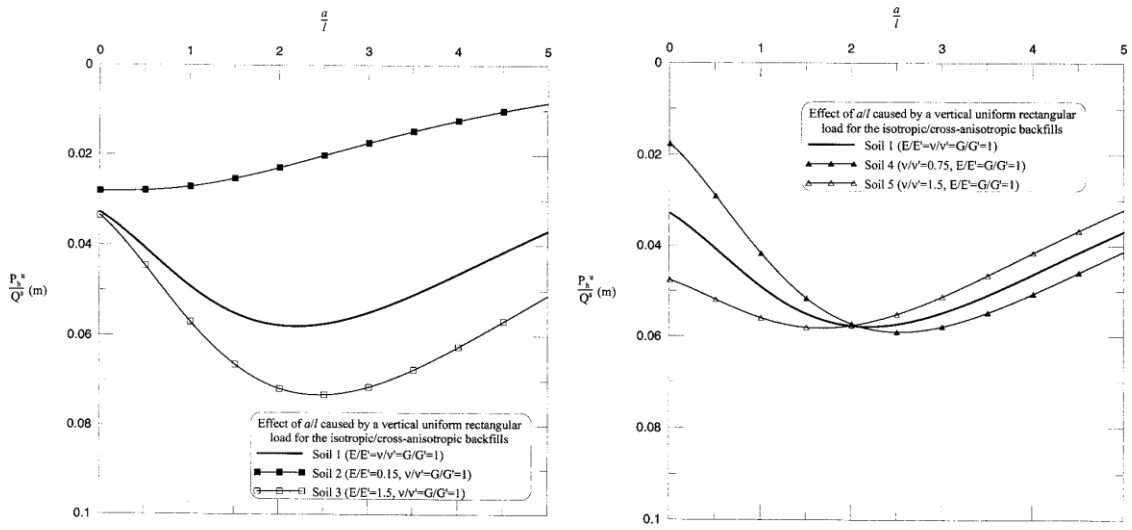

Figure 22. Influence of different E/E' and ν/ν' on lateral pressure (Wang, 2007)

Esmaeili et al. (2012) investigate the effect of train live loads on railroad bridge abutments. They use the same method that Baker (2002) uses to evaluate the effect of live loads on highway abutments. Esmaeili et al. (2012) use the Worldwide Railway Organization (UIC, 2006) manual UIC-776-1R as a reference for planning their study. In this manual, evaluating lateral earth pressures is based on the uniform infinite surcharge equal to the constant height of 1.7 m and the same unit weight of the backfill material. Applying the elasticity method, the research group calculate the shape and the magnitude of the earth pressure in the height of the wall and conduct a numerical integration to find the lateral earth force. In addition, the effects of different Poisson ratios on the lateral earth pressure are studied. The results show that using a uniform surcharge underestimates the lateral earth pressure compared with the elasticity solution for cases in which the Poisson ratios were equal to 0.1 and 0.2 as well as for the case in which the Poisson ratio is equal

to 0.3 with the height of the wall between 1.5 m and 7 m. In this research, rectangular and strip loading are the loading patterns used to find the lateral earth pressure when the train was at a right angle to the wall. Figure 23 presents the loading pattern applied in this study. Esmaeili and colleagues (2012) also suggest some equations using different Poisson ratios to find the horizontal earth pressure due to the surcharge.

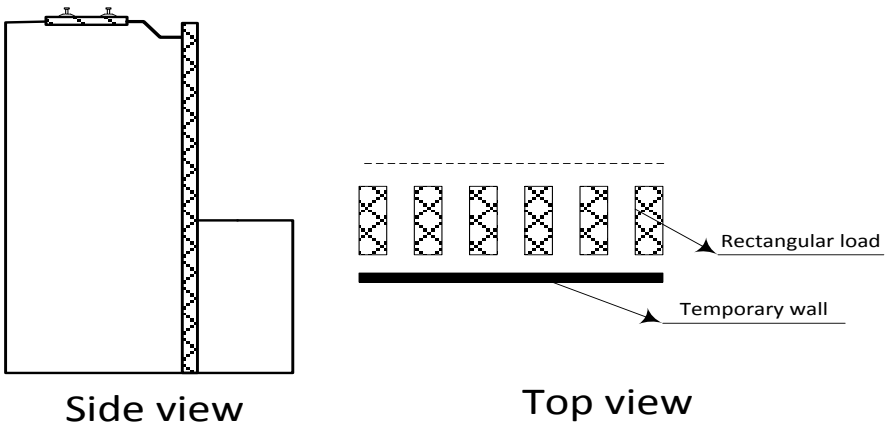

Figure 23. Rectangular loading pattern (after Esmaeili et al., 2012)

Even though AREMA (2010) and GTS (2004) provide two methods to calculate the surcharge induced lateral earth pressure for retaining walls and temporary shoring, respectively, the adequacy of both methods needs to be reassessed. The live railroad (E-80) represents a much higher surcharge load as compared with a highway load. The load was converted into an equivalent 240 psf. uniform load regardless of the wall height. Only within the last 15 years has the requirements changed to convert the load to an equivalent uniform load based on variable wall heights (Kim and Barker 2002; AASHTO 2010).

Nevertheless, the highway load HL-93 presents a much lower surcharge load compared with the railroad load E-80. The lateral earth pressure induced by railroad live load becomes the major load in the calculation. Overestimating the lateral earth pressure will lead to over-designed walls and shoring with unnecessarily increased cost; whereas, underestimates of the lateral earth pressure will lead to insufficiently designed structures that increase the risk and even probability of accidents such as derailments.

2.5 Research on the Influence of the Rigidity of the Wall on Lateral Earth Pressure

The rigidity and rotation of the wall have significant influence on the lateral earth pressure but have not been well addressed in practice yet. The Manual by US Army Corp of Engineers (1989) designed rigid walls using the trial wedge method and applied reduction factor to the lateral earth pressure obtained from trial wedge method to design flexible walls. The reduction factor varied, and the maximum reduction factor halved the surcharge induced lateral earth pressure.

Georgiadis et al. (1998) compare the results of their tests with those of a finite element model and determined which lateral wall deformations and rotations produced the best match to empirical bending moment relationships. They show that in the case of zero lateral movement, meaning nonyielding walls, the lateral pressure is much higher than in the case that of lateral movement, i.e, yielding walls (Figure 24.).

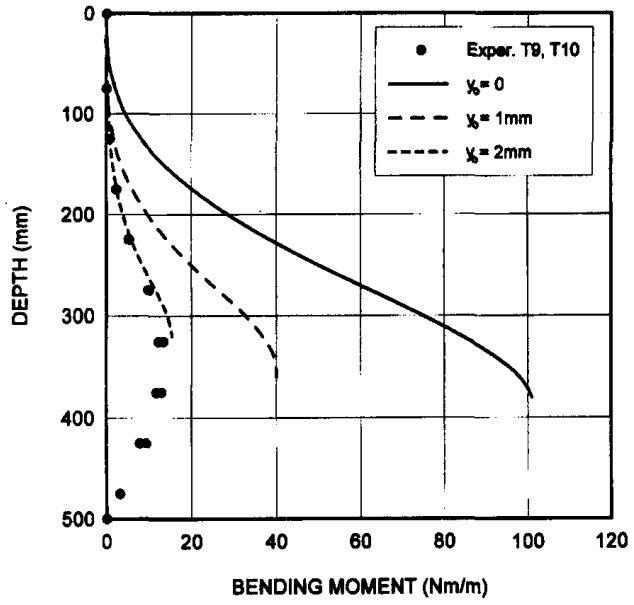

Figure 24. Effect of lateral wall movement on bending moment. (Georgiadis et al., 1998)

Huang et al. (1999) perform a comprehensive experimental study on the influence of wall rigidity and wall rotation on the lateral earth pressure. The study confirms the remarkable influence of the wall rigidity and wall rotation on the lateral earth pressure. They investigate the effect of bending rigidity of walls supported at the top and bottom. The rigidity of these walls is based on the EI of the walls where E is Young's modulus and I is the moment of inertia. While placing the backfill materials, the pressure behind the wall is measured using various load cells installed behind the wall. Figure 25 presents Huang et al.'s results of the wall deflection during this process (1999). The variations in deflection patterns for these walls are easily perceived, and the lateral deflection for a rigid wall (0.03 mm) is less than the maximum deflection (0.05 mm) suggested by Sherif et al. (1984).

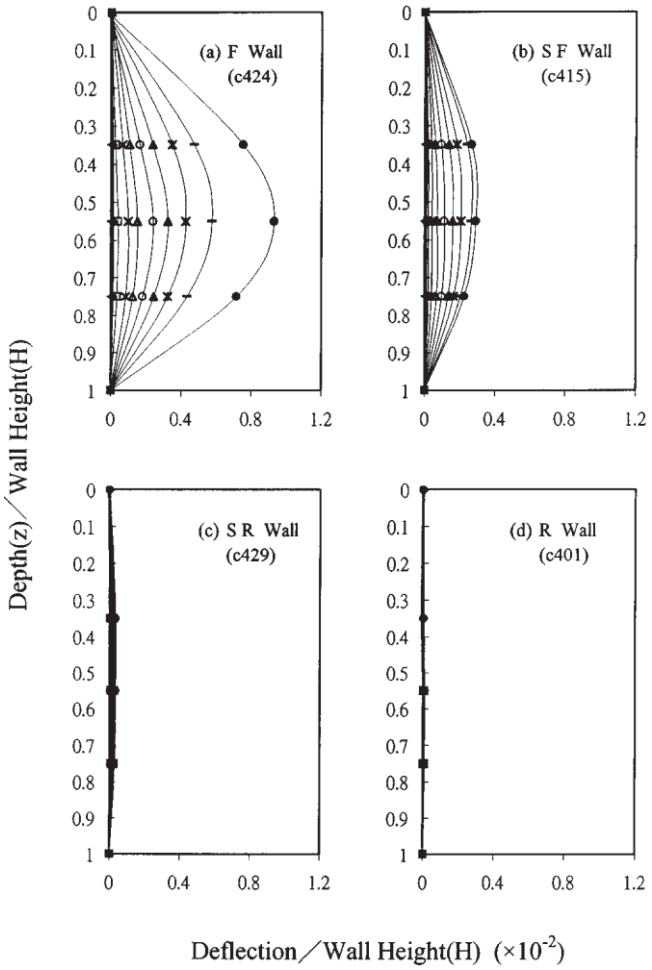

Figure 25. Deflection of wall with different rigidities (Huang et al., 1999)

The corresponding pressure distributions behind the wall from Huang et al. (1999) are presented in Figure 26. As expected, the most flexible wall has the most deflection and the least lateral pressure.

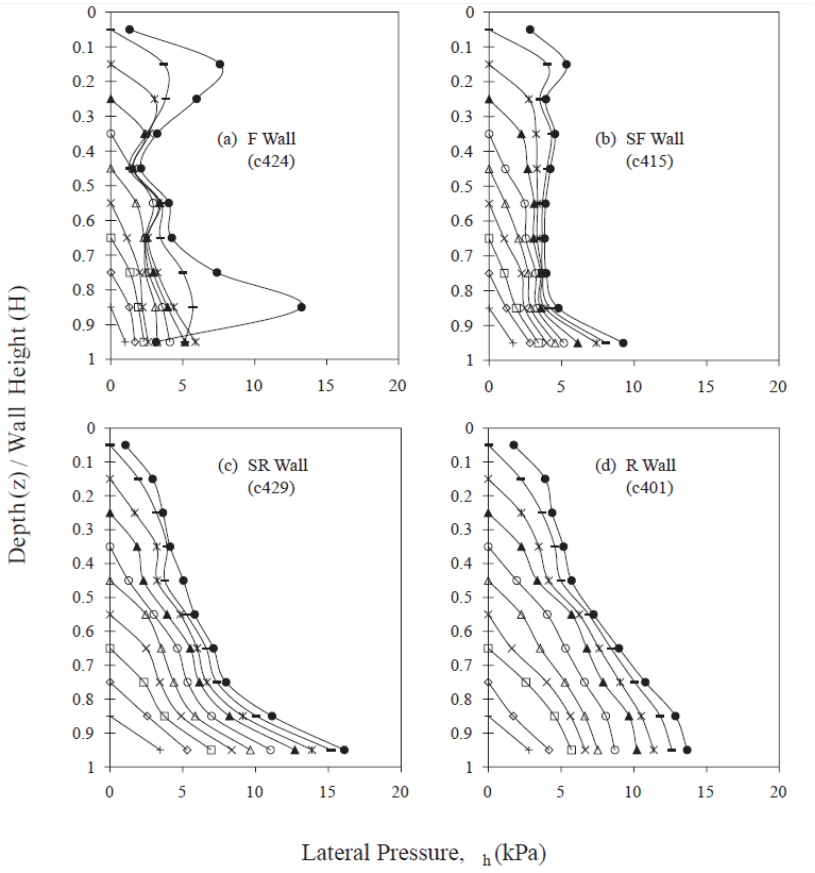

Figure 26. Lateral pressure with different rigidities (Huang et al., 1999)

Moreover, the rigid wall is brought to the active condition by moving the lateral support at the top of the wall (Huang et al, 1999). The results are shown in Figure 27, and from these we can conclude that greater movement, meaning the largest rotation angle, leads to the greatest reduction in stress from the at-rest condition to the active state and, hence, the lowest lateral pressure.

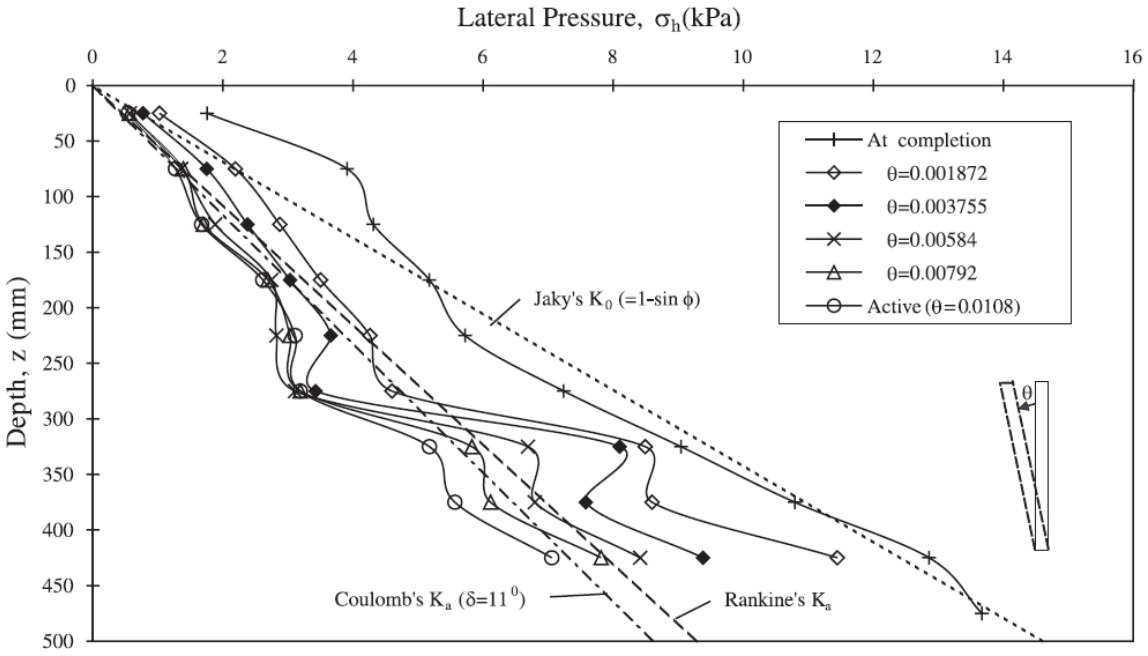

Figure 27. Lateral pressure with different wall rotation (Huang et al., 1999)

The influence of wall and shoring rigidity on the lateral earth pressure can be acknowledged by a few simplified approaches shown in Table 13. AASHTO (2010) uses the Boussinesq solution to calculate surcharge induced lateral earth pressure on rigid walls and a 2:1 force distribution for flexible walls. While acknowledged, the rigidity of walls is only distinguished qualitatively by two descriptive terms, rigid and flexible. The categorization of the rigid and flexible walls is highly empirical.

Table 13. Surcharge induced lateral earth pressure at rigid walls and flexible walls

	Rigid wall	Flexible wall
AASHTO (2010)	**Boussinesq solution** 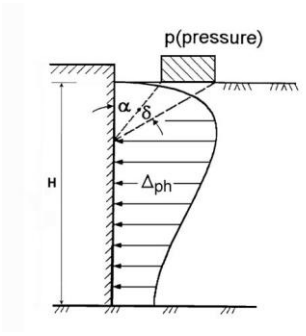	**Assuming 2:1 vertical stress distribution** 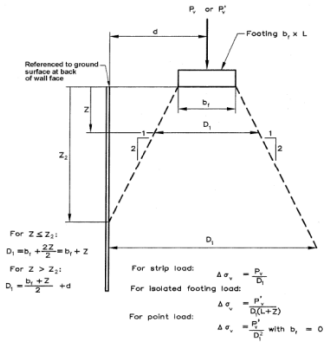
US Army Corp of Engineers (1989)	**Trial wedge method** 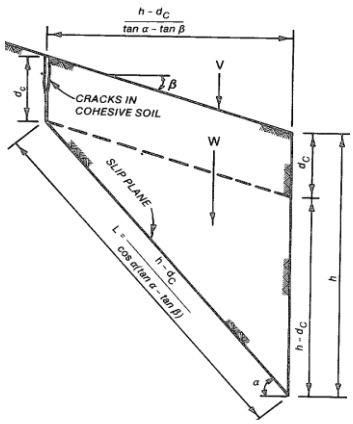	**Lateral earth pressure reduced by as much as half from lateral earth pressure on rigid wall, i.e., reduced by as much as half from the lateral pressure obtained from the trial wedge method.**

The retaining wall could be considered a rigid wall as the relative deflection ($\frac{\Delta}{H}$) is less than 0.0001 (Sherif et al. 1984; Huang et al. 1999). The lateral earth pressure decreases dramatically with the decrease of wall rigidity. Huang et al.'s findings (1999) are generally consistent with Clough and Duncan (1991). Apparently, a relative deflection ($\frac{\Delta}{H}$) as low as 0.001 can mobilize the active lateral earth pressure condition. With a 20 ft. wall, the required deflection to mobilize the soil into active status would be approximately $\frac{1}{4}$ in., which is less than the maximum allowable shoring deflection (3/8 in.). In other words, the

soil behind shoring is in an active lateral earth condition under the effect of surcharge. Deeming a wall system with an allowable deflection of 3/8 in, as rigid and using the Boussinesq solution as specified by GTS is inappropriate because, as pointed out by AASHTO (2010), the Boussinesq solutions are derived from elasticity theory for a semi-infinite medium and using Boussinesq solutions for rigid walls would be overly conservative.

2.6 Skewed Conditions

Usually the railroad runs parallel to the wall and shoring. The lateral earth pressure induced by live loads is calculated by the methods listed in Table 13. When the railroad is perpendicular to walls and shoring, the live load is considered uniformly distributed and the induced the lateral earth pressure is calculated either by the Coulomb or the Rankine theory active earth pressure. These approaches are similar to what has been used to design high retaining structures, but the converted distributed load from a railroad load is much higher than the distributed load from a highway load. Under some circumstances, though not often, the railroad intersects walls and shoring at an angle as shown in (c) of Figure 28. No method is available to calculate the lateral earth pressure for such situations.

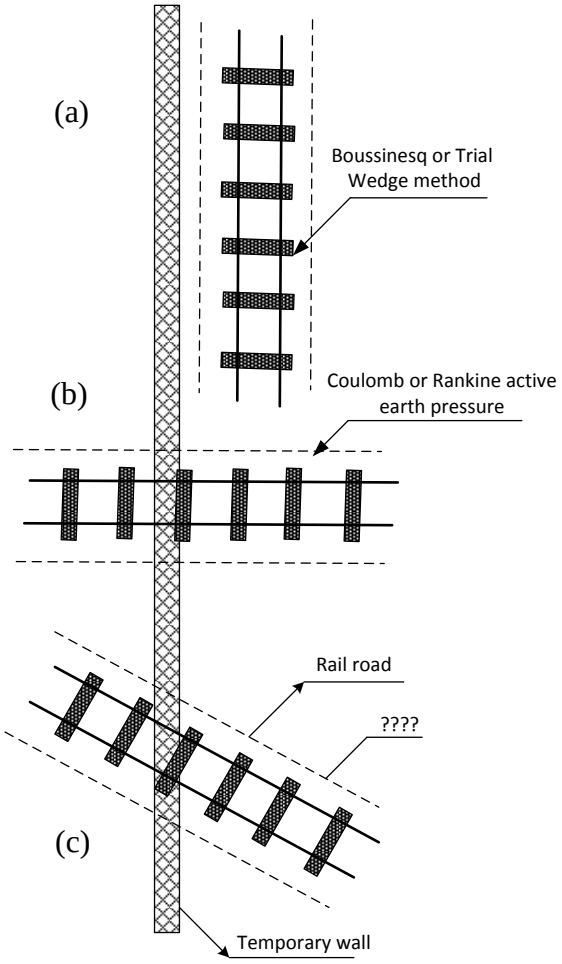

Figure 28. Appropriate methods to calculate lateral earth pressure for different angles between track and wall and shoring (GTS 2004; AREMA 2010

2.7 Estimating Lateral Deformation and Settlement Behind the Wall

The AREMA (2010) guidelines do not specify the maximum allowable settlement since the maximum allowable settlement varies depending on the class level of the railroad and the type of rails. However, AREMA (2010) affirms that the majority of railroad networks require a maximum settlement of less than ½ in and a maximum differential settlement of less than ¼ in (AREMA 2010). In contrast, the GTS specifies the allowable

shoring deflection to ensure the maximum rail movement is less than ¼ in, as listed in Table 14(GTS, 2004).

Table 14. Deflection criteria in GTS (GTS, 2004)

Horizontal distance from shoring to track C/L* measured at right angle from track (ft.)	Maximum horizontal movement of shoring system (in)	Maximum acceptable horizontal or vertical movement of rail (in)
12 < S** < 18	3/8	1/4
18 < S < 24	1/2	1/4

The allowable deflection for temporary shoring as listed in Table 14 is specified such to limit the horizontal and vertical movements of the rails to no greater than ¼ in. The assumption is made that as long as the deflection of the shoring is controlled to 3/8 in or ½ in, the movements of the rails will be maintained under ¼ in. The relationship between shoring deflection and rail movement must be validated, after which the allowable shoring deflection can be established.

2.8 Research on Excavation Induced Settlement and Lateral Deformation

The movement induced by excavation associated with retaining wall and/or shoring construction is a major concern, as the movement of rails influences the operation of the railroads. Railroads are rather sensitive to movement, including vertical and lateral movements (AREMA, 2010). AREMA's survey of numerous railroad networks concludes that the majority of railroads allows a maximum settlement of ½ in and a maximum

differential settlement of ¼ in (AREMA, 2010). The GTS (GTS, 2004) specifies a maximum allowable deflection of the shoring to ensure the maximum movement of the rail is less than ¼ in as listed in Table 14. Even though the GTS specifications for the shoring movement have been widely adopted for temporary shoring, the stringent requirement on the maximum allowable deflection has resulted in extensive discussion and various studies.

As early as the 1960s, research on excavation induced settlement was conducted (Peck, 1969). Over the years, a great deal of useful data has been published. Peck (1969) based on the field observations of sheet pile walls, soldier walls, and spandrel shape ground settlement suggested the empirical method shown in Figure 29. In the research on excavation settlement, Hsieh et al. 1998 divided the settlement profile into three different zones depending on the soil type and workmanship.

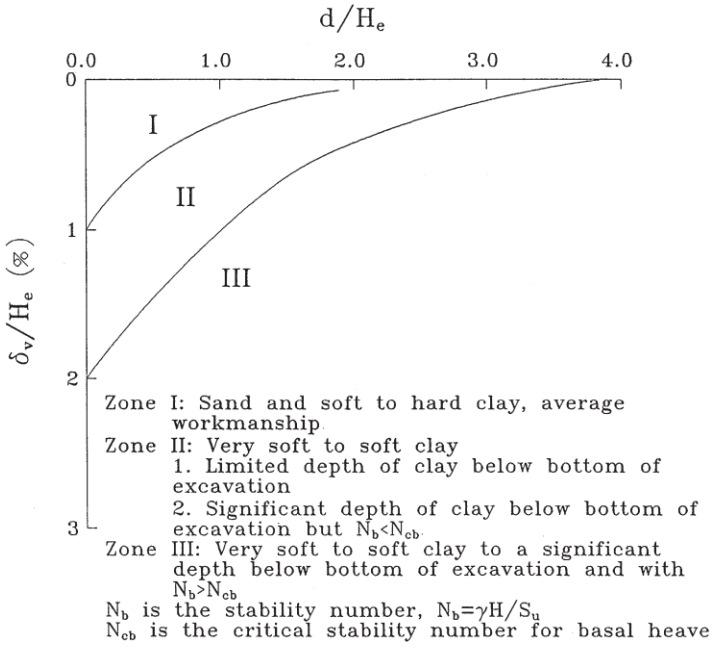

Figure 29. Peck's (1969) method to estimate the ground surface settlement (Peck, 1969).

Bowles (1988) proposes a method to predict the spandrel settlement shape due to excavation. His method is based on predicting the volume of lateral movement of soil mass (V_S) and estimating the active zone (D). The maximum ground settlement (δ_{vm}) can be derived by Equation 13. In addition, the parabolic shape for ground settlement is suggested for different distances to the wall (x) as reported by Equation 14 (Hsieh et al. 1998).

$$\delta_{vm} = \frac{4V_s}{D} \tag{13}$$

$$\delta_v = \delta_{vm} \left(\frac{x}{D}\right)^2 \tag{14}$$

Clough and O'Rourke (1990) study several case histories, finding that the maximum ground settlement can be spandrel or concave depending on the soil properties. Their results are presented in Figure 30.

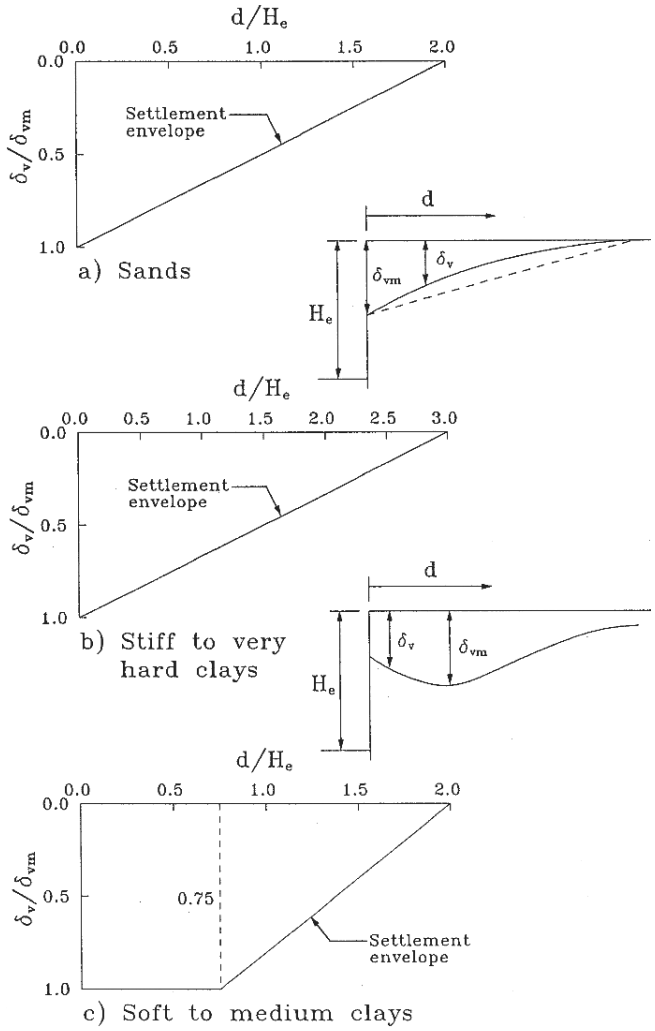

Figure 30. Clough and O'Rourke (1990) ground surface settlement profiles. (Clough and O'Rourke, 1990).

According to field observations in ten actual excavation cases, Ou et al. (1993) investigate the shape, features, and location of maximum ground surface settlement and wall lateral deformation in the center section of walls due to unbalanced force caused by excavation. The magnitude of maximum lateral wall deflection δ_{hm} as a function of the final excavation depth (H_o) is shown in Figure 31. The $\delta_{hm}$is between $0.002H_O$ and $0.005H_O$. These results are smaller than the value obtained by Peak (1969), which is about $0.01H_0$ for sheet pile walls and soldier walls. On the other hand, Ou et al.'s (1993) results are generally larger than Clough et al.'s (1990), which are $0.002H_0$ obtained from excavation in stiff clays, residual soils, and sand.

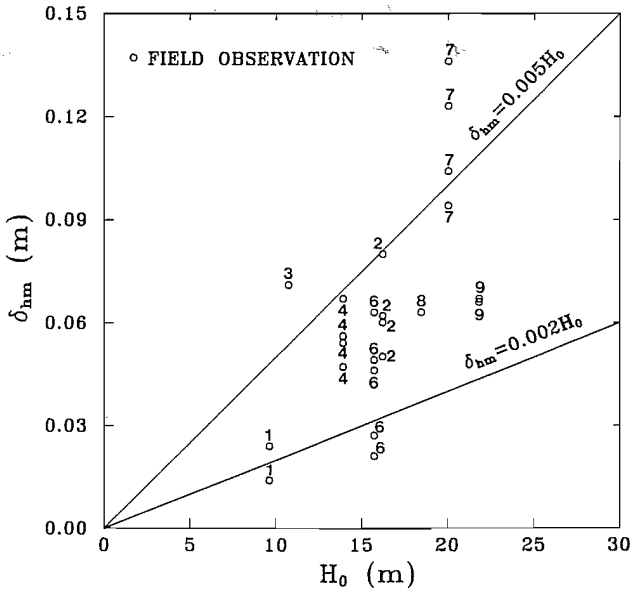

Figure 31.Maximum lateral deformation with excavation depth. (Ou et al., 1993)

The location and magnitude of maximum ground settlement and wall deflection are complex issues that depend on multiple factors. However, based on their results, they

infer that the maximum ground settlement (δ_{vm}) is related to the maximum wall deflection (δ_{hm}) regardless of the settlement profile shape and can be predicted using Equation 15:

$$\delta_{Vm} = (0.5\sim1.0)\ \delta_{hm} \tag{15}$$

Generally two different types of settlement and deflection can be obtained, (1) spandrel settlement, in which maximum surface settlement occurs very close to the wall and (2) concave settlement. In concave settlement, the maximum surface settlement occurs some distance from the supported wall; a good estimate for the distance of the maximum settlement from the wall is half of the excavation depth. These profiles are illustrated in Figure 32 show the location of maximum ground settlement related to the wall deflection shapes.

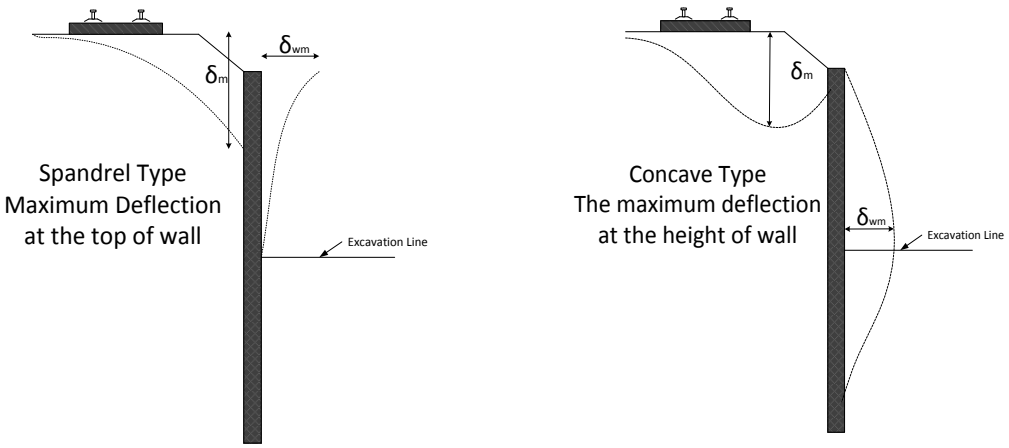

Figure 32. Settlement profiles (after Hsieh et al. 1998)

The shapes of the profiles depend on the permissible deflection of the retaining wall and shoring. The cantilever wall tends to develop maximum deflection at the top,

which likely generates a spandrel settlement profile. Determination of the maximum settlement has been attempted in two approaches, i.e., a theoretical solution and an empirical prediction (Hsieh and Ou, 1998). The empirical prediction, recommended by many researchers, has been more successful in estimating the maximum settlement induced by excavation. Based on numerous field monitoring data, Hsieh and Ou (1998) suggest an empirical method to predict both the spandrel and concave settlement profiles. They indicate the trilinear line to predict the spandrel type settlement as shown in Figure 33 where the line a-b-c is the upper limit and a-d-c represents the mean values of the results.

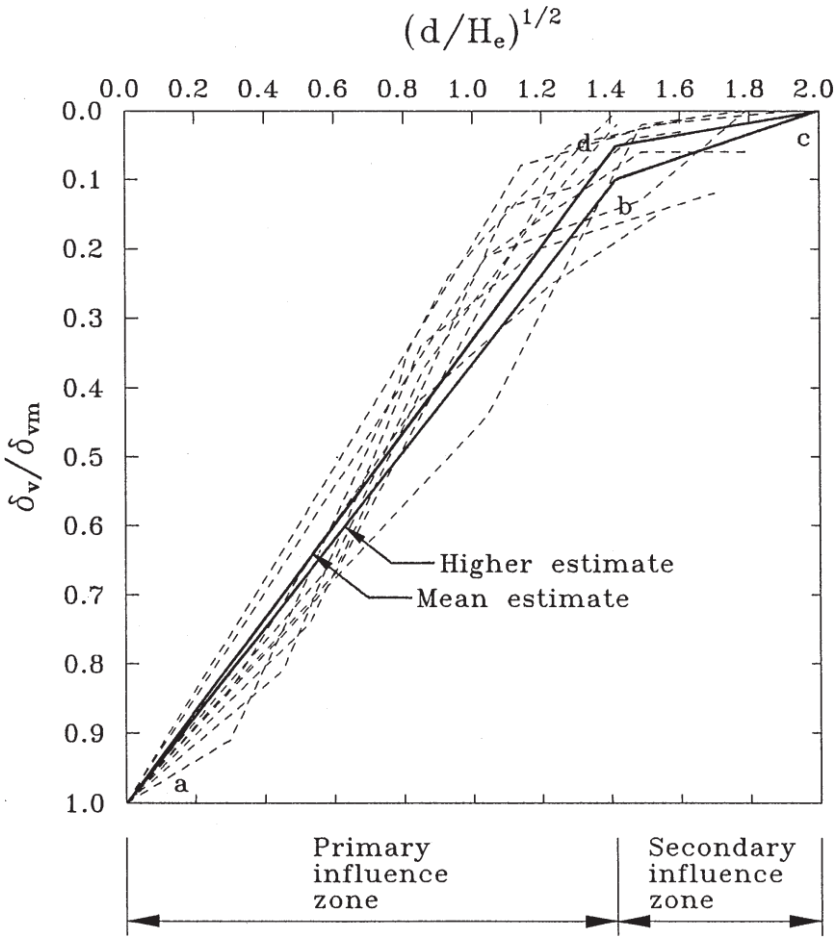

Figure 33. Hsieh and Ou's (1998) method for spandrel settlement profile

For the concave settlement profile, Hsieh and Ou (1998) suggest using the curve in Figure 34 to predict the shape of ground settlement. According to this figure, the maximum ground settlement appears to occur at $d = (0.5)H_0$ where d is the distance and H_0 is the excavation depth, and the settlement near the wall is half of the maximum ground settlement, $\delta_v = (0.5)\ \delta_{vm}$, which is close to Clough and O'Rourke's (1990) results of $\delta_v = (0.5{\sim}0.7)\ \delta_{vm}$.

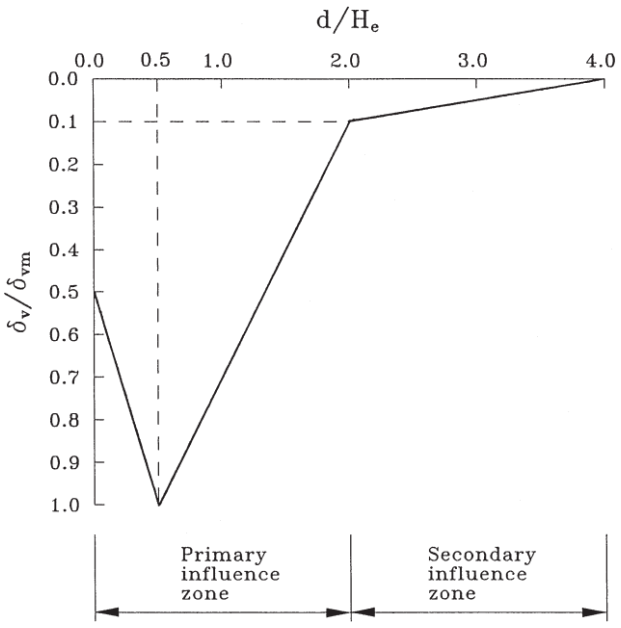

Figure 34. Hsieh and Ou's (1998) method for profiling concave settlement

In Hsieh and Ou (1998)'s research, nine case histories were studied and the results compared with results from different methods. They conclude that for concave settlement profile, generally Clough's (1990) and Hsieh's (1998) methods produce good predictions. Furthermore, in the spandrel case, Peck's (1969) method in some cases overestimates, while the Bowles's (1988) method underestimates. Again, for the spandrel profile, Clough's (1990) and Hsieh's (1998) methods give good estimates.

Poh et al. (2001) evaluate ground movement during wall construction. In this research, four case histories in Singapore are studied to investigate the effect of excavation on the diaphragm wall lateral deflection and ground surface settlement with regard to Singaporean soil properties. The authors conclude that the lateral deflection profile is related to some factors like soil type, excavation process time, wall length, and excavation

method (Poh et al. 2001). Based on their research, we see that ground settlement decreases as the distance from the wall increases. The maximum settlement in Poh et al.'s study (2001) is approximately 0.12% of the excavation depth, which is consistent with the upper bound of what proposed by Clough and O'Rourke (1990). Figure 35 presents the maximum soil settlement according to the distance from excavation based on this case history research.

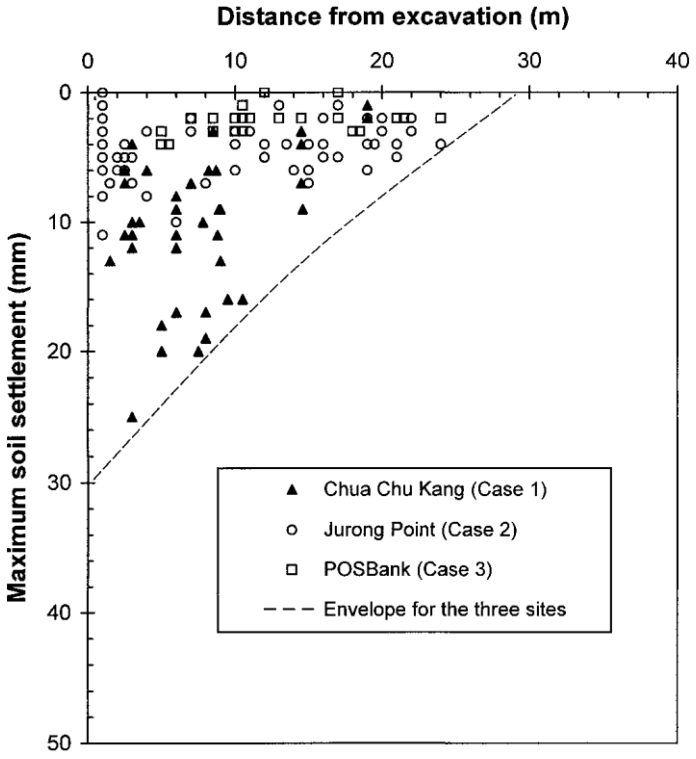

Figure 35. Soil settlement according to distance from excavation (Poh et al., 2001)

Wang et al. (2005) use field monitoring to evaluate the diaphragm wall deflection and ground surface settlement following six deep excavations in Shanghai, China.

Subsequently, these results are compared with results obtained from similar excavations in Taipei and Singapore. Their results show that a concave ground surface settlement is a typical profile of wall deflection increasing as the excavation proceeded. According to Wang et al.'s study (2005), the maximum deflection occurs near the excavation surface. Generally, the magnitude of wall deflection (δ_{hm}) obtained in their study falls between 0.0014H and 0.003H and is always less than 0.007H, where H is the excavation depth. In Singapore, H was between 0.003H and 0.01H; whereas, in Taipei H ranged from 0.003H to 0.007H. These differences can be explained by variation in soil properties, types of walls, and excavation methods.

Finally, Wang et al. (2005) compare the surface ground settlement in their research with Peck's (1969) as shown in Figure 36. The majority of settlement is located in Zone I and this research results are smaller than those reported by Peck (1969) for the same ground conditions.

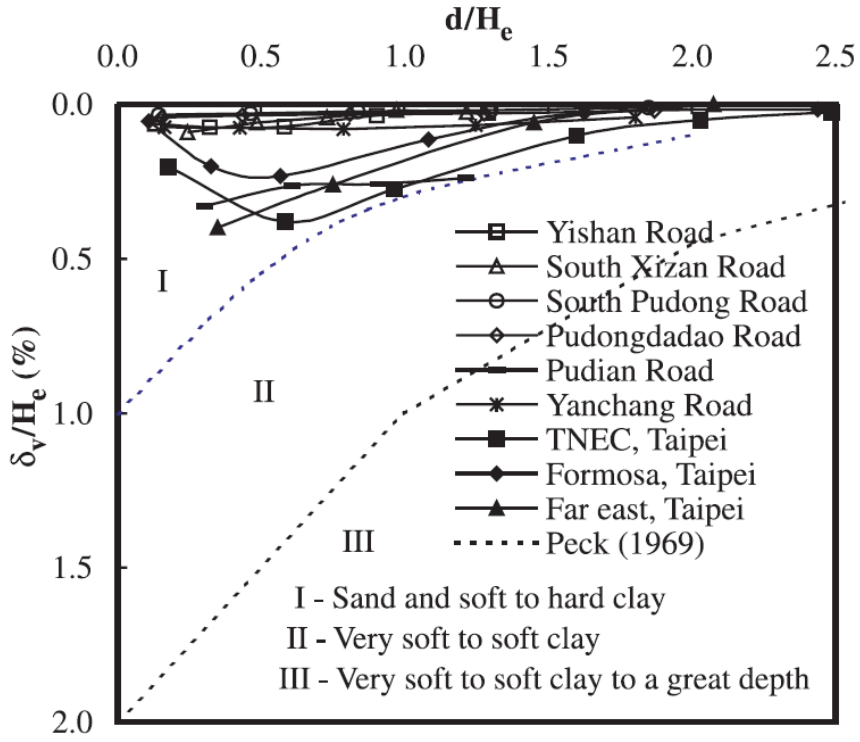

Figure 36. Comparison between the results of this research and those from Peck (1969) (Wang et al., 2005)

The relation between normalized settlement ($\frac{\delta_V}{\delta_{VM}}$) and the distance ratio ($\frac{d}{H_e}$) for the Shanghai case histories and in comparison with the results of Hsieh and Ou (1998) and Clough and O'Rourke (1990) are presented in Figure 37. Clearly, the settlements measured in Shanghai are wider and deeper than those results of other methods.

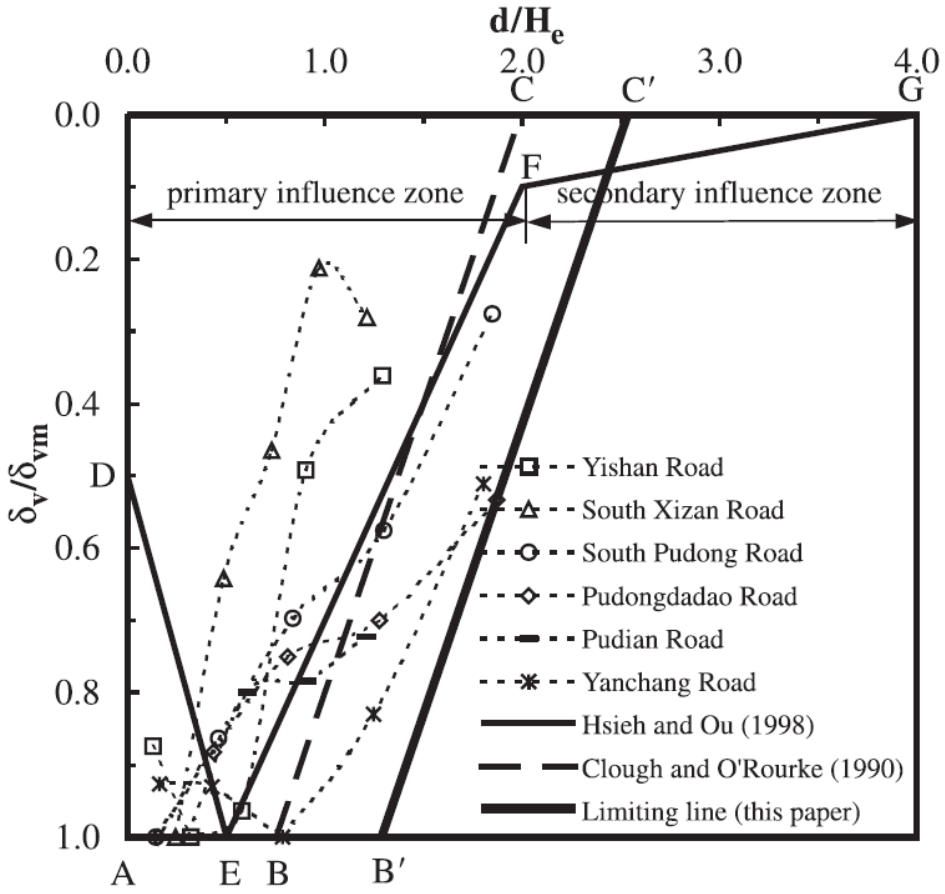

Figure 37. Comparison between results of this research and others (Wang et al., 2005)

Equation 16 shows the relationship between lateral wall deformation and maximum settlement in the Shanghai case studies (Wang et al., 2005).

$$\delta_{vm} = (0.2\sim0.6)\ \delta_{hm} \tag{16}$$

The results for Taipei lie between$= 0.5\delta_{hm}$ and $\delta_{hm} = 1.0\ \delta_{hm}$which is closer to the range reported by Ou et al. (1993). Figure 38 presents these results.

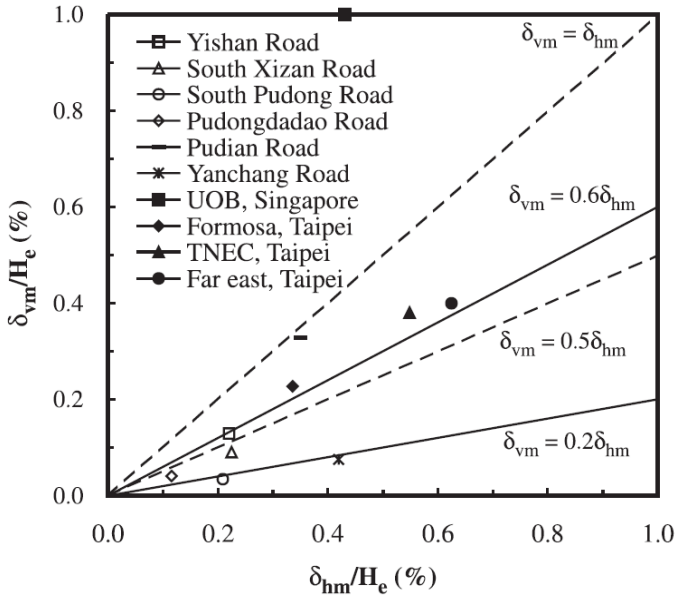

Figure 38. Maximum lateral deformation with ground surface (Wang et al., 2005)

Kung et al. (2007) propose a simplified semi-empirical method based on the finite element (FEM) analysis of a total of 144 representative and hypothetical excavation cases, and they verified the model using the results of 33 case histories in different locations. Kung et al.'s (2007) model consists of three component models and three different formulae based on regression methods. Model A predicts wall deformation (δ_{hm}) using the six parameters excavation depth (H_e), system stiffness ($\frac{EI}{\gamma_w h_{avg}^4}$), excavation width (B), the ratio of the average shear strength over the vertical effective stress ($\frac{S_u}{\sigma_v'}$), the ratio of the average initial Young modulus over the vertical effective stress ($\frac{E_i}{\sigma_v'}$), and the ratio of the depth to hard stratum measure from the excavation level over the excavation width ($\frac{T}{B}$ $when$ $\frac{T}{B} < 0.4$). Model B predicts the deformation ratio $R = \frac{\delta_{vm}}{\delta_{hm}}$ by using the three

main parameters of the normalized clay-layer thickness with respect to the wall length ($\frac{\sum H_{clay}}{H_{wall}}$), the normalized shear strength over the vertical effective stress ($\frac{S_u}{\sigma_v'}$), and the normalized initial Young modulus over the vertical effective stress ($\frac{E_i}{\sigma_v'}$). Model C calculates the ground surface settlement profile caused by excavation. The results of Kung et al.'s research (2007) compared to field observations in Figure 39 show reasonable compatibility.

(a)

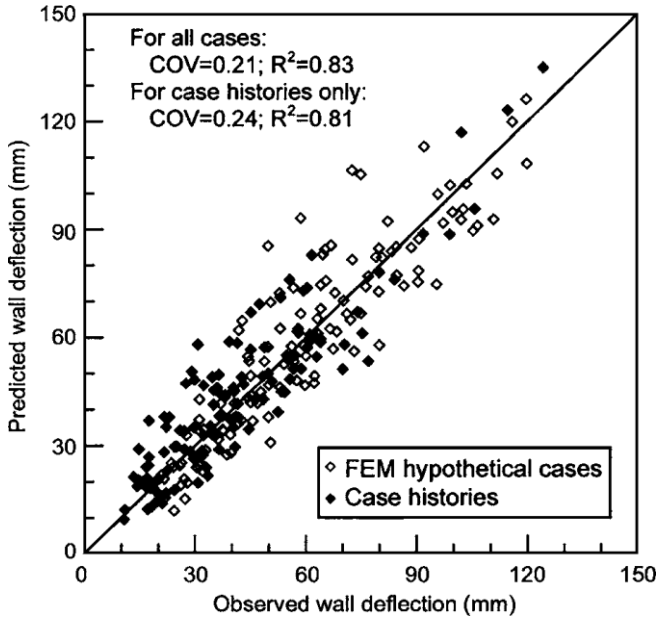

Figure 39. Results of Kung et al. models compared to field observations: (a) Wall deformation, (b) Maximum ground settlement, and (c) Settlement profile (Kung et al., 2007)

(b)

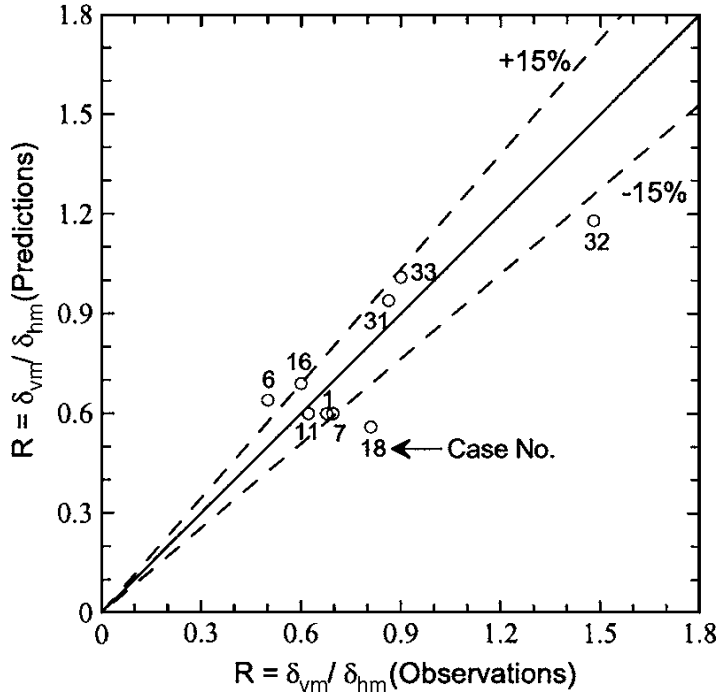

(c)

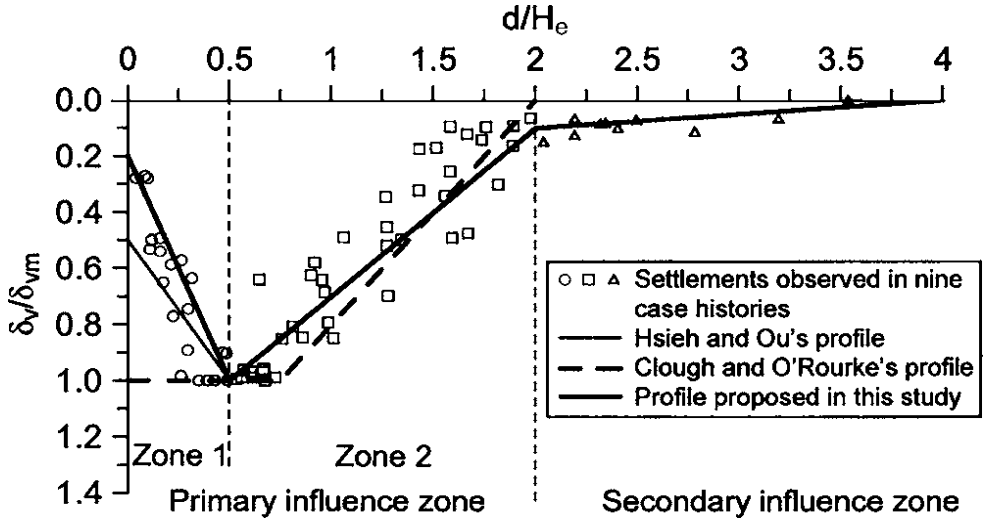

Figure 39. Continued

In engineering practice, the influence range is as important as maximum settlement. The representative spandrel models are presented in Figure 40. Except in the model proposed by Peck (1969) as shown in Figure 40. (a), the induced settlement (δ_v) at any location can be estimated based on the maximum settlement (δ_m) as shown in Figure 40. (b), (c) and (d). The Peck's model was based on the early age data mainly from 1950s to 1960 and has been found unduly conservative since the modern construction technology has advanced significantly.

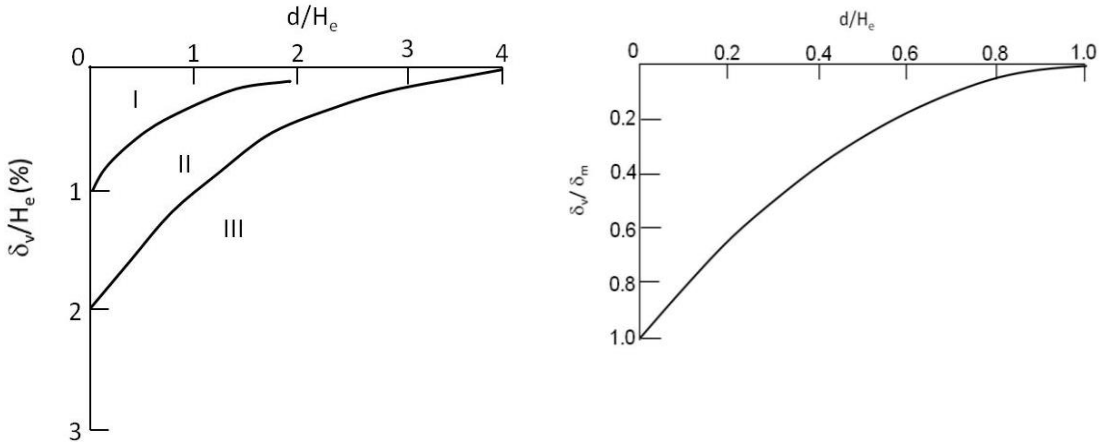

(a) (b)

Figure 40. Previously developed methods to estimate settlement due to excavation (a) A modified representation of Peck's 1969 model, (b) Adapted from Bowles (1969), (c) Clough and O'Rourke's method (1990), and (d) Hsieh and Ou's method (1998)

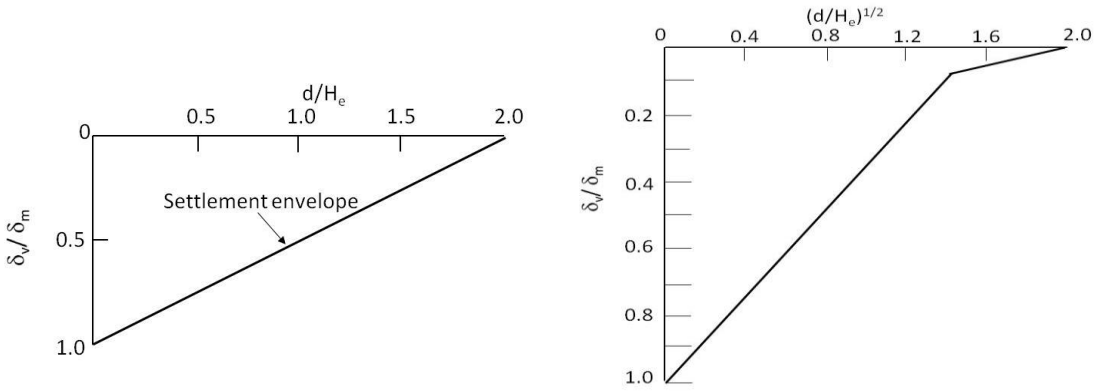

(c) (d)

Figure 40. Continued

In view of the results published to date, the current GTS specifications on allowable deflection possess at least two outstanding problems:

- The allowable wall and shoring deflection is specified without regard to the wall height
- The allowable wall and shoring is overly conservative for commonly used wall heights, namely, wall heights ranging from 10–20 ft.

All of the proposed models consider the induced settlement at distance d from the wall as a function of wall height. The higher the wall, the larger the settlement at d will be. Thus, specifying the wall deflection as independent of the wall height is a questionable practice. If the allowable deflection is defined as 3/8 in, according to Eq. 1, the induced maximum settlement will be no greater than 3/8 in. Settlements 12 ft. from the wall for three different wall heights are estimated using the Bowles method (year), the Clough and

O'Rourke method (1990), and the Hsieh and Ou method (1998); the results of these calculations are listed in Table 15.

Table 15. Settlement at 12 ft. from wall/shoring for δ_{wm} = 3/8 in.

Wall/shoring height, H_e (ft.)	Settlement at 12 ft. from wall/shoring in inches		
	Bowles method	*Clough and O'Rourke method*	*Hsieh and Ou method*
10	negligible	1/7	1/9
15	1/25	1/6	1/7
20	1/9	1/5	1/5

As wall height fluctuates from 10 to 20 ft., the induced settlement by 3/8 in wall/shoring deflection is consistently much less than ¼ in at 12 ft. from the excavation, which is the threshold presumed by GTS (2004). In other words, the limit set by GTS for the allowable wall deflection as 3/8 in. is overly conservative for the most commonly used wall heights which are in the range of 10–20 ft.

3 SITE INVESTIGATION

3.1 Introduction

The Union Pacific Railroad (UPRR) has two test sections at a single location near College Station. Each test section is 10 ft. high by 20 ft. long. The first test section is a cantilever sheet pile wall with an embedment depth of 20 ft.; the second is a cantilevered soldier pile wall with timber lagging. These two types of wall are popular shoring options, and thus, direct measurements will be made on wall systems representing a large proportion of the systems actually in use. Figures 41 and 42 show the 3-dimensional plane and view of the site. The wall alignments are parallel to the railroad track, and the instrumentation plan is based on this condition.

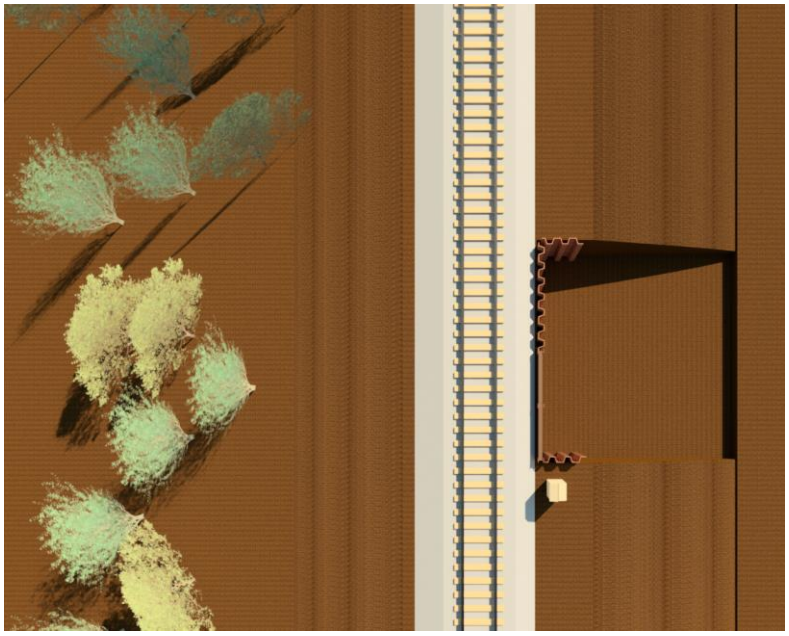

Figure 41. The 3D plane view of the site

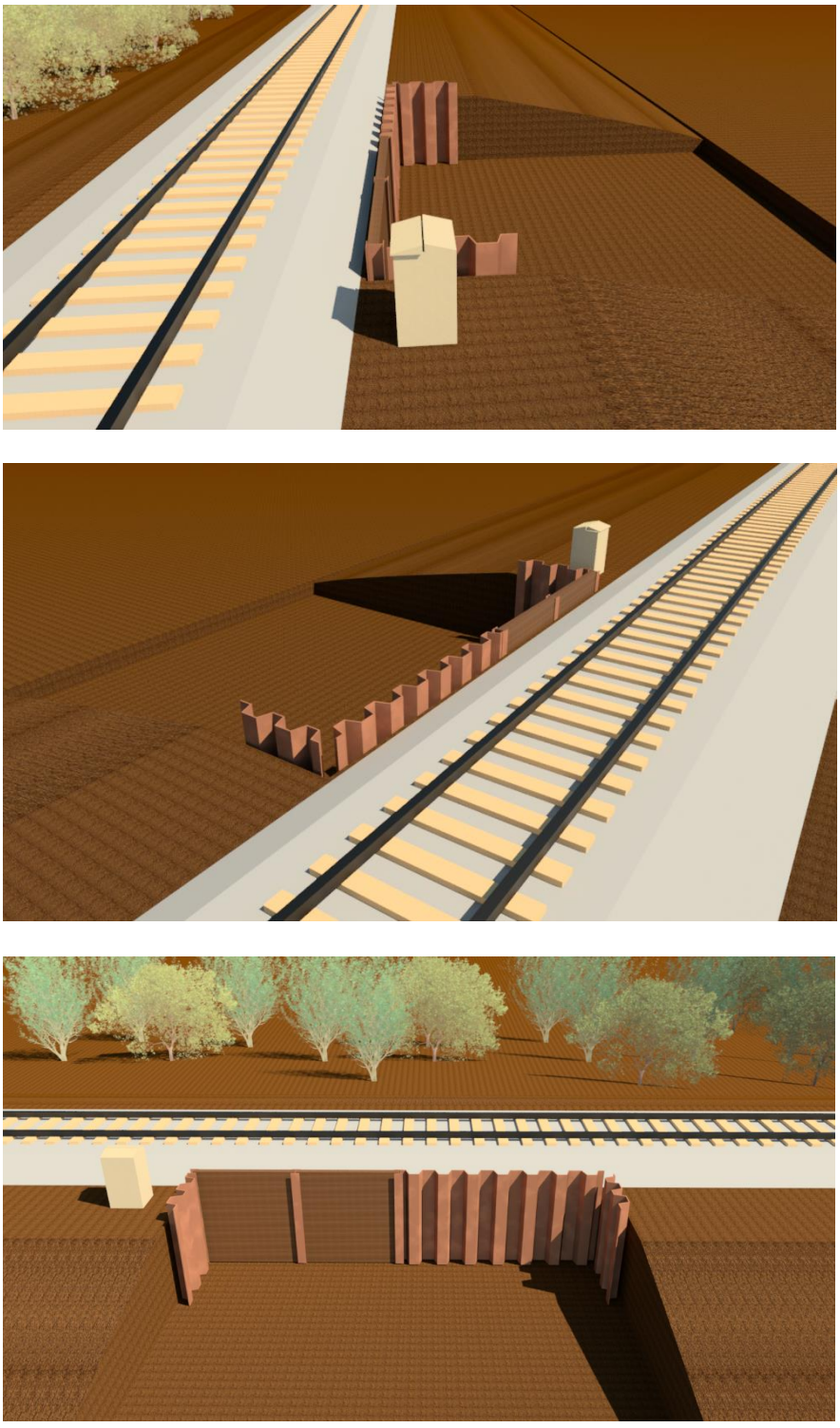

Figure 42. 3D view, side, back and front of the site

The 2D plane and section of the site are illustrated in Figure 43:

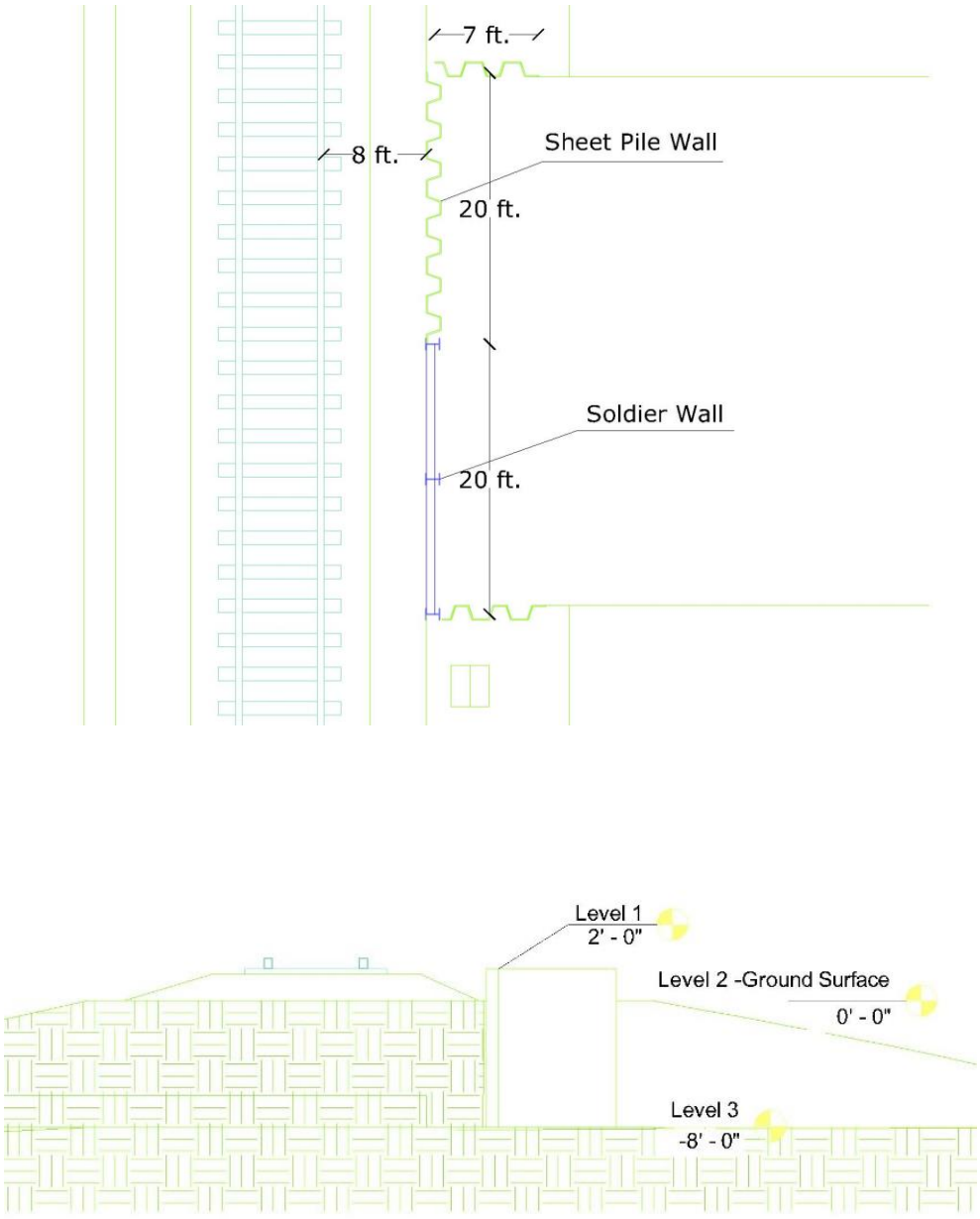

Figure 43. Plane and section of site

The back-slope of the excavation was designed based on local conditions, and two 14-ft. long wing walls were used at the sides of the planned excavation to retain the soil. Figure 44 displays the layout of the walls and wing walls.

Knowledge of in-situ soil conditions is very important to the success of field monitoring programs. During the site selection process, the research team worked with UPRR to locate a site where, to the extent practicable, soils were available. The first soil samples were collected during the wall installation. A specific program for site soil characterization was developed based on the results of some primary tests on these samples. The excavation of the pit provided an opportunity for detailed logging of soil stratification and collection of undisturbed soil samples for laboratory testing.

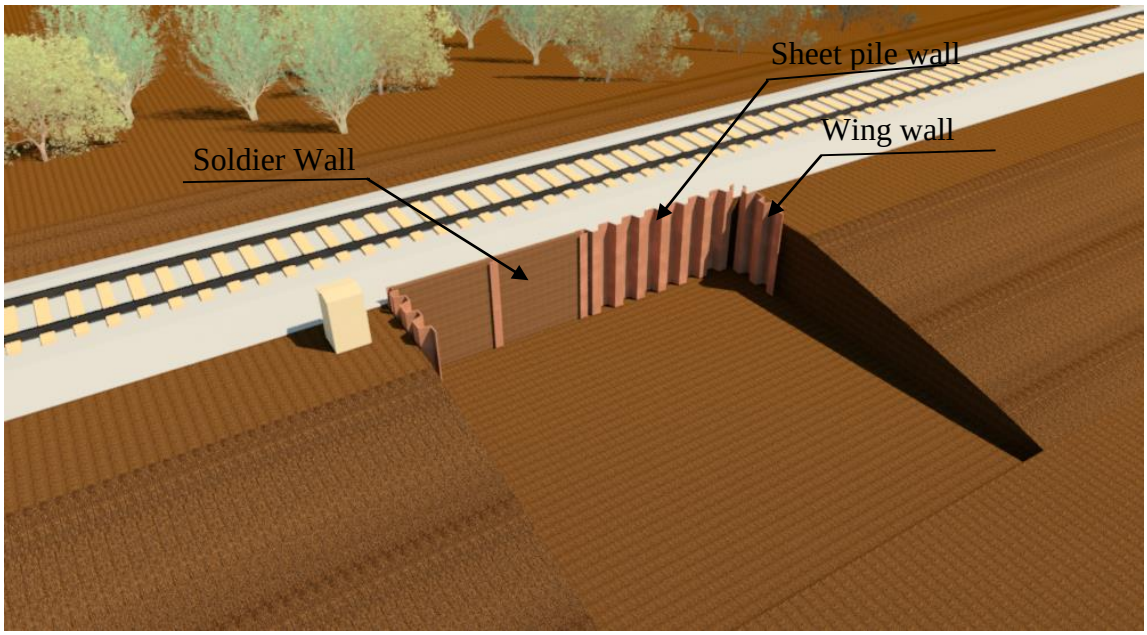

Figure 44. The position of walls and wing walls

3.2 Site Selection

On April 29, 2013, Doctors Gary Fry, Stefan Hurlebaus, and Charles Aubeny from the Texas Transportation Institute (TTI) met with Ronnie Behrens of UPRR to survey a length of UPRR track located in a section referred to as the 'Navasota Sub.' The team hy-railed the track in this region extending roughly from Mumford to Millican, Texas, from mile posts 91.50 to 63.

The main criteria for the location were the following three items:

1. Easy road access,

2. An embankment height of 10 ft. or more of fill to avoid the need for shoring on the back side of excavation, and

3. A freight train speed of at least 60 mph.

The team identified three suitable locations, which are listed in order of preference:

Mile post 68.80, just north of the intersection of Wellborn Road and Highway 40 in College Station, Texas. This location is near Texas A&M University in a curve with about 10 ft. of backfill that permits a train speed of 60 mph and parallels Wellborn Road (FM 2154). Once the wall and equipment were in place, it would be accessible without having to cross the tracks.

Mile post 86.00. This is 0.25 mi south of the State Highway OSR crossing at mile post 86.28.This location is in a curve with about 12 ft. fill and 60 mph train speed. Homola Road, a county road, parallels the tracks at this location. Once the wall and equipment were in place, it would be accessible without crossing the tracks.

Mile post 81.60. This location is just south of the railroad bridge crossing Highway 21 in College Station, Texas. This is not as easily accessible as the other two locations and would require more preparation to make it accessible, primarily in the form of creating a temporary access road and clearing brush.

The final selection of the site was left to UPRR, since they may have had operational and safety considerations unknown to the TTI team. On May 30, 2013, UPRR informally indicated to TTI that the first site at MP 68.60 was acceptable. Figure 45 shows the location of site.

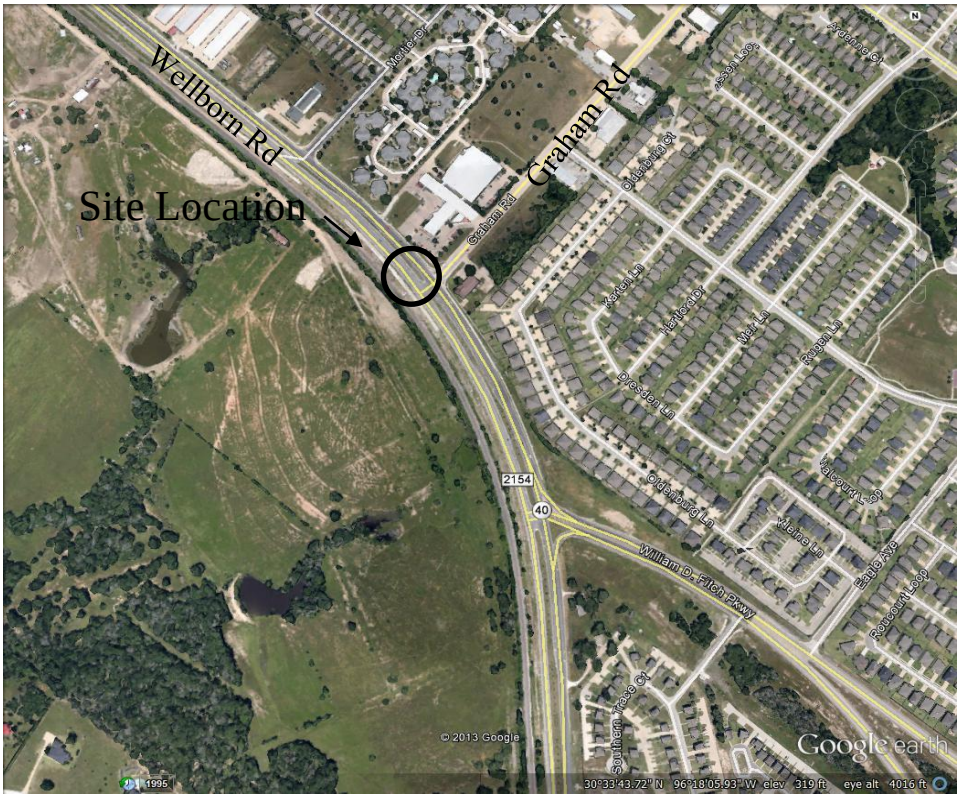

Figure 45. Site location (Source: "Test Site" 30°33'43.72'' N and 96°18'05.93'' W. Google Earth. 1995. July 20, 2013)

3.3 Wall Installation and Excavation

On October 11, 2013, the H-piles and sheet piles were installed at the study site. Excavation began at 9 a.m. on Wednesday, November 13, 2013. Excavation started first at the front of the soldier wall. During the excavation, the UPRR team used some temporary supports to prevent the soil from moving. The excavation process and lagging installation were completed around 9 p.m. on the same day. Excavation in front of the sheet pile wall started at 9 a.m. the following day and took 12 hours.

During these two days, the author of this dissertation, a doctoral student at Texas A&M University, collected soil samples in order to further investigate the soil composition and its impact on the tests to be conducted. In addition, professors Aubeny and Fry monitored the excavation and soil sample collection process during these two days.

The wall abuts a curved section of track with the minimum distance from the rail to the railway centerline being about 15 ft. Furthermore, a C15x33.9 channel section is secured to the top of both the sheet pile wall and the H-piles. The main features of these two walls are summarized in Table 16.

Table 16. The main features of walls

Wall	Section	Length in plane	Penetration	Excavation
		ft.	ft.	ft.
Soldier pile	HP 12*63	20	30	10
Sheet pile	PZ 27	20	30	10

3.3.1 Soldier Pile and Lagging Support Systems

The main components of soldier pile and lagging support systems are steel H-piles placed vertically with lagging between the piling to retain the soil. In the current project, the lagging consisted of timber, and the H-piles were installed by driving. H-piles are placed prior to excavation, and as the excavation is finished, lagging is placed between the soldier piles. The timeline for this project was as follows:

- Installation of the H-piles on October 11, 2013.
- Initiation of the excavation to the planed level on November 13, 2013.
- Installation of the lagging on November 13, 2013.

The H-piles were 30 ft. long in depth and 20 ft. long in plane. The exposed length of the piles was 10 ft. above the base of the excavation, meaning the wall is cantilevered with 10 ft. above ground and 20 ft. below ground. The H-piles were HP 12*63 sections, 12 in. wide by approximately 12 in deep. Three H-piles spaced 10 ft. apart were used in the pile/lagging section of the wall. The properties of these piles are presented in Table 17. The timber lagging was comprised of 8 in by 16 in sections of timber. Figure 46 shows the H-piles and lagging.

Table 17. HP section properties

Section	Area	Depth	Width	Thickness	Moment of inertia (I)
	in^2	in	in	in	in^4
HP 12 * 63	18.4	11.94	12.125	0.515	472

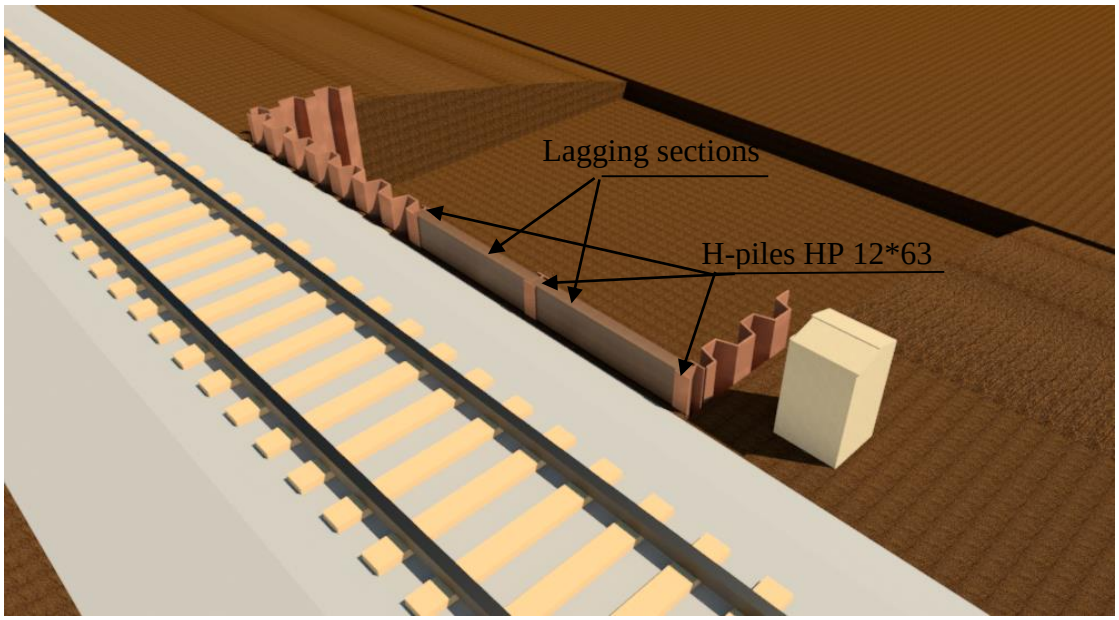

Figure 46. Soldier pile wall – H-piles and lagging

3.3.2 Sheet Pile Wall

The sheets used in this project were made of steel. They were installed before the excavation with the impact hammer. The sheets formed a resistant vertical wall that to support the soft soil which collapsed from the higher level to the lower level. Figure 47 shows the location of sheet pile walls. Constructing the sheet pile wall in this project involved five main stages as follows:

1. Laying out a sequence of sheet pile sections and ensuring that the sheet piles would interlock properly (October 11, 2013).

2. Driving (or vibrating) the individual sheet piles to the desired depth (October 11, 2013).

3. Driving the second sheet pile with the interlocks between the first sheet pile and second "locked" (October 11, 2013).

4. Repeating steps 2 and 3 until the wall perimeter is completed (October 11, 2013)

5. Excavation (November 13, 2013)

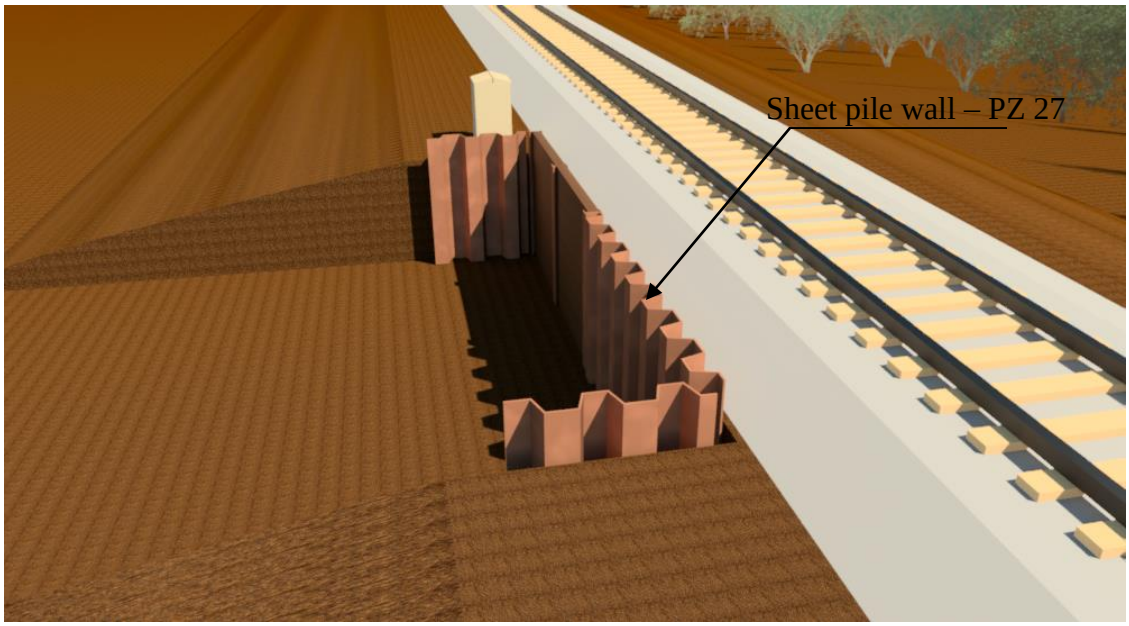

Figure 47. Sheet pile wall

The sheets used were PZ27 and 30 ft. deep and 20 ft. long in plane. Similar to the soldier wall constructed for this project, the exposed length of the piles is 10 ft. above the base of the excavation. The wall is cantilevered with 10 ft. above ground and 20 ft. below ground. Figure 48 shows the cross-section of sheets. The properties of the sheets are presented in Table 18.

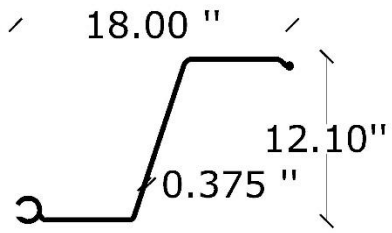

Figure 48. Cross-section of sheet piles

Table 18. Sheet section properties

Section	Area	Depth	Width	Thickness	Moment of inertia - I
	$in.^2$	in.	in.	in.	$in.^4/ft.$
PZ 27	12.2	12.1	18	0.375	187.3

3.4 Site Investigation and Soil Tests

The site investigation was done in two major steps. The first was collecting the soil samples after the wall installation in order to determine the primary properties of the soil such as the type, water content, Atterberg limit, and the gradation. These first soil samples were collected from the site by the research group on October 17, 2013. The UPRR team monitored the process of soil sampling in order to confirm the safety issues. Samples were collected on the track side of the middle of each of the walls. In total, two buckets of soil samples were collected and transferred to the Geotechnical Engineering Lab of the Zachry Department of Civil Engineering at Texas A&M University for analysis. The results of these tests will be presented in later sections.

The second part involved taking samples of undisturbed soils at various depths to provide data on the soil strength profile and other major properties of soil including unit weight, water content, and. During the second phase, the Hand Vane Test was done at different depths to find the in place undrained shear strength of the soil. In addition, in order to determine undrained shear strength of the soil, the research team designed a series of triaxial shear tests. The triaxial test designed also provided estimates of the Young's modulus (E), which was then used in the finite element modeling of the walls.

3.5 Lab Testing

A series of lab tests to evaluate the properties of the soil such as gradation, water content, unit weight, the Atterberg limit, and undrained shear strength were carried out. The results of these tests could provide direct input for routine design procedures and for the finite element studies of these walls. The details of these are presented in the following sections.

3.5.1 Water Content Test

The research group used the ASTM D2216-98 standard to find the water content of the soil in the different samples. The first samples were obtained six days after the wall installation and were for basic investigation. The second phase of sampling was conducted during the excavation in order to sample at different depths and locations to identify water content variation with depth. In order to have good samples in deeper soils, a soil sampling tube set (H-4362 by Humboldt Mfg. Co.) was used. After collection, each sample was sealed in plastic Ziploc® bags to minimize the moisture loss. The water content determination was done on the same day as the sampling to minimize the error and

moisture loss. Figure 49 shows the soil sampling device and the process of sampling. The results of these tests are presented in Tables 19 and 20.

(a) The soil sampling kit

(b) A researcher taking a soil sample at a depth of 4 ft.

Figure 49. Sampling the soil

Table 19. Water content of samples from 17 October 2013

Live Load Effects of Railroads on Retaining Walls and Temporary Shoring					
Water Content of first sample				**Date: 09/17/2013**	
Sample	Mass of cup (gr)	Mass of cup + soil (wet) (gr)	Mass of cup + soil (oven dry) (gr)	Mass of water (gr)	Water content %
#1	44.87	196.45	176.45	20	15.1998784
#2	45.12	175.14	148.95	26.19	25.22392372
#3	25.4	84.07	72.5	11.57	24.56475584
#4	44.41	192.11	162.9	29.21	24.65186936
			Water Content		22.41010683

Table 20. Water content of samples taken 13–14 November 2013

Live Load Effects of Railroads on Retaining Walls and Temporary Shoring							
Water Content of first sample						**Date: 11/14/2013-11/13/2013**	
Sample	Wall	Depth	Mass of cup (gr)	Mass of cup + soil (wet) (gr)	Mass of cup + soil (oven dry) (gr)	Mass of water (gr)	Water content %
#1	Soldier-wall	Ground surface	37.94	220.15	181.48	38.67	26.94
#2	Soldier-wall	2 ft	27.13	181.21	148.57	32.64	26.88
#3	Soldier-wall	4 ft	44.65	220.18	184.58	35.6	25.44
#4	Soldier-wall	6 ft	44.62	215.61	179.2	36.41	27.05
#5	Soldier-wall	8 ft	25.79	132.7	104.4	28.3	36.00
#6	Sheet pile wall	Ground surface	46.67	234.42	193.11	41.31	28.21
#7	Sheet pile wall	2 ft	45.25	200.44	169.06	31.38	25.35
#8	Sheet pile wall	4 ft	44.35	152.11	127.61	24.5	29.43
#9	Sheet pile wall	6 ft	44.1	138.58	117.42	21.16	28.86
#10	Sheet pile wall	8 ft	44.57	199.11	161.12	37.99	32.60
#11	Sand cone test	8 ft	44.67	197.98	157.95	40.03	35.34

3.5.2 Particle-Size Distribution

The ASTM D6913-04, ASTM D2217 -85, ASTM D422 -63, ASTM D421 -85, and ASTM C136 – 06 were used to determine the soil particle size and type of the soil. Due to the fact that the soil was highly cohesive, the research team decided to evaluate the gradation of soil using the wet sieve analysis method. The soil was soaked for about 24 hours, after which it was washed with water in sieves of declining sizes. It was first placed in the biggest sieve, and rinsed until the water under the sieve ran clear. At this point, all the particles smaller than sieve mesh have passed through the sieve.

The results of the wet sieve analysis showed that more than 50% of the soil particles were smaller than 0.075 mm (no. 200 sieve), which is the boundary between course and fine material. By definition, this means that the soil was a fine soil. By finding the Atterberg limit of soil, the soil was categorized in CH group. Results of the sieve analysis are presented in Table 21 and Figure 50. Figure 51 displays the process of wet sieve analysis.

Table 21. Soil gradation

Live Load Effects of Railroads on Retaining Walls and Temporary Shoring					
Particle-Size Analysis of Soil			Date of sampling: 09/17/2013	Date of test: 09/23/2013	
Sieve No./ Size (mm)	**Weight of pan (g)**	**Weight of sieve +soil (g)**	**Weight of soil retained (gr)**	**Percentage retained (%)**	**Percent passed (%)**
4(4.75)	140.16	378.32	238.16	3.99	96.01
20(.85)	300.48	425.58	125.1	2.10	93.91
40(0.425)	317.51	370.72	53.21	0.89	93.02
60(0.25)	350.63	514.48	163.85	2.74	90.28
200(0.075)	644.08	2154.98	1510.9	25.31	64.97
Pan	1020.42	4898.87	3878.45	64.97	0.00
Total weight of soil (g)		5969.67			

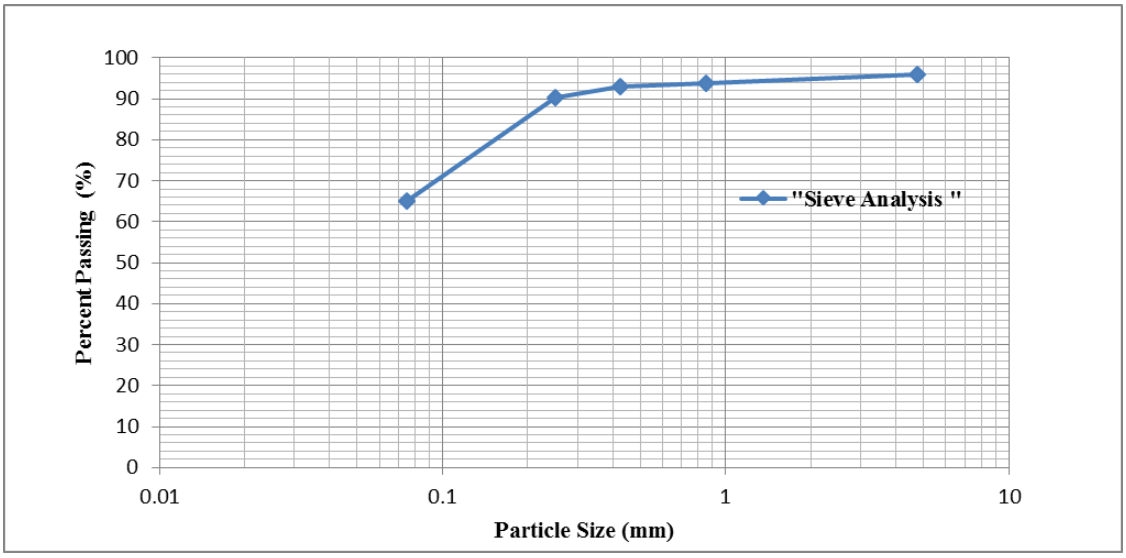

Figure 50. Sieve analysis

Figure 51. Wet sieve analysis

3.5.3 Atterberg Limit

To calculate the Atterberg limit, the ASTM D4318-10 was followed to determine the liquid limit, plastic limit, and plasticity index of soil first. The Atterberg Limit test was done on both the samples obtained shortly after the wall installation and during the excavation from the deeper layers of soils. With reference to the standard, the wet preparation method and multiple liquid limit method that are more precise than other methods were chosen by research group.

These two tests were performed on the portion of soil that passed the 0.425 mm (no. 40) sieve. In the wet preparation method, each sample is soaked until all lumps have softened and the fine grains no longer adhere to each other. The multipoint liquid limit test requires that at least three trials with different water contents be performed; the data from the trials were then plotted to find the water content corresponding to 25 drops.

To measure the plastic limit, the soil material is pressed together and rolled into a 3.2 mm diameter thread. This process is repeated until the thread crumbles can no longer be pressed together and rerolled. The results of these tests are summarized in Tables 22 to 33. Figures 52 to 63 show the results of the multipoint liquid limit test.

Table 22. Atterberg limit after wall installation

Live Load Effects of Railroads on Retaining Walls and Temporary Shoring					
Atterberg Limit-LL		sample #1	Date of sampling: 09/17/2013		Date of test: 09/23/2013
Can No.	1.00	2.00	3.00	4.00	5.00
Mass of can (g)	15.08	15.03	44.62	44.26	44.46
Mass of wet soil + can (g)	40.52	52.51	85.03	74.78	80.50
Mass of dry soil + can (g)	33.37	42.60	74.38	66.78	71.23
Mass of dry soil	18.29	27.57	29.76	22.52	26.77
mass of water (g)	7.15	9.91	10.65	8.00	9.27
Water content, (%)	39.09	35.94	35.79	35.52	34.63
No. of drops	14	20	24	28	35
Liquid Limit = 36 %					
Can No.	1.00	2.00		***Plastic Index : 22***	
Mass of can (g)	22.93	25.78			
Mass of wet soil + can (g)	33.20	31.28			
Mass of dry soil + can (g)	31.83	30.63			
Mass of dry soil	8.90	4.85		***Soil Type : CL***	
mass of water (g)	1.37	0.65			
Water content, (%)	15.39	13.40			
Plastic Limit = 14 %					

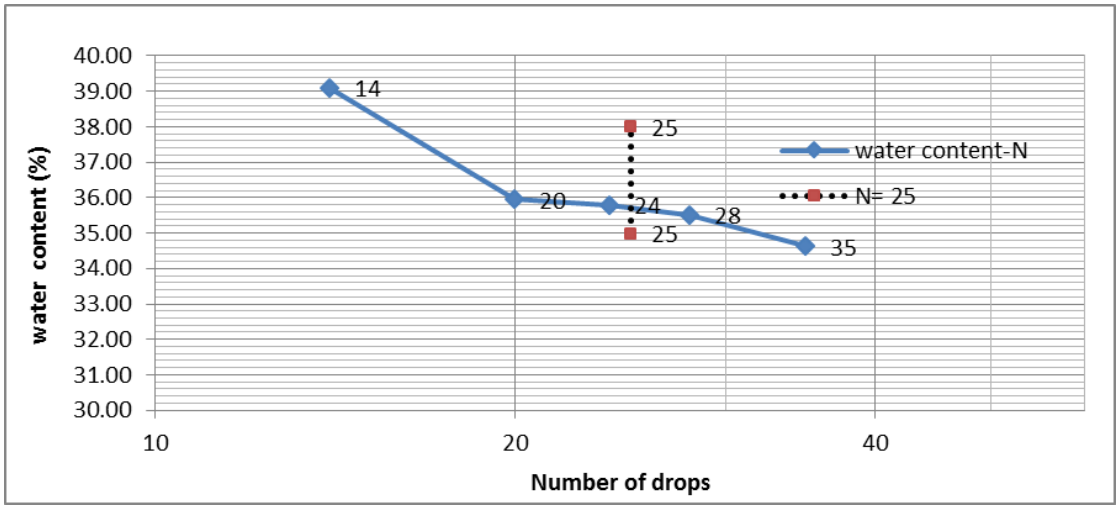

Figure 52. The results of the multipoint liquid limit test. Number of drops vs. water content from the surface soil samples after wall installation

Table 23. Atterberg limit during excavation – ground surface – Soldier wall

Live Load Effects of Railroads on Retaining Walls and Temporary Shoring			
Depth : Ground Surface			Soldier Wall
Atterberg Limit-LL	sample #4	Date of sampling: 11/13/2013	Date of test: 11/21/2013
Can No.	1.00	2.00	
Mass of can (g)	1.00	1.00	
Mass of wet soil + can (g)	15.49	13.82	
Mass of dry soil + can (g)	10.68	9.58	
Mass of dry soil	9.68	8.58	
mass of water (g)	4.81	4.24	
Water content, (%)	49.69	49.42	
No. of drops	30	16	
Liquid Limit =		***50***	
Can No.	1.00		
Mass of can (g)	1.00	***Plastic Index :***	***25***
Mass of wet soil + can (g)	13.00		
Mass of dry soil + can (g)	10.63		
Mass of dry soil	9.63		
mass of water (g)	2.37	***Soil Type : CH***	
Water content, (%)	24.61		
Plastic Limit =	***25***		

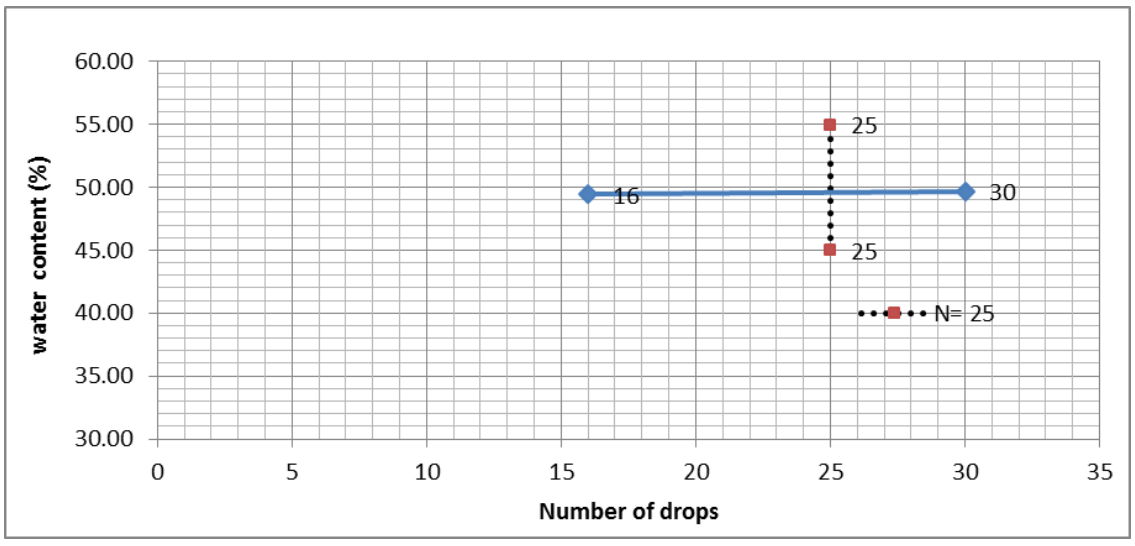

Figure 53. The multipoint liquid limit test. Number of drops vs. water content ground surface – Soldier wall

Table 24. Atterberg limit during excavation – ground surface – Sheet pile wall

Live Load Effects of Railroads on Retaining Walls and Temporary Shoring			
Depth : Ground Surface			Sheet Pile Wall
Atterberg Limit-LL	sample #6	Date of sampling: 11/13/2013	Date of test: 11/21/2013
Can No.	1.00	2.00	3.00
Mass of can (g)	1.00	1.00	1.00
Mass of wet soil + can (g)	16.03	19.40	18.47
Mass of dry soil + can (g)	11.28	13.03	12.28
Mass of dry soil	10.28	12.03	11.28
mass of water (g)	4.75	6.37	6.19
Water content, (%)	46.21	52.95	54.88
No. of drops	44	20	15
Liquid Limit =		***52***	
Can No.	1.00		
Mass of can (g)	1.00	***Plastic Index :***	***27***
Mass of wet soil + can (g)	15.90		
Mass of dry soil + can (g)	12.89		
Mass of dry soil	11.89		
mass of water (g)	3.01	***Soil Type : CH***	
Water content, (%)	25.32		
Plastic Limit :	***25***		

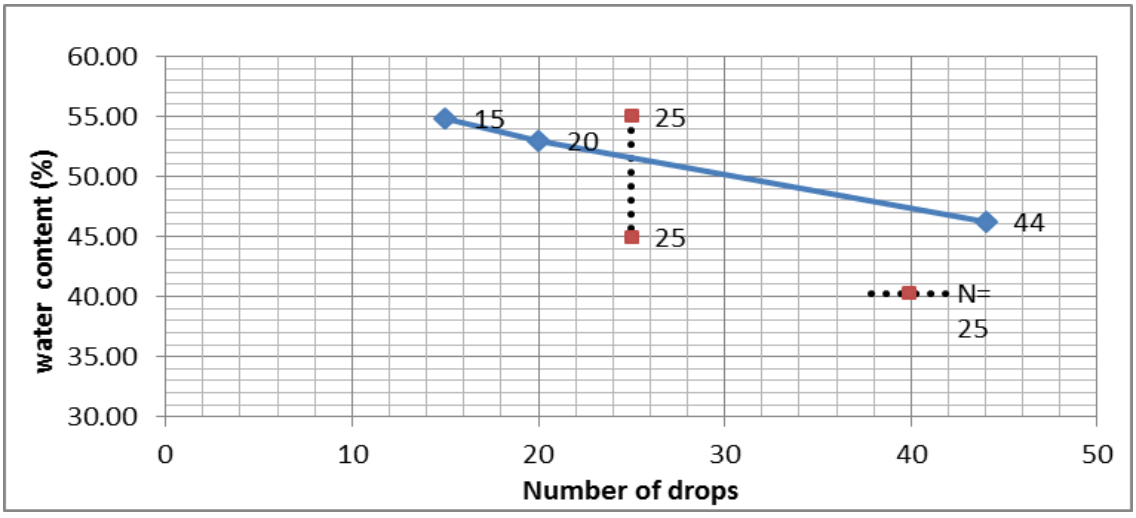

Figure 54. The multipoint liquid limit test. Number of drops vs. water content ground surface – Sheet pile wall

Table 25. Atterberg limit during excavation – 2 ft. depth – Soldier wall

Live Load Effects of Railroads on Retaining Walls and Temporary Shoring			
Depth : 2 ft			Soldier Wall
Atterberg Limit-LL	sample #3	Date of sampling: 11/13/2013	Date of test: 11/20/2013
Can No.	1.00	2.00	3.00
Mass of can (g)	1.00	1.00	1.00
Mass of wet soil + can (g)	14.15	17.48	16.50
Mass of dry soil + can (g)	10.79	13.19	12.31
Mass of dry soil	9.79	12.19	11.31
mass of water (g)	3.36	4.29	4.19
Water content, (%)	34.32	35.19	37.05
No. of drops	29	25	14
Liquid Limit =		***35***	
Can No.	1.00		
Mass of can (g)	1.00	***Plastic Index :***	***19***
Mass of wet soil + can (g)	10.53		
Mass of dry soil + can (g)	9.24		
Mass of dry soil	8.24		
mass of water (g)	1.29	***Soil Type : CL***	
Water content, (%)	15.66		
Plastic Limit :	***16***		

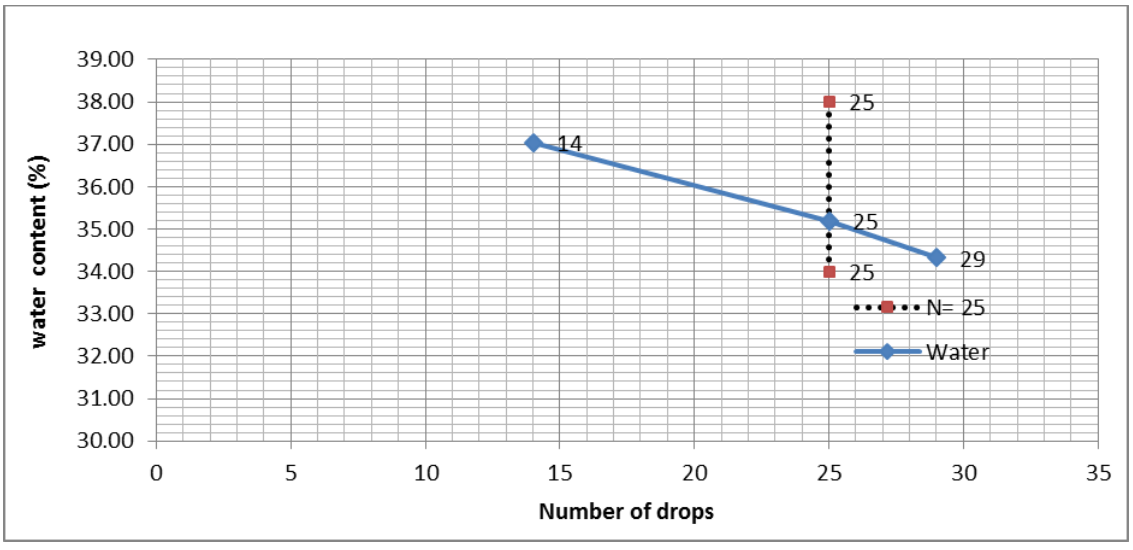

Figure 55. The multipoint liquid limit test. Number of drops vs. water content 2 ft. depth – Soldier wall

Table 26. Atterberg limit during excavation – 2 ft. depth – Sheet pile wall

Live Load Effects of Railroads on Retaining Walls and Temporary Shoring			
Depth : 2 ft			Sheet Pile Wall
Atterberg Limit-LL	sample #9	Date of sampling: 11/13/2013	Date of test: 11/22/2013
Can No.	1.00	2.00	3.00
Mass of can (g)	1.00	1.00	1.00
Mass of wet soil + can (g)	13.53	14.56	14.26
Mass of dry soil + can (g)	10.56	11.32	10.82
Mass of dry soil	9.56	10.32	9.82
mass of water (g)	2.97	3.24	3.44
Water content, (%)	31.07	31.40	35.03
No. of drops	28	17	12
Liquid Limit =		***31***	
Can No.	1.00		
Mass of can (g)	1.00	***Plastic Index :***	***13***
Mass of wet soil + can (g)	15.97		
Mass of dry soil + can (g)	13.73		
Mass of dry soil	12.73		
mass of water (g)	2.24	***Soil Type : CL***	
Water content, (%)	17.60		
Plastic Limit :	***18***		

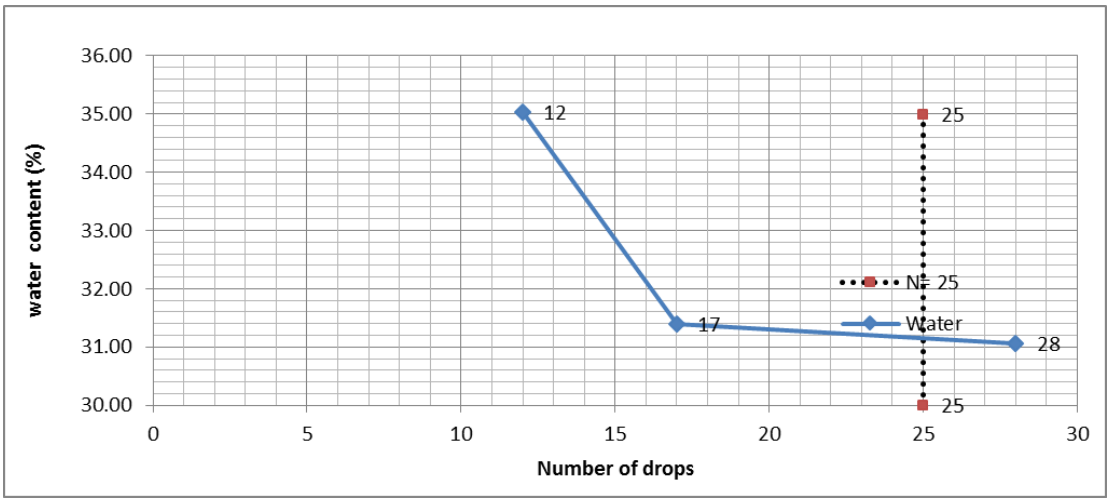

Figure 56. The multipoint liquid limit test. Number of drops vs. water content 2 ft. depth – Sheet pile wall

Table 27. Atterberg limit during excavation – 4 ft. depth – Soldier wall

Live Load Effects of Railroads on Retaining Walls and Temporary Shoring			
Depth : 4 ft			Soldier Wall
Atterberg Limit-LL	sample #1	Date of sampling: 11/13/2013	Date of test: 11/20/2013
Can No.	1.00	2.00	3.00
Mass of can (g)	1.00	1.00	1.00
Mass of wet soil + can (g)	15.81	13.83	13.93
Mass of dry soil + can (g)	10.91	9.49	9.43
Mass of dry soil	9.91	8.49	8.43
mass of water (g)	4.90	4.34	4.50
Water content, (%)	49.45	51.12	53.38
No. of drops	53	28	19
Liquid Limit =		***52***	
Can No.	1.00		
Mass of can (g)	1.00	***Plastic Index :***	***30***
Mass of wet soil + can (g)	12.00		
Mass of dry soil + can (g)	10.02		
Mass of dry soil	9.02		
mass of water (g)	1.98	***Soil Type : CH***	
Water content, (%)	21.95		
Plastic Limit :	***22***		

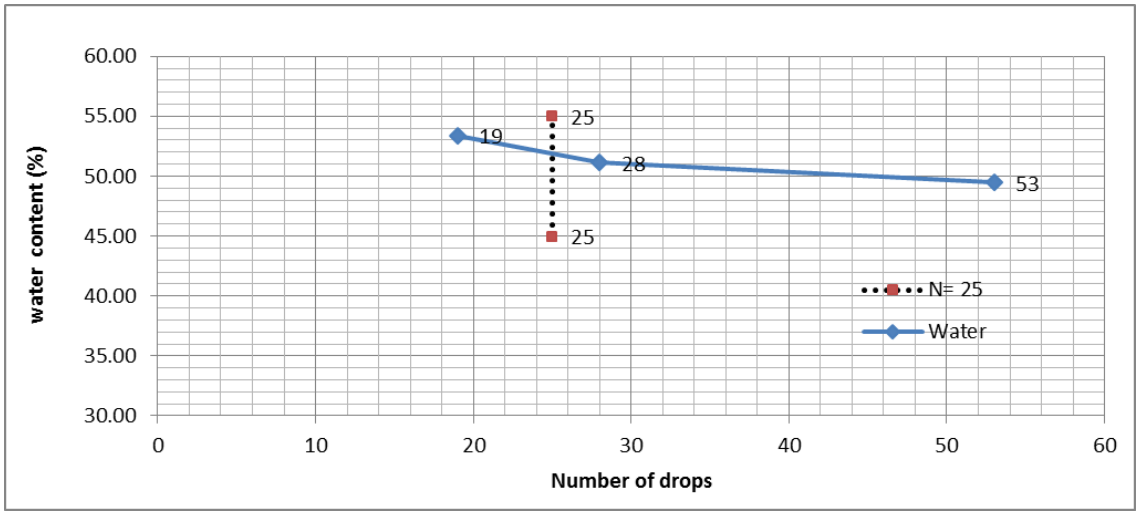

Figure 57. The multipoint liquid limit test. Number of drops vs. water content 4 ft. depth – Soldier wall

Table 28. Atterberg limit during excavation – 4 ft. depth – Sheet pile wall

Live Load Effects of Railroads on Retaining Walls and Temporary Shoring			
Depth : 4 ft			Sheet Pile Wall
Atterberg Limit-LL	sample #8	Date of sampling: 11/13/2013	Date of test: 11/22/2013
Can No.	1.00	2.00	3.00
Mass of can (g)	1.00	1.00	1.00
Mass of wet soil + can (g)	13.36	13.21	15.97
Mass of dry soil + can (g)	9.06	8.66	10.22
Mass of dry soil	8.06	7.66	9.22
mass of water (g)	4.30	4.55	5.75
Water content, (%)	53.35	59.40	62.36
No. of drops	54	25	17
Liquid Limit =		***59***	
Can No.	1.00		
Mass of can (g)	1.00	***Plastic Index :***	***40***
Mass of wet soil + can (g)	15.02		
Mass of dry soil + can (g)	12.74		
Mass of dry soil	11.74		
mass of water (g)	2.28	***Soil Type : CH***	
Water content, (%)	19.42		
Plastic Limit =	***19***		

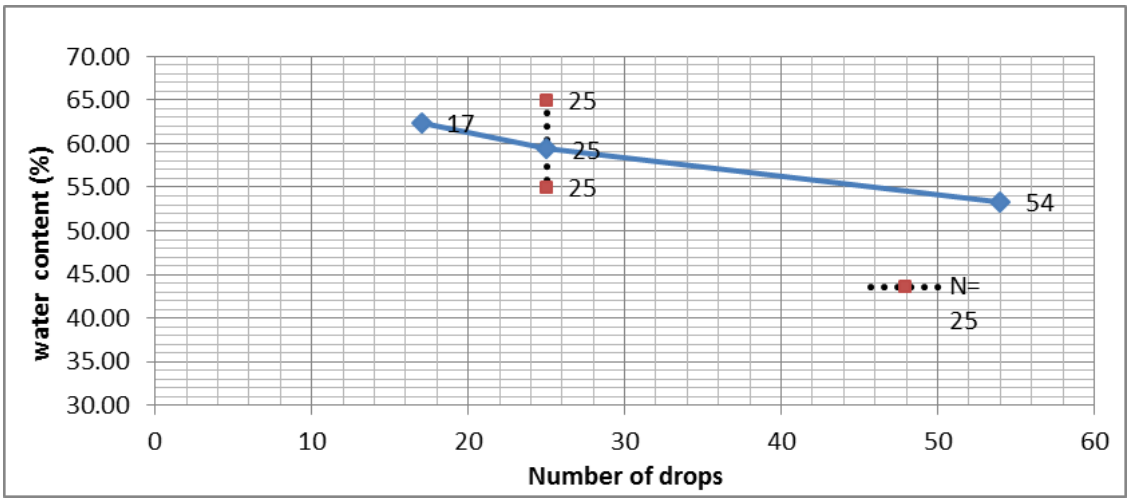

Figure 58. The multipoint liquid limit test. Number of drops vs. water content 4 ft. depth – Sheet pile wall

Table 29. Atterberg limit during excavation – 6 ft. depth – Soldier wall

Live Load Effects of Railroads on Retaining Walls and Temporary Shoring			
Depth : 6 ft			Soldier Wall
Atterberg Limit-LL	sample #10	Date of sampling: 11/13/2013	Date of test: 11/23/2013
Can No.	1.00	2.00	3.00
Mass of can (g)	1.00	1.00	1.00
Mass of wet soil + can (g)	13.51	15.26	17.20
Mass of dry soil + can (g)	9.35	10.27	11.47
Mass of dry soil	8.35	9.27	10.47
mass of water (g)	4.16	4.99	5.73
Water content, (%)	49.82	53.83	54.73
No. of drops	36	22	18
Liquid Limit =		***53***	
Can No.	1.00		
Mass of can (g)	1.00	***Plastic Index :***	***29***
Mass of wet soil + can (g)	15.67		
Mass of dry soil + can (g)	12.86		
Mass of dry soil	11.86		
mass of water (g)	2.81	***Soil Type : CH***	
Water content, (%)	23.69		
Plastic Limit =	***24***		

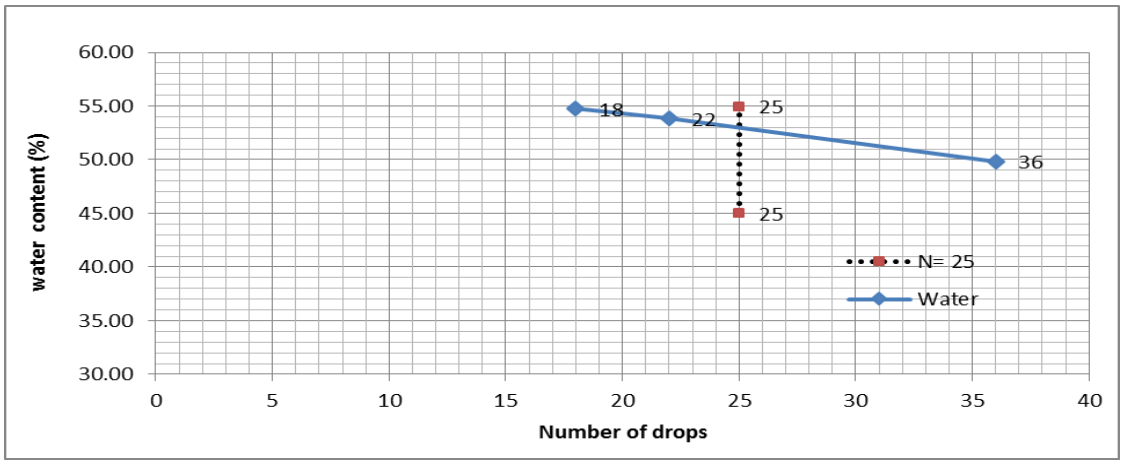

Figure 59. The multipoint liquid limit test. Number of drops vs. water content 6 ft. depth – Soldier wall

Table 30. Atterberg limit during excavation – 6 ft. depth – Sheet pile wall

Live Load Effects of Railroads on Retaining Walls and Temporary Shoring			
Depth : 6 ft			Sheet Pile Wall
Atterberg Limit-LL	sample #2	Date of sampling: 11/13/2013	Date of test: 11/20/2013
Can No.	1.00	2.00	3.00
Mass of can (g)	1.00	1.00	1.00
Mass of wet soil + can (g)	12.18	13.85	14.95
Mass of dry soil + can (g)	7.97	8.88	9.45
Mass of dry soil	6.97	7.88	8.45
mass of water (g)	4.21	4.97	5.50
Water content, (%)	60.40	63.07	65.09
No. of drops	60	24	14
Liquid Limit =		***63***	
Can No.	1.00		
Mass of can (g)	1.00	***Plastic Index :***	***41***
Mass of wet soil + can (g)	10.36		
Mass of dry soil + can (g)	8.69		
Mass of dry soil	7.69		
mass of water (g)	1.67	***Soil Type : CH***	
Water content, (%)	21.72		
Plastic Limit =	***22***		

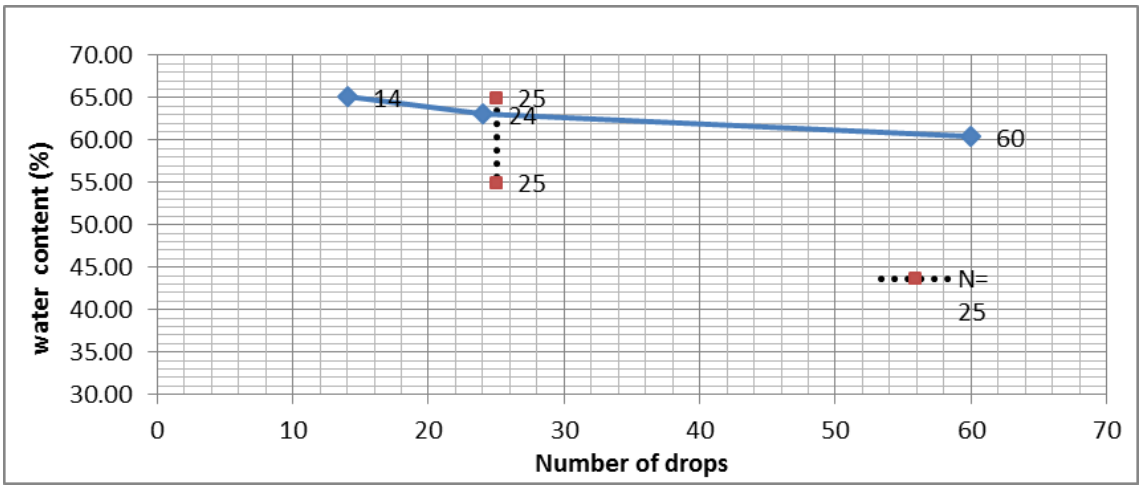

Figure 60. The multipoint liquid limit test. Number of drops vs. water content 6 ft. depth – Sheet pile wall

Table 31. Atterberg limit during excavation – 8 ft. depth – Soldier wall

Live Load Effects of Railroads on Retaining Walls and Temporary Shoring			
Depth : 8 ft			Soldier Wall
Atterberg Limit-LL	sample #7	Date of sampling: 11/13/2013	Date of test: 11/22/2013
Can No.	1.00	2.00	3.00
Mass of can (g)	1.00	1.00	1.00
Mass of wet soil + can (g)	10.36	11.23	14.82
Mass of dry soil + can (g)	6.80	7.17	9.12
Mass of dry soil	5.80	6.17	8.12
mass of water (g)	3.56	4.06	5.70
Water content, (%)	61.38	65.80	70.20
No. of drops	51	23	17
Liquid Limit =		***66***	
Can No.	1.00		
Mass of can (g)	1.00	***Plastic Index :***	***40***
Mass of wet soil + can (g)	10.79		
Mass of dry soil + can (g)	8.76		
Mass of dry soil	7.76		
mass of water (g)	2.03	***Soil Type : CH***	
Water content, (%)	26.16		
Plastic Limit =	***26***		

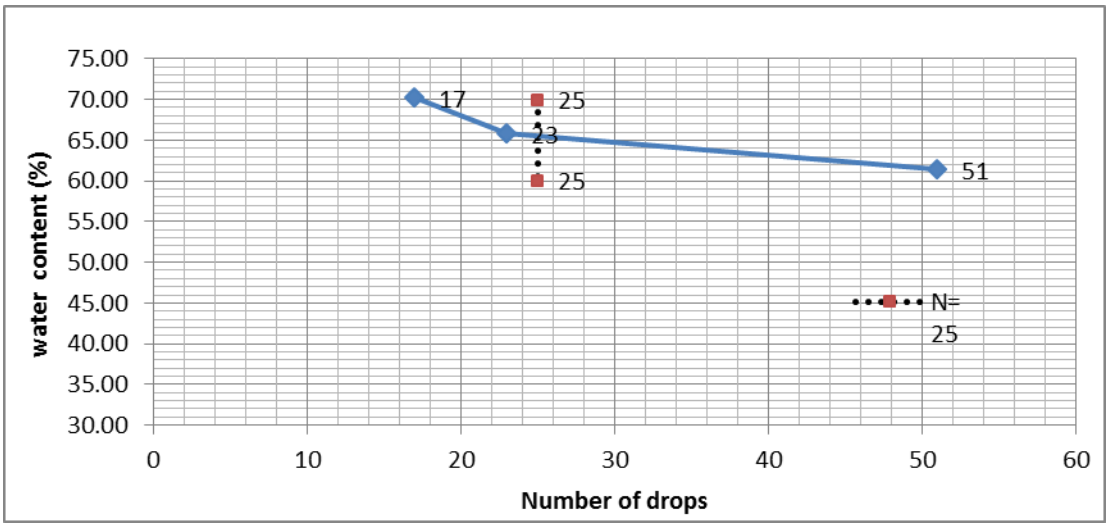

Figure 61. The multipoint liquid limit test. Number of drops vs. water content 8 ft. depth – Soldier wall

Table 32. Atterberg limit during excavation – 8 ft. depth – Sheet pile wall

Live Load Effects of Railroads on Retaining Walls and Temporary Shoring			
Depth : 8 ft			Sheet Pile Wall
Atterberg Limit-LL	sample #5	Date of sampling: 11/13/2013	Date of test: 11/21/2013
Can No.	1.00	2.00	3.00
Mass of can (g)	1.00	1.00	1.00
Mass of wet soil + can (g)	12.31	14.35	14.45
Mass of dry soil + can (g)	7.66	8.64	8.56
Mass of dry soil	6.66	7.64	7.56
mass of water (g)	4.65	5.71	5.89
Water content, (%)	69.82	74.74	77.91
No. of drops	49	30	21
Liquid Limit =		***76***	
Can No.	1.00		
Mass of can (g)	1.00	***Plastic Index :***	***44***
Mass of wet soil + can (g)	13.02		
Mass of dry soil + can (g)	10.09		
Mass of dry soil	9.09		
mass of water (g)	2.93	***Soil Type : CH***	
Water content, (%)	32.23		
Plastic Limit =	***32***		

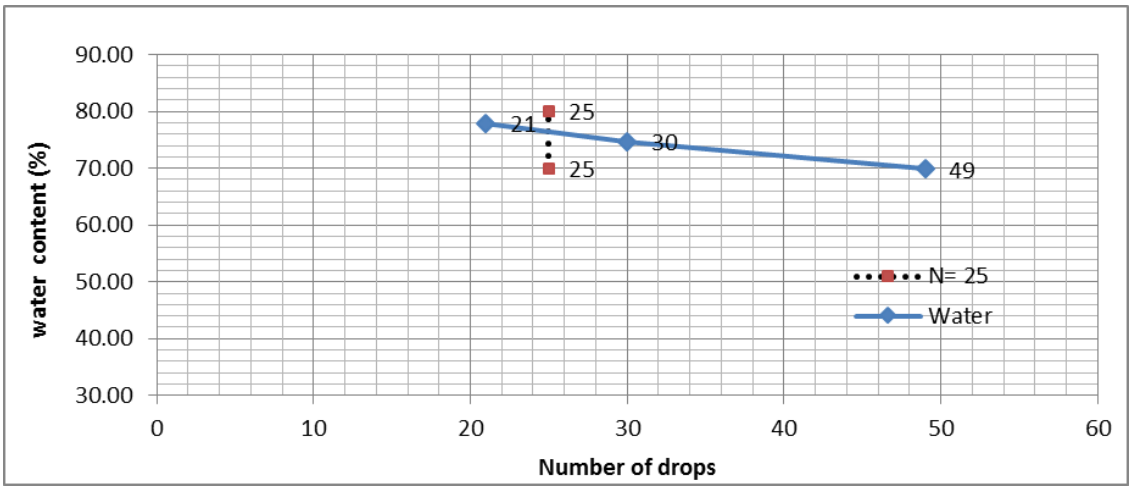

Figure 62. The multipoint liquid limit test. Number of drops vs. water content 8 ft depth – Sheet pile wall

Table 33. Atterberg limit during excavation – Sand cone sample

Live Load Effects of Railroads on Retaining Walls and Temporary Shoring			
Depth : 8 ft - Sand cone			Sheet Pile Wall
Atterberg Limit-LL	sample #1	Date of sampling: 11/13/2013	Date of test: 11/23/2013
Can No.	1.00	2.00	3.00
Mass of can (g)	1.00	1.00	1.00
Mass of wet soil + can (g)	12.15	15.10	13.81
Mass of dry soil + can (g)	7.56	9.29	8.18
Mass of dry soil	6.56	8.29	7.18
mass of water (g)	4.59	5.81	5.63
Water content, (%)	69.97	70.08	78.41
No. of drops	33	25	19
Liquid Limit =		***70***	
Can No.	1.00		
Mass of can (g)	1.00	***Plastic Index :***	***37***
Mass of wet soil + can (g)	14.35		
Mass of dry soil + can (g)	11.01		
Mass of dry soil	10.01		
mass of water (g)	3.34	***Soil Type : CH***	
Water content, (%)	33.37		
Plastic Limit :	***33***		

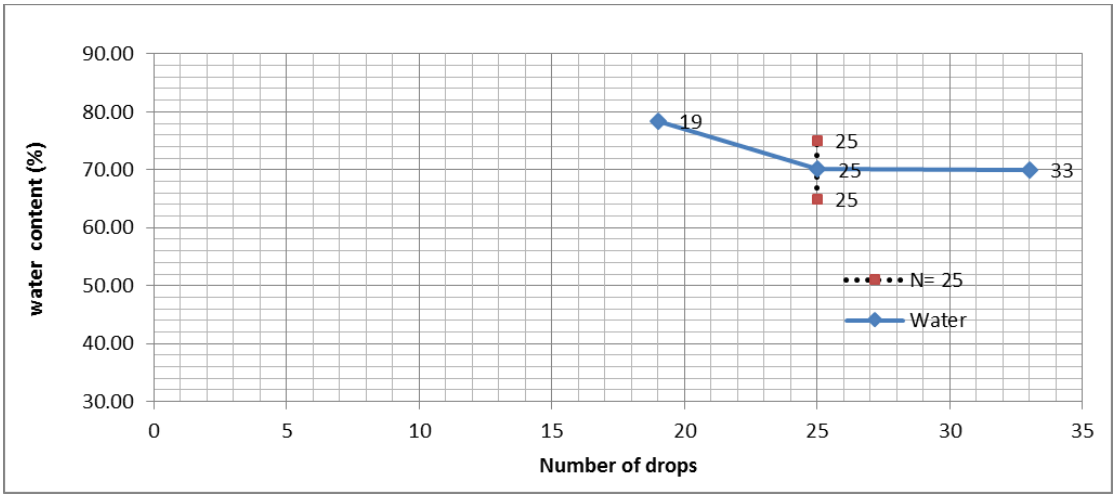

Figure 63. The multipoint liquid limit test. Number of drops vs. water content Sand cone sample

3.5.4 Density and Unit Weight of Soil in Place

The soil sampled was fine; therefore, the research team decided to use the sand cone apparatus method to more accurately estimate of unit weight of the samples. The ASTM D1556-07 was applied to find the unit weight of soil

To conduct this test, first a hand-excavated hole is dug, and all the material from the hole is saved in a container. The hole is then filled with sand that is dry, clean, and uniform in density and grading, uncemented, durable, and free flowing. The density of the sand is known, and the volume of the hole is then calculated based on the quantity of the sand that fits into the hole. The in place wet density of the soil is calculated by dividing the wet mass of the removed soil by the volume of the hole. Table 34 presents the results of this test, while Figure 64 shows the procedures of this test.

Table 34. Sand-Cone test results

Live Load Effects of Railroads on Retaining Walls and Temporary Shoring	
Sand Cone Test	Date : 11/14/13
Jar + Sand	6300.65 gr
Jar + Sand after test	3428.8 gr
Sand in Hole and cone	2871.85 gr
sand in hole	1172.51 gr
Unit weight of sand	107.7 pcf
Volume of Hole (m^3)	0.000679 m^3
Mass of wet soil	1317.95 gr
Unit weight of soil	19.02 KN/m^3
	121 pcf
Water Content	35.34%
Dry Unit weight of soil	89.4 pcf

Figure 64. The procedures of the Sand-Cone test

3.5.5 Hand Vane Test

The undrained shear strength of the soil samples taken during excavation was analyzed using the Hand Vane Test per guideline ASTM D2573-08. In this test, a rod with four-bladed thin vanes at the end was forced into undisturbed soil, and the resistance to rotation of the rod was determined by reading the gage on the top of the rod. This test provides researchers with an estimate of in-situ undrained shear strength of soil. A CL-612 Hand Vane Tester from ELE International was used in this test. The diameter of the

vanes is about 19 mm, and the length of the rod is about 50 cm. Figure 65 shows the device used and someone using it. The results of the Hand Vane Test are reported in Table 35.

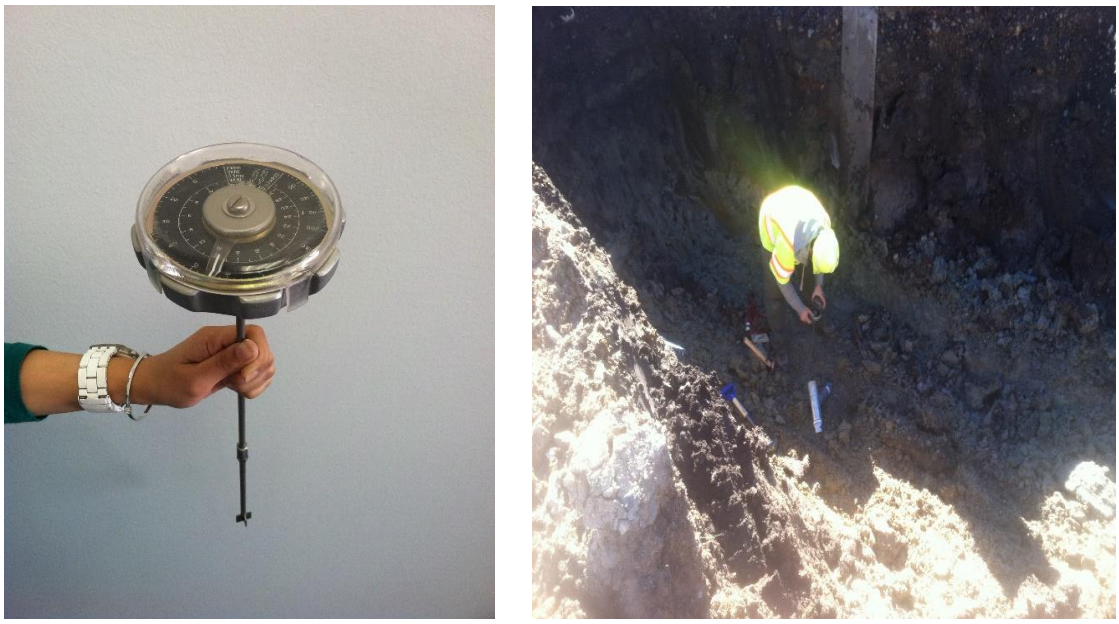

Figure 65. Hand Vane test

Table 35. Hand Vane test results

Live Load Effects of Railroads on Retaining Walls and Temporary Shoring					
Hand Vane test-Water Content				Date : 11/13/13 -11/14/13	
		Sheet Pile Wall		Soldier Wall	
		Water Content %	Strength (psf)	Water Content %	Strength (psf)
Top of the wall	0				
Ground Surface	-2	28.21	1274.00	26.94	1169.50
	-4	25.35	657.80	26.88	751.80
	-6	29.43	1127.80	25.44	1128.00
	-8	28.86	1556.00	27.05	1587.00
End of excavation	-10	32.60	2631.00	36.00	2339.00

3.5.6 Unconfined Compression Test

3.5.6.1 Sampling

In order to have high-quality, undisturbed samples for the unconfined compression test, researchers decided to use the Shelby Tube to collect the soil samples. Ten 3 by 12 in. Shelby Tubes, were used to collect intact soil samples during the excavation suitable for laboratory tests of engineering properties. Ten soil samples were taken for this test. Figure 66 provides a diagram of the locations of the samples collected for this test, and Figure 67 displays a Shelby Tube used for data collection in this study and the soil after sampling sample was taken.

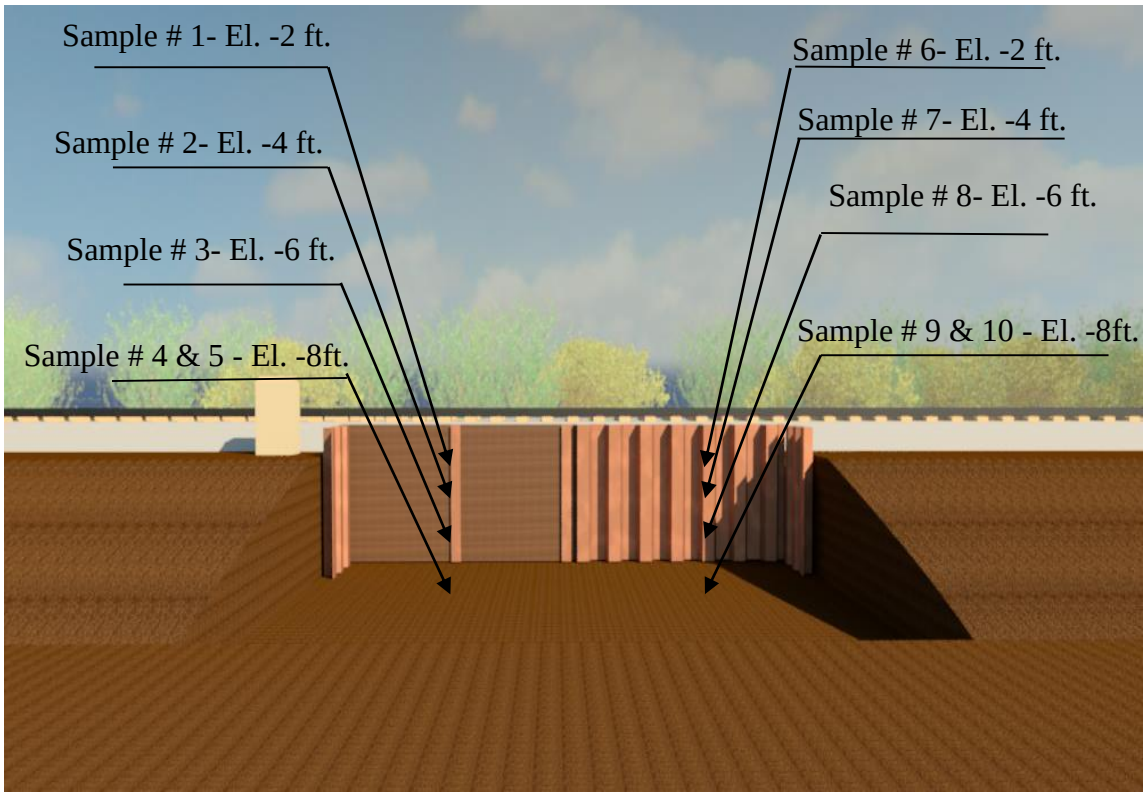

Figure 66. The locations of samples

(a) A Shelby Tube used to take undisturbed samples in this project

(b) The soil after taking an undisturbed sample

Figure 67. Collecting undisturbed soil samples

To obtain the samples, ASTM D1587-08 was followed. At different depths during the excavation, digging was stopped to collect the samples. The Shelby Tubes were pushed into the soil to collect samples of undisturbed soil in different locations. The samples were sealed using both plastic bag and an end cap to minimize moisture loss and changes in soil properties. In total, 10 samples were collected. The horizontal sample ejector EI23-1370 was used to extrude the samples in the lab. Figure 68 shows the sample ejector.

Figure 68. The horizontal sample ejector

3.5.6.2 Performing the test

To determine the unconfined compression strength (qu) and the undrained shear strength (su) of the soil, researchers followed ASTM D2166-06. The specimen were prepared in the lab in accordance with the generally accepted standards. The samples were trimmed to reach the correct dimensions, which consist of a diameter of 1.5 in and a height-to-diameter ratio between 2 and 2.5. Figure 69 shows the specimen being prepared for the test.

(a) The sample being trimmed to the correct dimensions

(b) The sample ready to go

Figure 69. Preparing the sample for testing

To measure force, pressure, and volume change characteristics, an Omega LC101-3k load cell, brand PX602-100 pressure transducers, and a brand PX409-2.5 differential pressure transducer, respectively, were employed. Data were acquired using a National Instruments (NI) hi-speed USB carrier data acquisition box (NI USB 9162) with 24-bit full bridge analog input and an additional with 10 volt external power supply. NI's LabVIEW program was used to record time and millivolt readings of the sensors. Figure 70 shows the devices used in these tests.

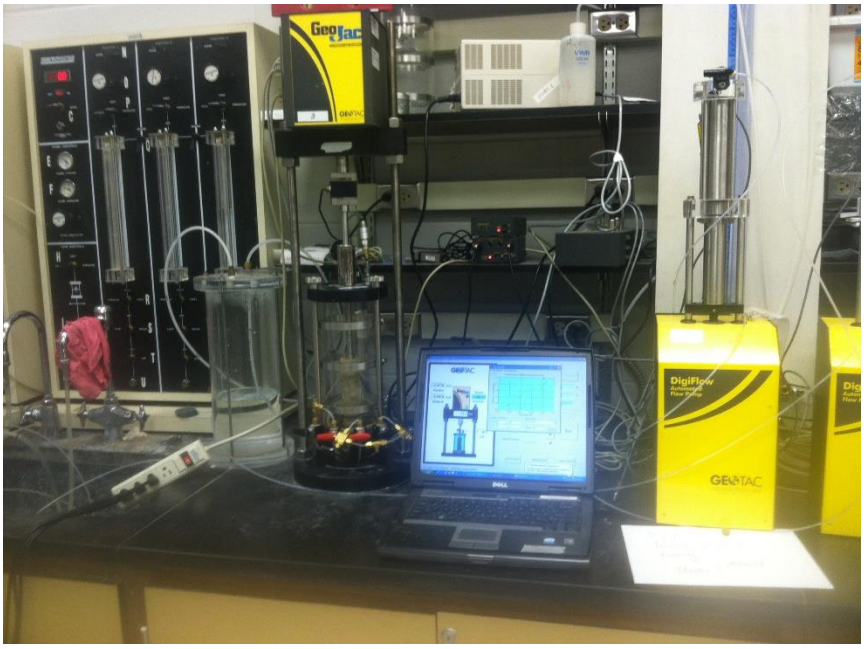

Figure 70. The load frame (right), Triaxial chamber (left), and LabVIEW software (laptop)

The unconfined compression test was run six times for different soil conditions, specifically depth, to identify the soil engineering properties. The tests were all strain-controlled tests, and the rate of loading was about 0.1% per minute. The test was run for 4, 6, and 8 ft. depths both for samples near the soldier pile wall and those near the sheet pile wall. Figure 71 shows a specimen being loaded and a deformed sample. In the calculation, the correction due to the effect of a membrane was considered, and the summary of results of the tests are presented in Table 36. The details of the tests are in Tables 37 to 42.

Table 36. Unconfined Compression test results

Live Load Effects of Railroads on Retaining Walls and Temporary Shoring				
Unconfined Compression Test-Water Content				Date : 12/01/13 -12/04/13
		Sheet Pile Wall		
		Initial Water Content %	Final Water Content %	Strength (psf)
Top of the wall	0			
Ground Surface	-2			
	-4	28.80	25.17	929.00
	-6	30.00	29.27	2370.00
	-8	27.20	31.30	2594.00
End of excavation	-10			

Live Load Effects of Railroads on Retaining Walls and Temporary Shoring				
Unconfined Compression Test-Water Content				Date : 12/01/13 -12/04/13
		Soldier Wall		
		Initial Water Content %	Final Water Content %	Strength (psf)
Top of the wall	0			
Ground Surface	-2			
	-4	34.00	29.00	1826.00
	-6	28.40	26.50	1636.00
	-8	30.80	29.50	2226.00
End of excavation	-10			

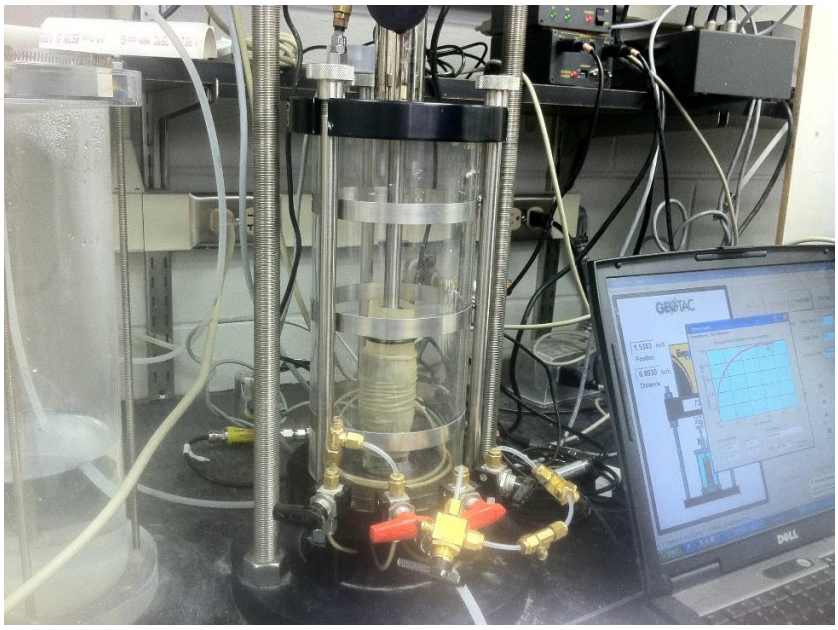

(a) Loaded sample

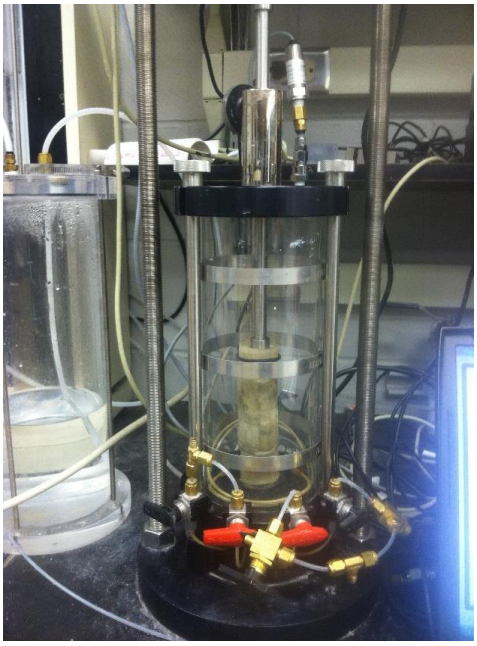

(b) Triaxial chamber

(c) Deformed sample afterconducting tests

Figure 71. Loading the sample

Table 37. Unconfined Compression test – 2 ft. depth – Sheet pile wall

Live Load Effects of Railroads on Retaining Walls and Temporary Shoring							
Wall Type : Sheet Pile Wall				Test Date: 12/01/13			
TRIAXIAL DATA SHEET - UNCONFINED COMPRESSION TEST							
Sample Information							
Soil Type:	CL			Height (inch):	3.282		
Depth (ft):	2			Diameter (inch):	1.5		
Soil Details							
LL :	31	PL:	18	PI:	13		
Water content							
Before Test				After Test			
	wet	dry			wet	dry	
Tin (gr)	1.46	1.46		Tin (gr)	1.52	1.52	
Tin + Soil (gr)	22.67	17.92		Tin + Soil (gr)	202	161.68	
Soil	21.21	16.46		Soil	200.48	160.16	
Initial Water Content :		28.85784		Final water content:		25.17483	
Total Unit Weight							
Weight (gr):	202.06			Volume (inch^3) :	5.799772738		
ϒ (pcf) = 132							
Results							
Undrained shear strength (su) (psf) :				929			

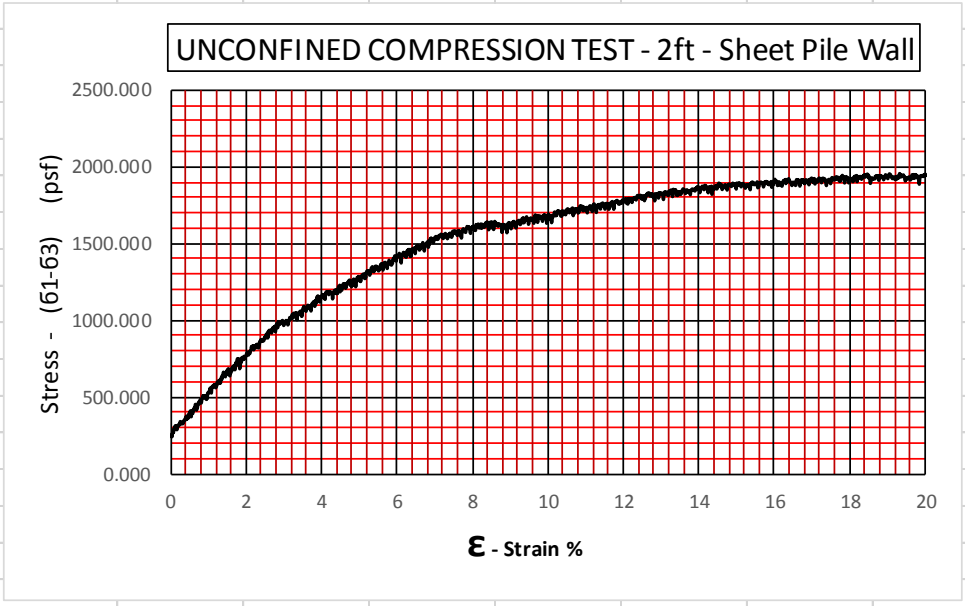

Table 38. Unconfined Compression test – 2 ft. depth – Soldier wall

Live Load Effects of Railroads on Retaining Walls and Temporary Shoring							
Wall Type : Soldier Wall				Test Date: 11/29/13			
TRIAXIAL DATA SHEET - UNCONFINED COMPRESSION TEST							
Sample Information							
Soil Type:	CL			Height (inch):	3.267		
Depth (ft):	2			Diameter (inch):	1.5		
Soil Details							
LL :	35	PL:	16	PI:	19		
Water content							
Before Test				After Test			
	wet	dry			wet	dry	
Tin (gr)	1.53	1.53		Tin (gr)	1.3	1.3	
Tin + Soil (gr)	21.33	16.26		Tin + Soil (gr)	179.91	139.03	
Soil	19.8	14.73		Soil	178.61	137.73	
Initial Water Content :		34.41955		Final water content:		29.68126	
Weight (gr):	180.4			Volume (inch^3) :	5.77326555		
ϒ (pcf) = 119							
Results							
Undrained shear strength (su) (psf) :				1826			

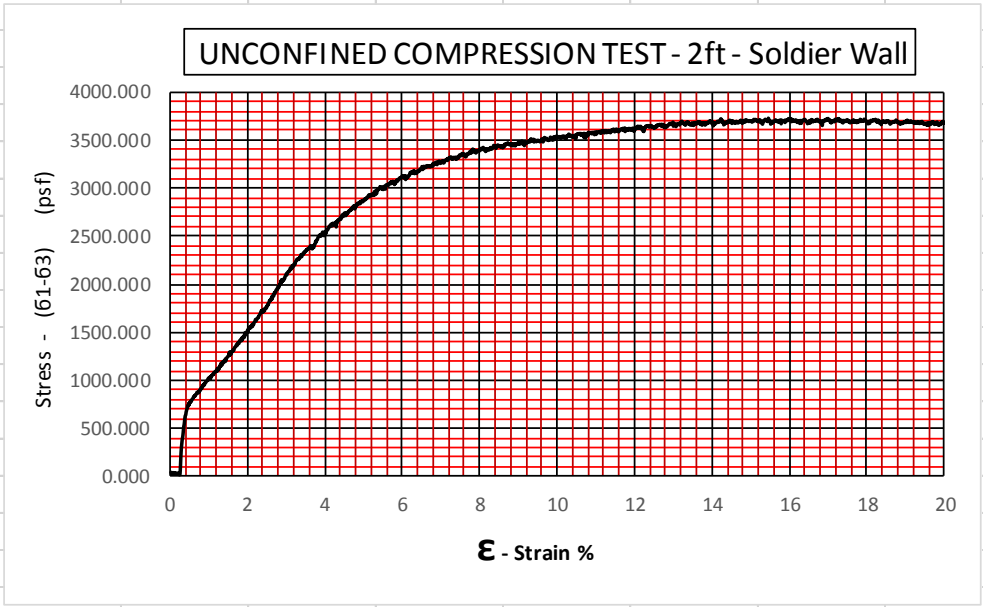

Table 39. Unconfined Compression test – 4 ft. depth – Sheet pile wall

Live Load Effects of Railroads on Retaining Walls and Temporary Shoring							
Wall Type : Sheet Pile Wall				Test Date: 12/03/13			
TRIAXIAL DATA SHEET - UNCONFINED COMPRESSION TEST							
Sample Information							
Soil Type:	CH			Height (inch):	3.212		
Depth (ft):	4			Diameter (inch):	1.5		
Soil Details							
LL :	59	PL:	19	PI:	40		
Water content							
Before Test				After Test			
	wet	dry			wet	dry	
Tin (gr)	1.54	1.54		Tin (gr)	1.52	1.52	
Tin + Soil (gr)	21.97	17.25		Tin + Soil (gr)	190.7	147.86	
Soil	20.43	15.71		Soil	189.18	146.34	
Initial Water Content :		30.04456		Final water content:		29.27429	
Total Unit Weight							
Weight (gr):	189.54			Volume (inch^3) :	5.676072527		
ϒ (pcf) = 127.15							
Results							
Undrained shear strength (su) (psf) :				2370			

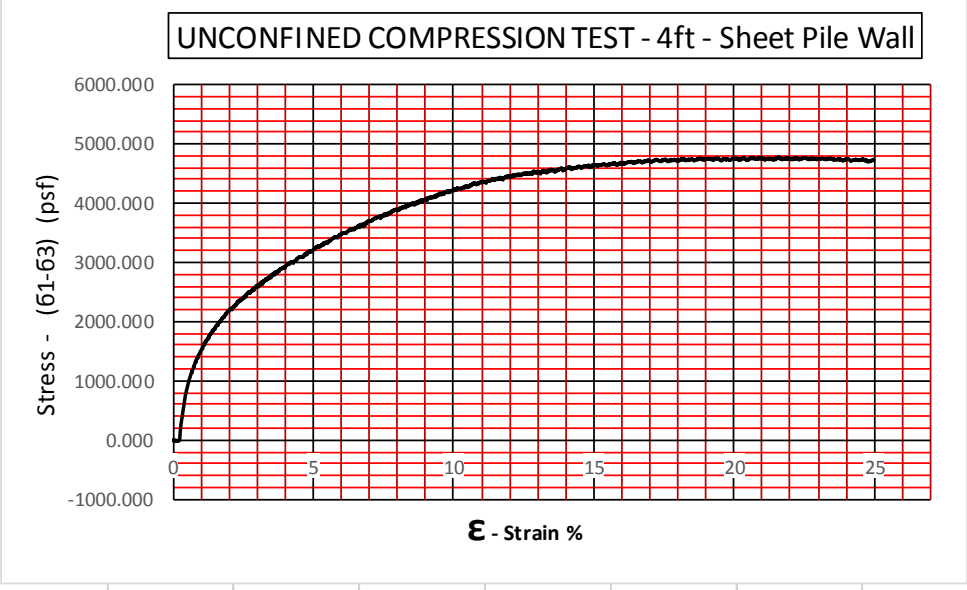

Table 40. Unconfined Compression test – 4 ft. depth – Soldier wall

Live Load Effects of Railroads on Retaining Walls and Temporary Shoring							
Wall Type : Soldier Wall				Test Date: 12/2/13			
TRIAXIAL DATA SHEET - UNCONFINED COMPRESSION TEST							
Sample Information							
Soil Type:	CH			Height (inch):	3.385		
Depth (ft):	4			Diameter (inch):	1.5		
Soil Details							
LL :	52	PL:	22	PI:	30		
Water content							
Before Test				After Test			
	wet	dry			wet	dry	
Tin (gr)	1.54	1.54		Tin (gr)	1.52	1.52	
Tin + Soil (gr)	38.29	30.14		Tin + Soil (gr)	195.54	154.78	
Soil	36.75	28.6		Soil	194.02	153.26	
Initial Water Content :		28.4965		Final water content:		26.59533	
Weight (gr):	194.36			Volume (inch^3) :	5.981788762		
ϒ (pcf) = 123.7							
Results							
Undrained shear strength (su) (psf) :	1636						

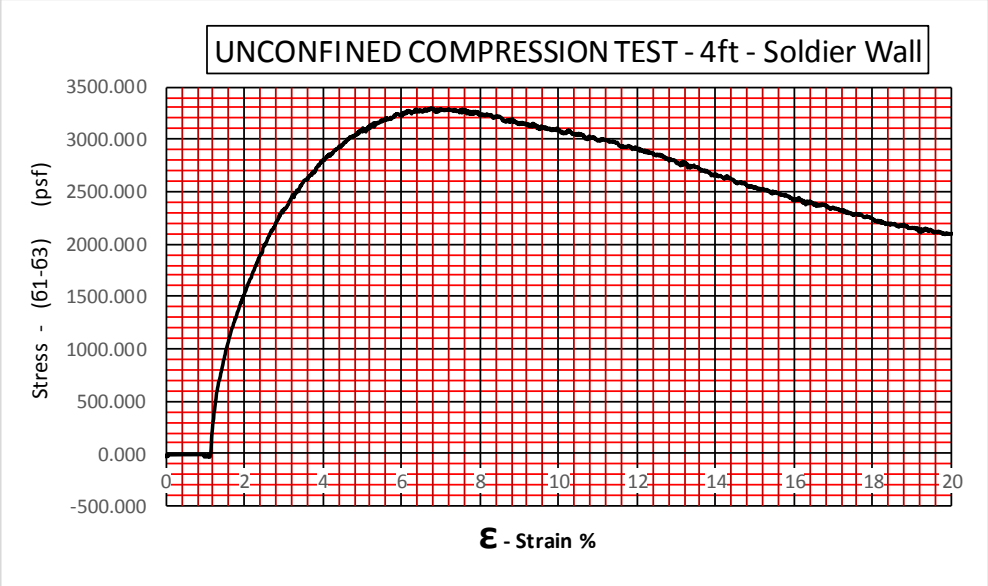

Table 41. Unconfined Compression test – 6 ft. depth – Sheet pile wall

Live Load Effects of Railroads on Retaining Walls and Temporary Shoring							
Wall Type : Sheet Pile Wall				Test Date: 12/01/13			
TRIAXIAL DATA SHEET - UNCONFINED COMPRESSION TEST							
Sample Information							
Soil Type:	CH			Height (inch):	3.055		
Depth (ft):	6			Diameter (inch):	1.5		
Soil Details							
LL :	63	PL:	22	PI:	41		
Water content							
Before Test				After Test			
	wet	dry			wet	dry	
Tin (gr)	1.31	1.31		Tin (gr)	1.53	1.53	
Tin + Soil (gr)	20.01	16.01		Tin + Soil (gr)	179.97	137.43	
Soil	18.7	14.7		Soil	178.44	135.9	
Initial Water Content :		27.21088		Final water content:		31.30243	
Total Unit Weight							
Weight (gr):	179.18			Volume (inch^3) :	5.398630626		
ϒ (pcf) = 126.4							
Results							
Undrained shear strength (su) (psf) :				2594			

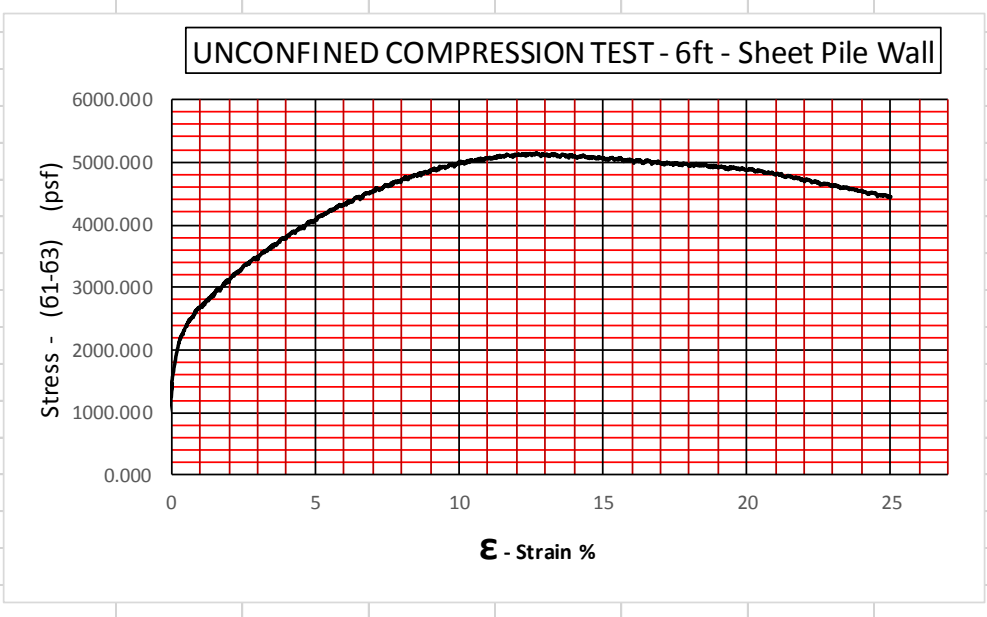

Table 42. Unconfined Compression test – 6 ft. depth – Soldier wall

Live Load Effects of Railroads on Retaining Walls and Temporary Shoring							
Wall Type : Soldier Wall				Test Date: 12/02/13			
TRIAXIAL DATA SHEET - UNCONFINED COMPRESSION TEST							
Sample Information							
Soil Type:	CH			Height (inch):	3.437		
Depth (ft):	6			Diameter (inch):	1.5		
Soil Details							
LL :	53	PL:	24	PI:	29		
Water content							
Before Test				After Test			
	wet	dry			wet	dry	
Tin (gr)	1.53	1.53		Tin (gr)	25.81	25.81	
Tin + Soil (gr)	19.27	15.09		Tin + Soil (gr)	232.32	185.17	
Soil	17.74	13.56		Soil	206.51	159.36	
Initial Water Content :		30.82596		Final water content:		29.5871	
Total Unit Weight							
Weight (gr):	207.53			Volume (inch^3) :	6.073680347		
ϒ (pcf) = 130							
Results							
Undrained shear strength (su) (psf) :				2262			

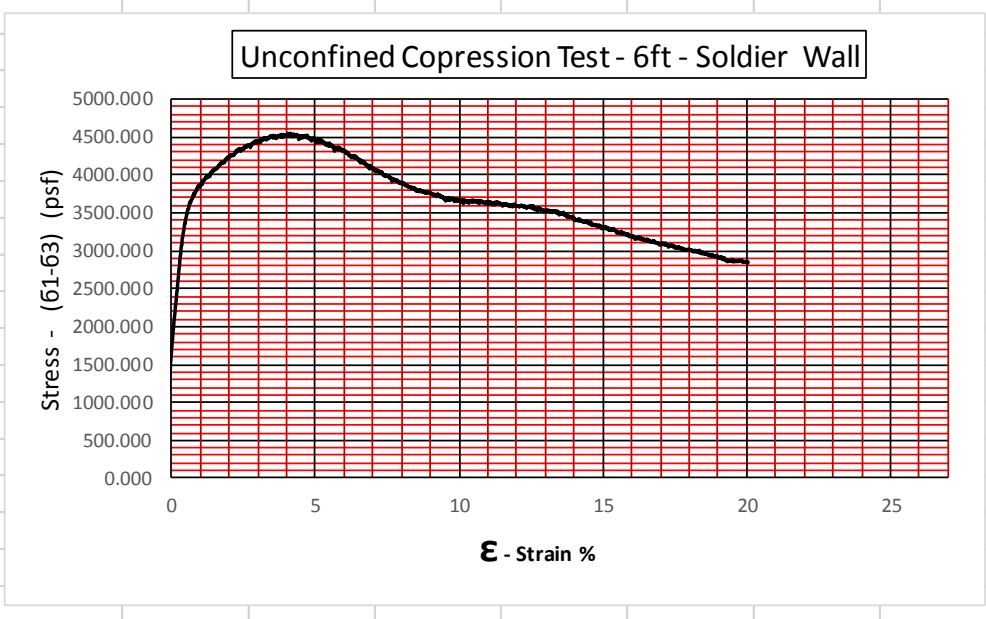

3.6 Overview of Soil Test Results

The results of both the Hand Vane tests and the unconfined compression tests resulted in reasonably consistent trends such as the undrained shear strength of the soil increases by depth. In the unconfined compression tests, the minimum and the maximum undrained shear strength of the soil samples were approximately 929 psf. and 2594 psf., respectively. Upper and lower bounds of these properties can be defined in the simulation procedure to allow prediction of the wall's behavior during loading. Figures 72 and 73 show the profile of water content, unit weight, and undrained shear strength of the soil in two different walls.

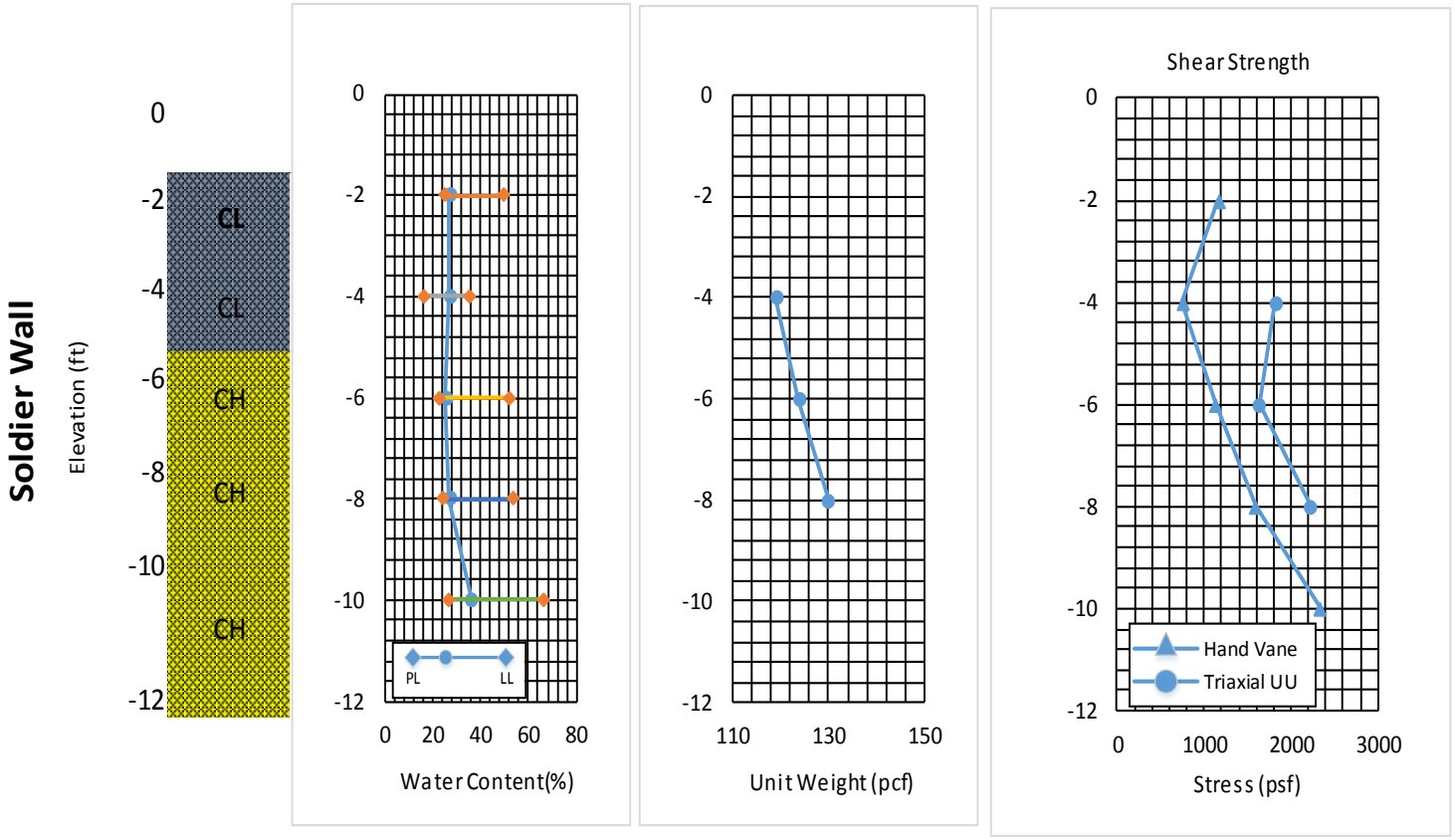

Figure 72. The profile of water content, unit weight, and the strength of soil for the soldier pile wall

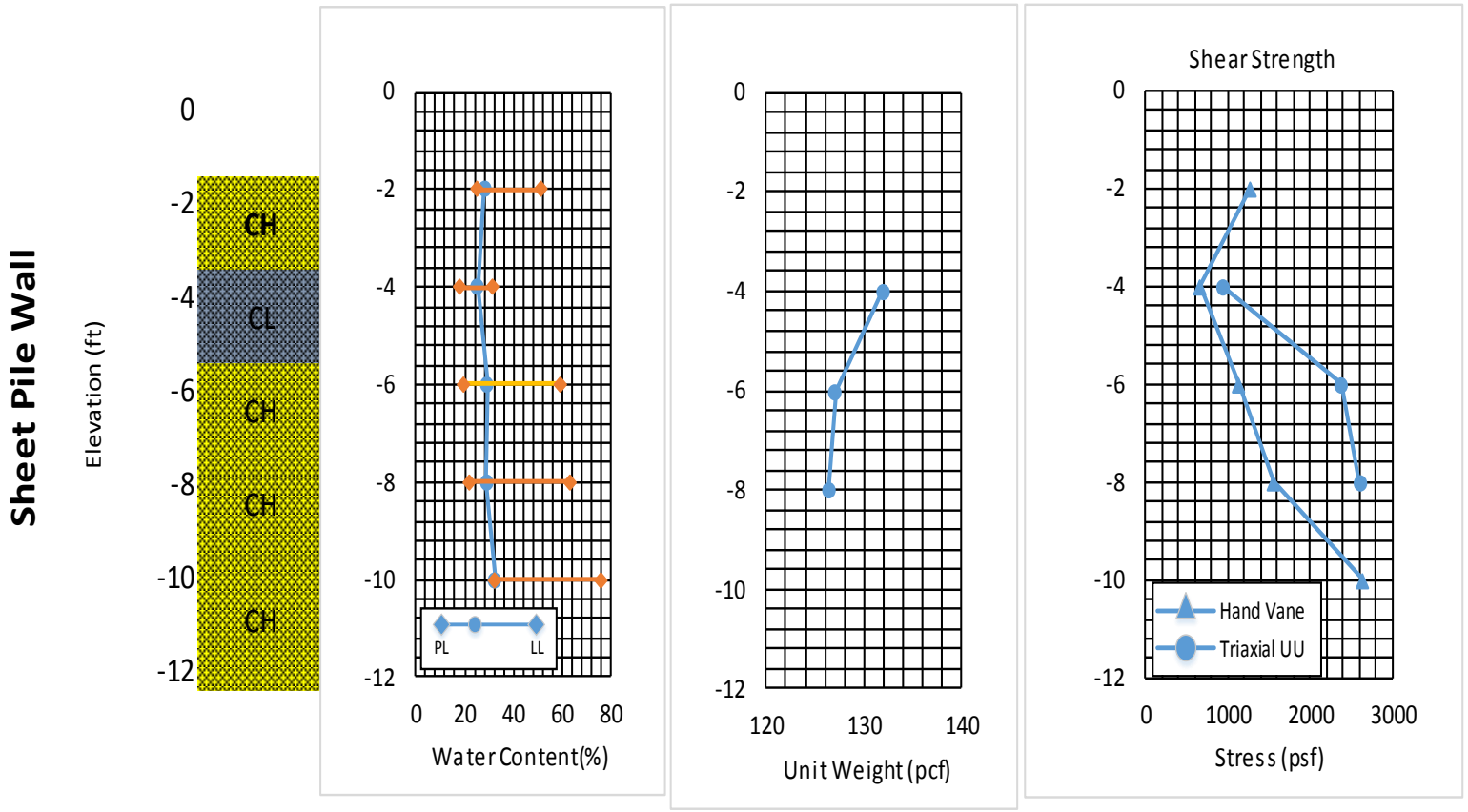

Figure 73. The profile of water content, unit weight, strength of soil – Sheet pile wall

4 THE NUMERICAL SIMULATION

4.1 Introduction

In this section, numerical simulations of live load effects on lateral deflections of temporary shoring systems and permanent retaining structures are constructed and tested. The test wall data collected in this project are, by nature, valid only for the specific values of wall height, wall stiffness, wall length, wall orientation, and soil stiffness conditions measured at this test site. The purpose of the numerical studies is to provide insights into the expected response of other wall systems at other sites in light of the data collected for this study at this test site. Soil-wall systems are complex nonlinear systems, so any extrapolations must be used with caution. Nevertheless, when combined with appropriate expert engineering judgment, the numerical studies are expected to provide meaningful information regarding the degree to which the wall performance data from the test site may or may not be applied to other walls and site conditions.

4.2 Outline

This section is comprised of six main subsections. First, the background section introduces the application of elasticity theory to retaining walls. Relatively simple closed-form expressions are obtainable from elasticity theory which are very useful for applied design as well as for validating more complex numerical solutions. However, there are some limitations to the simple, plane-strain solutions, which are discussed. Then comes a subsection about finite element models which addresses the development of a three-dimensional (3D) model for finite length retaining walls, including the selection of the mesh; a mesh sensitivity analysis; the material model; boundary conditions; and an

assessment of the accuracy of the model. Tension tends to naturally develop near the top of a retaining wall; the closed-form analytical solutions will actually show this effect. However, transmission of tension across the soil-wall interface is unlikely. Accordingly, a discussion is included on how the finite element model was modified to mitigate this effect. Following the discussion of the finite element model, the parametric study subsection investigates the effects of wall length, height and flexural stiffness; soil stiffness; and the distance between the live load and the wall on lateral wall deflections. Next, I compare and contrast the predictions of the elastic beam model and of the finite element simulations, creating a simplified theory based on the analysis of an elastic beam loaded by horizontal stresses computed using the Boussinesq theory. The sheet pile analysis subsection addresses the implications of modeling a 3D sheet pile wall using a plane-strain sheet pile wall of uniform thickness. In the final subsection, a 3D model of the test site presents predictions of live load deflections for the wall at the project test site.

4.3 Background

The conventional approach of modeling live loading near the earth retaining structure in Figure 74 assumes (1) the live load applied at the ground surface induces the horizontal stresses σ_x in the wall, and (2) wall responds to the horizontal stress according to classical beam bending theory. Horizontal stress is typically estimated using classical elasticity theory and assuming a perfectly rigid wall extending to infinite depth. For an infinitely long strip load of intensity q and width B, the horizontal stress is as follows in the set of equations labeled Equation 17:

$$\sigma_x = \frac{2q}{\pi}\{\alpha - \sin\alpha\cos(\alpha + 2\beta)\}$$
$$\tan\beta = \frac{x - B/2}{z} \qquad (17)$$
$$\tan(\alpha + \beta) = \frac{x + B/2}{z}$$

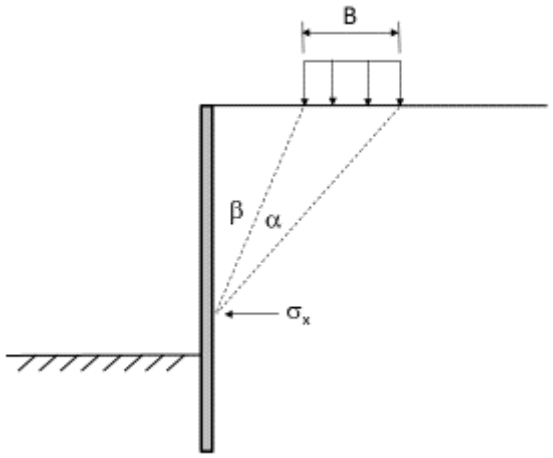

Figure 74. Stress on a wall due to live loads

Eq. 17 produces a vertical stress profile that varies with depth z. For computing deflections, this system is analyzed as a vertical beam. The horizontal stress is treated as a distributed load that is integrated twice in order to compute the bending moment diagram M(z). Noting that the moment, M, divided by the beam stiffness, EI, equals the curvature of the beam, y'' = M/EI, the curvature is integrated twice to compute the deflected shape of the 'beam'; i.e., the retaining wall. The integration requires two constants of integration, which are provided by assuming the beam is fixed at some point (Figure 75). This point

of fixity is established by judgment and experience and is generally taken as 0 to 0.75 times the embedment depth D.

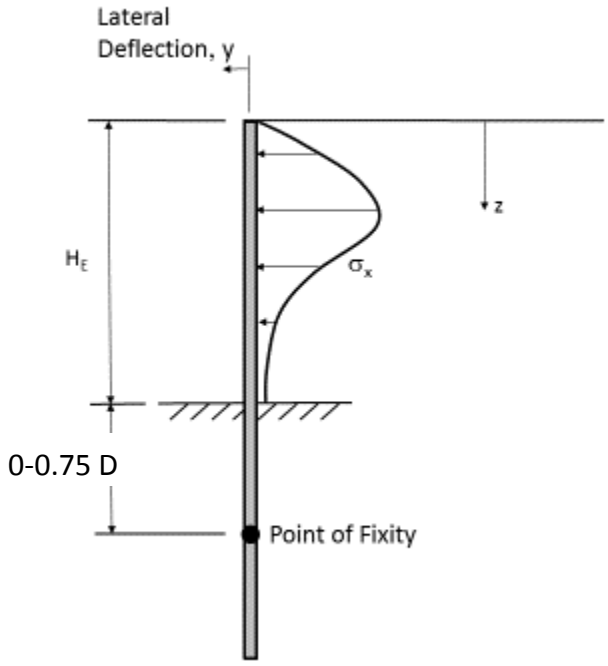

Figure 75. Beam model for wall behavior

The conventional method of analysis is grounded in solid principles of mechanics; thus, it certainly needs to be considered as a sound first approximation of wall behavior. Nevertheless, several limitations in such an analysis need to be recognized:

1. Actual wall systems have finite length L into the page, so 3D effects need to be quantified.

2. The base of the wall is not necessarily fixed, so the entire wall could translate and rotate. For stiff wall systems, wall deflections are likely to be dominated by rigid body translation and rotation governed by soil stiffness; i.e., the Young's modulus of the soil Es, which is entirely omitted from the conventional analysis. Assuming a point of fixity below the base of the excavation partly alleviates this issue, since it allows for wall displacement and rotation in the soil mass. However, guidance on selecting the assumed depth of the point of fixity is not well defined.
3. The wall is treated as a plane strain beam. Actual wall systems may deviate significantly from this idealization. For example, most sheet pile constructions used in retaining wall systems are z-sections.

4.4 Finite Element Model

To investigate the issues associated with the actual 3D geometry of the real wall systems discussed above, the walls were modeled using the finite element method.

4.4.1 Software

The software used, the development of the finite element mesh, the material model, and measures for dealing with the tendency for tension to develop near the top of the wall are covered here. The research team chose ABAQUS 3D (ver. 6.12, 2012) as the finite element solver to model the shoring systems. ABAQUS is a powerful finite element software that helps researchers model the real conditions of the site with accurate results. Due to the fact that this model requires extensive computational resources, the input files of the models were uploaded to the EOS cluster (IBM iDataplex Cluster, 2010), use of

which was provided by the Texas A&M supercomputing facility, to perform the simulations. Running the models on supercomputers allowed for have faster simulations and more parametric studies.

4.4.2 Model Dimensions, Boundaries, and Discretization

Figure 76 shows a typical 3D mesh developed for the finite element modelsThe parametric study of finite element models considered symmetric wall excavations in the x-direction. The far field lateral boundaries shown in Figure 76 were selected to minimize boundary effects. Dimensions of the models are approximately three times longest wall in each direction and about three times deepest wall in depth. Accordingly, the north-south axis of the model (X-direction) is 120 ft.; the east-west axis of the model (Y-direction) is 360 ft.; and the height of the model (Z-direction) is 120 ft. Figure 76 shows the geometry of the 3D model.

Taking advantage of symmetry to minimize the computational effort, the mesh of one-half of the excavation-wall system was modeled, with the plane of symmetry being the x = 0 plane. The wall length considered in the study varied from 20 ft. to 100 ft. Figures 77 to 80 show models with different wall lengths. Additionally, the walls were modeled for different depths of excavation, ranging from 8 ft. to 12 ft., thus including the most common depths of excavation in railroad projects.

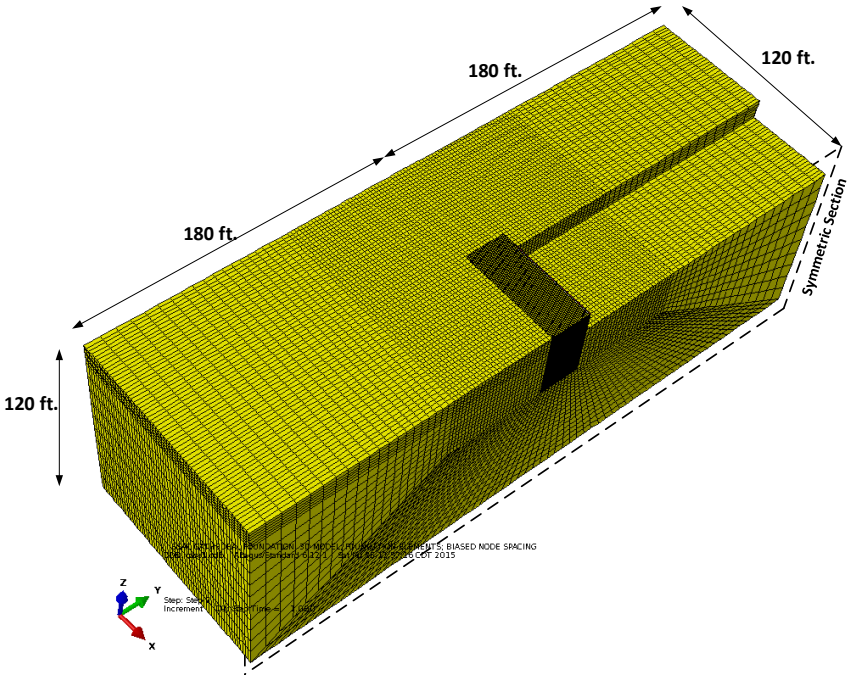

Figure 76. The geometry of the finite element model, a parametric study

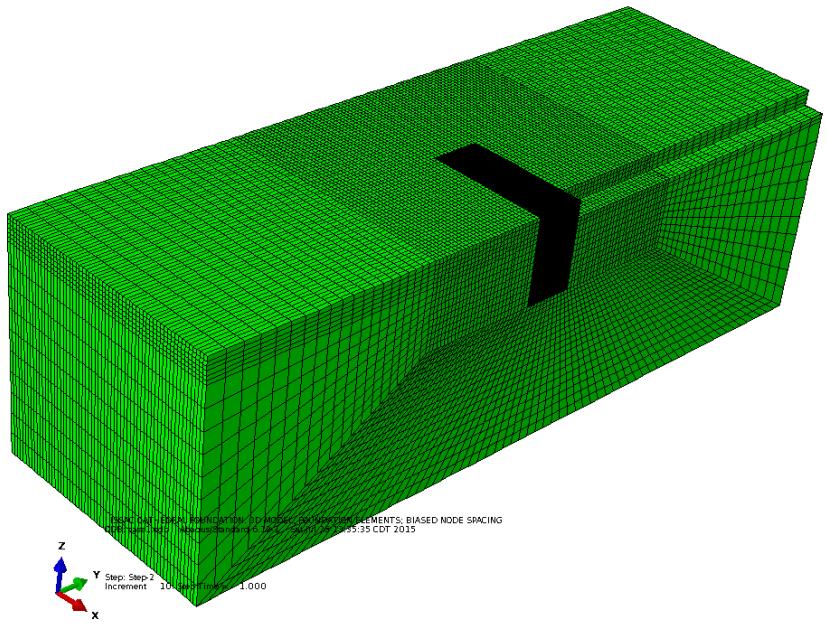

Figure 77. ABAQUS 3D model with length of wall = 20 ft.

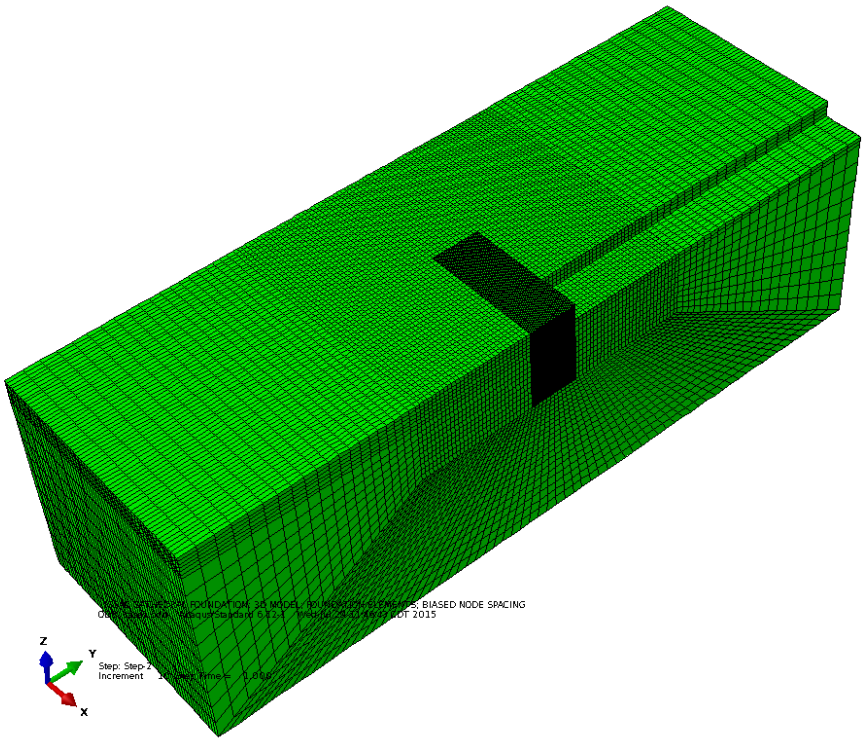

Figure 78. ABAQUS 3D model with length of wall = 40 ft.

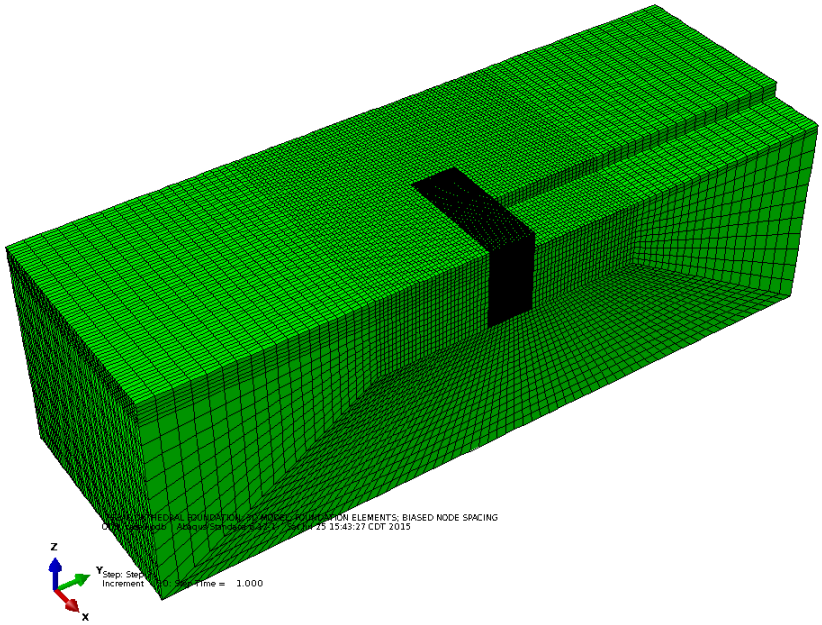

Figure 79. ABAQUS 3D model with length of wall = 60 ft.

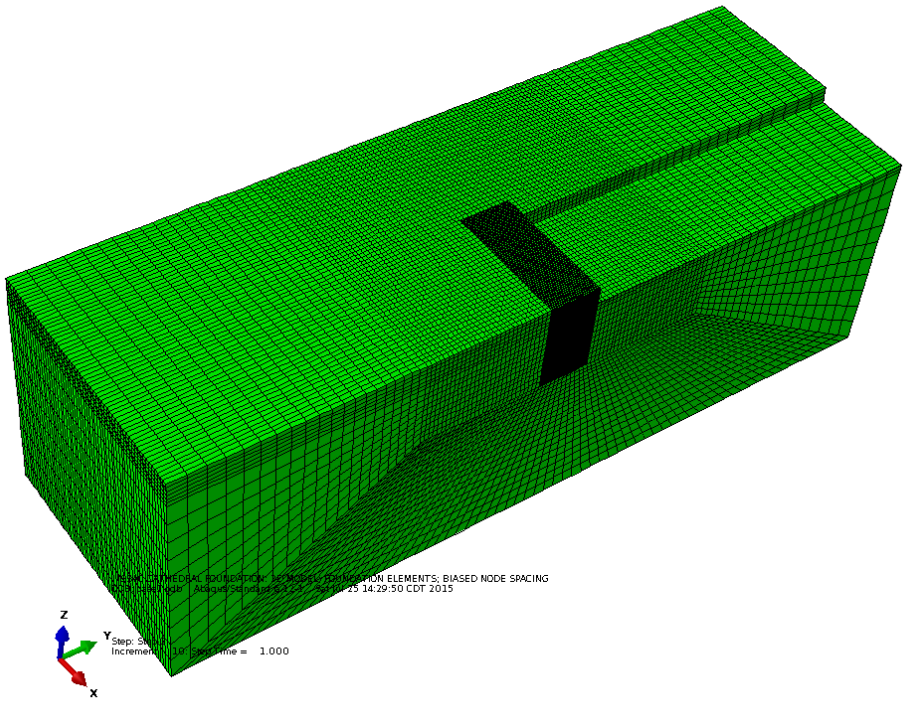

Figure 80. ABAQUS 3D model – length of wall = 100 ft.

To achieve acceptable accuracy with reasonable computation time, the entire domain of the numerical model was spatially discretized into six parts as shown in Figure 81. In addition, the finite element model was designed to have coarser elements further from the wall itself and finer elements around and under the wall. Each model consisted of a total of 667,680 eight-node brick elements (C3D8) and continuum shell elements (SC8R).

The boundaries of the finite element models were fixed in the horizontal direction on all four sides of the models and in both the horizontal and vertical directions at the bottom of the models. The wall sections and piles were modeled separately, but both were

tied to the surrounding soil to eliminate the contact difficulties in our finite element simulations.

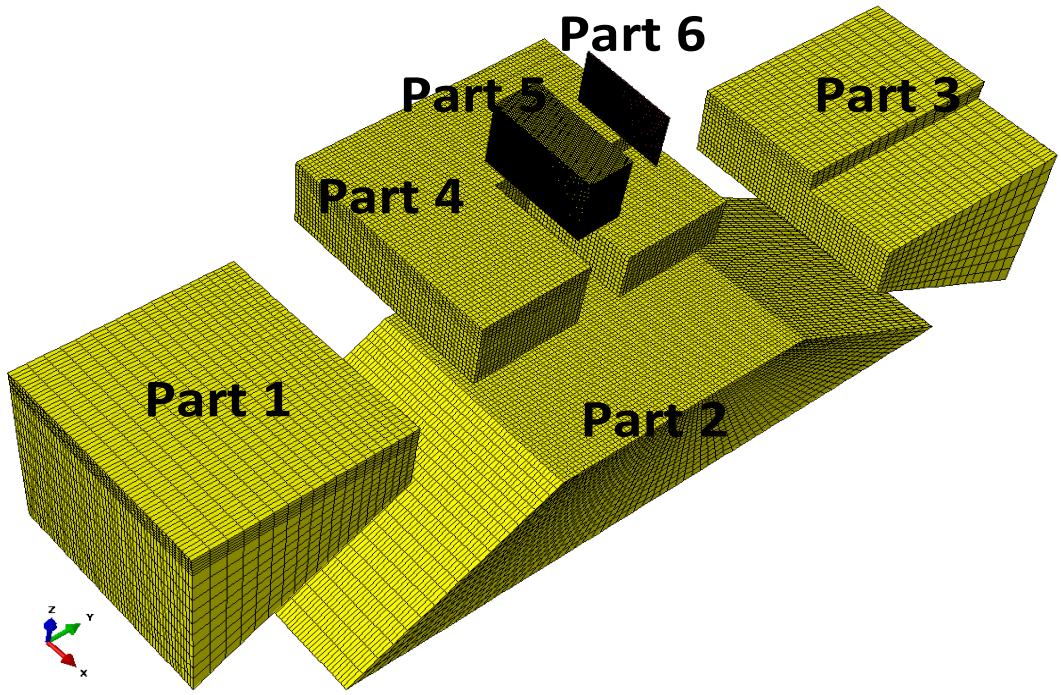

Figure 81. The six parts of the finite element model

4.4.3 Mesh Generation

ABAQUS standard (ver. 6.12, 2012) was used to generate the finite element mesh. The research team attempted to create a finer mesh under and around the wall and coarser mesh further from the wall in order to have more accurate results and save the time of each simulation. As mentioned above, six different parts of the model were defined, and each part was defined with different mesh properties. This approach was judged to provide greater accuracy and confidence in the results as well as higher precision in the parametric

studies. Figure 82 shows a typical 3D mesh developed for finite element models, and the different parts of the model with the corresponding mesh for each.

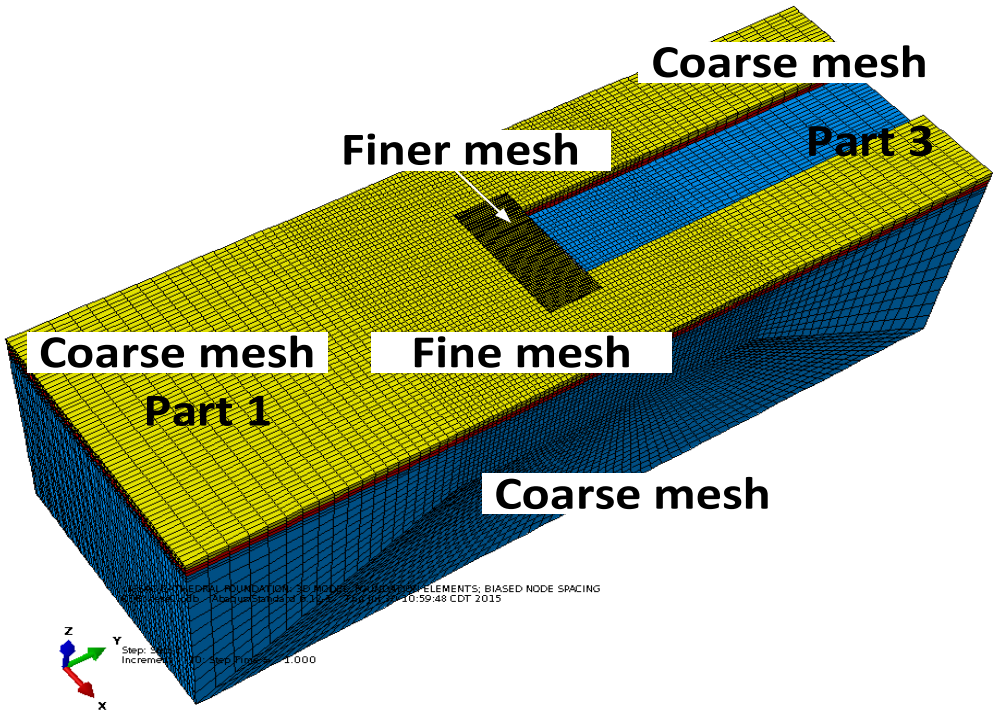

Figure 82. Mesh sizes according to parts

4.4.4 3D Mesh Refinement Analysis

Developing sufficiently fine mesh– mesh with sufficiently small element sizes to assure a converged solution is essential to producing results that can be used with confidence. A displacement-based finite element analysis using full integration tends to over-predict system stiffness and under-predict deformations. As the mesh is refined, deformations will converge to values that approach the exact solution.

The aim of this part is to investigate the influence of mesh sizes on the maximum lateral deflection of the wall and to find a proper size of mesh that provides accurate results with a reasonable simulation time and computational resource requirements. To find the effect of mesh size, a mesh refinement analysis was conducted. Different models with different mesh sizes were developed, and lateral deflections at the top of wall were monitored. Then, the results of the various models were compared to each other and the effects of change in mesh size were studied. Based on these results, a mesh size of 0.5 ft. was chosen for future studies and simulations. A summary of these results can be seen in Figure 83; Figure 84 shows the different models developed for the refinement analysis.

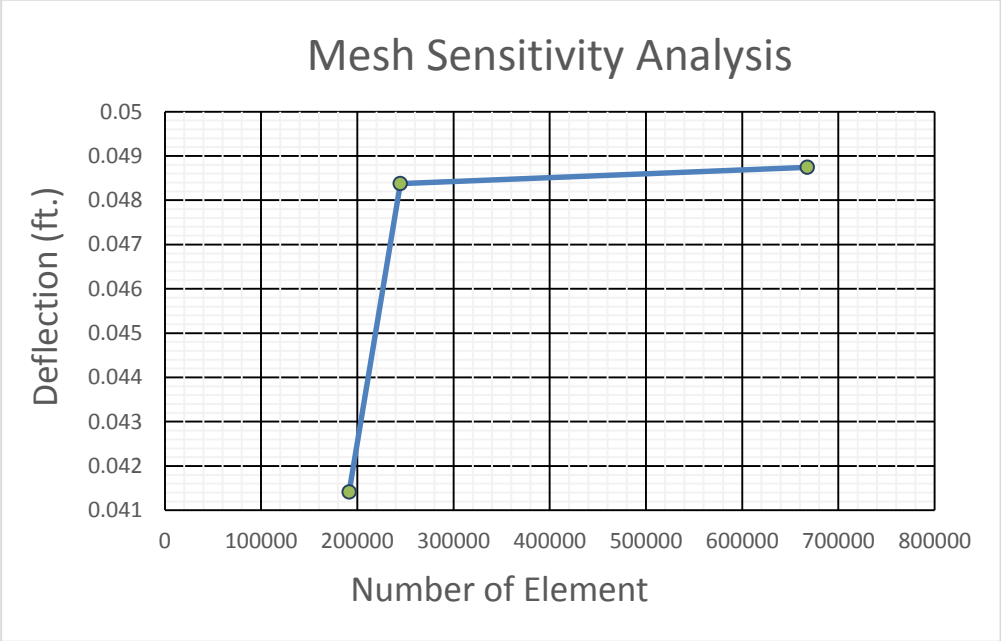

Figure 83. Results of the mesh refinement analysis

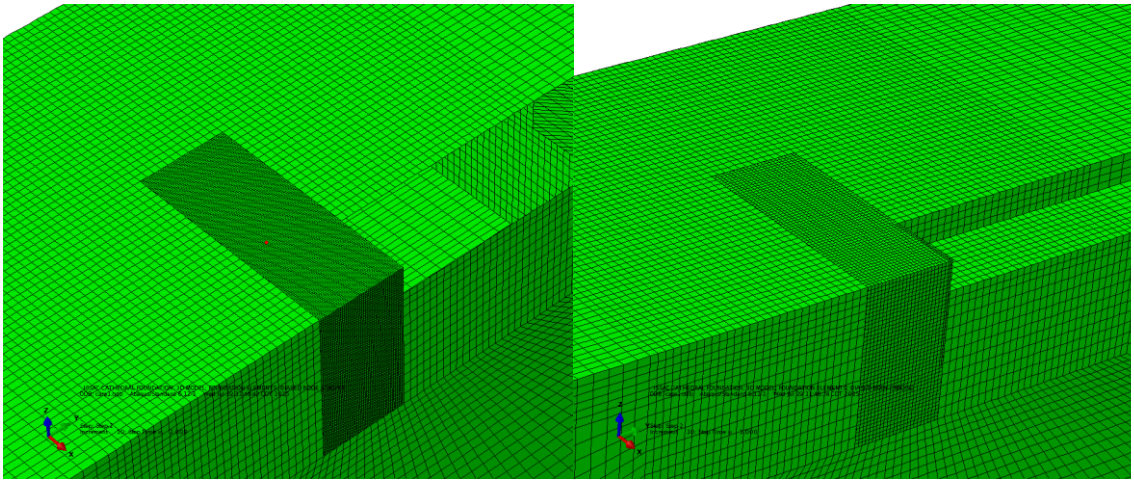

Model 1. Size of mesh element = 0.5 ft. ***Model 2.*** Size of mesh element = 1.0 ft.

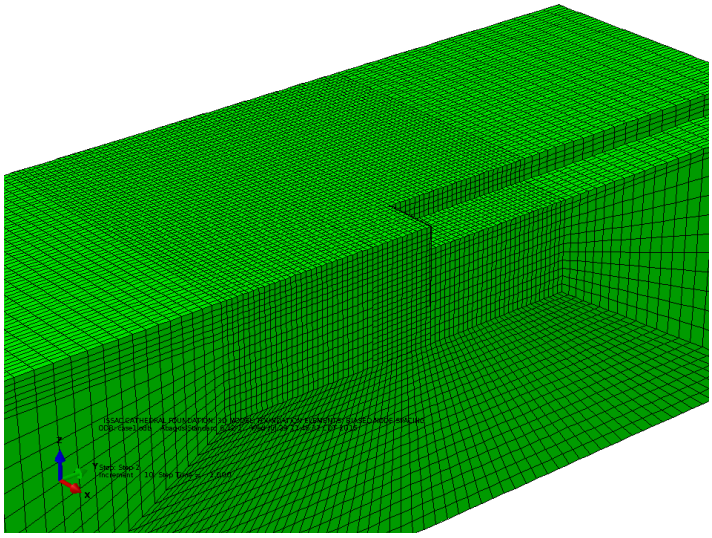

Model 3. Size of mesh element = 2.0 ft.

Figure 84. Models used in the mesh refinement analysis

In order to find the accuracy of the finite element models results, vertical stresses derived from finite element analyses were compared with vertical stresses calculated using the Boussinesq theory. A summary of these results are presented in Figure 85. This comparison of the different calculations of the vertical stresses shows good agreement between the results obtained by the two different methods and confirms the accuracy of the finite element results. The difference in the vertical stress as calculated by the two methods is less than 1% (Figure 85)

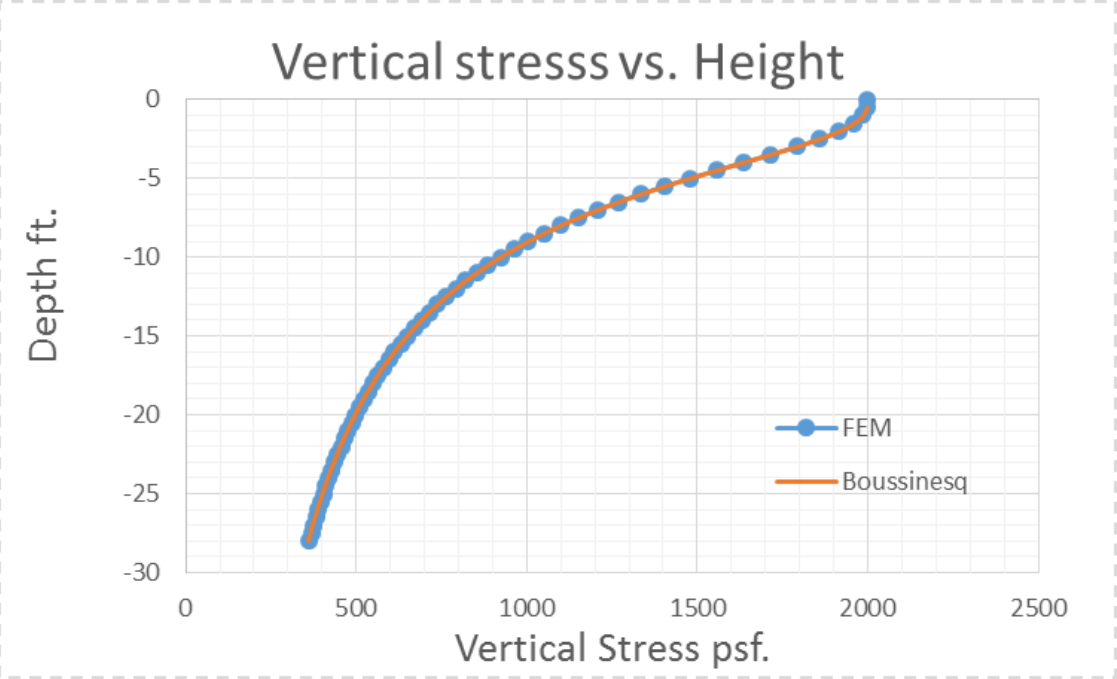

Figure 85. Comparison of vertical stresses according to the Boussinesq theory to those from the finite element model

4.5 Material Models

For material modeling, the linear elastic model as defined by ABAQUS (ver. 6.12, 2012) was adopted to both model soil and walls. In the parametric studies, a single value for Young's modulus Es and Poisson's ratio was assigned to all soil. Young's modulus was varied as will be described in the discussion of the parametric study. Poisson's ratio for the soil $\mu = 0.45$ was used in all simulations. Wall stiffness was controlled by specifying the wall modulus E and moment of inertial I to achieve a specific target value of EI. The bending stiffness EI was varied as will be described in the discussion of the parametric study.

4.6 Boundary Conditions and Interfaces

For the horizontal far-field boundaries, zero horizontal displacements were set as $ux = 0$ at large positive and large negative distances from the wall in the x-direction and as $uy = 0$ at large distances from the wall in the y-direction. On the plane of symmetry $x = 0$, the displacement boundary condition $uy = 0$ was enforced. The analyses assumed full bonding between the soil and the wall. This sometimes resulted in tension at the soil-wall interface, which is discussed below.

4.7 Treatment of Tension

A number of material model simulations showed a tendency for tension to develop at the soil-wall interface at the top of the wall. Since transmission of tension across this interface is physically unlikely, this issue required considerable attention. The magnitude of the tension was large enough to noticeably decrease deflections at the top of the wall. In many cases, instead of the wall deflection pattern assuming the classical shape of a

loaded cantilever beam, the wall was pulled back in the opposite direction due to the tension. Since a primary focus of this study is lateral wall deflections due to live loads, simply accepting a zone of tension at the top of the wall was considered unacceptable. ABAQUS actually has a no-tension option available for elastic materials; however, the ABAQUS model warns that invoking this option can generate numerically unstable systems.

In this study, an attempt was made to use the no-tension option, but numerical instability did, in fact, occur. Separation at tension zones across the soil-wall interface can be conceptually modeled using the ABAQUS (ver. 6.12, 2012) capabilities for contact surfaces. This investigation also attempted to implement the contact surface capabilities of ABAQUS. Although the simulations were numerically successful in the sense that convergence was achieved, examination of the results indicated that they were highly suspect. For example, according to the model results, soil in the region of the soil-wall gap was often in compression, which is the exact opposite of what should occur in a zone of gapping.

The option that was finally selected for mitigating the tendency for tension to develop at the soil-wall interface was to define an elastic transition zone between the wall and soil near the ground surface. A reduced Young's modulus was assigned to this transition zone. After some experimentation, researchers found that assigning Young's modulus Etrans to the soil in the transition zone equal to 1/80 of that of the surrounding soil, Etrans = Es/80, successfully inhibited the transmission of tension from the soil to the wall. The depth of this transition zone was chosen to be about 20% of the depth of

excavation. The approach of reducing the soil stiffness in the zone where tension tended to form has a significant advantage in that it preserves the linearity of the system so that convergence issues are avoided. Additionally, in the context of a parametric study, linear systems are highly desirable because parameters such as wall length and height can be varied without concern of nonlinear effects.

4.8 Parametric Study

4.8.1 Design of the Parametric Study

To understand the effects of wall-excavation geometry, soil stiffness, and wall stiffness on lateral wall movements, a parametric study was undertaken that systematically varies the relevant parameters. Figure 86 illustrates the parameters that considered.

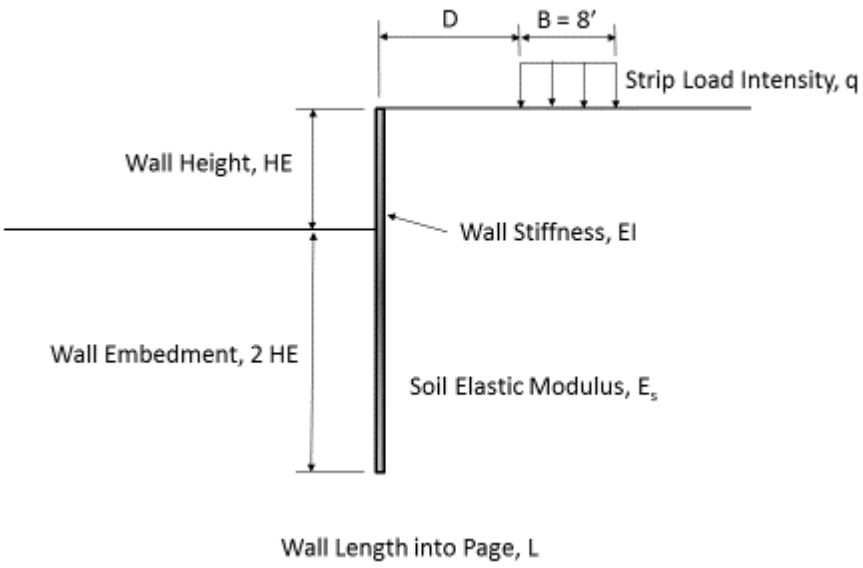

Figure 86. Parameters affecting wall behavior and included in the parametric study

As noted in the development of the finite element model, the focus here is on live load effects; that is, the incremental lateral deflections on the wall that occur when a train passes near a wall. A typical train is very long relative to the length of a typical wall; therefore, the live load may reasonably be considered as an infinite strip load of width B and intensity q. The following parameters were considered in this parametric study:

1. Excavation height, HE. Based on discussions with the Texas Department of Transportation, wall heights in the range of HE = 8–12 ft. below ground were of primary interest.

2. Stress intensity, q. Based on the Cooper E80 load criterion, a strip load intensity of q = 2000 psf. was used in the analyses. This is based on an infinite load of 8 kips/ft. distributed across an 8-ft. width.

3. Strip load width, B. Based on a track width of 4.7 ft. and accounting for spreading of the applied load through the ballast, a single strip load B = 8 ft. was used throughout the parametric study.

4. Wall embedment, Common practice for walls adjacent to railroads requires a wall embedment equal to twice the excavation height. Therefore, an embedment depth of 2HE was used for all cases considered.

5. Distance from edge of strip load to wall, D. This value was varied from 6 to 10 ft. in the parametric study.

6. Wall length, L. the length of the wall excavation in the third dimension was varied from 20 to 100 ft. in addition to the infinitely long wall (plane strain) case.

7. Soil stiffness, E_S. Soil Young's modulus was varied over a range considered representative of soft to stiff clays, E_S = 62.5 to 4200 ksf.

8. Flexural stiffness of wall, EI. Wall stiffness was characterized in terms of bending stiffness EI, where E = Young's modulus of the wall material and I = the moment of inertia of the wall section. Based on the literature review of wall systems ranging from relatively flexible soldier pile/lagging systems, sheet piles, and drilled shaft walls, flexural stiffnesses in the range of EI = 17,134,452 to 376,957,947 lb.ft.^{2}/ft were considered in the analyses. (E: psf., and I: ft^4/ft.)

Even a simplified excavation-wall model is influenced by a relatively large number of variables that can interact in complex ways, sometimes in ways that are not intuitively obvious. To aid in understanding the possible interactions among the variables, presenting the results of parametric studies in terms of dimensionless ratios is often useful so that the relative influence of the effect of varying a given parameter can be more clearly assessed. Toward this end, the following dimensionless parameters were used in this parametric study:

1. q_s/E_s = ratio of the applied load intensity to Young's soil modulus was varied over a range of 0.00043 to 0.028.

2. HE/L = ratio of excavation height to length of wall was varied over a range of 0.0 to 0.6, with H_E/L = 0 being the plane-strain case.

3. B/HE = ratio of load width to excavation height was varied over a range of 0.66 to 1.

4. D/HE = ratio of distance from edge of strip load to excavation height was varied over a range of 0.5 to 1.25.

5. EI/qHE^4 = ratio of flexural stiffness of wall to soil stiffness was varied over a range of 0.4 to 46.

Wall lateral deflections vary along the depth of the wall. The parametric studies report lateral deflections at the top, mid-depth and base of the excavation.

4.9 Results and Discussion of Parametric Study

4.9.1 Effects of Soil Stiffness on Lateral Deflection, q_s/E_s

The applied load intensity relative to the Young's modulus of the soil governs a fundamental aspect of wall response. Figures 87 and 88 for B/HE = 0.66 and B/HE=1, respectively, show the derived trends. The Boussinesq solution for a strip load actually shows all strain components to be proportional to this ratio. Accordingly, simple linear relationships exist between wall deflection and normalized load intensity q_s. Further, lateral deflections scale directly to the value of Young's modulus. These analyses were performed for a wall stiffness EI = $17.1(10)^6$ lb/ft.^{2}, which is the lowest stiffness considered in the parametric study.

The intent here is to investigate wall response when soil stiffness dominates deformations. The influence of increased wall stiffness is discussed subsequently. Closer proximity of the load to the wall (D/H = 0.5 versus 0.83) increases deflection by up to 25%. The wall length L also significantly influences the deflection response, indicating that 3D effects are significant. For example, for B/HE = 1, the normalized deflection $\Delta u_s/HE$ at the top of the wall is nearly double for a long wall L/H_E = 12.5 when compared

to a short wall *L/HE* = 2.5. The width of the strip load relative to the wall height, *B/HE*, is also seen to be significant in all cases.

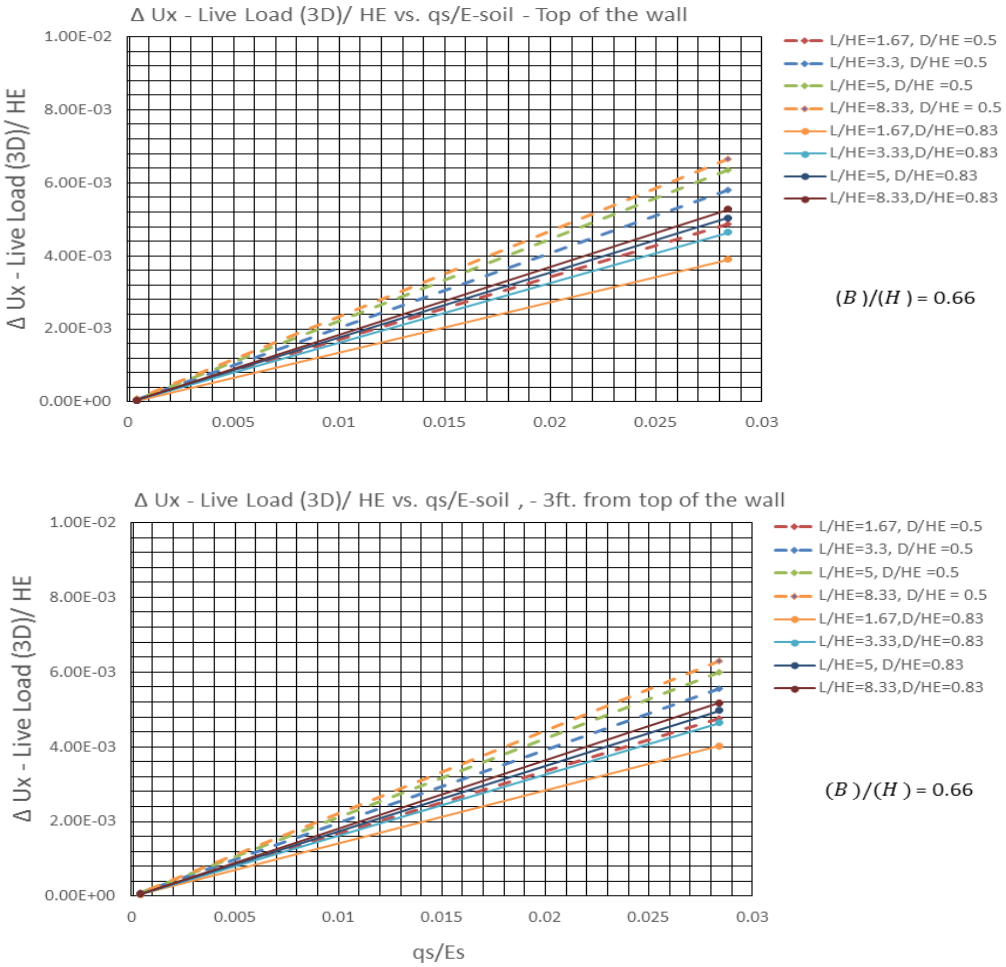

Figure 87. Deflection at different locations vs. wall stiffness, B/HE = 0.66

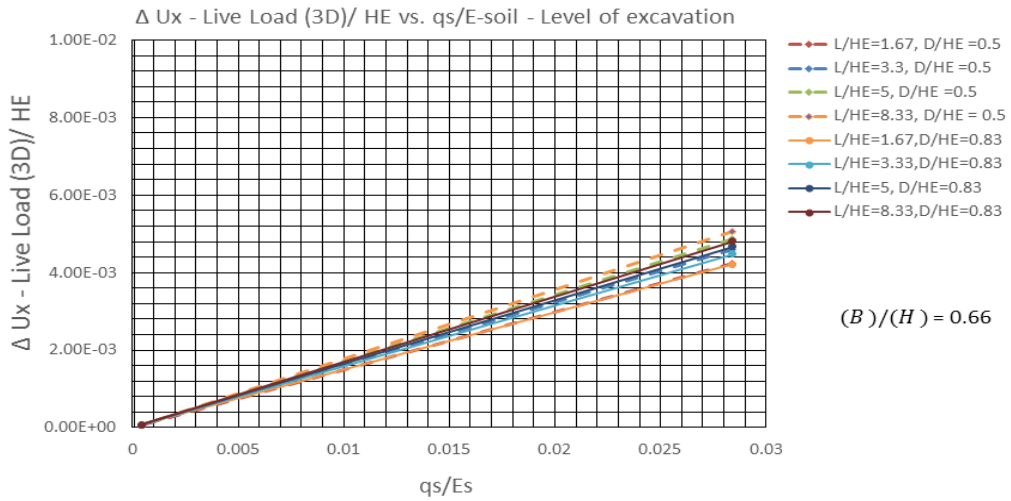

Figure 87. Continued

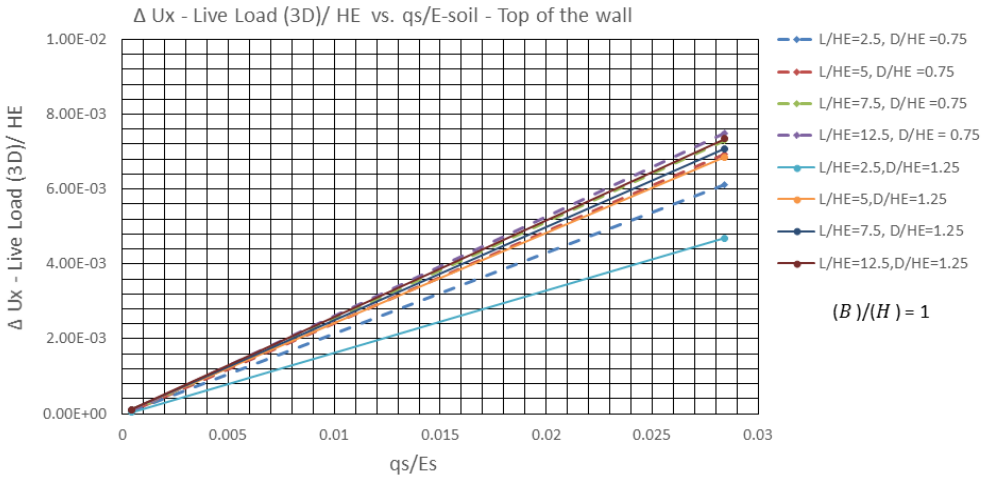

Figure 88. Deflection at different locations vs. soil stiffness, B/HE = 1

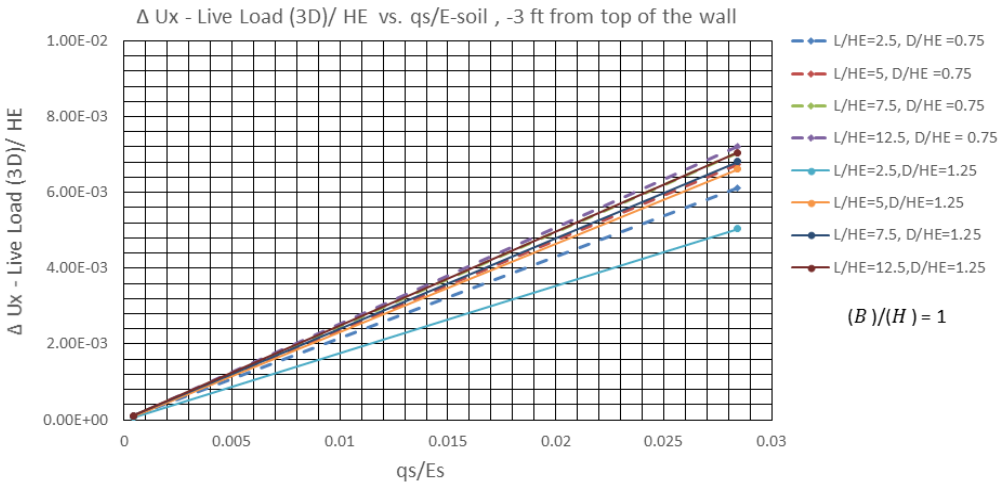

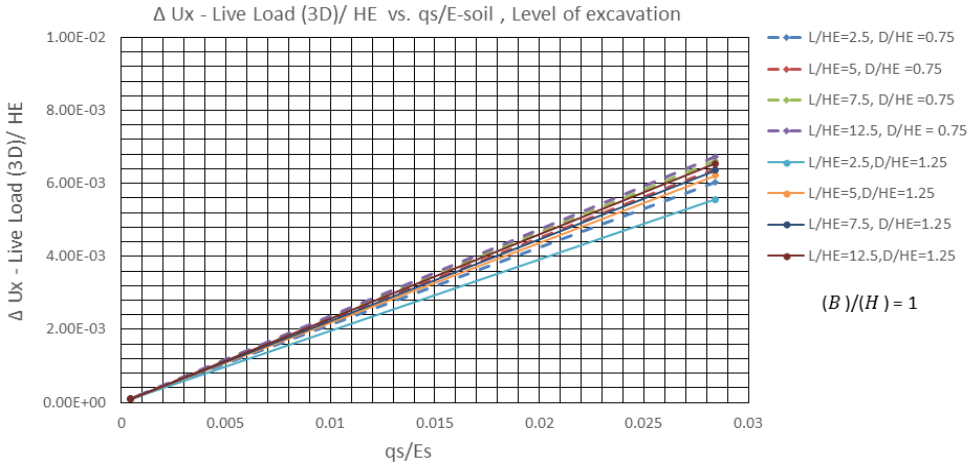

Figure 88. Continued

4.9.2 Effect of Wall Stiffness on Lateral Deflection EI /qHE^4

The previous subsection considered the effects of soil stiffness E_s. Consideration now is given to the effects of wall stiffness, as characterized by its flexural stiffness EI. The study was performed for two soil Young's modulus, E_s = 62.5 ksf and E_s = 4200 ksf. Figures 89 to 94 show the finite element predicted lateral deflections for B/HE = 0.66 and

1.0, respectively. The plots indicate a high sensitivity to soil stiffness, with the results being rather insensitive to the wall flexural stiffness. This result is largely a consequence of the tendency of the wall to undergo greater rigid body translations in softer soil as opposed to stiff soil. While expecting larger displacements to occur in a wall in soft soil is entirely reasonable, considering wall response in terms of the absolute magnitude of lateral displacements can mislead engineers with regard to the effectiveness of the wall system. For this reason, considering the increase in lateral displacement of the wall due to excavation and wall installation, Δu_x - $\Delta u_{x\text{-no\_wall}}$, is useful. Figures 95 to 106 show the finite element predicted relative lateral deflections for B/H_E = 0.66 and 1.0, respectively.

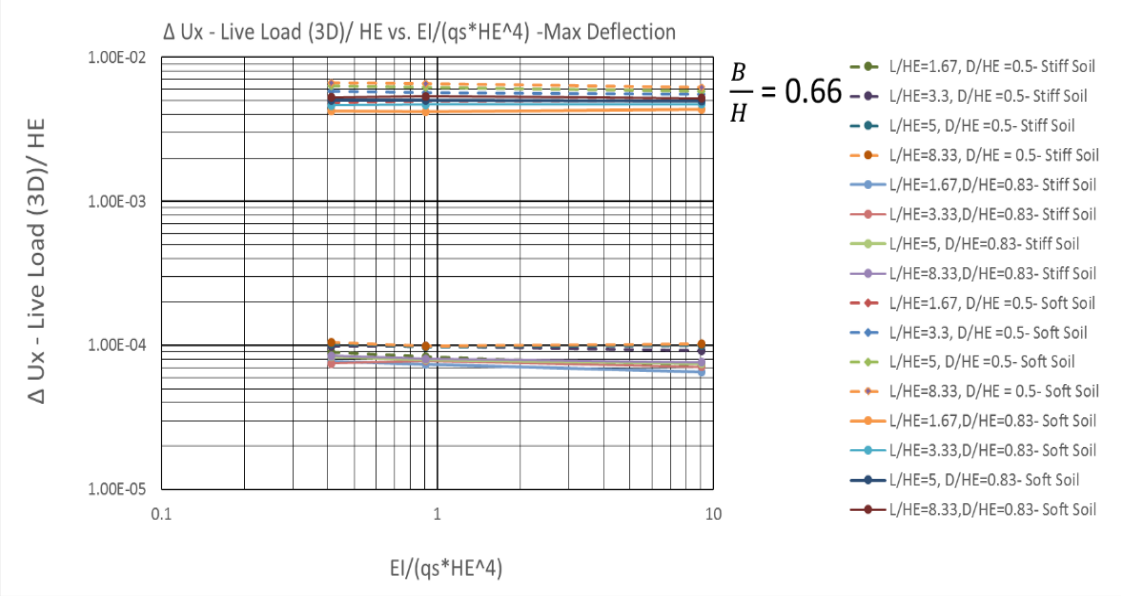

Figure 89. Total maximum deflection vs. wall stiffness, B/H_E = 0.66, 3D analysis

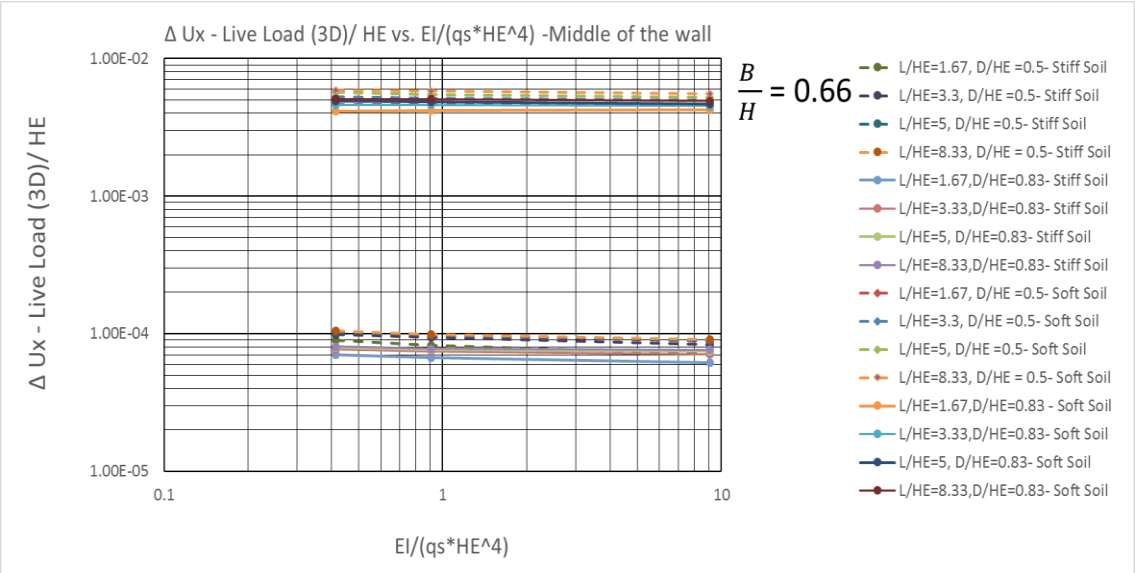

Figure 90. Total deflection at middle of the wall vs. wall stiffness, B/H_E = 0.66, 3D analysis

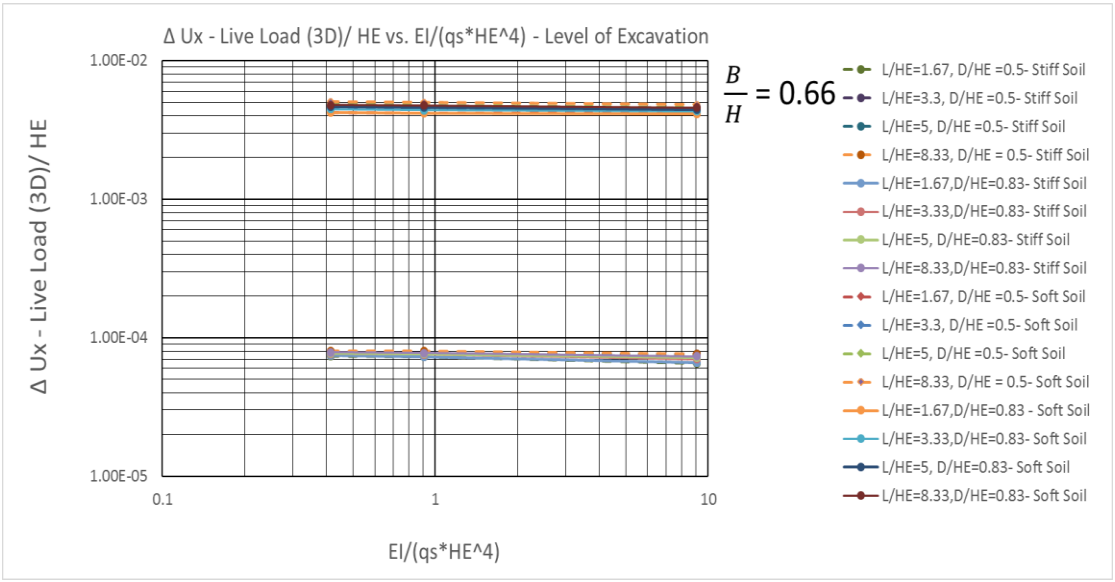

Figure 91. Total deflection at level of excavation vs. wall stiffness, B/H_E = 0.66, 3D analysis

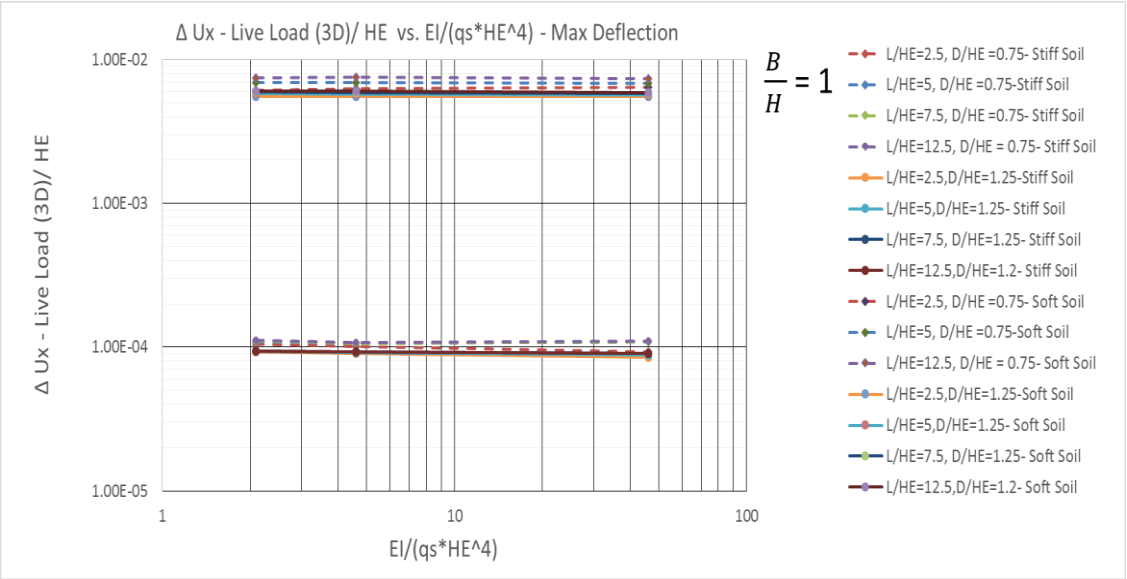

Figure 92. Total maximum deflection vs. wall stiffness, $B/H_E = 1.00$, 3D analysis

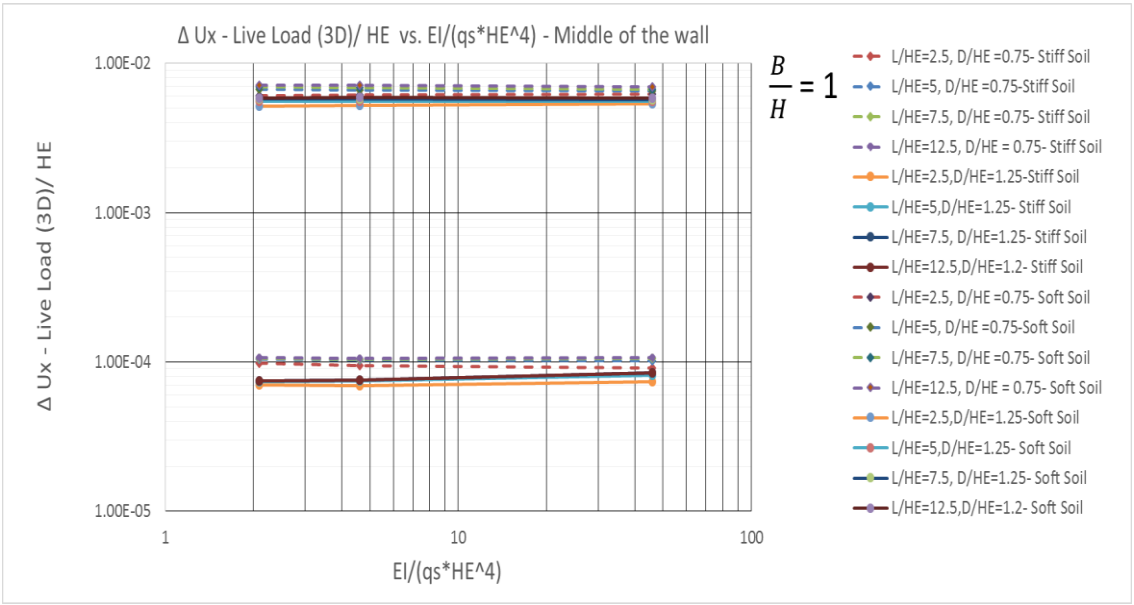

Figure 93. Total deflection at middle of the wall vs. wall Stiffness, $B/H_E = 1.00$, 3D analysis

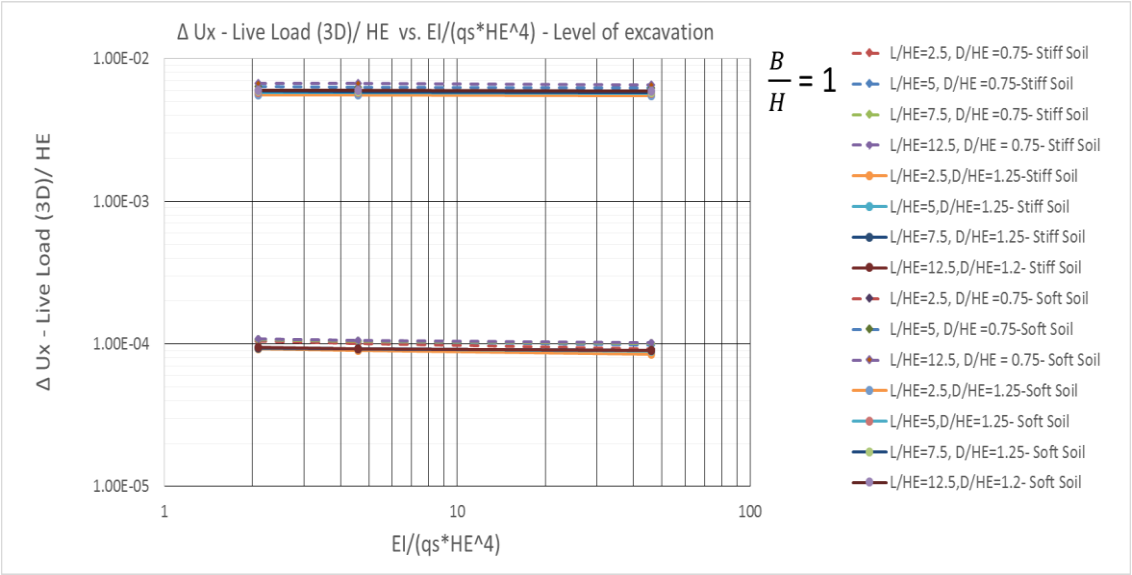

Figure 94. Total deflection at level of excavation vs. wall stiffness, $B/H_E = 1.00$, 3D analysis

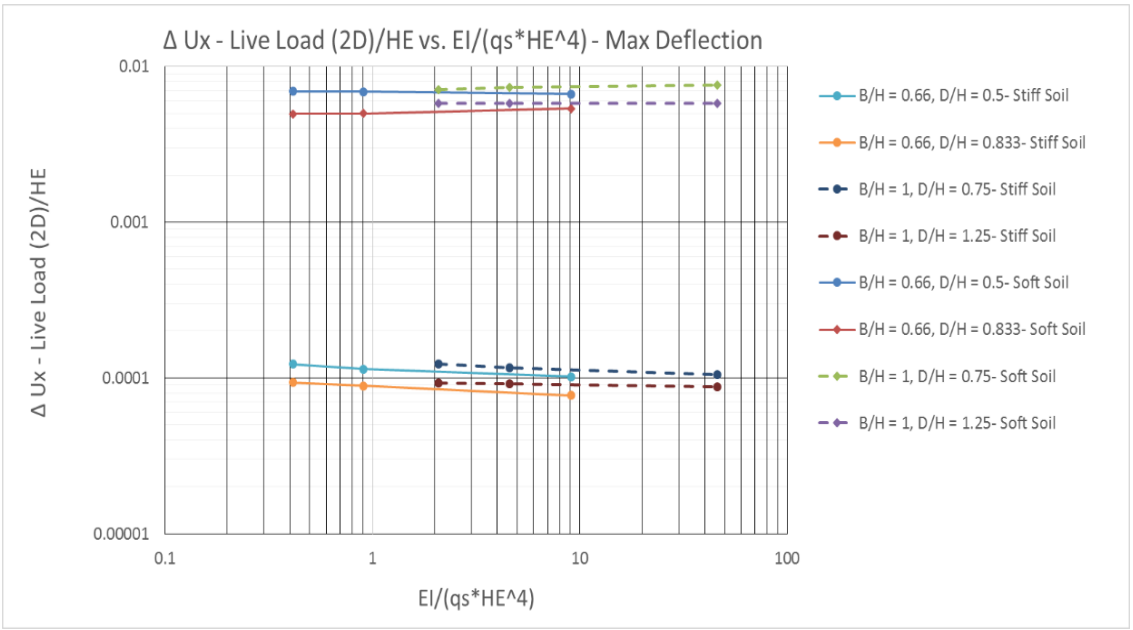

Figure 95. Total maximum deflection vs. wall stiffness, 2-dimensional analysis

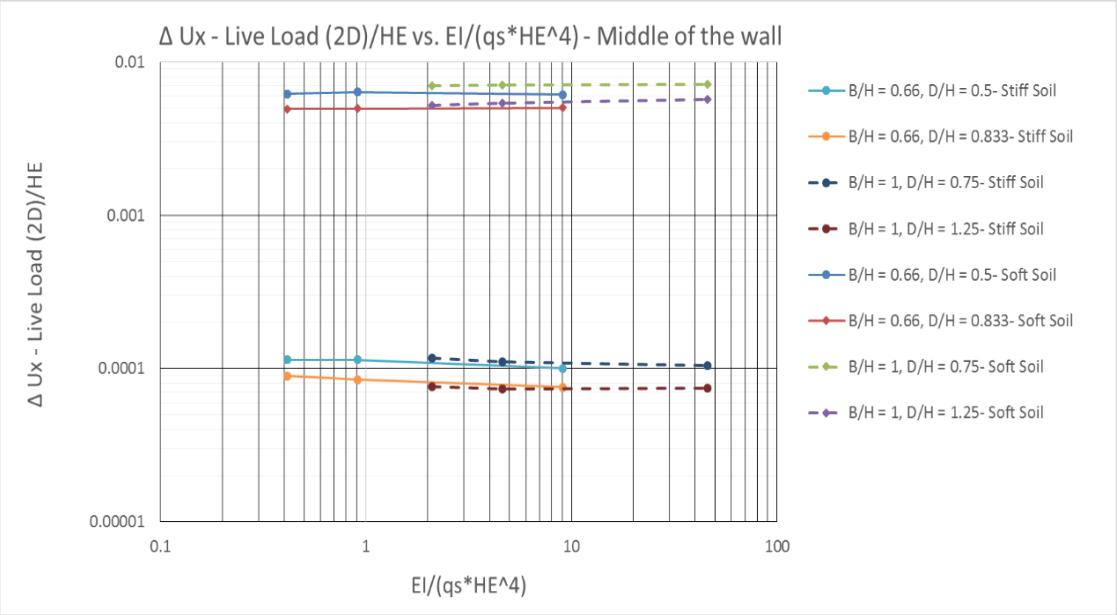

Figure 96. Total deflection at middle of the wall vs. wall stiffness, 2-dimensional analysis

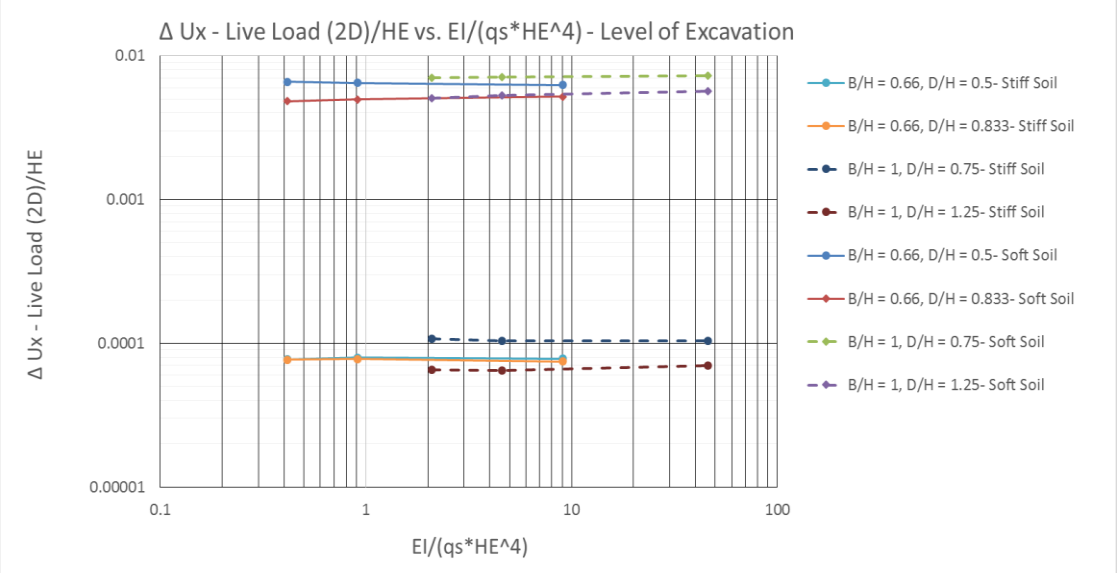

Figure 97. Total deflection at level of excavation vs. wall stiffness, 2-dimensional analysis

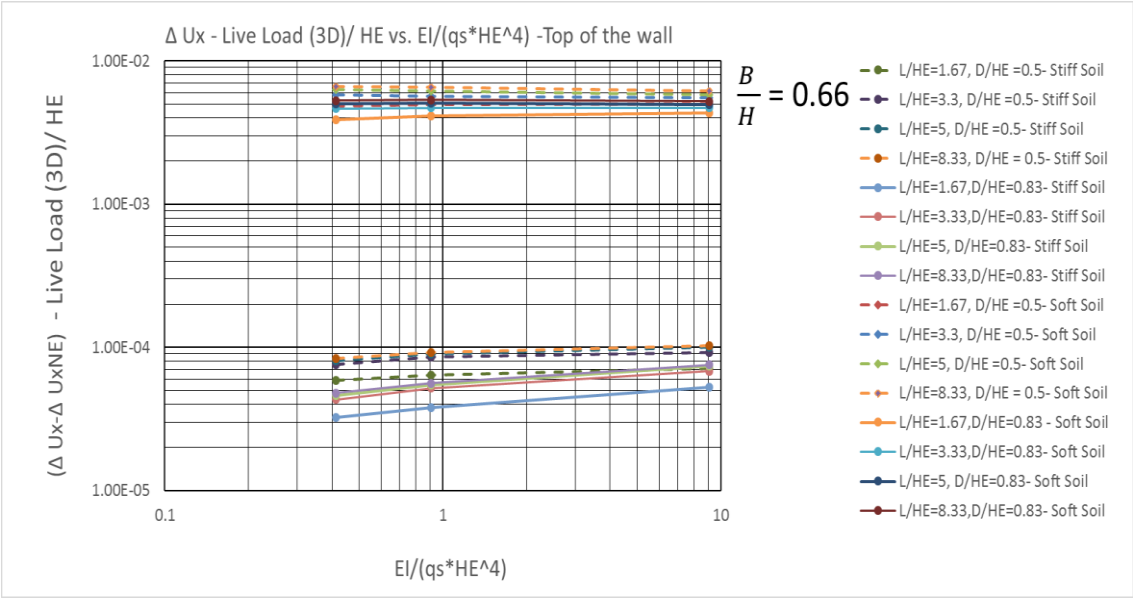

Figure 98. Relative deflection at top of the wall vs. wall stiffness, $B/H_E = 0.66$, 3D analysis

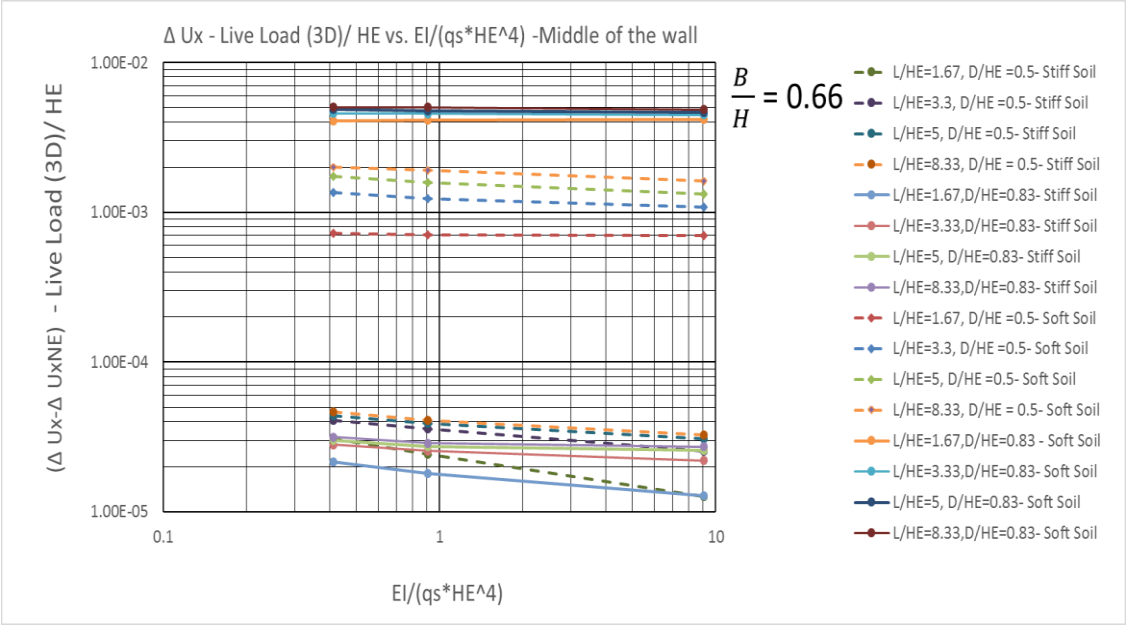

Figure 99. Relative deflection at middle of the wall vs. wall stiffness, $B/H_E = 0.66$, 3D analysis

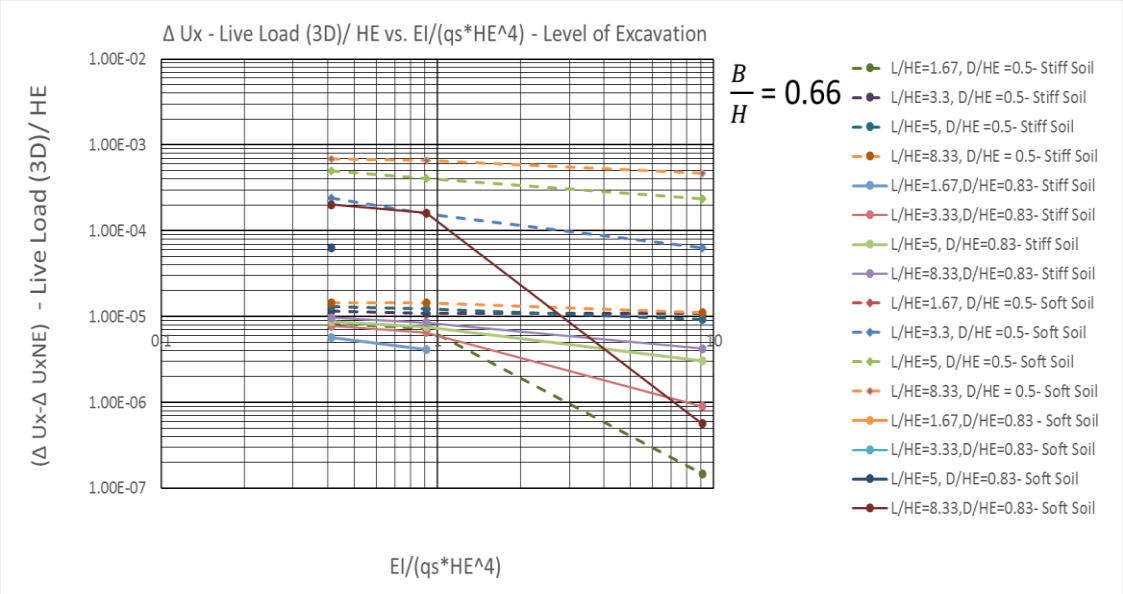

Figure 100. Relative deflection at level of excavation vs. wall stiffness, B/H$_E$ = 0.66, 3D analysis

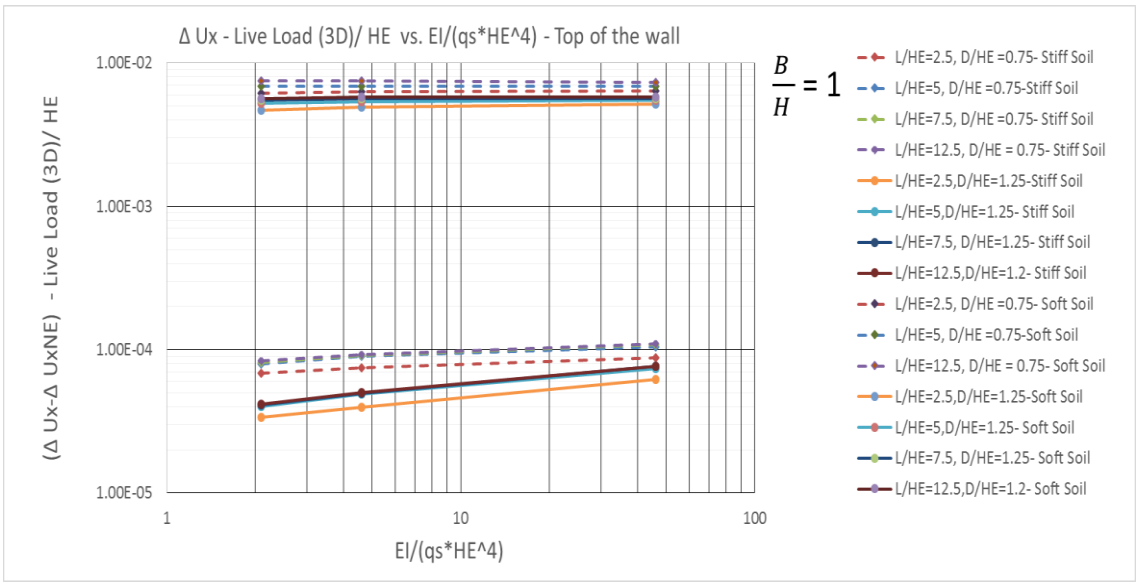

Figure 101. Relative deflection at top of the wall vs. wall stiffness, B/H$_E$ = 1.00, 3D analysis

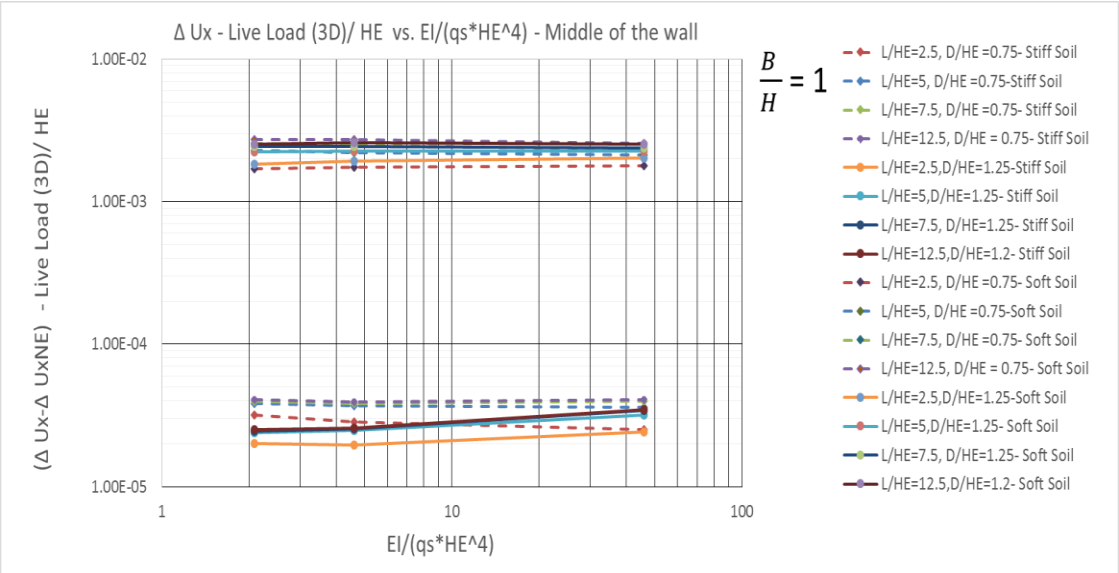

Figure 102. Relative deflection at middle of the wall vs. wall stiffness, B/H_E = 1.00, 3D analysis

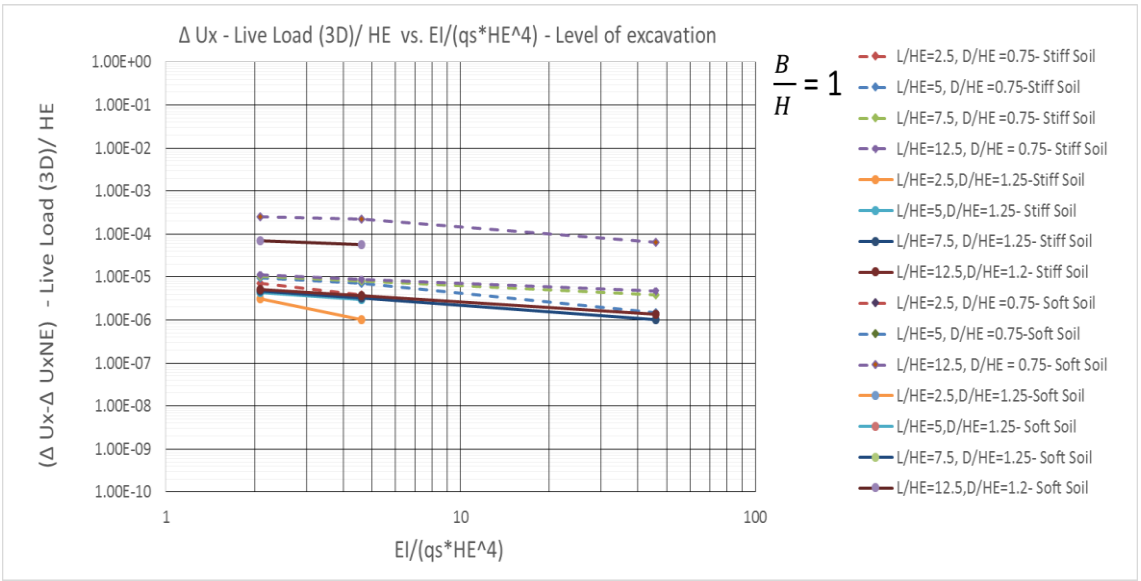

Figure 103. Relative deflection at level of excavation vs. wall stiffness, B/H_E = 1.00, 3D analysis

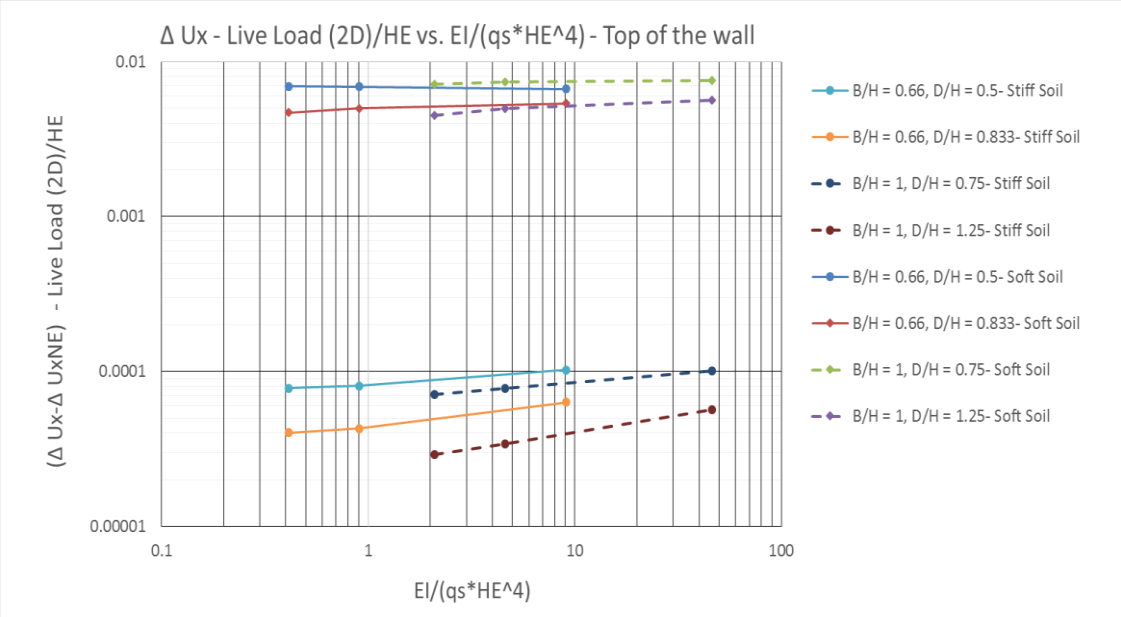

Figure 104. Relative deflection at top of the wall vs. wall stiffness, 2-dimensional analysis

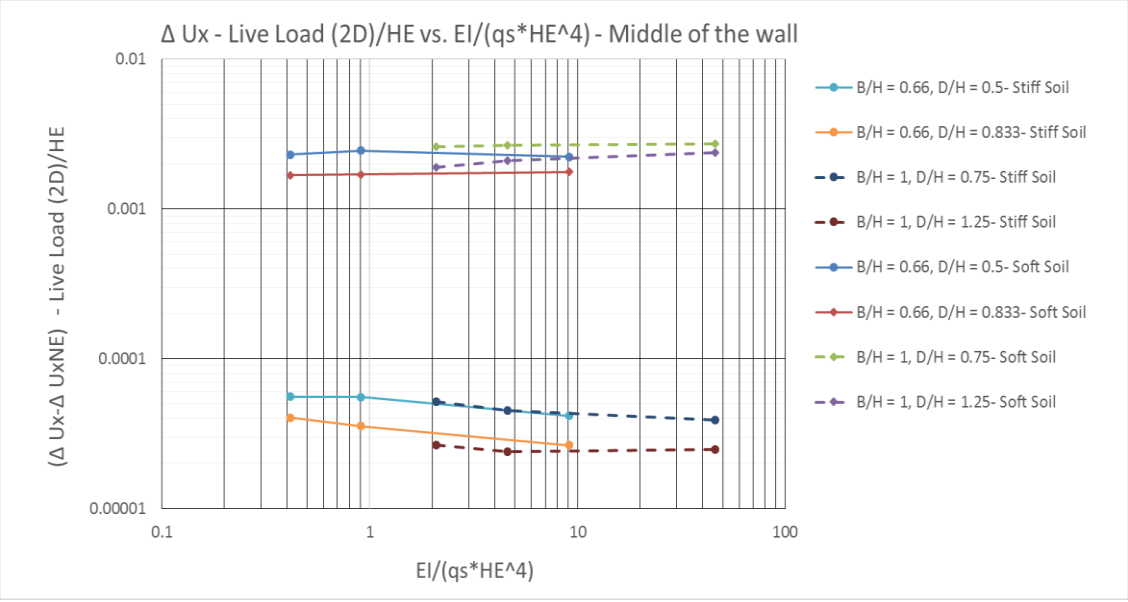

Figure 105. Relative deflection at middle of the wall vs. wall stiffness, 2-dimensional analysis

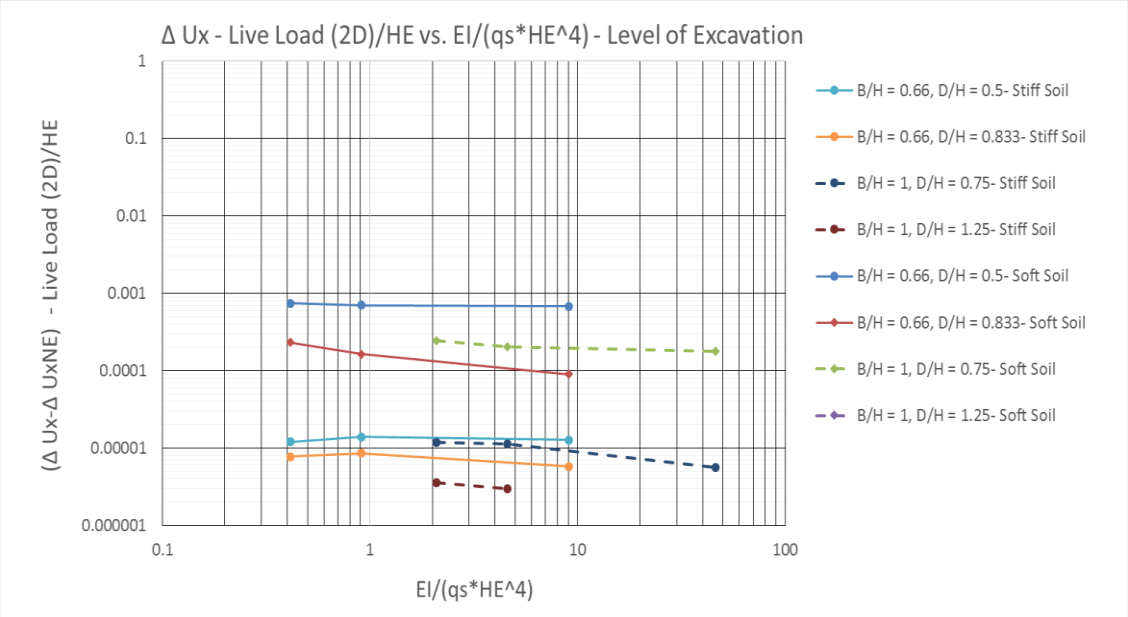

Figure 106. Relative deflection at level of excavation vs. wall stiffness, 2-dimensional analysis

Due to the finite stiffness E_s of the soil, lateral deflections will occur due to live loading even in the absence of an excavation. Therefore, the most significant aspect of wall behavior is the increase in displacement beyond that expected to occur under conditions of no wall. The displacement $\Delta u_{x\text{-}no\_wall}$ can be interpreted as the displacement profile at a distance D from the edge of the strip load, located far from the wall in the y-direction. Typical profiles of predicted wall displacement with and without the excavation and wall installation (Figures 107 and 108) show the displacement at the base of the excavation to be roughly equal to the lateral displacement that would have occurred in the soil mass if no wall or excavation were present. Thus, evaluating wall and excavation behavior in terms of increments of displacement between the case with no excavation and

the case with excavation along the height of the wall for two cases of soft and stiff soil is more desirable (Equation 18).

$$\Delta u_{x\text{-inc}} = \Delta u_x - \Delta u_{x\text{-no\_wall}} \quad (18)$$

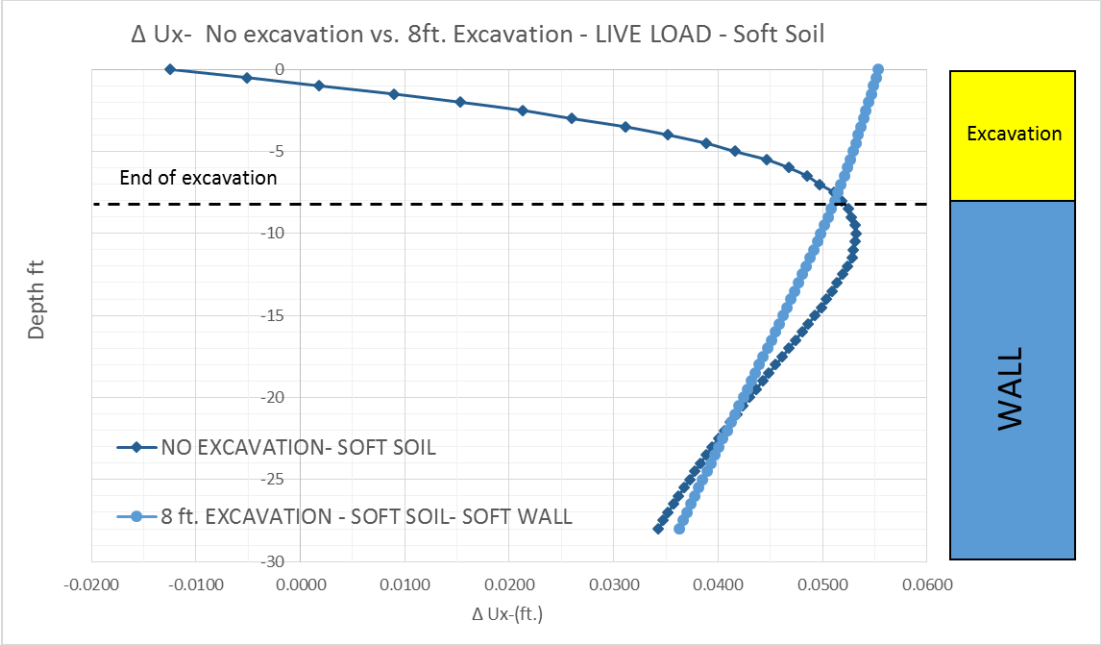

Figure 107. Total deflection, no excavation vs. 8 ft. of excavation, soft soil case

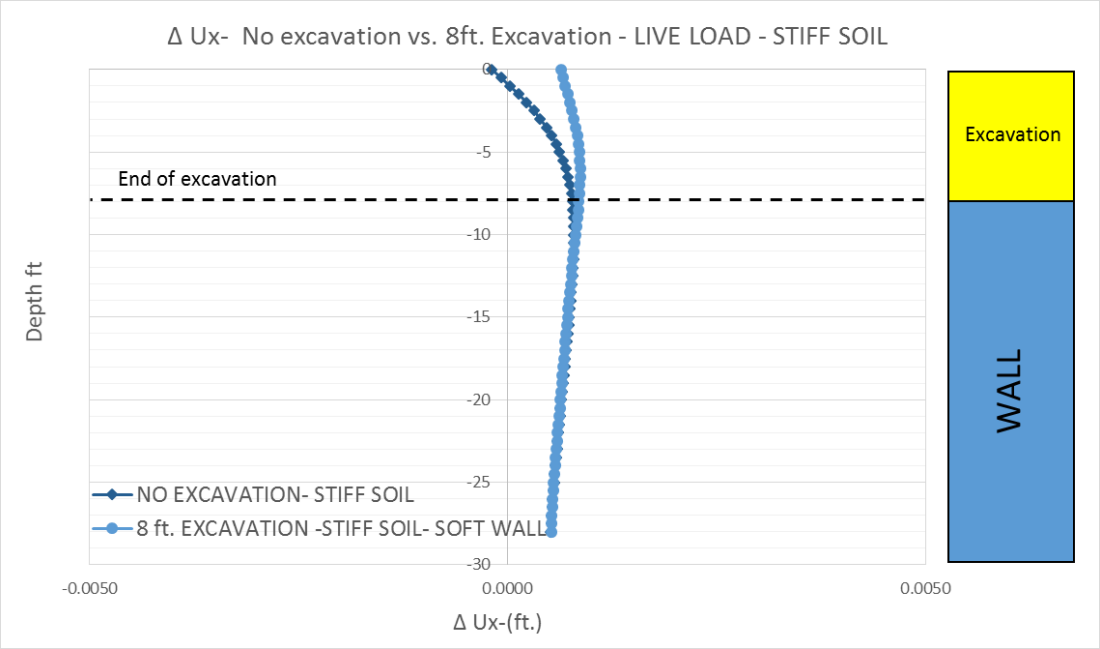

Figure 108. Total deflection, no excavation vs. 8 ft. of excavation, stiff soil case

This should not be construed to imply that the translational component of wall displacement is not important. However, recognizing that wall translational displacement is largely governed by soil stiffness and that its magnitude is insensitive to details of the excavation geometry and wall stiffness is critical.

The predictions still show greater movements for walls and excavations in soft soils than in stiff soils, but the differences/predictions for structural movement in soft soil are not as extreme as when total displacements Δu_x are considered. Figures 109 and 110 show the finite element, FE, predicted $\Delta u_{x\text{-}inc}$ for soft and stiff soil, respectively.

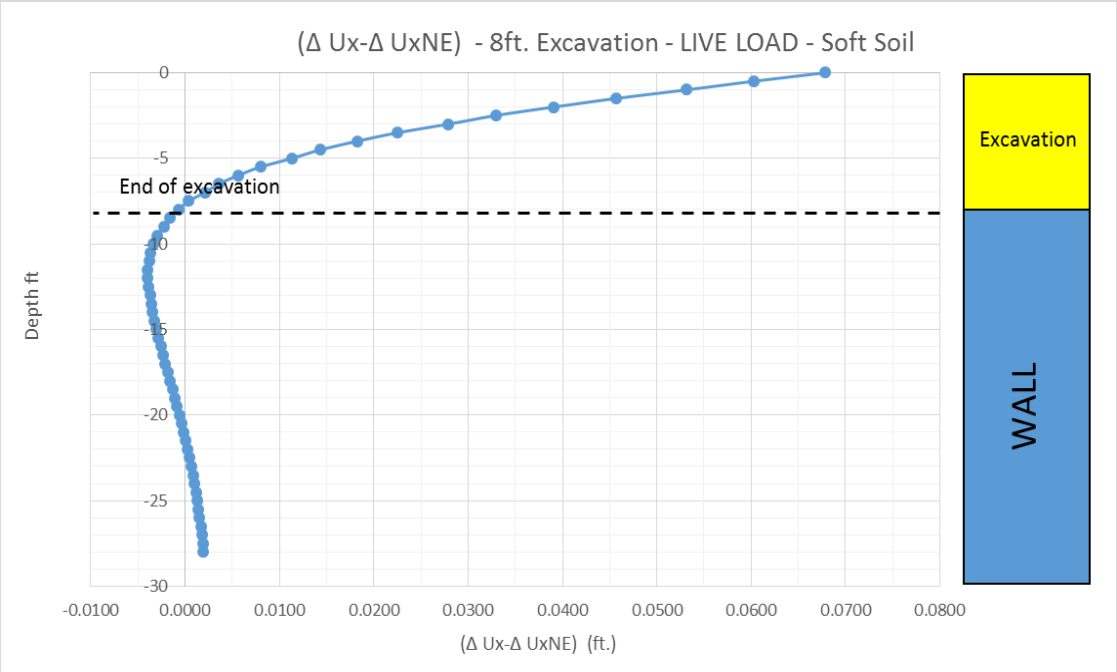

Figure 109. Relative deflection, $\Delta u_{x\text{-}inc}$, 8 ft. of excavation, soft soil case

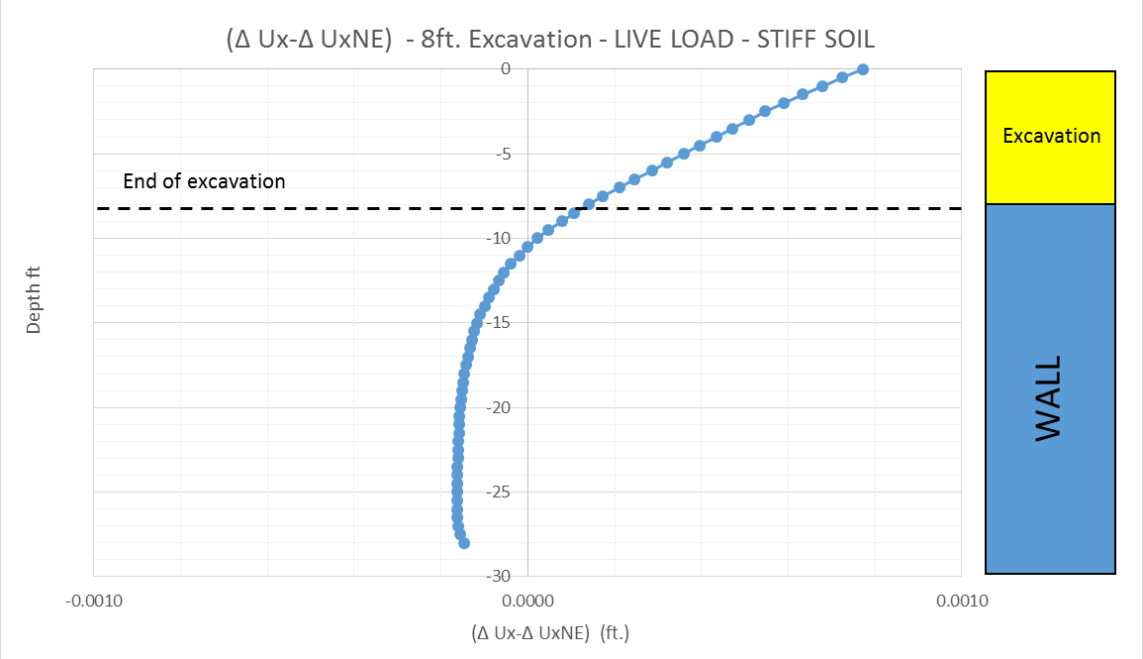

Figure 110. Relative deflection, $\Delta u_{x\text{-}inc}$, 8 ft. of excavation, stiff soil case

4.9.3 Effect of Length of Excavation on the Lateral Deformation, HE/L

The effects of the length of excavation on wall displacement are presented in this section. Figures 111 to 116 show finite element predictions of wall lateral displacement at the top, middle and base of the wall for various wall lengths. The case of an infinitely long wall, HE/L = 0, corresponds to the two-dimensional plane strain condition

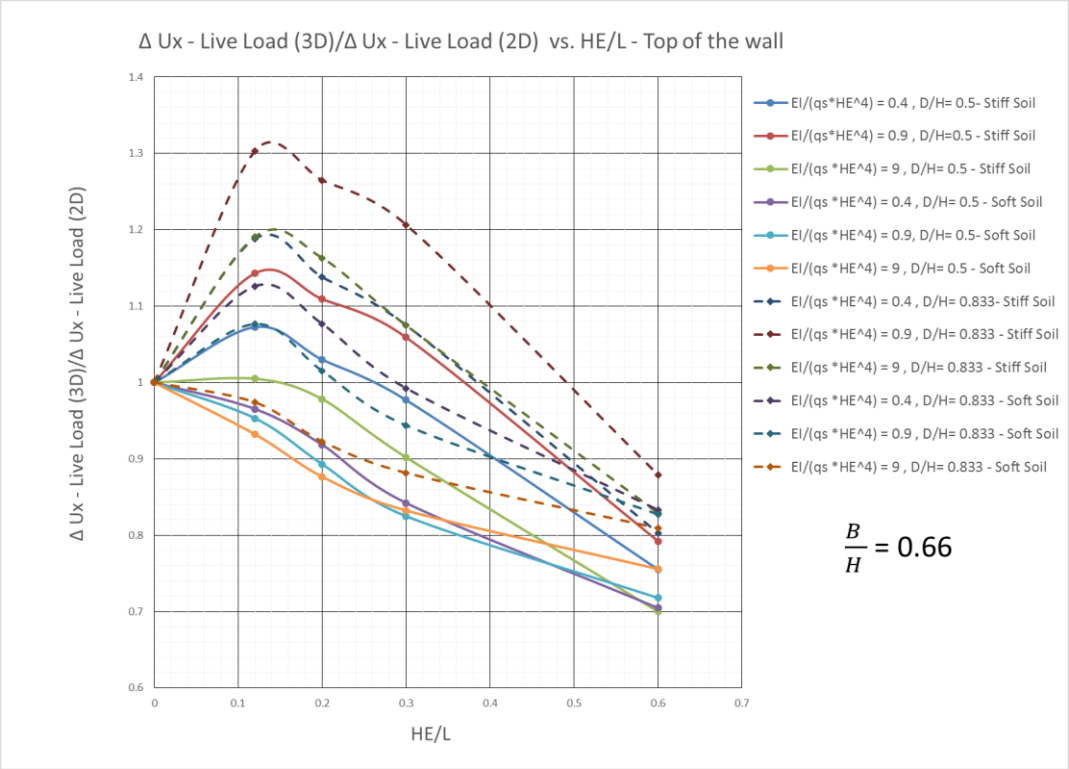

Figure 111. Total deflection at top of the wall vs. wall height, $B/H_E = 0.66$

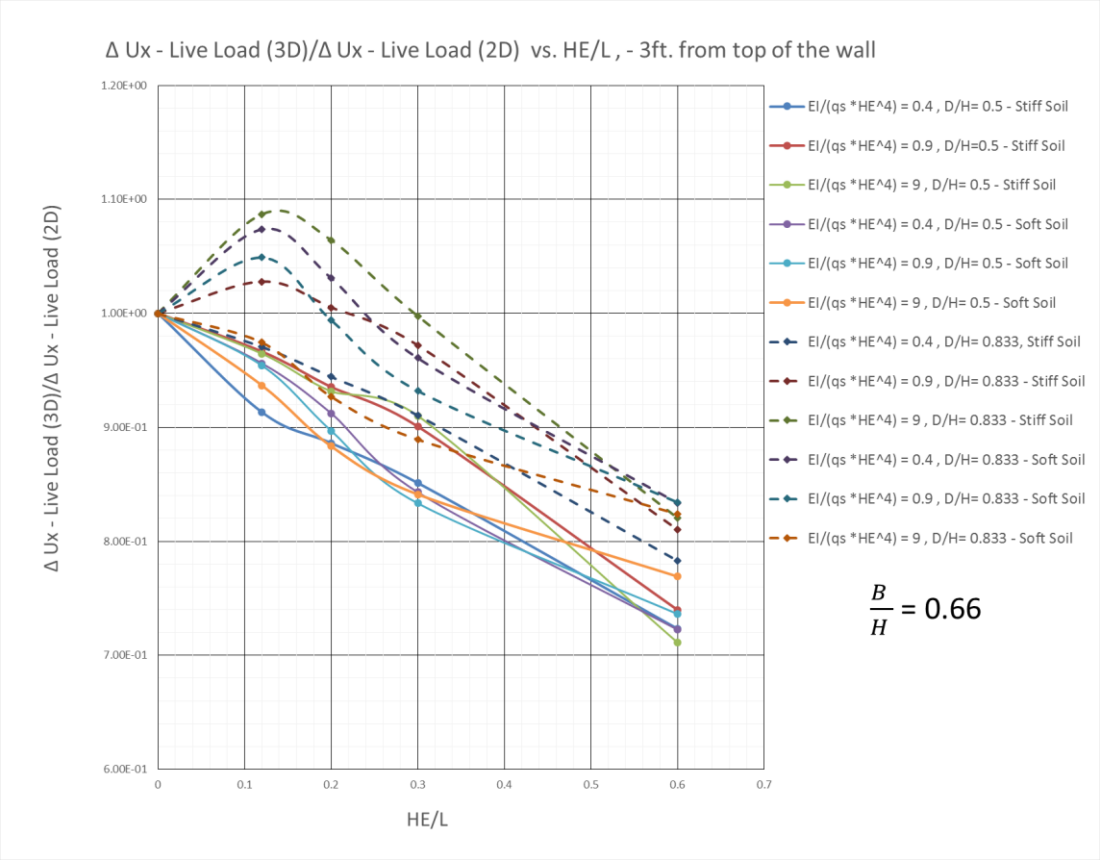

Figure 112. Total deflection at -3 ft. from top of the wall vs. wall height, $B/H_E = 0.66$

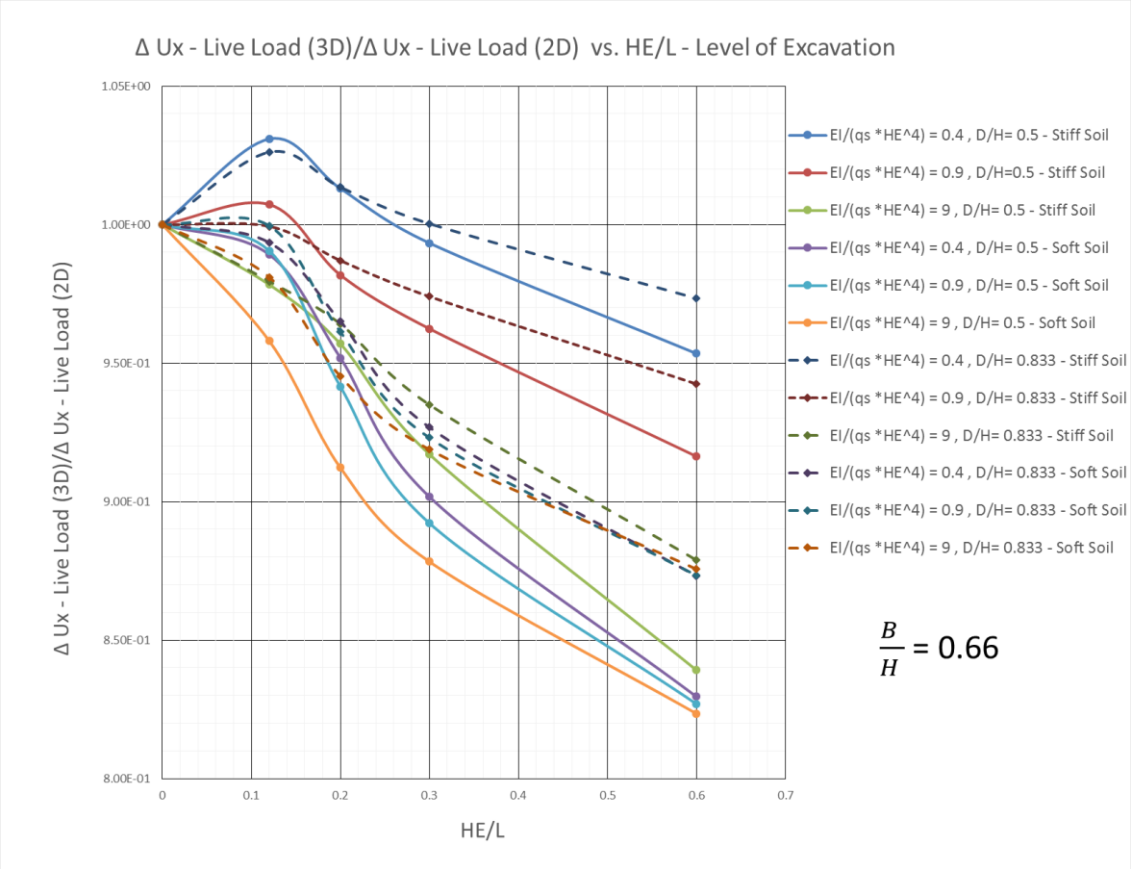

Figure 113. Deflection at level of excavation vs. wall height, $B/H_E = 0.66$

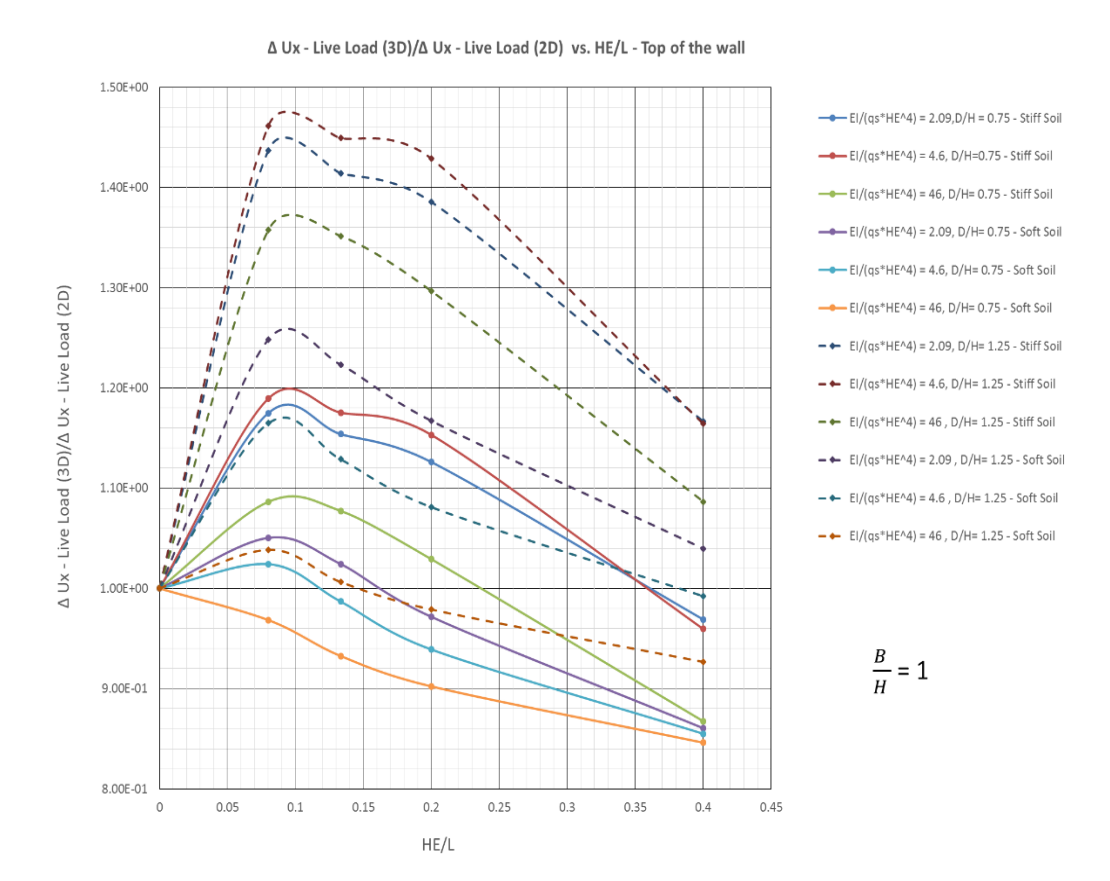

Figure 114. Total deflection at top of the wall vs. wall height, $B/H_E = 1.00$

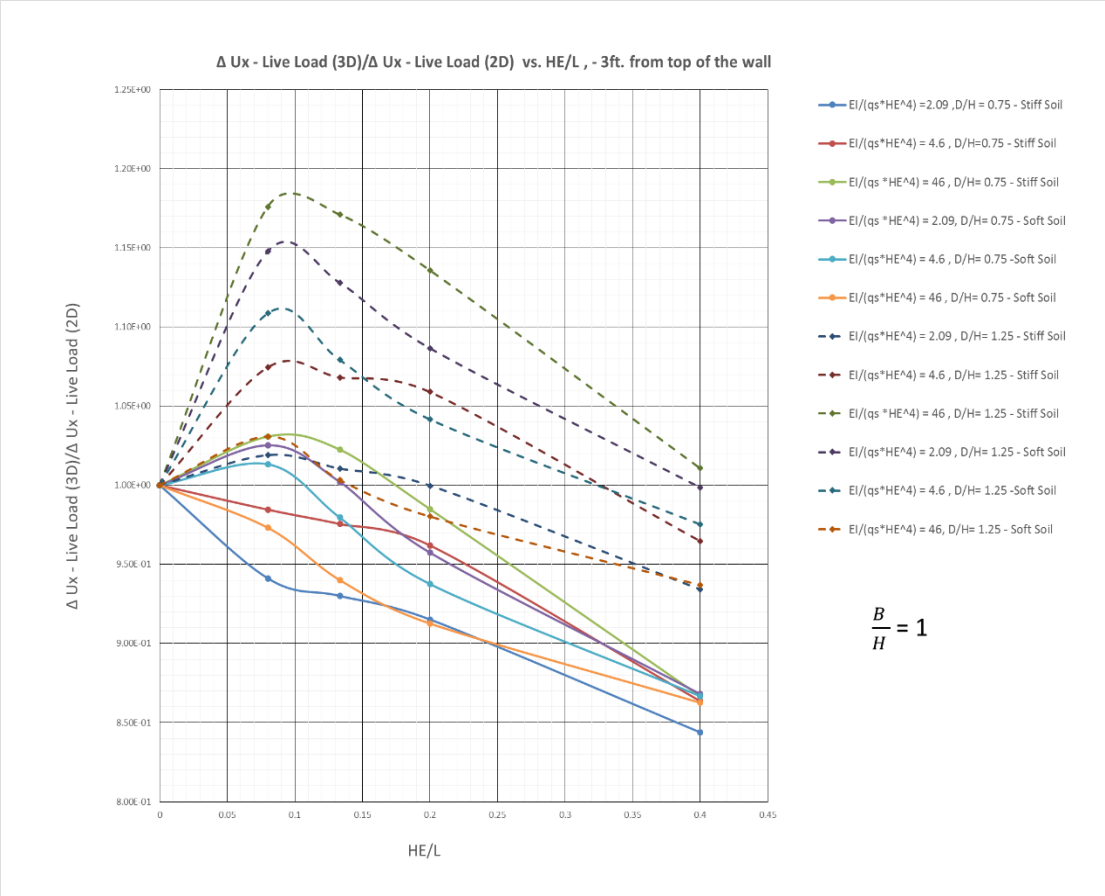

Figure 115. Total deflection at -3 ft. from top of the wall vs. wall height, $B/H_E = 1.00$

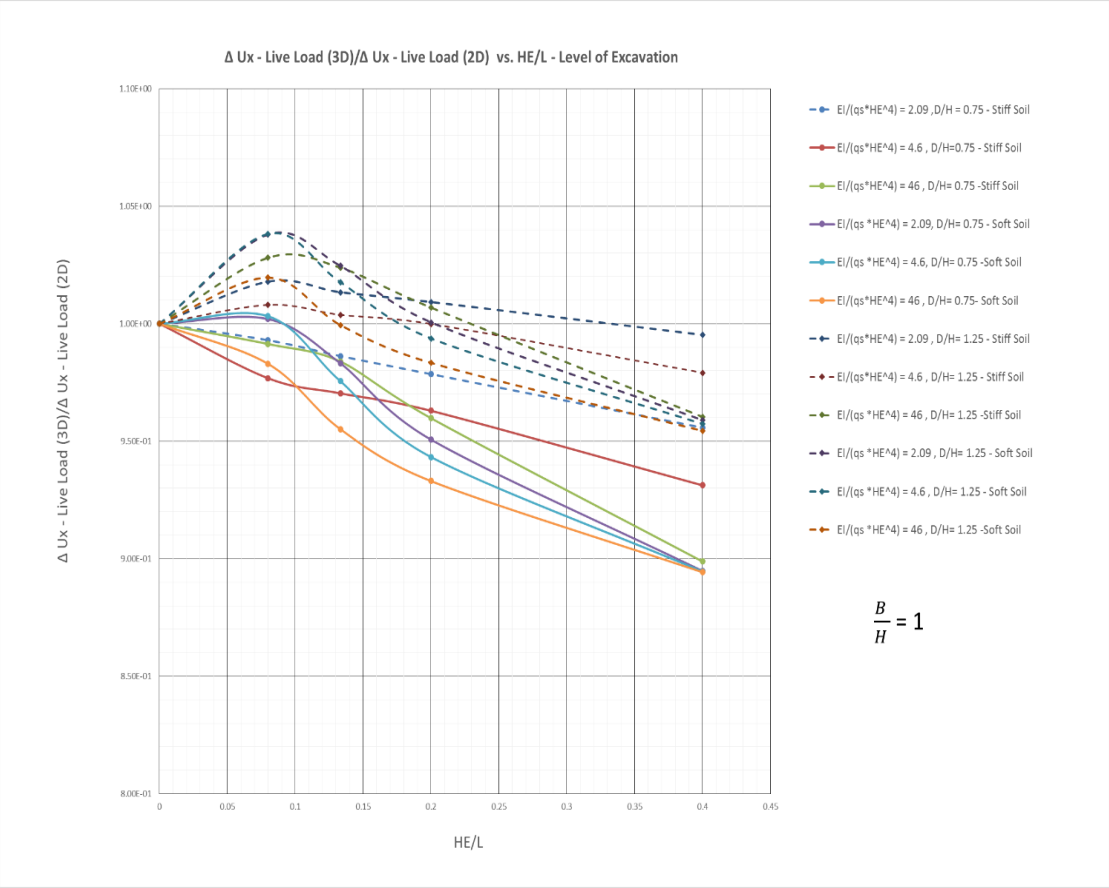

Figure 116. Total deflection at level of excavation vs. wall height, $B/H_E = 1.00$

4.10 Comparisons between the Elastic Beam Model and Boussinesq Stresses

As mentioned in previous sections, Boussinesq theory was recommended in the Guideline for Temporary Shoring (GTS, 2004) to find the horizontal stresses on walls. The lateral deflection calculations made using this analytical approach were compared to the results from the finite element model. Generally, the lateral deflection predicted by Boussinesq theory is higher than that predicted by the finite element model for stiff soil and lower than the finite element model predictions for very soft soil. These results show that the Boussinesq theory is more conservative for stiff soil but not conservative enough in predicting the deflection in soft soil. In addition, the ratio of B/HE can affect the lateral deflection predictions. A summary of the finite element model and Boussinesq results are shown in Figures 117 to 124.

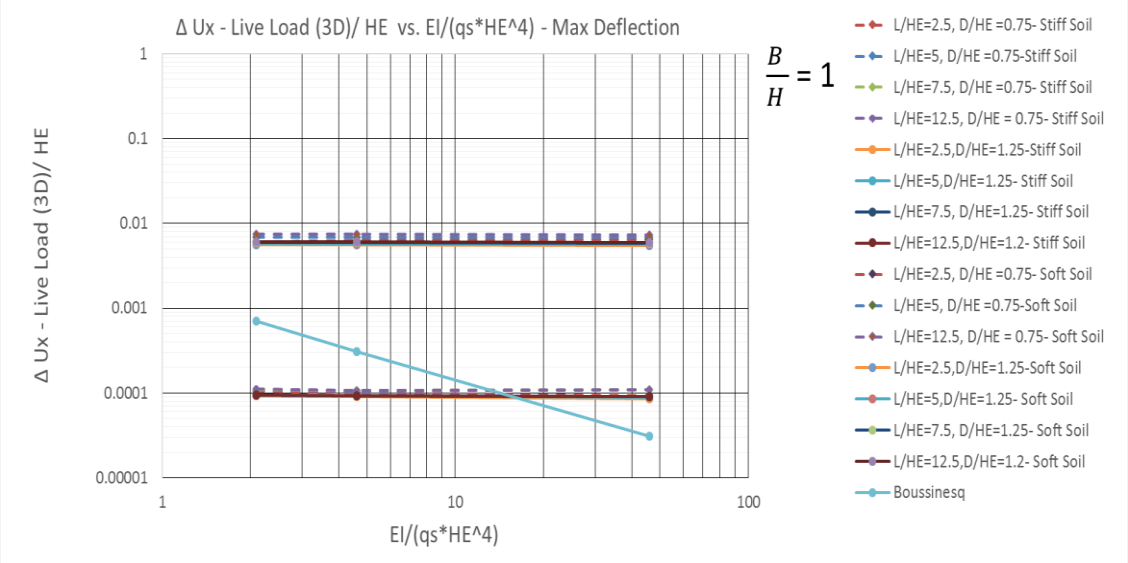

Figure 117. Maximum total deflection for different soil vs. Boussinesq theory, B/HE = 1.00, 3D model

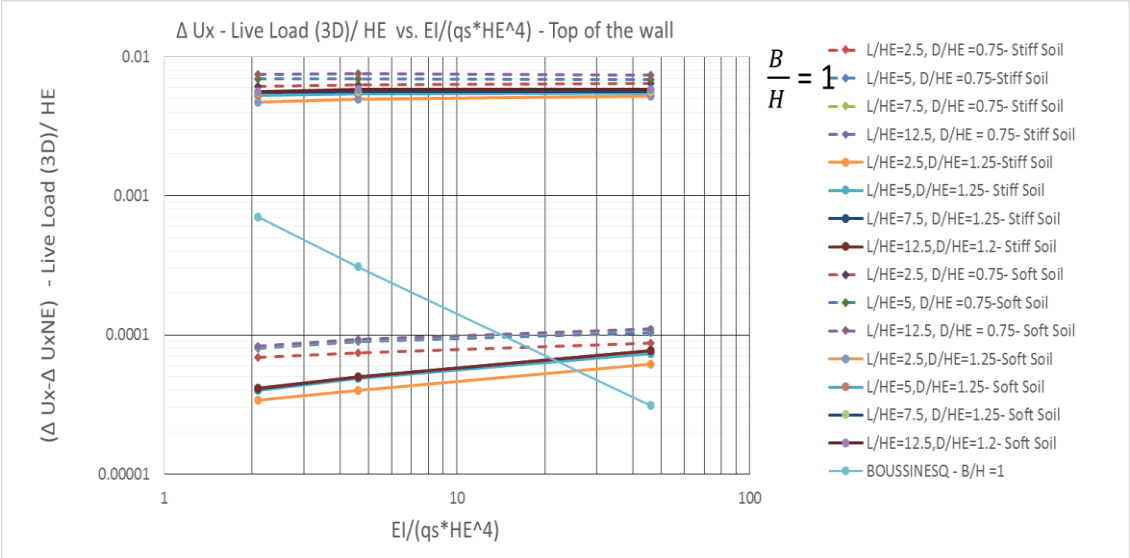

Figure 118. Relative deflection for different soil at top of the wall vs. Boussinesq theory, B/HE = 1.00, 3D model

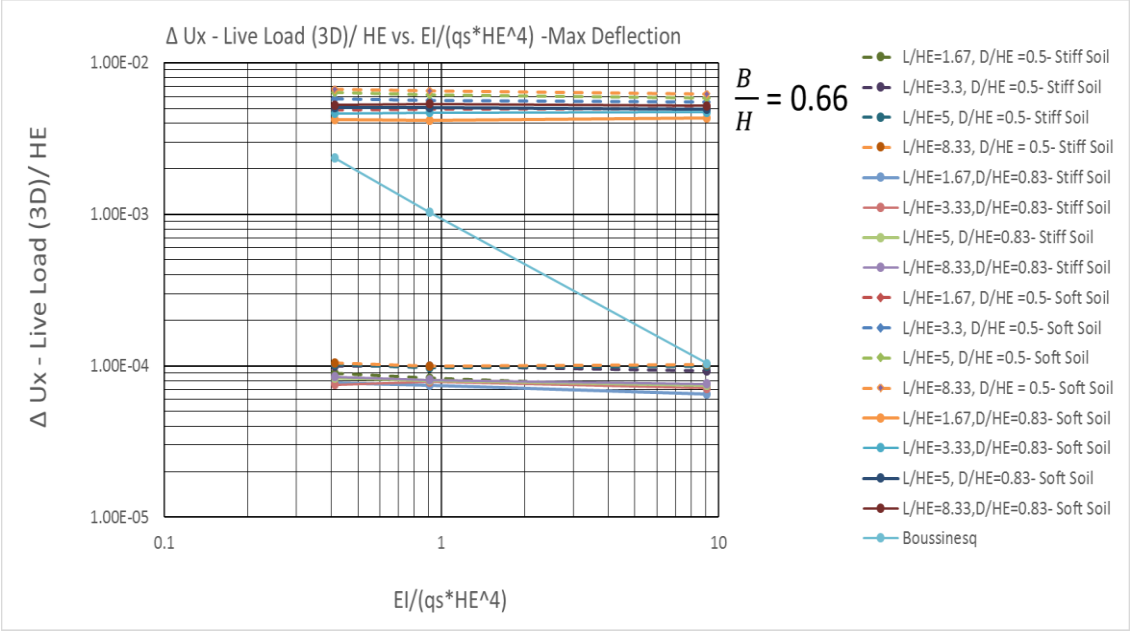

Figure 119. Maximum total deflection for different soil vs. Boussinesq Theory, B/HE = 0.66, 3D model

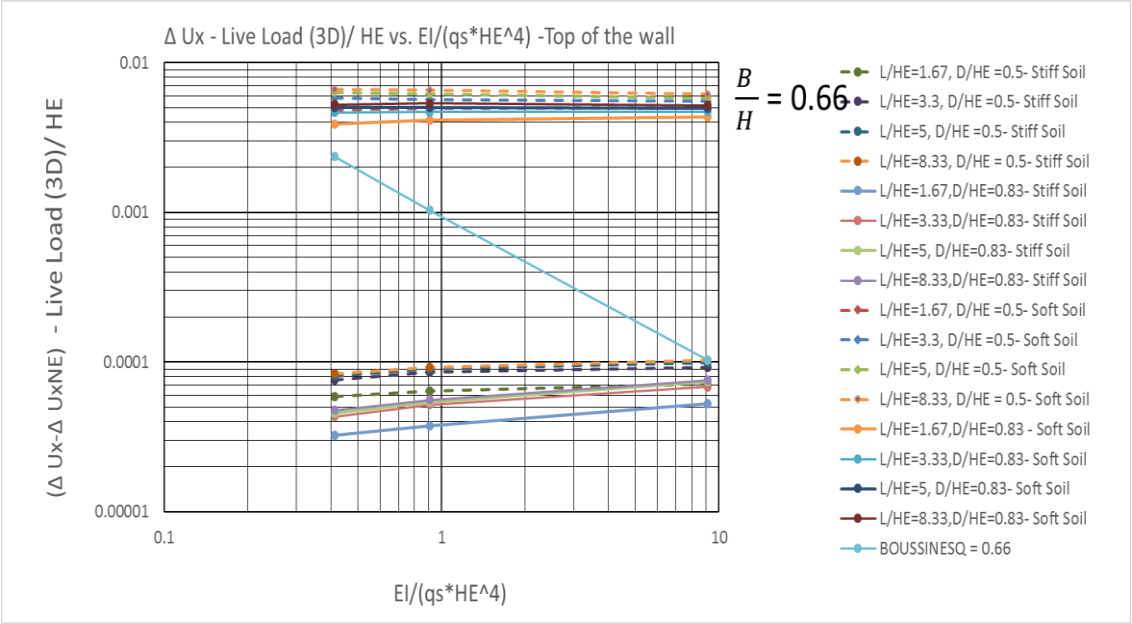

Figure 120. Relative deflection for different soil at top of the wall vs. Boussinesq theory, B/HE = 0.66, 3D model

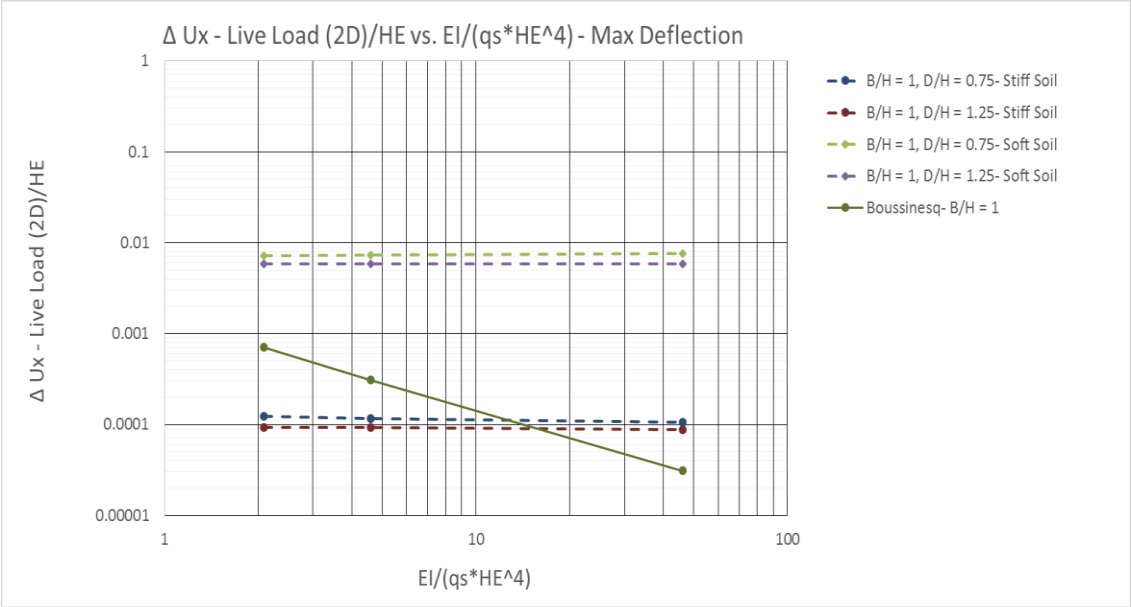

Figure 121. Maximum total deflection for different soil vs. Boussinesq theory, B/HE = 1.00, 2-dimensional model

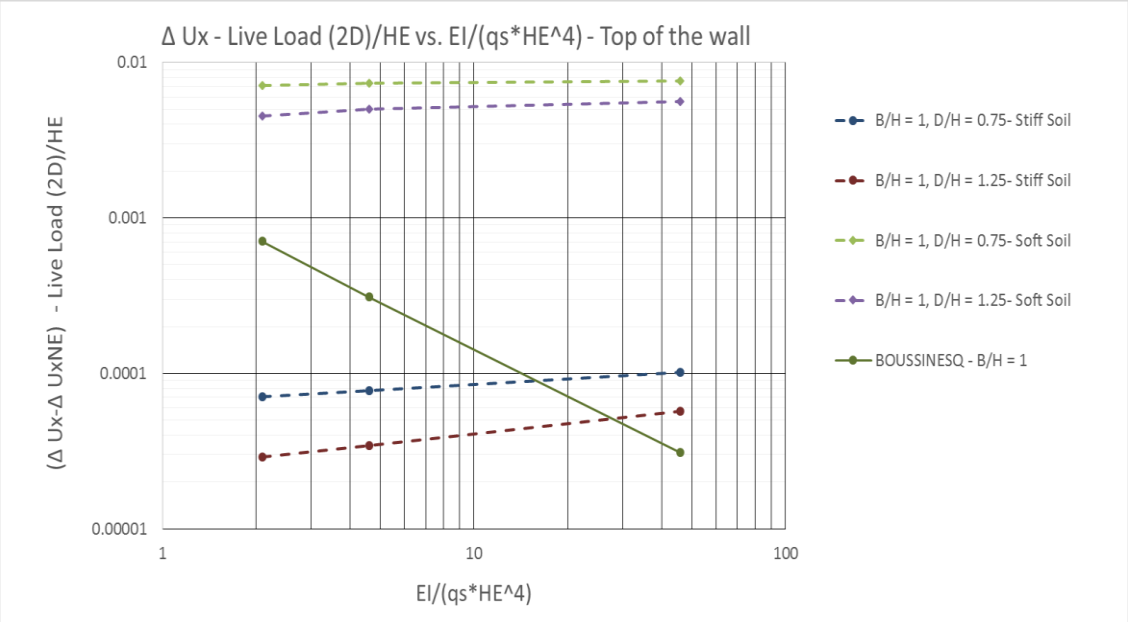

Figure 122. Relative deflection for different soil at top of the wall vs. Boussinesq theory, B/HE = 1.00, 2d model

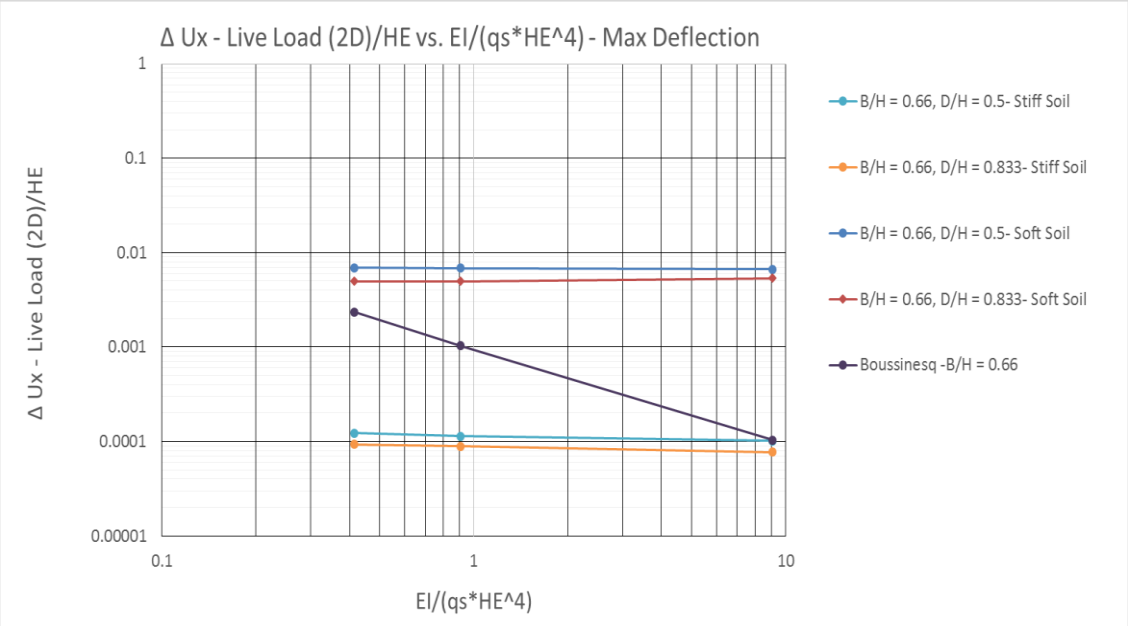

Figure 123. Maximum total deflection for different soil vs. Boussinesq theory, B/HE = 0.66, 2-dimensional model

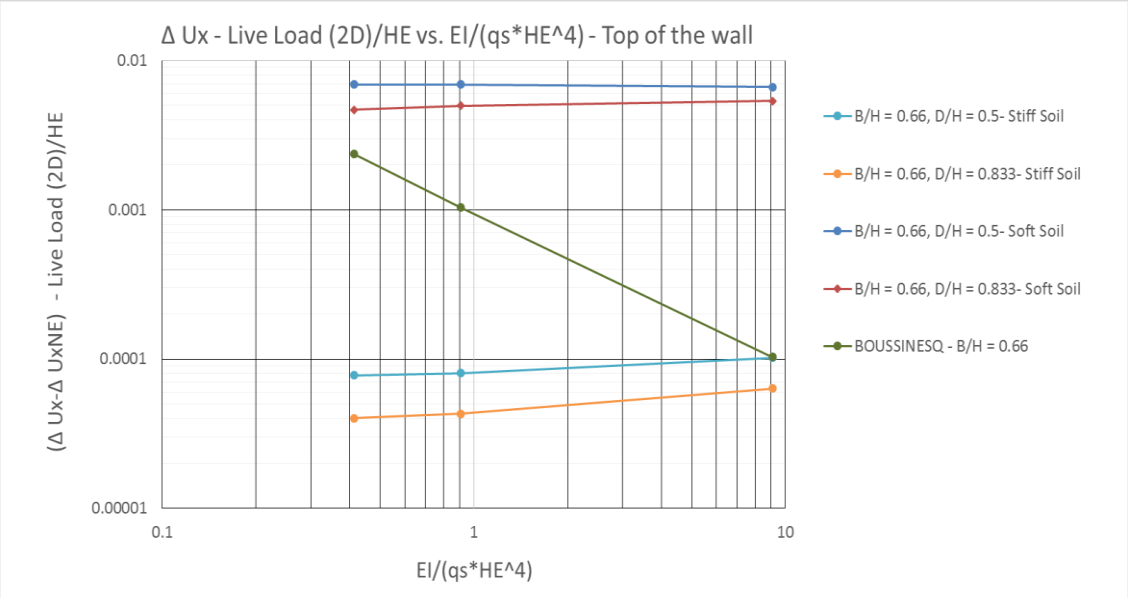

Figure 124. Relative deflection for different soil at top of the wall vs. Boussinesq theory, B/HE = 0.66, 2-dimensional model

4.11 Three-Dimensional Modeling and Analysis of Sheet Pile Sections

Three different sections of sheet pile walls were modeled in ABAQUS (ver. 6.12, 2012), and the results were compared to find the effects of shape and interlocking, called the hinging effect, in the behavior of the walls. The results of these simulations are presented in Table 44. The results indicate that the shape of the sections has a noticeable effect on the results, especially in sheet pile walls (Chung et al., 2012). The deflection of sheet pile walls connected with interlocking is some 1.48 times greater than that of the rectangular sections used in the ABAQUS modeling. Such a difference is not noticeable in soldier pile walls and, therefore, can be neglected in that context. Figures 125 to 127 show different sections of sheet pile wall modeled by ABAQUS (ver. 6.12, 2012).

Table 43. Summary of the finite element results

The comparision of maximum deflection of three different pile models				
		ELEMNT		
		CONTINUM ELEMNT	CONTINUM SHELL	
		C3D8R	SC8R-SC6R	
WALL TYPE				Factored Deflection
FLAT (RECTANGULAR)	MAX DEFLECTION (in.)	-4.76731	-4.62	1
SHEETPILE CONNECTED WITHOUT INTERLOCK		-6.18005	?	1.296339026
SHEETPILE CONNECTED WITH INTERLOCK		-7.1	?	1.489309485

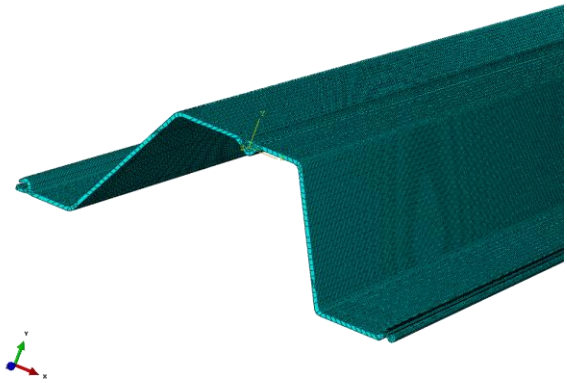

Figure 125. Sheet pile connected with interlocking

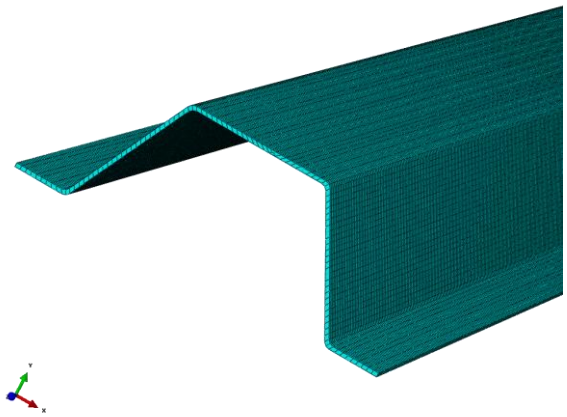

Figure 126. Sheet pile connected without interlocking

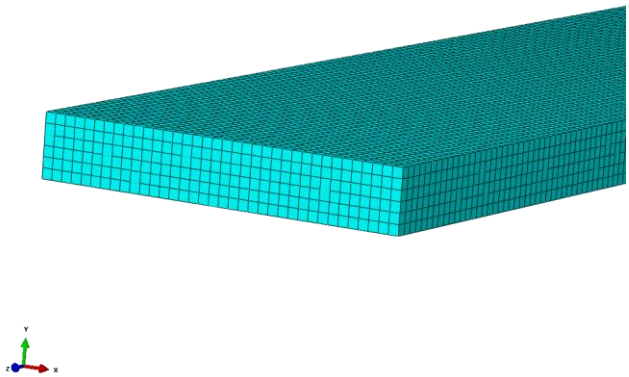

Figure 127. Rectangular section of sheet pile walls

4.12 3D Model – Site Conditions

At the College Station site, two different types of the walls were installed to investigate the behavior of the walls in real conditions rather than simulated or test conditions. In order to compare the results from the numerical studies and models to the data obtained from the site, the actual site conditions for two different sections of walls were modeled in ABAQUS 3D (ver. 6.12, 2012) to find the effect of train live loads on the installed walls. Furthermore, to perform the numerical analyses, soil properties were selected based on the results of tests previously conducted on the site. Figure 128 shows the real site conditions. Figures 129 and 130 show the models created in ABAQUS 3D (ver. 6.12, 2012).

Figure 128. Two different walls installed on site, a soldier pile wall on the left and a sheet pile wall on the right

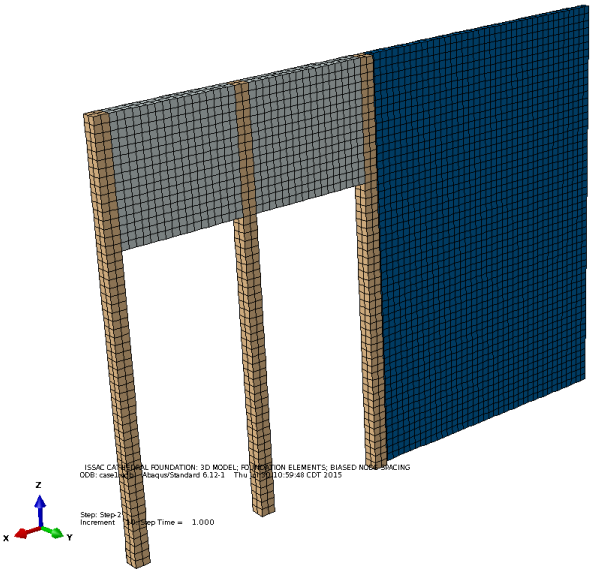

(a) Undeformed Wall

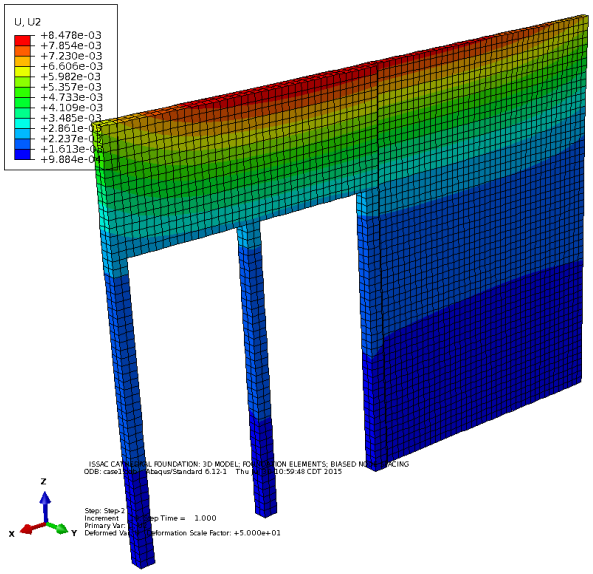

(b) Deformed Wall

Figure 129. Two different walls modeled in ABAQUS

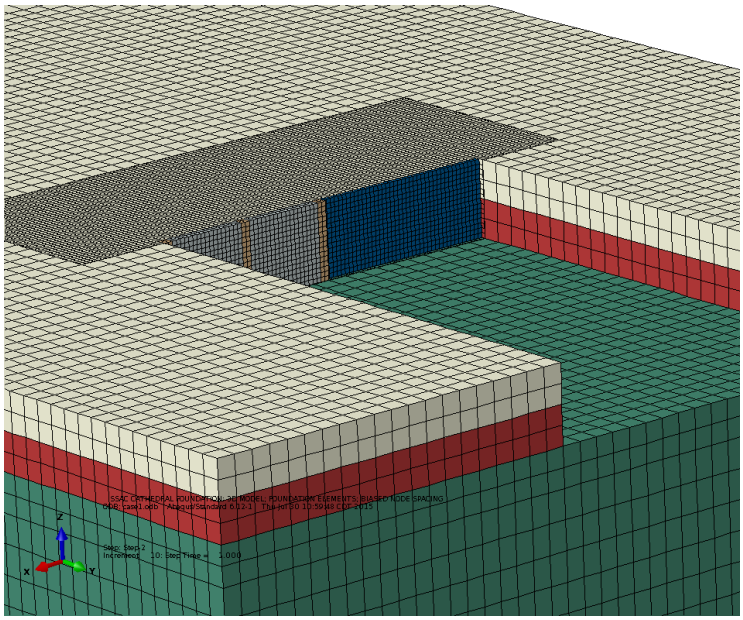

(a) Finite element model of site before loading

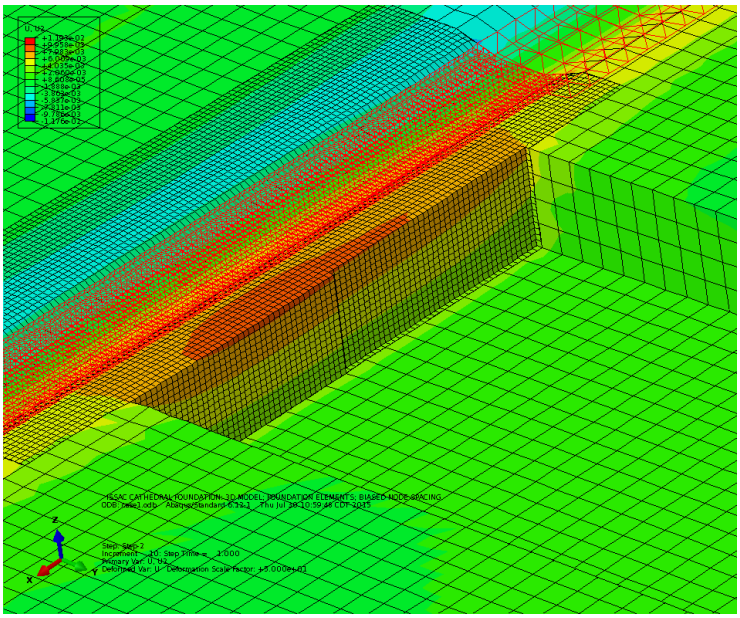

(b) Finite element model of site after loading

Figure 130. 3D live load model in ABAQUS

4.12.1 Material Properties

In the site condition, based on the information found from soil samples and tests, soil profile consists of three different layers. In addition, the walls and beams material were chosen as steel. The material properties of these models are listed in Table 44.

Table 44. Material properties – site Condition

Materials	Elevation	Modulus of Elasticity	Poisson's ratio	Unit weight	Friction angle	cohesion
	ft.	psf.		psf.	deg	psf.
Soil-layer 1	0 to -4	220000	0.45	125	0	2000
Soil-layer 2	-4 to -10	1081250	0.45	125	0	2410
Soil-layer 3	-10 to -60	1562500	0.45	125	0	2817
Steel		4180000000	0.1	490	-	-
Timber		288214982	0.35	120	-	-

4.12.2 Results

The results of these simulations for one loading case, the train live load case, and in different locations are presented in Table 45. Based on the finite element results, the maximum deflection of the walls occurred at the middle of the length of the walls. Figures 131 to 135 show the deflection of the walls versus depth of the walls at different locations. Figure 136 compares the maximum horizontal deflection at different locations. Figure 137 shows a plane view of deflection of the installed walls in addition to a comparison between the deflections of the installed walls to a uniform wall

Table 45. Summary of results for the model of actual site conditions

Deflection (inch) - Top of the wall		
LOCATION	FEM	SITE
SOL.PILE SOUTH	7.45E-02	
SOL.PILE MIDDLE	1.00E-01	
SOL.PILE NORTH	9.84E-02	
SH.PILE MIDDLE	9.49E-02	
SH.PILE NORTH	7.91E-02	

* "SOL." indicates the soldier pile wall; "SH" refers to the sheet pile wall

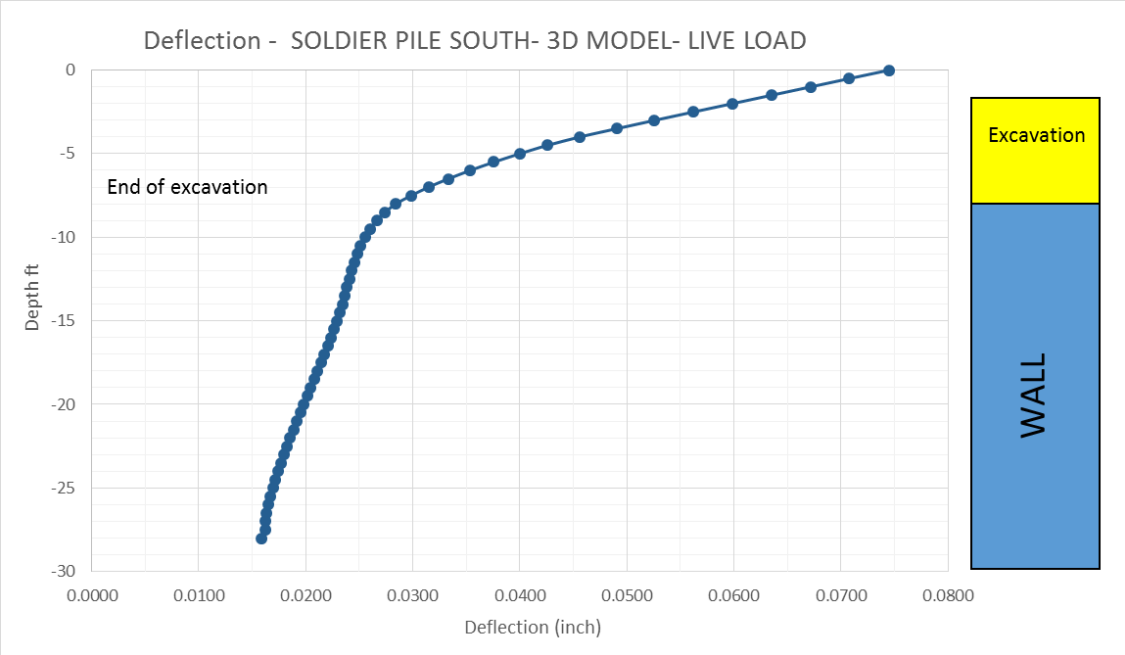

Figure 131. Deflection at the south pile of the soldier pile wall because of live load

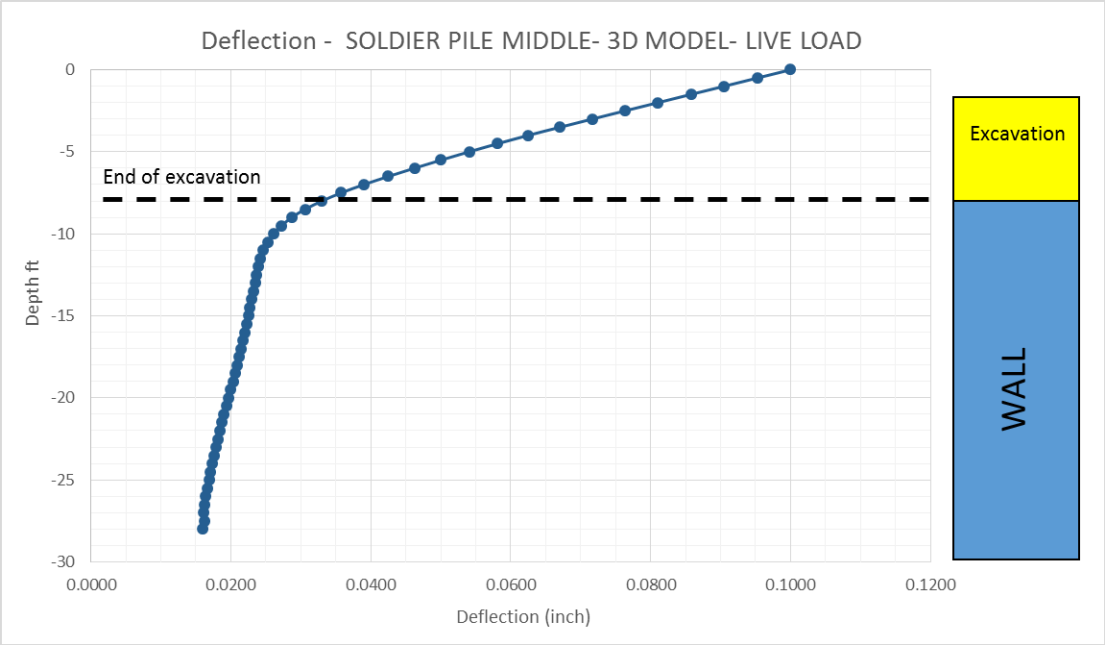

Figure 132. Deflection at the middle of the soldier pile wall because of live load

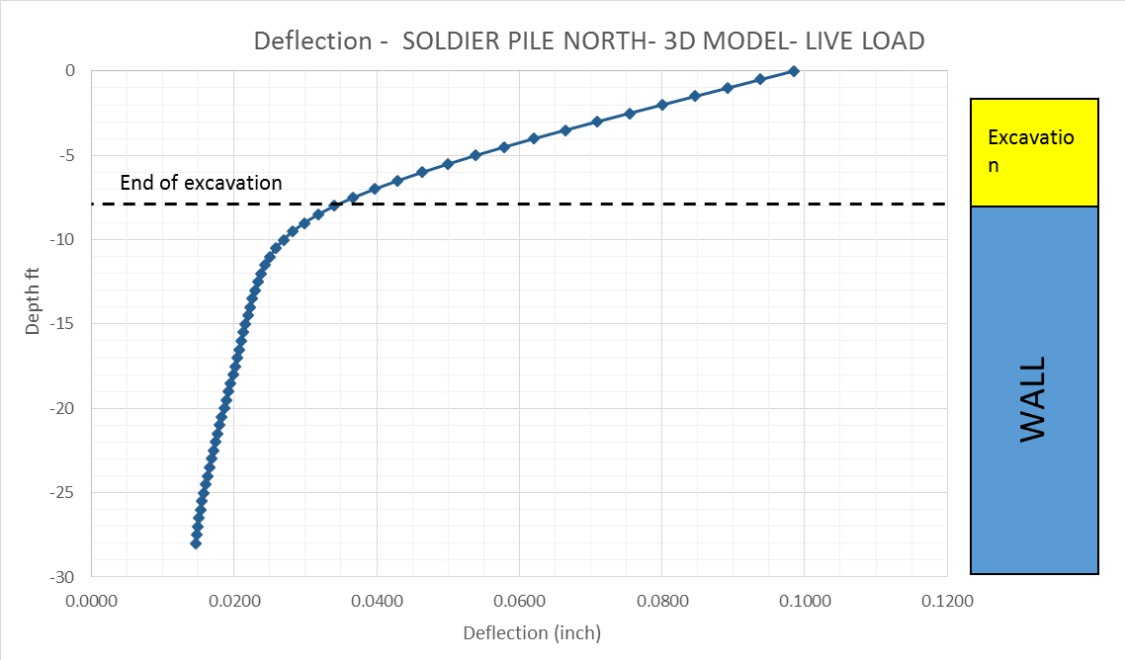

Figure 133. Deflection at the north pile of the soldier pile wall because of live load

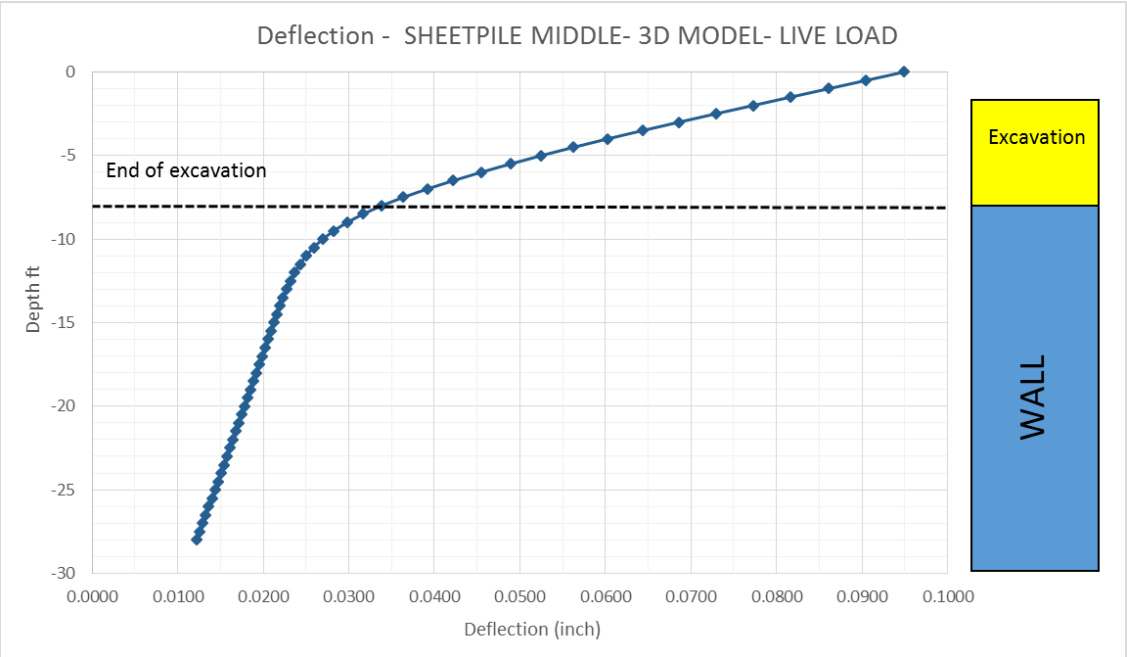

Figure 134. Deflection at the middle of the sheet pile wall because of live load

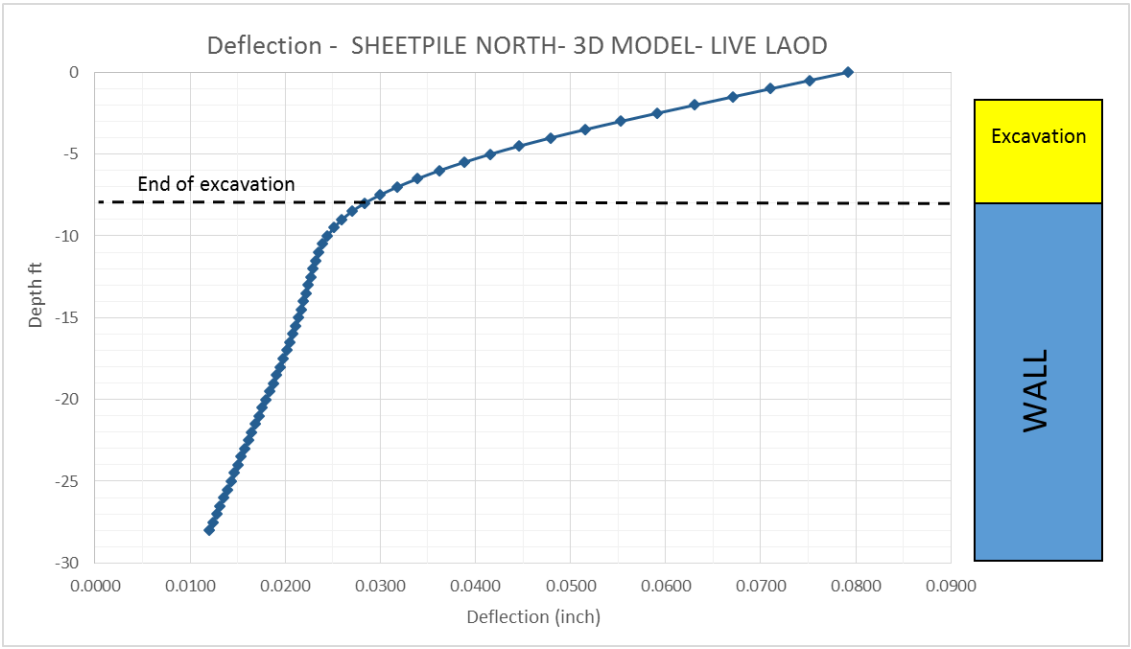

Figure 135. Deflection at the north of the sheet pile wall because of live load

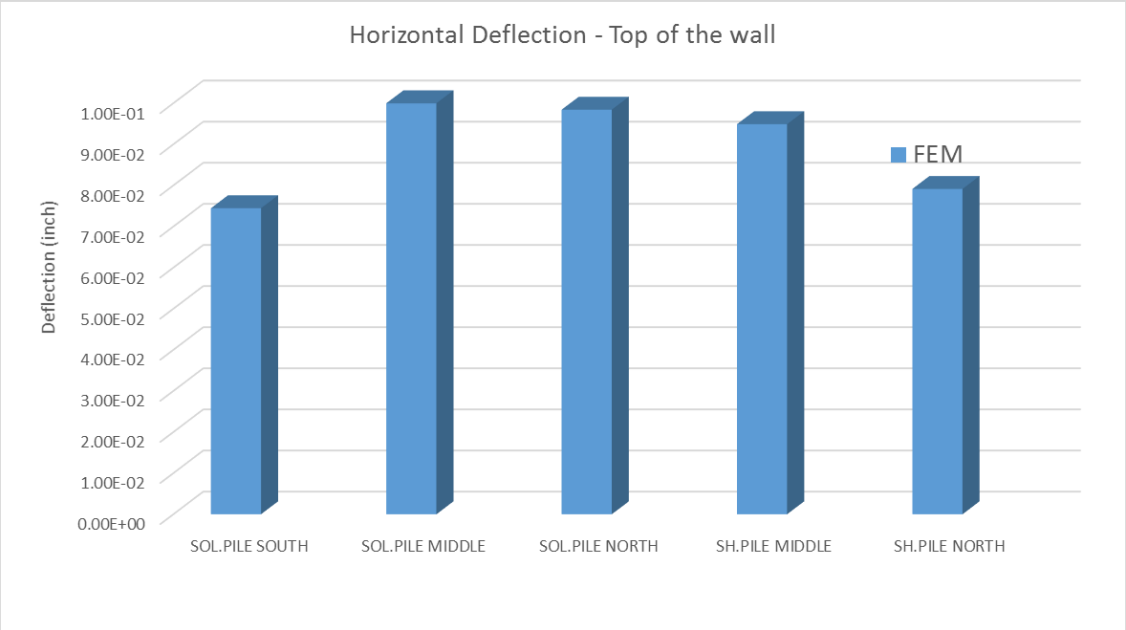

Figure 136. Deflection at different locations because of live loads

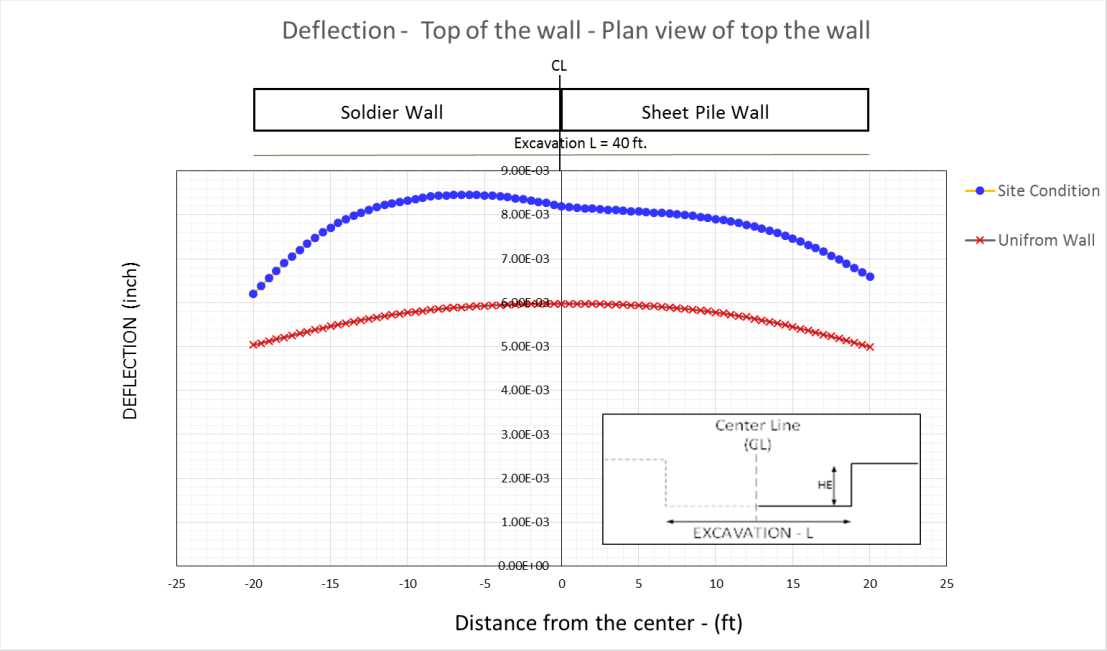

Figure 137. Comparison of deflection for site wall vs. uniform wall – plane view – because of live load

5 PLASTIC DEFORMATION OF SOIL DUE TO CYCLIC LOADING

5.1 Introduction

The fundamental problem that leads to this part of the research is that conventional constitutive models cannot predict the ratcheting behavior of the soil due to the dynamic loads of trains. On this account, the nonlinear isotropic/kinematic hardening model with the Von Mises failure criterion defined by Armstrong and Fredrick (1966) and Chobache (1979, 1991) is used to model the ratcheting behavior of the soil. The model was originally used to model the cyclic behavior of steel under uniaxial cyclic loading. Anastasopoulos et al. (2011) confirmed the accuracy of the nonlinear isotropic/kinematic hardening model in geotechnical engineering applications. In fact, they showed that this model could be used in modeling the cyclic behavior of soils. This section is dedicated to introducing this constitutive model and its application in geotechnical engineering especially as it relates to the current research.

5.2 The Nonlinear Isotropic/Kinematic Hardening Model

In the kinematic hardening model, the Von Mises failure criterion is used along with the nonlinear hardening and the associated plastic flow rule. The pressure-independent yield surface is defined by the function F as below (Equation 19):

$$F = f(\sigma - \alpha) - \sigma^0 = 0 \tag{19}$$

where $\sigma^0$is the yield stress and $f(\sigma - \alpha)$ is the equivalent Von Mises stress with respect to the back stress α. The equivalent Von Mises stress in the deviatoric stress space could be rewritten as in Equation 20:

$$f(\sigma - \alpha) = \sqrt{\frac{3}{2}(S - \alpha^{dev}) : (S - \alpha^{dev})} \quad (20)$$

where S is the deviatoric stress tensor and α^{dev} is the deviatoric part of the backstress tensor. The associated plastic flow rule of the model is definded by Equation 21:

$$\dot{\varepsilon}^{pl} = \dot{\bar{\varepsilon}}^{pl} \frac{\partial F}{\partial \sigma} \quad (21)$$

where $\dot{\varepsilon}^{pl}$ is the rate of plastic flow and $\dot{\bar{\varepsilon}}^{pl}$ is the equivalent plastic strain rate. The nonlinear isotropic/kinematic hardening model consists of two main parts. The first part covered the isotropic hardening behavior of the material, and the second part covered the nonlinear kinematic hardening component of the model. Isotropic hardening section describes the change in the size of yield surface as a function of plastic deformation (Equation 22) (Anastasopoulos et al. 2011, ABAQUS ver. 6.12, 2012):

$$\sigma^0 = \sigma_0 + Q_\infty(1 - e^{-b\bar{\varepsilon}^{pl}}) \quad (22)$$

where σ^0 is defined as the yield surface size, σ_0 is the yield size at zero plastic strain, Q_∞ is the maximum change in the size of yield surface, and b is the rate at which the size of the yield surface changes as plastic stain develops.

The kinematic hardening part of the model describes the translation of the yield surface in stress space through the backstress α. The evolution law of this model consists of two parts that cover the translation of the yield surface in the stress space through the backstress and a relaxation term which introduces the nonlinearity. Equation 23 describes the nonlinear kinematic hardening model (ABAQUS ver. 6.12, 2012):

$$\dot{\alpha}_k = C_k \frac{1}{\sigma^0}(\sigma - \alpha)\dot{\bar{\varepsilon}}^{pl} - \gamma_k \alpha_k \dot{\bar{\varepsilon}}^{pl} \quad (23)$$

where C_k is the initial kinematic hardening modulus and Υ_k determines the rate at which the kinematic hardening modulus decreases with plastic deformation progress.

5.3 Components of the Elastoplastic Constitutive Model

The yield criterion in the elastoplastic constitutive model is defined in Equation 24

$$F = f(\sigma - \alpha) - \sigma^0 = 0$$

$$\sqrt{\frac{3}{2}(\tau_{ij} - \alpha_{ij}) : (\tau_{ij} - \alpha_{ij})} - \sigma^0 = 0 \tag{24}$$

$$\sqrt{\frac{3}{2}(\tau_{ij} - \alpha_{ij}) : (\tau_{ij} - \alpha_{ij})} - \ \sigma_0 + Q_\infty \left(1 - e^{-b\bar{\varepsilon}^{pl}}\right) = 0$$

The total strain increment is derived by adding the elastic strain ($\dot{\varepsilon}_{ij}^{e}$) and the plastic strain ($\dot{\varepsilon}_{ij}^{p}$) as in Equation 25:

$$\dot{\varepsilon}_{ij} = \ \dot{\varepsilon}_{ij}^{e} + \dot{\varepsilon}_{ij}^{p} \tag{25}$$

Since the plastic flow is associated, the plastic flow develops in the normal direction to the yield surface (Equation 26):

$$\dot{\varepsilon}_{ij}^{p} = \dot{\Lambda} \frac{\partial f}{\partial \sigma_{ij}} \tag{26}$$

ABAQUS defined the isotropic hardening rule as in Equation 27:

$$\sigma^0 = \ \sigma_0 + Q_\infty (1 - e^{-b\bar{\varepsilon}^{pl}}) \tag{27}$$

Constitutive law is defined by Equation 28 (Lemaitre and Chaboche 1990, ABAQUS ver. 6.12, 2012):

$$\dot{\alpha}_k = \ C_k \frac{1}{\sigma^0} (\sigma - \alpha) \dot{\bar{\varepsilon}}^{pl} \ - \gamma_k \alpha_{ij} \dot{\bar{\varepsilon}}^{pl} \tag{28}$$

where

$$\dot{\bar{\varepsilon}}^{pl} = \sqrt{\frac{2}{3}\,\dot{\varepsilon}_{ij}^{p}\dot{\varepsilon}_{ij}^{p}} \tag{29}$$

The gradient of yield surface is characterized by Equation 30:

$$\dot{f} = \frac{\partial f}{\partial \tau_{ij}}\,\dot{\tau}_{ij} + \frac{\partial f}{\partial \alpha_{ij}}\,\dot{\alpha}_{ij} + \frac{\partial f}{\partial \sigma^{0}}\,\dot{\sigma}^{0} = 0 \tag{30}$$

and the gradient of yield surface with respect to the deviatoric stress is described by Equation 31:

$$\frac{\partial f}{\partial \tau_{ij}} = \frac{3\,(\tau_{ij} - \alpha_{ij})}{2 * \sqrt{\frac{3}{2}(\tau_{ij} - \alpha_{ij})(\tau_{ij} - \alpha_{ij})}}$$

$$\frac{\partial f}{\partial \alpha_{ij}} = \frac{-3\,(\tau_{ij} - \alpha_{ij})}{2 * \sqrt{\frac{3}{2}(\tau_{ij} - \alpha_{ij})(\tau_{ij} - \alpha_{ij})}} \tag{31}$$

and

$$\frac{\partial f}{\partial \sigma^{0}} = -1$$

$$\dot{\sigma}^{0} = b(Q_{\infty} - \sigma^{0})\dot{\bar{\varepsilon}}^{pl}$$

By substituting Equation 31 into 30 we get Equation 32:

$$\frac{\partial f}{\partial \tau_{ij}}\left(\dot{\tau_{ij}} - \dot{\alpha_{ij}}\right) - \dot{\sigma}^{0} = 0 \tag{32}$$

Using the following general elasticity equation (Equation 33)

$$\dot{\sigma}_{ij} = E_{ijkl}\,\dot{\varepsilon}_{kl}^{e}$$

$$\dot{\sigma}_{ij} = E_{ijkl}\,(\dot{\varepsilon}_{kl} - \dot{\varepsilon}_{kl}^{pl}) \tag{33}$$

$$\dot{\sigma}_{ij} = E_{ijkl}\,(\dot{\varepsilon}_{kl} - \dot{\Lambda}\frac{\partial f}{\partial \sigma_{kl}})$$

and then substituting Equation 33 into Equation 32 we obtain Equation 34:

$$\frac{\partial f}{\partial \sigma_{ij}}\left[E_{ijkl}\left(\dot{\varepsilon}_{kl}-\ \dot{\varepsilon}_{kl}^{pl}\right)-\ C_k\frac{1}{\sigma^0}(\sigma-\alpha)\dot{\bar{\varepsilon}}_{kl}^{pl}+\gamma_k\alpha_{ij}\dot{\bar{\varepsilon}}_{kl}^{pl}\right]-\ \dot{\sigma}^0=0 \tag{34}$$

where

$$\dot{\bar{\varepsilon}}^{pl}=\ \sqrt{\frac{2}{3}\ \dot{\varepsilon}_{ij}^{p}\dot{\varepsilon}_{ij}^{p}}=\ \sqrt{\frac{2}{3}\dot{\Lambda}\frac{\partial f}{\partial \sigma_{ij}}\dot{\Lambda}\frac{\partial f}{\partial \sigma_{ij}}}=\dot{\Lambda}\sqrt{\frac{2}{3}\frac{\partial f}{\partial \sigma_{ij}}\frac{\partial f}{\partial \sigma_{ij}}} \tag{35}$$

Equation 34 could be rewritten as Equation 36, 37, or 38:

$$\begin{aligned}\frac{\partial f}{\partial \sigma_{ij}}\Bigg[&E_{ijkl}\left(\dot{\varepsilon}_{kl}-\ \dot{\varepsilon}_{kl}^{pl}\right)-\ C_k\frac{1}{\sigma^0}\sigma_{ij}\dot{\Lambda}\sqrt{\frac{2}{3}\frac{\partial f}{\partial \sigma_{ij}}\frac{\partial f}{\partial \sigma_{ij}}}+C_k\frac{1}{\sigma^0}\alpha_{ij}\dot{\Lambda}\sqrt{\frac{2}{3}\frac{\partial f}{\partial \sigma_{ij}}\frac{\partial f}{\partial \sigma_{ij}}}\\&+\gamma_k\alpha_{ij}\dot{\Lambda}\sqrt{\frac{2}{3}\frac{\partial f}{\partial \sigma_{ij}}\frac{\partial f}{\partial \sigma_{ij}}}\Bigg]-\ b(Q_\infty-\sigma^0)\dot{\Lambda}\sqrt{\frac{2}{3}\frac{\partial f}{\partial \sigma_{ij}}\frac{\partial f}{\partial \sigma_{ij}}}=0\end{aligned} \tag{36}$$

$$\begin{aligned}&\frac{\partial f}{\partial \sigma_{ij}}E_{ijkl}\dot{\varepsilon}_{kl}-\frac{\partial f}{\partial \sigma_{ij}}E_{ijkl}\dot{\Lambda}\frac{\partial f}{\partial \sigma_{ij}}-\frac{\partial f}{\partial \sigma_{ij}}C_k\frac{1}{\sigma^0}\sigma_{ij}\dot{\Lambda}\sqrt{\frac{2}{3}\frac{\partial f}{\partial \sigma_{ij}}\frac{\partial f}{\partial \sigma_{ij}}}\\&+\frac{\partial f}{\partial \sigma_{ij}}C_k\frac{1}{\sigma^0}\alpha_{ij}\dot{\Lambda}\sqrt{\frac{2}{3}\frac{\partial f}{\partial \sigma_{ij}}\frac{\partial f}{\partial \sigma_{ij}}}+\frac{\partial f}{\partial \sigma_{ij}}\gamma_k\alpha_{ij}\dot{\Lambda}\sqrt{\frac{2}{3}\frac{\partial f}{\partial \sigma_{ij}}\frac{\partial f}{\partial \sigma_{ij}}}\\&-b(Q_\infty-\sigma^0)\dot{\Lambda}\sqrt{\frac{2}{3}\frac{\partial f}{\partial \sigma_{ij}}\frac{\partial f}{\partial \sigma_{ij}}}\end{aligned} \tag{37}$$

(38)

$$\frac{\partial f}{\partial \sigma_{ij}} E_{ijkl} \dot{\varepsilon}_{kl} = \dot{\Lambda} \left[\frac{\partial f}{\partial \sigma_{ij}} E_{ijkl} \frac{\partial f}{\partial \sigma_{ij}} + \frac{\partial f}{\partial \sigma_{ij}} C_k \frac{1}{\sigma^0} (\sigma_{ij} - \alpha_{ij}) \sqrt{\frac{2}{3} \frac{\partial f}{\partial \sigma_{ij}} \frac{\partial f}{\partial \sigma_{ij}}} \right.$$

$$\left. - \frac{\partial f}{\partial \sigma_{ij}} \gamma_k \alpha_{ij} \sqrt{\frac{2}{3} \frac{\partial f}{\partial \sigma_{ij}} \frac{\partial f}{\partial \sigma_{ij}}} + b(Q_\infty - \sigma^0) \sqrt{\frac{2}{3} \frac{\partial f}{\partial \sigma_{ij}} \frac{\partial f}{\partial \sigma_{ij}}} \right]$$

$\dot{\Lambda}$ is a scaler multiplier that controls the magnitude of the plastic strain and can be defined as

$$\dot{\Lambda} = \frac{\frac{\partial f}{\partial \sigma_{ij}} E_{ijkl} \dot{\varepsilon}_{kl}}{H + E_{ijkl} \frac{\partial f}{\partial \sigma_{ij}} \frac{\partial f}{\partial \sigma_{ij}}} \tag{39}$$

where H defines the hardening rule as in Equation 40:

$$H = \frac{\partial f}{\partial \sigma_{ij}} C_k \frac{1}{\sigma^0} (\sigma_{ij} - \alpha_{ij}) \sqrt{\frac{2}{3} \frac{\partial f}{\partial \sigma_{ij}} \frac{\partial f}{\partial \sigma_{ij}}} - \frac{\partial f}{\partial \sigma_{ij}} \gamma_k \alpha_{ij} \sqrt{\frac{2}{3} \frac{\partial f}{\partial \sigma_{ij}} \frac{\partial f}{\partial \sigma_{ij}}} + b(Q_\infty - \sigma^0) \sqrt{\frac{2}{3} \frac{\partial f}{\partial \sigma_{ij}} \frac{\partial f}{\partial \sigma_{ij}}} \tag{40}$$

The general framework of the current elastoplastic model is summarized above. By writing a MATLAB® (R2013a, 2013) code, the behavior of the material under assumed strain increment can be monitored. Using this method, the stress-strain curve of the material for different kind of loads and materials can be derived and compared to the test data in order to check the accuracy of the model. Figure 138 shows a sample stress-strain curve due to cyclic loading.

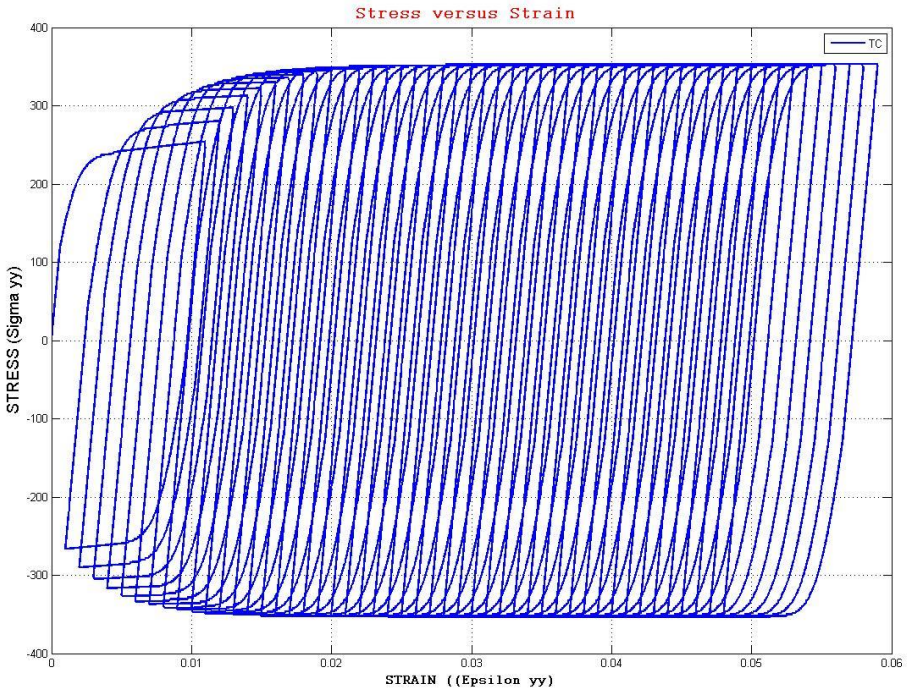

Figure 138. Stress-strain curve from a model of the ratcheting behavior of material

5.4 Model Parameters

The nonlinear isotropic/kinematic hardening model consists of five variables that can be defined as constitutive model input in ABAQUS (ver. 6.12, 2012). These five variables are as follows:

σ_0: The size of the yield surface in the elastic zone

C: The initial hardening modulus

γ: The rate at which the hardening modulus decreases with increasing plastic strain

Q_∞: The maximum increase in the elastic range in loading and unloading

b: The rate at which the maximum size of yield surface is reached as plastic strain develops

In this section, a parametric study completed to show the effects of the five parameters listed above on the stress-strain curve is described. A total of 24 models were developed. Tables 46 to 49 show the input variables and parameters used in these models.

Table 46. Parametric study - varying C

	σ^0	C	ϒ	Q_{max}	b
Model Main	120	218500	1956.6	120	13.2
Model 1	120	54625	1956.6	120	13.2
Model 2	120	109250	1956.6	120	13.2
Model 3	120	163875	1956.6	120	13.2
Model 4	120	273125	1956.6	120	13.2
Model 5	120	327750	1956.6	120	13.2
Model 6	120	437000	1956.6	120	13.2

Table 47. Parametric study - varying Gamma

	σ^0	C	ϒ	Q_{max}	b
Model Main	120	218500	1956.6	120	13.2
Model 7	120	218500	489.15	120	13.2
Model 8	120	218500	978.3	120	13.2
Model 9	120	218500	1467.5	120	13.2
Model 10	120	218500	2445.8	120	13.2
Model 11	120	218500	2934.9	120	13.2
Model 12	120	218500	3913.2	120	13.2

Table 48. Parametric study - varying Q_{max}

	σ^0	C	ϒ	Q_{max}	b
Model Main	120	218500	1956.6	120	13.2
Model 13	120	218500	1956.6	30	13.2
Model 14	120	218500	1956.6	60	13.2
Model 15	120	218500	1956.6	90	13.2
Model 16	120	218500	1956.6	150	13.2
Model 17	120	218500	1956.6	180	13.2
Model 18	120	218500	1956.6	240	13.2

Table 49. Parametric study - varying b

	σ^0	C	ϒ	Q_{max}	b
Model Main	120	218500	1956.6	120	13.2
Model 19	120	218500	1956.6	120	3.3
Model 20	120	218500	1956.6	120	6.6
Model 21	120	218500	1956.6	120	9.9
Model 22	120	218500	1956.6	120	16.5
Model 23	120	218500	1956.6	120	19.8
Model 24	120	218500	1956.6	120	26.4

From the parametric study reported in this section, we can conclude the following:

- Increasing the C increasse the plastic part and decreases the elastic part.
- By increasing γ, the rate of plastic hardening decreases.
- Increasing Q_∞ increased the plastic yield limit.
- By increasing b, the rate at which the plastic yield was reached increased.

The results of these simulations are presented in Figures 139 to 142.

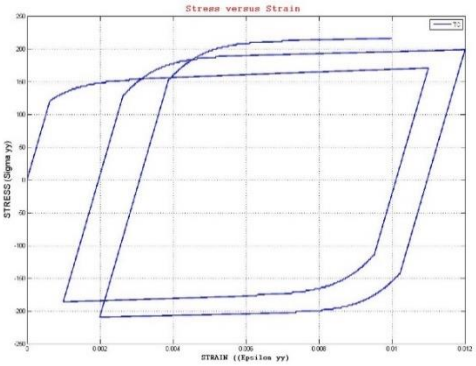

MODEL 1

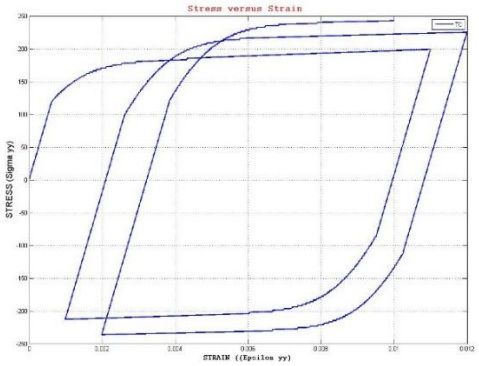

MODEL 2

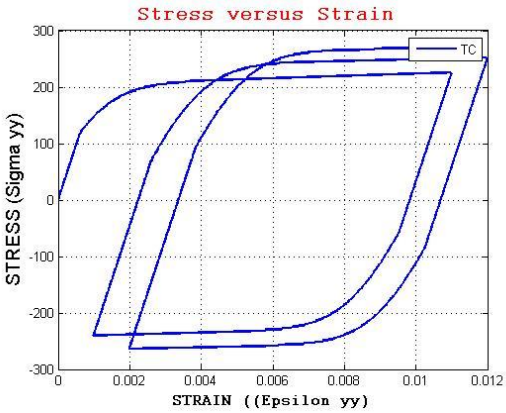

MODEL 3

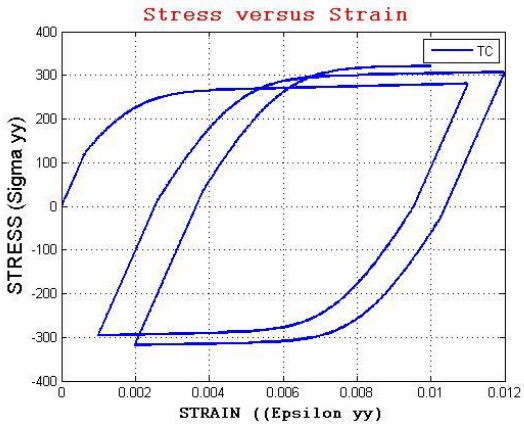

MODEL 4

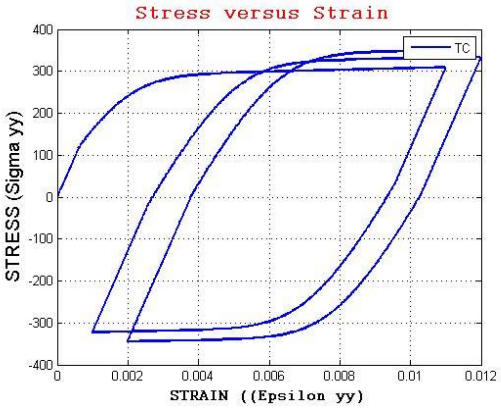

MODEL 5

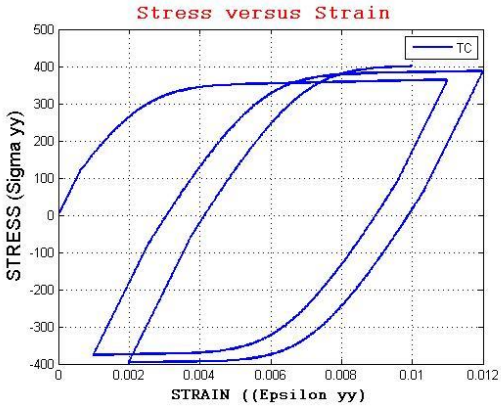

MODEL 6

Figure 139. Effects of C on the cyclic stress-strain curve

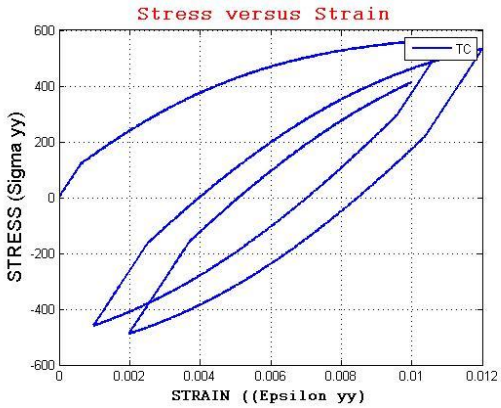

MODEL 7

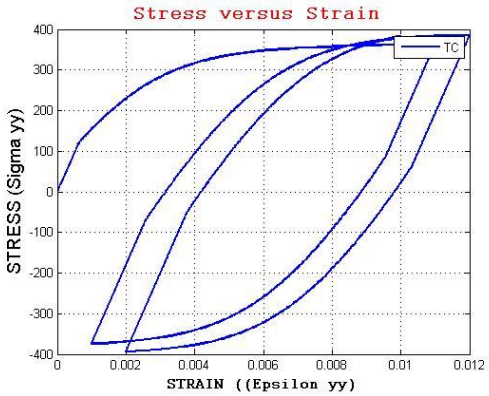

MODEL 8

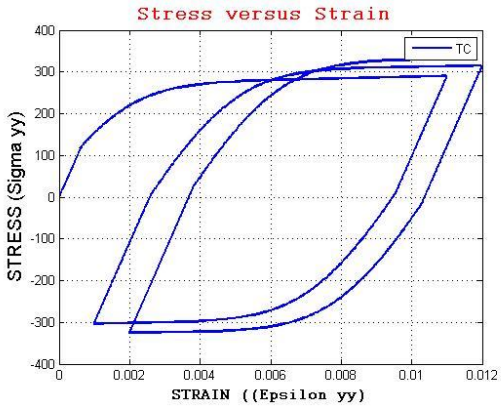

MODEL 9

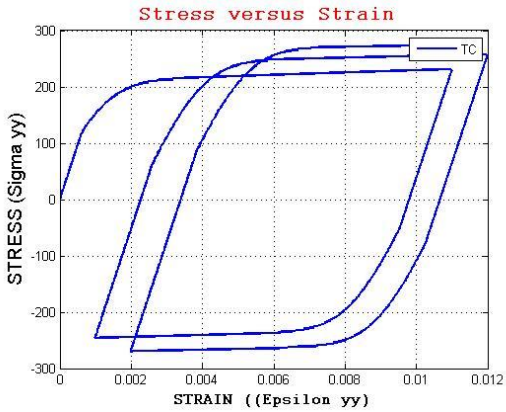

MODEL 10

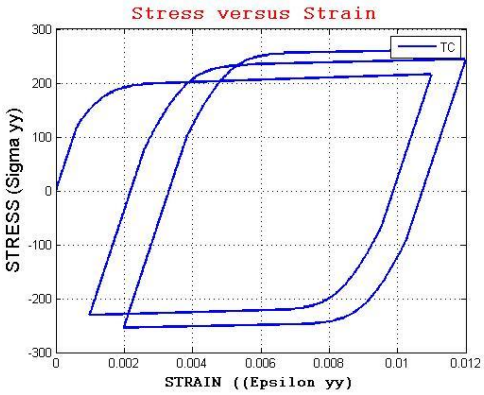

MODEL 11

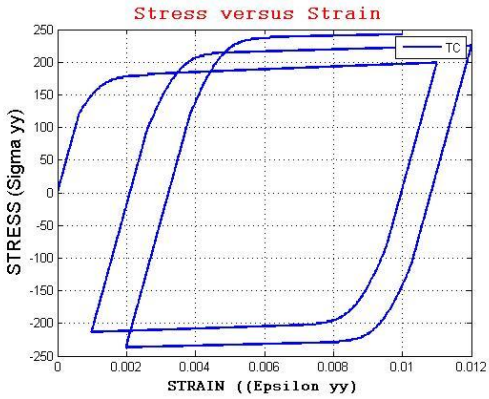

MODEL 12

Figure 140. Effects of ϒ on the cyclic stress-strain curve

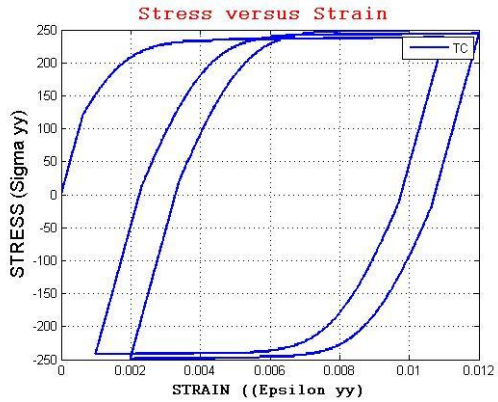

MODEL 13

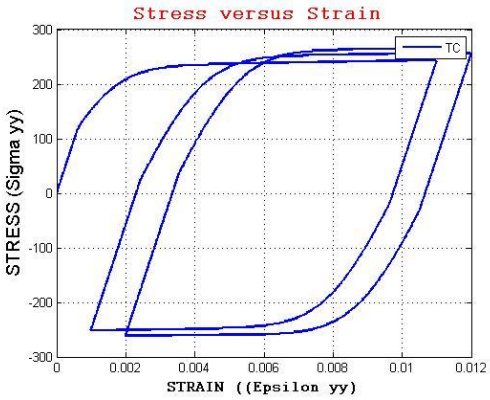

MODEL 14

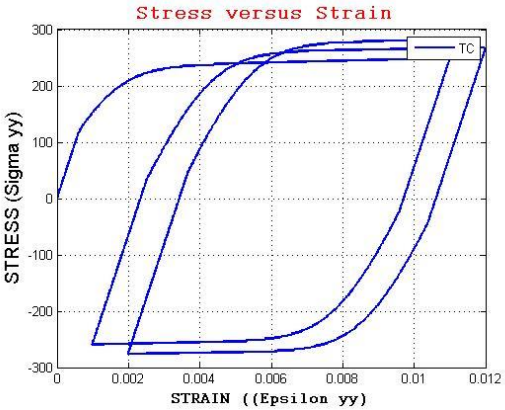

MODEL 15

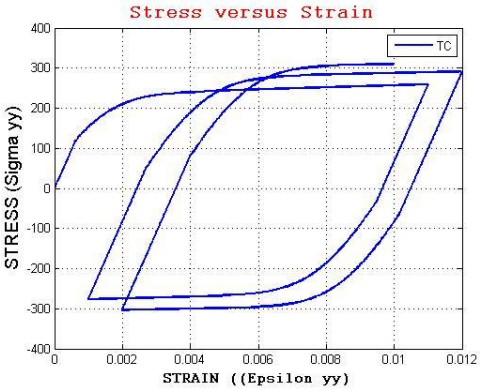

MODEL 16

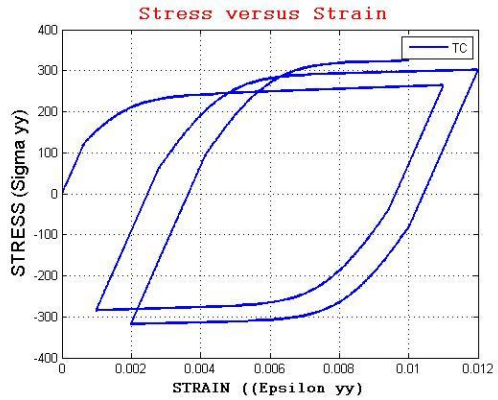

MODEL 17

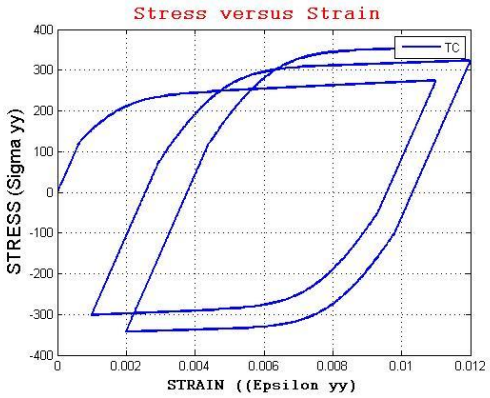

MODEL 18

Figure 141. Effects of Q_{max} on the cyclic stress-strain curve

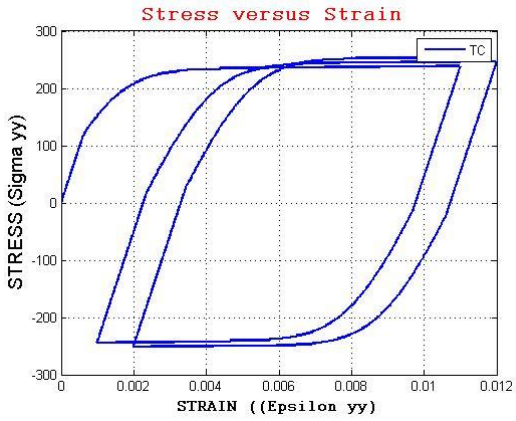

MODEL 19

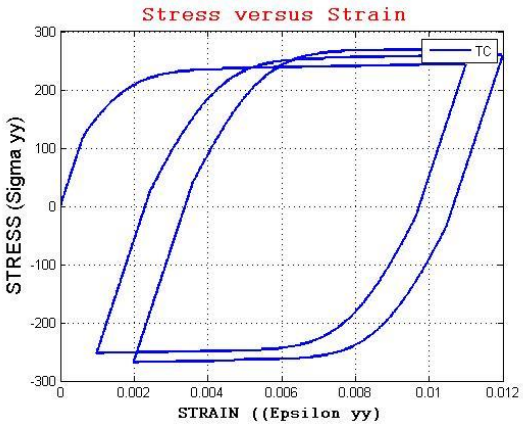

MODEL 20

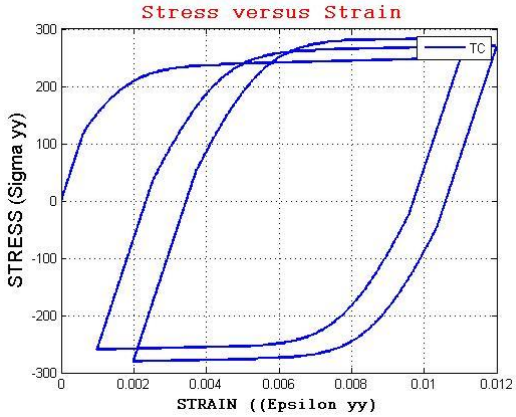

MODEL 21

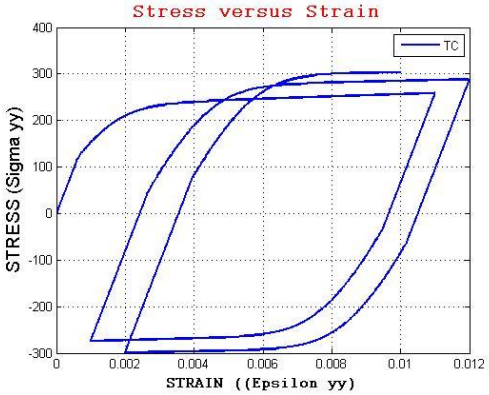

MODEL 22

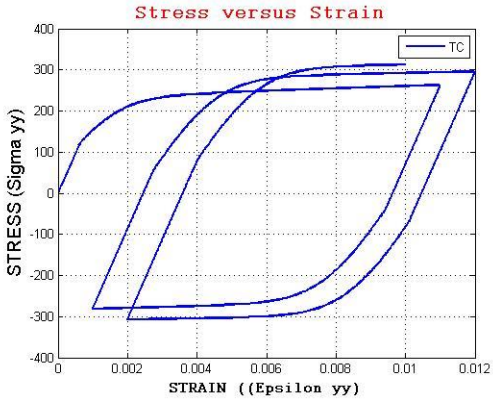

MODEL 23

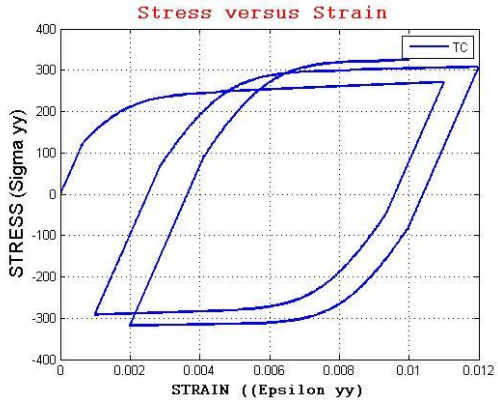

MODEL 24

Figure 142. Effects of b on the cyclic stress-strain curve

5.5 Application of Nonlinear Isotropic/Kinematic Hardening Model in the Current Research

The dynamic behavior of the soil can cause increasing the soil settlement or lateral wall deflection with the passing of time. Because of this behavior, modelling the ratcheting behavior of soil is necessary in order to predict the behaviour of the structures due to the dynamic loadings. The nonlinear isotropic/kinematic hardening model available in ABAQUS (ver. 6.12, 2012) is one of the methods that can be used to model the behavior of materials due to the cyclic loadings (Anastasopoulos et al. 2011). The most difficult part of this method is finding values for the model variables based on the laboratory tests, in other words calibrating the model. In order to calibrate the model, one needs accurate laboratory data. Parameterization of the model is also a challenge. Several methods of finding the parameters of the model have been suggested in the literature (Nguyen Van Do et al. (2015), Anastasopoulos et al. 2011, Mahmoudi et al. 2011, Rezaiee-Pajand et al. 2009, Broggiato et al. 2008) .,.

Unfortunately, data are currently lacking, which delays progress predicting the behavior of soil due to the cyclic loading of trains. Further investigation of the effects of cyclic loading on the behavior of soils in railroads is necessary to improve train safety when excavating around tracks. Because Figure 143 shows a sample of two-dimensional finite element results for the current research using nonlinear isotropic/kinematic hardening constitutive model. As is shown, wall deflection could increase over time due to the dynamic loading of the soil. . In fact, with time, this method could lead to accurately predicting the behavior of the soil.

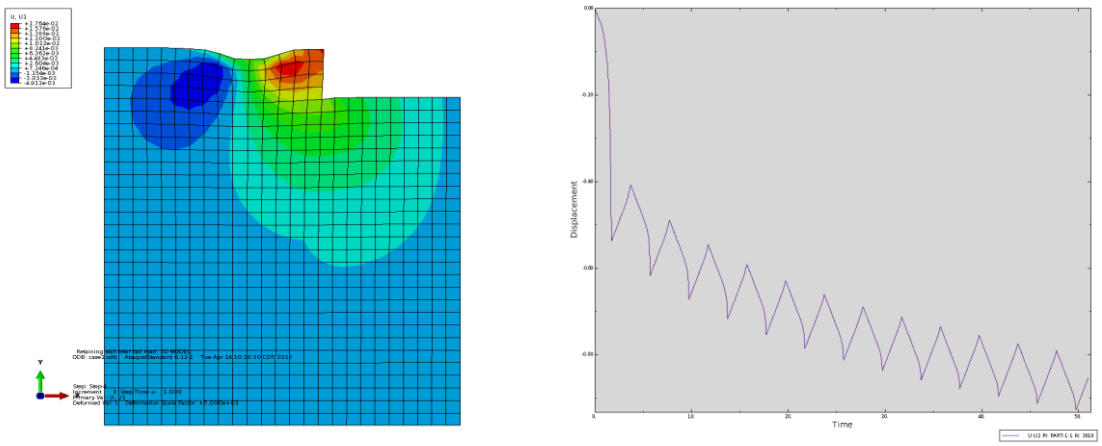

Figure 143. Two-dimensional model of the shoring systems using a cyclic plasticity model

6 CONCLUSIONS AND PROPOSAL FOR FUTURE WORK

6.1 Summary and Conclusions

More than 200 numerical models were developed in this study with the goals of (1) simulating real site conditions, (2) investigating the plane-strain condition, (3) analyzing mesh sensitivity, and finally, (4) conducting parametric studies. The results of the models are summarized in this below:

- With closer proximity of the load to the wall (D/H = 0.5 versus 0.83), deflection increases by up to 25%. The wall length L also significantly influences the deflection response, indicating that 3D effects are significant. For example, for B/H_E =1, the normalized deflection $\Delta u_s / H_E$ at the top of the wall is nearly double for a long wall L/H_E = 12.5 when compared to a short wall of L/H_E = 2.5. The width of the strip load relative to the wall height, B/H_E, is also shown to be significant in all cases.
- Generally, by increasing the wall stiffness, the maximum lateral deflection of the walls decreases. As an example, in the case of live loads in stiff soil, the maximum lateral deflection decreases about 10% when the stiffness of the system is increased by about 22 times the lowest assumed EI in the walls.
- Changing the strength parameter of soil, Young Modulus, has a major effect on the lateral deformation of walls. In fact, the effect of the strength of different soil types is greater than the effect of different wall stiffness on the behavior of the walls.

- Different soil behind and in front of the walls could have major effects on the results of the deflection. Indeed, by increasing the strength parameters of the soil, the lateral deflection of the wall decreases. By increasing the Young modulus of soil about 66 times, the total deflection of the wall decreases by about 80 times.
- In some cases, especially in stiff soil, the deflection of the wall increases as the the flexural rigidity EI increases. This phenomenon occurs because of different shapes of deflection and different deflection trends in rigid and soft walls. In rigid walls, the whole body of the wall rotates as a single body, and the maximum deflection occurs at top of the wall. In contrast, flexible walls have a tendency to bend, and the maximum lateral deflection happens at the middle of the wall.
- The study of the lateral deflection of the walls demonstrates that wall deflection can be classified into two main categories: rigid body motion or rigid deflection and flexible deflection. In rigid deflection, the whole body of the wall moves and rotates. In flexible deflection, the walls act like a beam and bends along the height of the wall. Only the flexible deflection of the walls can be predicted by Boussinesq method;It cannot predict rigid deflection of wals. This should be taken into account in designs.
- Due to the finite stiffness E_s of the soil, lateral deflections due to live loads occur even in the absence of excavation. The displacement $\Delta u_{x\text{-}no\_wall}$ can be interpreted as the displacement profile at distance D from the edge of the strip load, located far from the wall in the y-direction. As expected, this displacement is larger in soft soil than in stiff soil.

- After excavation, the lateral deflections of the walls increase. The shape of the wall after excavation, the absolute value of the deflection, and the location of the deflection completely depend on the soil deflection properties before excavation.
- Some tension stresses and negative deflection exust at the ground surface even when there is no excavation. This occurrence could be explained by Hooke's law when σ_Z is much larger than σ_X and σ_Y. In this condition, ϵ_x is negative and some tension stresses occurr at the ground surface.

$$\text{Hooke's law:} \quad \epsilon_x = \frac{1}{E}\left(\sigma_X - \mu\sigma_Y - \mu\sigma_Z\right)$$

- Results of parametric studies show the displacement at the base of the excavation to be roughly equal to the lateral displacement that would have occurred in the soil mass if no wall or excavation were present.
- Looking at the relative deflection of the wall demonstrated that the maximum relative displacement happens at top of the wall, which is in agreement with beam theory.
- The ratio of the depth of excavation to the length of the wall (L/H_E) plays a crucial rule in the wall's behavior. Based on this finding, in some cases plane-strain models predict more deflection than 3D finite element models, and in other cases, the plane-strain method underestimates the lateral deflection of the walls. For instance, in most of the cases when D/H is equal to 0.83 or 1.25, the deflections predicted by 3D analysis are greater than the deflection predicted by the plane-strain method. The maximum difference is around 45% for the case of B/H = 1

with the minimum about 30% for B/H = 0.66. Furthermore, both parameters B/H and D/H can have a major effect on the behavior of the walls.

- The models illustrate that the ratios $H_E/L \approx 0.1$ for the case of B/H = 1 and H_E/L = 0.12 for the case of B/H = 0.66 are the critical values at which the greatest differences between deflections calculated using 3d models and those calculated with the plane-strain models materialize.
- Generally, in the same ratio of D/H and B/H, the ratio of deflections calculated in 3D models compared to plane-strain models in stiff soil are higher than the ones in soft soil.
- Comparison of the maximum horizontal deflection according to the Boussinesq theory and the finite element model demonstrated that the Boussinesq theory predicts larger deflections in stiff soil while underestimating deflections in soft soil. It means the Boussinesq theory is more conservative for stiff soil. Moreover, the parameter B/H can have a major effect on the prediction of horizontal deflection. As an example, in the case of B/H = 0.66, the lateral deflection predicted by Boussinesq theory falls exactly between predicted lateral deflection by finite element for soft soil and stiff soil. But for B/H = 1, in some cases, the Boussinesq theory underestimates the lateral deflection for stiff soil. Therefore, the width of the strip load relative to the wall height, B/HE, is also seen to have noticeable effects on the results.

- By increasing the depth of the excavation, the walls' lateral deflections increase. For example, by increasing depth of excavation from 8 ft. to 12 ft., the lateral deflection increases about 30% in the sheet pile wall due solely to the live load.
- By increasing the distance between the load and the wall, the lateral deflections of the wall decrease. For instance, by increasing D from 6 ft. to 10 ft., the lateral deflection decreases about 15%.
- Comparison of the deflection of the real sheet pile wall sections and rectangular sections used in ABAQUS models reveals a difference between the deflections predicted by different models. In fact, a factor named shape factor should be considered in calculations to predict the lateral deflection of sheet pile walls.

6.2 Future Research

Excavation near railroads results in larger vertical deflection in the subsoil due to the combination of static and dynamic loads. More lateral wall deflection due to dynamic live loads can cause major problems in designing of temporary shoring systems and retaining walls. In addition, in practice the depth of wall embedment has been chosen two times of the depth of excavation that could be studied and modified to have more economical designs. Additionally, modeling of the popular soldier pile wall is complex and has not yet been completely studied. Different deflections in lagging in comparison to the piles can cause more vertical settlement and thus more problems. Studying the effect of pile spacing on the behavior of the soldier pile walls can result in more economical designs. The sheet pile wall is, practically speaking, uniform along its length, so strains and deflections are measured at the same location. By contrast, soil arching behind the

lagging of a soldier pile wall causes earth pressure redistribution as shown in Figure 144, where the maximum deflection occurs at mid-span and the maximum earth pressure at end-span. Therefore, for the soldier pile/timber lagging wall, lateral deflections and rail displacements need to be measured at the wall's mid-span while strains are measured on the H-piles. The effects of soil arching on the behavior of soldier walls and differential deflection along the wall's length have not been studied completely and more research in these areas is needed.

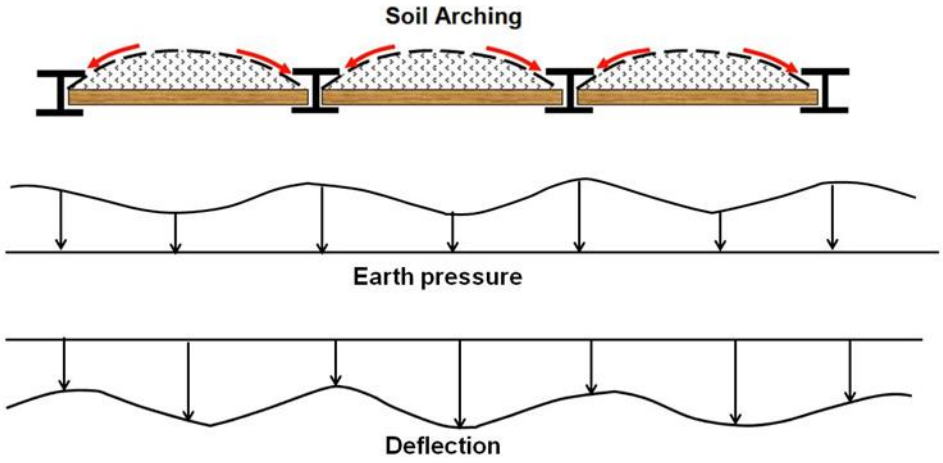

Figure 144. Earth pressure and deflection in a soldier pile wall with lagging

Future research approaches could be based on the finite element modeling. The 3D finite element models allow researchers to study the effect of dynamic train live loads on the behavior of temporary shoring systems. In future research, live loads of trains near an excavation could be modeled by using LSDYNA, a finite element software. Results of dynamic lateral deflection models in the software could be compared to the results of static

lateral deflection and of some conventional methods such as the Boussinesq theory to propose a ratio of dynamic deflection to static deflection. In fact, this ratio could help the designer better understand dynamic lateral deflection and help them create safer designs. Also, 3D finite element models made using ABAQUS (ver. 6.12, 2012) could be used to study the effect of different depths of embedment, different pile spacing, and different lateral deflection at piles and lagging in soldier pile walls. Finally, based on the results achieved by finite element methods, some recommendations could be proposed to develop an improved understanding of the effects of live loads on shoring walls to support possible modifications of existing design procedures.

To sum up, the anticipated outcomes of future numerical simulations could be to investigate the following relationships:

- The effects of dynamic live load surcharge on wall lateral deflection in comparison with static lateral deflection;
- The effects of the different depths of embedment on the wall lateral deflection;
- The effects of different lateral deflections at piles and laggings on vertical settlement of the tracks;
- The effects of soil arching on the behavior of soldier wall piles and wall lateral deflection; and
- The effects of different pile spacing on the lateral deflection of the soldier walls.

More knowledge and better understanding of said relationships will help create safer, more economical railroads that allow faster and cleaner transport of goods and people with fewer risks and accidents.

REFERENCES

AASHTO. (1994). LRFD specification for highway bridges, 1st Ed., Washington, DC.

AASHTO (2010). AASHTO LRFD Bridge Design Specification. 5th, Editon, 626pp

Abaqus, A. B. A. Q. U. S. (2012). Standard: user's manual version 6.12.Simulia, USA.

Anastasopoulos, I., Gelagoti, F., Kourkoulis, R., & Gazetas, G. (2011). Simplified constitutive model for simulation of cyclic response of shallow foundations: validation against laboratory tests. Journal of Geotechnical and Geoenvironmental Engineering, 137(12), 1154-1168.

Association of American Railroads (2012). Class I Railroad Statistics. Association of American Railroads.

Association of American Railroads (2012). A Short History of U.S. Freight Railroads. Association of American Railroads.

Association of American Railroads (2012). An Overview of America's Freight Railroads. Association of American Railroads.

Association of American Railroads (2012). Freight Railroads in United States. Association of American Railroads.

Association of American Railroads (2012). Freight Railroads in Texas. Association of American Railroads.

ASTM D2216. (1998). Standard Test Method for Laboratory Determination of Water (Moisture) Content of Soil and Rock by Mass. Philadelphia: American Society for Testing and Materials.

ASTM D6913-04 (2009). Standard test methods for particle size distribution (gradation) of soils using sieve analysis. West Conshohocken, PA: ASTM International (Accessed: 2014. http://www. astm. org/Standards/D6913. htm).

ASTM D2217-85 (1998). Standard Practice for Wet Preparation of Soil Samples for Particle-Size Analysis and Determination of Soil Constants, ASTM International, West Conshohocken, PA, 1998, DOI: 10.1520/D2217-85R98, www.astm.org.

ASTM D422 – 63 (2007). Standard Test Method for Particle-Size Analysis of Soils, ASTM International, West Conshohocken, PA, 2007, DOI: 10.1520/D0422, www.astm.org.

ASTM D421 – 85 (2007). Standard Practice for Dry Preparation of Soil Samples for Particle-Size Analysis and Determination of Soil Constants, ASTM International, West Conshohocken, PA, DOI: 10.1520/D0421-85R07, www.astm.org.

ASTM C136 – 06 (1984), Standard Test Method for Sieve Analysis of Fine and Coarse Aggregates, ASTM International, West Conshohocken, PA, DOI: 10.1520/C0136-06, www.astm.org.

ASTM D4318 – 10 (2003), Standard Test Methods for Liquid Limit, Plastic Limit, and Plasticity Index of Soils, ASTM International, West Conshohocken, PA, DOI: 10.1520/D4318, www.astm.org.

ASTM D1556 – 07 (2207), Standard Test Method for Density and Unit Weight of Soil in Place by the Sand-Cone Method, ASTM International, West Conshohocken, PA, DOI: 10.1520/D1556-07, www.astm.org.

ASTM D2573 – 08 (2008), Standard Test Method for Field Vane Shear Test in Cohesive Soil, ASTM International, West Conshohocken, PA, DOI: 10.1520/D2573-08, www.astm.org.

ASTM D1587 – 08 (2012). Standard Practice for Thin-Walled Tube Sampling of Soils for Geotechnical Purposes, ASTM International, West Conshohocken, PA, 2012, DOI: 10.1520/D1587-08R12E01, www.astm.org

ASTM D2166 / D2166M – 13 (2013), Standard Test Method for Unconfined Compressive Strength of Cohesive Soil, ASTM International, West Conshohocken, PA, DOI: 10.1520/D2166_D2166M, www.astm.org.

AREMA (2010). Manual for Railway Engineering, American Railway Engineering and Maintenance-of-Way Association, Volume 2: 1312pp.

Bowles, J.E. (1988). Foundation Analysis and Design. 4th ed., McGraw-Hill Book Company, New York.

Broggiato, G. B., Campana, F., & Cortese, L. (2008). The Chaboche nonlinear kinematic hardening model: calibration methodology and validation. Meccanica, 43(2), 115-124.

California Department of Transportation, (2011). Trenching and Shoring Manual, CalTrans, Revision 1

Chaboche, J. L., Dang Van, K., & Cordier, G. (1979). Modelization of the strain memory effect on the cyclic hardening of 316 stainless steel. In Structural mechanics in reactor technology. Transactions. Vol. L.

Chaboche, J. L. (1986). Time-independent constitutive theories for cyclic plasticity. International Journal of plasticity, 2(2), 149-188.

Chaboche, J. L. (1989). Constitutive equations for cyclic plasticity and cyclic viscoplasticity. International journal of plasticity, 5(3), 247-302.

Chaboche, J. L. (1991). On some modifications of kinematic hardening to improve the description of ratchetting effects. International journal of plasticity, 7(7), 661-678.

Chang, M. F. (1997). Lateral earth pressures behind rotating walls. Canadian Geotechnical Journal, 34(4), 498-509.

Chung R. Song, Alexander Cheng. Ahmed Al-Ostaz., & Raju Mantena. (2012). Structural, Material, and Geotechnical Solutions to Levee and Floodwall Construction and Retrofitting-VOLUME III STRUCTURAL SOLUTIONS. OAK RIDGE NATIONAL LABORATORY.

Clough, G. W., and O'Rourke, T. D. (1990). Construction-induced movements of in situ walls., Proceeding of Design and performance of Earth Retaining Structures, ASCE Special Conference, Ithaca, New York, 430-470pp.

Clough, G. W., and J. M. Duncan. (1991). Earth Pressures. Foundation Engineering Handbook, 2nd Edition. H. Y. Fang, ed. Van Nostrand Reinhold, New York, NY, Chap. 6.

Esmaeili, M., & Fatollahzadeh, A. (2012). Effect of Train Live Load on Railway Bridge Abutments. Journal of Bridge Engineering, 1, 279.

Frederick, C. O., & Armstrong, P. J. (2007). A mathematical representation of the multiaxial Bauschinger effect. Materials at High Temperatures, 24(1), 1-26.

Georgiadis, M., & Anagnostopoulos, C. (1998). Lateral pressure on sheet pile walls due to strip load. Journal of geotechnical and geoenvironmental engineering, 124(1), 95-98.

Google Inc. (2013). Google Earth. Available from https://www.google.com/ maps

Greco, V. R. (2006). Lateral earth pressure due to backfill subject to a strip of surcharge, Geotechnical and Geological Engineering (2006) 24: 615–636.

GTS - Guidelines for Temporary shoring (2004). Burlington North Santa Fe Railway and Union Pacific. 25pp

Motta, E. (1994). Generalized coulomb active-earth pressure for distanced surcharge, Journal of Geotechnical Engineering, 120 (6) : 1072-1079.

Hsieh, P. G., and Ou, C.-Y. (1998). Shape of ground surface settlement profiles caused by excavation, Canadian Geotechnical Journal, 1004-1017pp.

Huang, C. C., Meng, F. Y., Chou, Y. C. (1999). The effect of the bending rigidity of a wall on lateral pressure distribution, Canadian Geotechnical Journal, 36: 1039-1055.

Kim, J. S. and Barker, R. M. (2002). Effect of live load surcharge on retaining walls and abutments, Journal of Geotechnical and Geoenvironmental Engineering, Vol. 128, No. 10, October 1, 2002, 803-813

Kung, G. T., Juang, C. H., Hsiao, E. C., & Hashash, Y. M. (2007). Simplified model for wall deflection and ground-surface settlement caused by braced excavation in clays. Journal of geotechnical and geoenvironmental engineering, 133(6), 731-747.

International Union of Railways. (2006). "Loads to be considered in railway bridge design." UIC Code 776-1 R, 5th Ed., International Union of Railways, Paris

Liu, X., Saat, M., & Barkan, C. (2012). Analysis of causes of major train derailment and their effect on accident rates. Transportation Research Record: Journal of the Transportation Research Board, (2289), 154-163.

Mahmoudi, A. H., Pezeshki-Najafabadi, S. M., & Badnava, H. (2011). Parameter determination of Chaboche kinematic hardening model using a multi objective Genetic Algorithm. Computational Materials Science, 50(3), 1114-1122.

MANUAL, E. (1989). Retaining and Flood Walls. US Army.

MATLAB and Statistics Toolbox Release 2013a, (2013), The MathWorks, Inc., Natick, Massachusetts, United States.

Ou, C. Y., Hsieh, P. G., and Chiou, D. C. (1993). Characteristic of ground surface settlement during excavation, Canadian Geotechnical Journal, 30 (5): 758-767pp.

Peck, R. B. (1969). Deep excavation tunneling in soft ground. Proceedings of the 7th International Conference on Soil Mechanics and Foundation Engineering, State-of-the-Art-Volume, Mexico City, 225-290pp.

Poh, T. Y., Goh, A. T. C., & Wong, I. H. (2001). Ground movements associated with wall construction: case histories. Journal of geotechnical and geoenvironmental engineering, 127(12), 1061-1069.

Rezaiee-Pajand, M., & Sinaie, S. (2009). On the calibration of the Chaboche hardening model and a modified hardening rule for uniaxial ratcheting prediction. International Journal of Solids and Structures, 46(16), 3009-3017.

Rowe, P. W. (1950). The distribution of lateral earth pressure on a stiff wall due to surcharge., Civil Engineering and Public Works Review, 45 (532) : 654-657pp.

Sherif, M. A., Fang, Y. S., and Sherif, R. I. (1984). KA and Ko behind rotating and non-yielding walls, Journal of Geotechnical Engineering, ASCE, 110 (1): 41-56pp.

Smethurst, J. A., and Powrie, W. (2007). Monitoring and analysis of discrete bending piles used to stabilize a railway embankment, Geotechnique, 57 (8): 663-677pp.

Tatsuoka, F., Tateyama, M., and Koseki, J. (1996). Performance of soil retaining walls for railway embankments, Special Issue of Soils and Foundations, 311-324pp.

U.S. Army Corps of Engineers (1989). Engineering and Design: Retaining and Flood Walls, CECW-ED Engineer Manual 1110-2-2502, 448.

Van Do, V. N., Lee, C. H., & Chang, K. H. (2015). A constitutive model for uniaxial/multiaxial ratcheting behavior of a duplex stainless steel. Materials & Design, 65, 1161-1171.

Wang, Z. W., Ng, C. W., & Liu, G. B. (2005). Characteristics of wall deflections and ground surface settlements in Shanghai. Canadian geotechnical journal, 42(5), 1243-1254.

Wang, C. D. (2007). Lateral force and centroid location caused by horizontal and vertical surcharge strip loads on a cross-anisotropic backfill. International Journal for Numerical and Analytical Methods in Geomechanics, 31(13), 1443-1475.

Wang, C. D. (2007). Lateral force induced by rectangular surcharge loads on a cross-anisotropic backfill. Journal of Geotechnical and Geoenvironmental Engineering, 133(10), 1259-1276.